Processing and interpretation of reflection seismic data from Isfjorden, Svalbard

Master of Science thesis

Ingrid Haugland

Department of Earth Science

University of Bergen

June 2022

Abstract

The geology of the present-day Svalbard is complex and has formed through several million years of repeated episodes of orogeneses, uplift, deformation and erosion. This has resulted in complex deformation structures and fault zones, as well as an abnormal high seabed velocity (>4.5 km/s). These factors represent a challenge for both processing and interpretation. This study attempts to process and interpret four 2D multichannel seismic lines that were acquired in inner Isfjorden, Sassenfjorden and Nordfjorden during the 2002 SVALEX student course. The lines include the major N-S trending Billefjorden Fault Zone (BFZ) in Sassenfjorden and the Blomesletta Fault in Nordfjorden.

The seismic data was initially contaminated by strong and short-interval multiples that almost completely hid the primary reflections. The main focus during processing was to attenuate these in the best possible way to obtain a multiple-free seismic image without significantly reducing the overall data quality. This was approached by the application of various processing sequences, in which deconvolution and f-k filtering were essential and applied several times. Stacking and muting also had positive effects in reducing the remaining multiple energy.

Stratigraphic units from the seabed till basement have been interpreted, which include the base Jurassic, Triassic, Permian, Carboniferous and Devonian sedimentary successions, and the crystalline basement "Hecla Hoek". The fault geometry of the BFZ has been interpreted as a major reverse western fault and normal eastern fault, both dipping steeply to the east. The BFZ has likely been reactivated several times, but its formation is linked to the Caledonian Orogeny that lasted from Early Ordovician to Early Devonian. The reverse fault displaces the basement rock against the Devonian basin, while the normal fault coexists with the presence of a distinct syn-rift half-graben structure, formed during the Caledonian collapse. The Blomesletta Fault is interpreted as a reverse fault, overlain by thrust faults that root in a décollement in the lower Permian unit. The décollement is linked to the formation of the West Spitsbergen Fold-and-Thrust belt in the Tertiary. Two steep east-verging normal faults are identified in the basement rock, which are likely to be part of a larger fault-bounded rift basin that characterises the Hecla Hoek. A layer-parallel igneous sill intrusion is interpreted along the top-Permian reflector.

Acknowledgement

Table of contents

Table of figures

Tables

Abbreviations

AI – acoustic impedance

BFZ – Billefjorden Fault Zone

BP – band-pass filter

BR – band-reject filter

CDP – common-depth-point

CMP – common-mid-point

CTB – Central Tertiary Basin

DMO – dip-move-out

HFC – Hornsund Fault Complex

HP – high-pass filter

LP – low-pass filter

Ma – million years ago

NMO – normal moveout

R_C – reflection coefficient

RMS – root mean square

TWT – two-way traveltime

WSFTB – West Spitsbergen Fold-and-Thrust Belt

1 Introduction

1.1 Study area and seismic data

Svalbard is a part of an archipelago of islands situated on the north-western corner of the Eurasian plate, on the Barents Sea Shelf, between 76°N - 81°N and 10°E - 35°E (Fookes, 2008). It is surrounded by sea, with the Barents Sea to the east, the Artic Ocean to the north and the Norwegian-Greenland Sea to the west. Svalbard offers a large and well-preserved geological diversity. The stratigraphic successions are more or less complete, ranging from Late Precambrian till present. The artic climate of Svalbard leaves about 60% of the landmass covered by glaciers (Hjelle, 1993), while the remaining land shows unusually well-exposed geology due to little soil and no woodland. These factors combined provide unique insight to the geological evolution of Svalbard (Worsley, 1986; Hjelle 1993; Fookes, 2008).

The study area is located in inner Isfjorden, Sassenfjorden and Nordfjorden. Several 2D multichannel seismic lines were collected as a part of the SVALEX 2002 student course (Mjelde, 2003). This study will use four of these seismic lines, which includes line 3, line 4, line 5 and line 6. An overview of the study area is given in Figure 1.1.

Figure 1.1: Overview of the study area. Map A gives a large-scale overview of Svalbard, while map B is a close-up of the study area in inner Isfjorden, Nordfjorden and Sassenfjorden. The red lines indicate the multichannel seismic lines that are used in this study, while the arrows indicate the shooting direction. The figure is modified from Norsk Polarinstitutt (2022).

1.2 Aim of study

The geology of Svalbard has been exposed to deformation, uplift and erosion repeatably through several tens of millions of years. This has resulted in a complex geology and an unusual hard sea-bottom. In marine seismic this represents a challenge of strong multiples that overshadow primary energy from real geological structures. This study focuses on two aspects. First, the aim is to enable a better understanding of the challenges related to sea-bottom multiples in shallow-marine seismic processing and how to attenuate these to get the best possible seismic image. Second, to enable a better understanding of the subsurface geology of Isfjorden through interpretation of 2D seismic data. Related background studies will be actively used and connected to new observations, in order to obtain the best possible interpretation of the stratigraphic and structural features of the area. This study will discuss structural interpretation options of the large-scale Billefjorden Fault Zone (BFZ) and the Blomesletta Fault.

2 Geological framework

This chapter will give an overview of the tectonic setting of the present-day Svalbard and the geological evolution that formed the archipelago. The main deformation structures will be included, followed by the stratigraphy of the study area, to give an understanding of the geological framework of Svalbard.

2.1 Tectonic setting

Svalbard is the only part of the Barents Sea shelf that is exposed, which makes the archipelago an excellent site to study the geological evolution of the area. The exposure of the islands is a result of the uplift during Late Mesozoic and Cenozoic crustal movements. A bathymetric map of the North Atlantic is given in Figure 2.1. It shows that the Eurasian basin (EB) is located north of Svalbard, which has a steep and passive continental margin. The Yermak Plateau (YP) is to the NW of the archipelago and is thought to have formed by hotspots in the Cretaceous. Identification of numerous Cretaceous sills and dykes in Svalbard is believed to be related to this magmatism (Dallmann, 2015). The Hornsund Fault Complex (HFC) and Greenland Fracture Zone (GF) are continental transform fault systems located offshore to the west of Svalbard. These formed as a response to the seafloor spreading in the North Atlantic, which separated the Barents Sea Shelf from Greenland. The Knipovich Ridge is a structurally complex area with a central oceanic spreading ridge segmented by several transform faults. The Barents Sea Shelf is a platform area located SE of Svalbard, mainly consisting of sedimentary basins and highs. These formed through episodes of transform faulting and crustal extensions during the formation of the Atlantic Ocean (Dallmann, 2015).
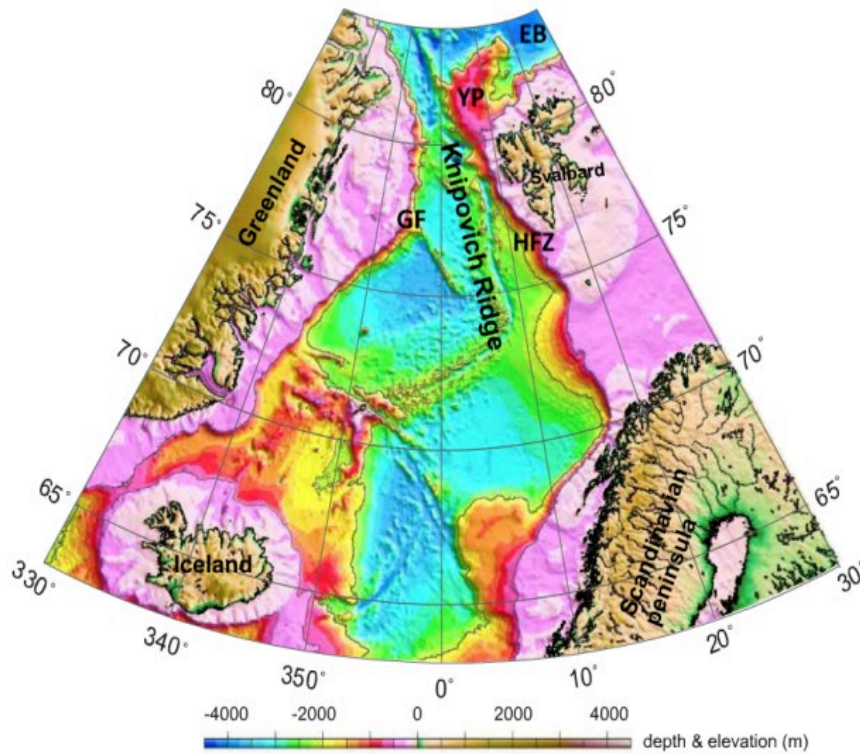
Figure 2.1: Bathymetric map of the North Atlantic, modified from Kandilarov et al. (2008). Eurasian Basin (EB), Yermak Plateau (YP), Greenland Fracture Zone (GF), Hornsund Fault Complex (HFC).

The geology of Svalbard is characterised by distinct, long-lived NNW-SSE trending fault zones. These have a long history of movements extending back to the Late Devonian (Worsley, 1986). The major fault zones, such as the BFZ, have been responsible for the distribution of depositional areas (Dallmann, 2015). The geological structure of Svalbard is strongly influenced by the West Spitsbergen Fold-and-Thrust Belt (WSFTB) that formed in the Early Eocene. Major E-NE-directed folding and thrusting formed a complex fold-and-thrust belt in Western Spitsbergen, from Kongsfjorden in the north to Sørkapp in the south. A "thick-skinned" fold-thrust complex formed in the western hinterland, exposing the basement strata, while a "thin-skinned" or foreland zone formed in the east with a decreasing rate of deformation (Dallmann, 2015). The central zone part of the foreland zone is characterised by fold-thrust units above décollements, while the eastern zone is a frontal duplex system that is bounded by the BFZ and Lomfjorden Fault Zone (Bergh et al., 1997). Isfjorden, the largest fjord in Svalbard, is crossing central parts of the WSFTB in an NE-SW direction. The following figure (Figure 2.2) displays a geological map of the present-day Svalbard.
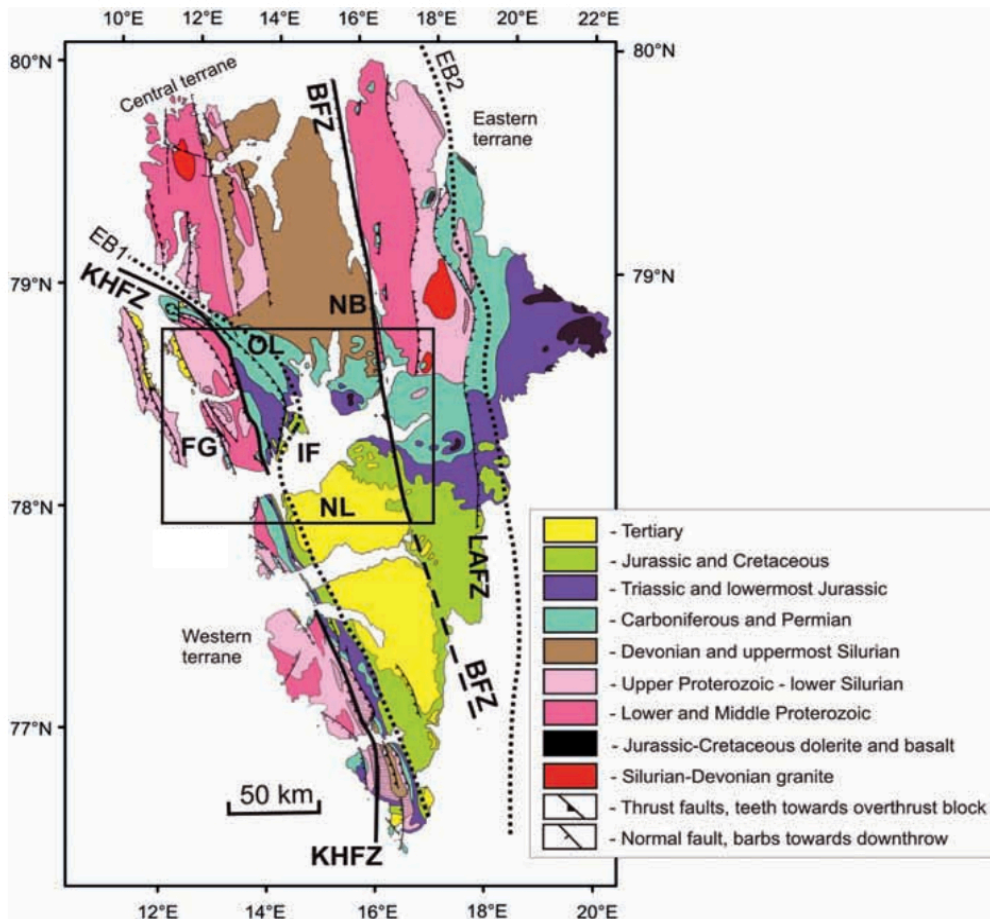
Figure 2.2: Geological map of Svalbard, highlighting the main geological features of the archipelago. Kongsfjorden–Hansbreen Fault Zone (KHFZ), Billefjorden Fault Zone (BFZ), Lomfjorden–Agardbukta Fault Zone (LAFZ), Forlandsundet Graben (FG), Oscar II Land (OL), Isfjorden (IF), Nordfjorden block (NB); Nordenskiöld Land (NL), western boundary of the WSTFB (EB1), eastern boundary of the WSTFB (EB2). Modified from Hjelle (1993).

2.2 Geological history

2.2.1 Precambrian

The basement rock of Svalbard, referred to as Hecla Hoek, defines rocks of Late Proterozoic to Early Palaeozoic in age (Worsley, 1986). The geological evolution of the basement is long and complex, with evidence of repeated orogenic episodes over several hundred millions of years (Dallmann, 2015). The metamorphosed and strongly deformed basement contrasts distinctly with the overlying younger strata, which is unmetamorphosed and only locally deformed (Worsley, 1986; Hjelle, 1993).

2.2.2 Palaeozoic

The Cambrian-Ordovician successions mainly consist of fossil-rich carbonate rocks. The Cambrian was a time when Svalbard was situated in the Southern Hemisphere with tropical conditions. The Caledonian Orogeny, lasting from Early Ordovician to the Early Devonian, was a period of mountain building. It formed as a result of the collision between the North American (Laurentia) and Northern Europe (Fennoscandian) plate, involving a large-scale thrust system and the construction of an intercontinental mountain range. This left highly deformed and metamorphosed basement rocks preserved on both sides of the North Atlantic Ocean. In Svalbard, this affected all rocks younger than of Devonian age (Dallmann, 2015). The following figure (Figure 2.3) displays how the North Atlantic and Svalbard was affected by strike-slip movement towards the end of the Orogeny, which is believed to have affected the BFZ.
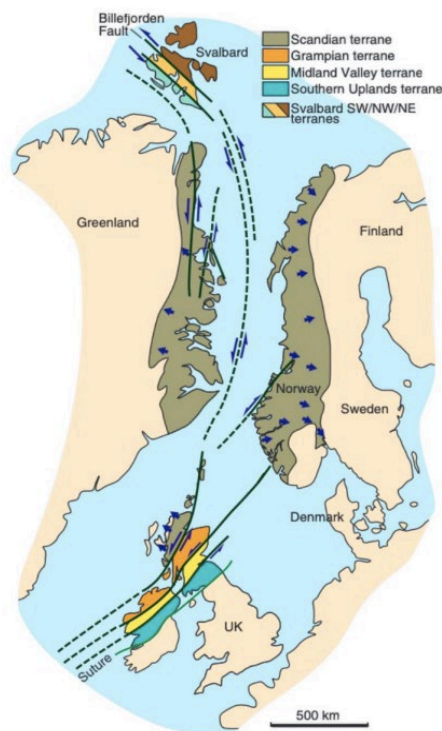
Figure 2.3: A simplified map of the North Atlantic, reconstructing the Caledonian Orogeny in the Early Devonian. Large strike-slip faults transect the North Atlantic Caledonides, including Svalbard and the BFZ (Fossen, 2010).

An orogenic collapse followed in the Devonian as the tectonic stresses of the Earth's crust weakened and changed direction. Extensional forces collapsed the mountain chain and formed a depression in the northern Spitsbergen. Svalbard drifted from 5° to 20° N, the climate warmed and the landscape was exposed to excessive monsoon-like precipitation and erosion. Fault-

bounded rift basins developed on subsiding crustal blocks, where eroded material from the mountain chain accumulated. This formed the "Old Red" sandstone rift troughs in the north-western part of Svalbard. A new phase of tectonic activity occurred in the Late Devonian, called the Svalbardian Event. This caused concentrated crustal movement along N-S trending fault zones, including the BFZ, and led to folding and faulting of Devonian rocks (Worsley, 1986; Dallmann, 2015).

The Carboniferous started off warm and humid but shifted towards semi-arid to arid conditions towards the middle of the period. Svalbard drifted further north during the Carboniferous, from around 20°N to 35°N, and was positioned on the coastal northern margin of Pangea (Figure 2.4) (Dallmann, 2015). The land area of Svalbard was relatively flat during the first part of the period, with alluvial plains, lagoons and lakes (Hjelle, 1993). The warm climate favoured the deposition of coal, along with terrestrial, fluvial and alluvial deposits. Sea level started to rise in mid-Carboniferous, and the depositional environment changed to marine by the Upper Carboniferous (Hjelle, 1993). Active rifting was reactivated during this period, which created rift valleys subsiding along pre-existing major fault zones, including the BFZ. This created distinct N-S trending horst-graben structures. Active rifting ceased by the end of the Carboniferous and most of the remaining highs were progressively flooded. This allowed for the accumulation of a thick succession of evaporites and carbonates on a stable, warm and shallow-marine shelf (Dallmann, 2015). This formed the boundary between the underlying mid-Carboniferous succession of clastic deposits and upper organic material (Worsley, 1986).
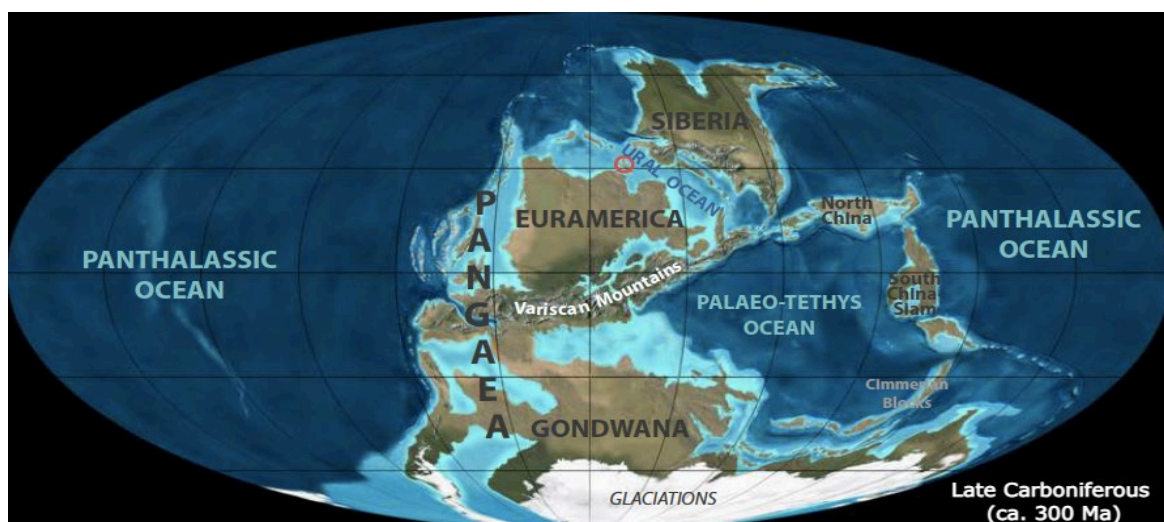
Figure 2.4: Global palaeogeography during the Late Carboniferous. Svalbard is encircled in red. Modified from Dallmann (2015).

The Permian marks the complete consolidation of Pangea. Svalbard drifted from about 30°N to 45°N and was situated on the northern margin of the supercontinent as part of a broad, epicontinental shelf sea. This shelf, named the Franklinian Shelf, comprised shallow platforms and deeper basins, which today are exposed in the Barents Sea (Dallmann, 2015). Predominantly carbonates and evaporates were deposited in the Early Permian during fully- to marginal marine conditions in a warm and dry climate. Uplift and a long-term sea level fall followed, which led to weathering and erosion and a discontinuity in the stratigraphic sequence. A large-scale regional transgression of the sea occurred in Late Permian that records open-marine deposits in temperate- to cold water conditions (Worsley, 1986; Dallmann, 2015).

2.2.3 Mesozoic

Svalbard continued to drift during the Mesozoic era, from 45°N to 60°N (Hjelle, 1993). The transition between the Palaeozoic and Mesozoic is distinct, as it marks the most devastating mass extinction in Earth's history (Hjelle, 1993; Dallmann, 2015). It was a rather tectonically stable time with a damp and temperate climate. Thick sedimentary successions were deposited on a large shelf sea, forming a large depositional basin during the Middle to Late Triassic (Figure 2.5) (Dallmann, 2015).
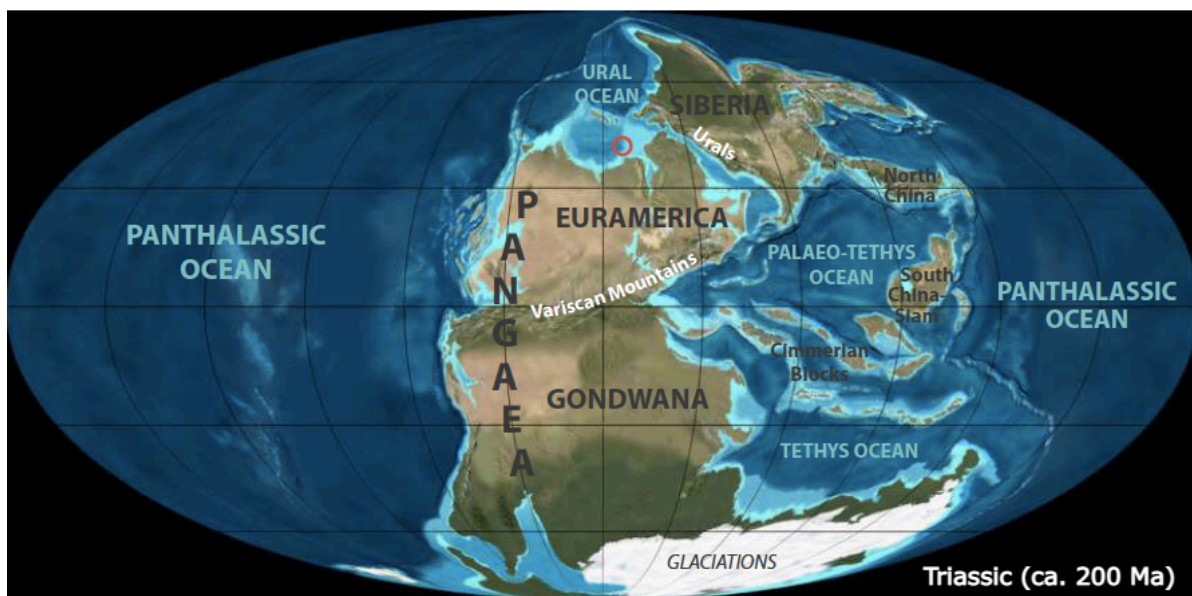
Figure 2.5: Global palaeogeography during the Triassic. Svalbard is encircled in red. Modified from Dallmann (2015)

The climate shifted to warm and humid in the Jurassic, which was a period dominated by numerous sea level changes due to reorganisation of the continental plates. The break-up of the

supercontinent Pangaea started in Early Jurassic and was complete by the end of Late Jurassic. Svalbard and several internal basin highs in the Barents Sea underwent uplift during the Middle Jurassic. This resulted in sea level fall and rapid progradation of shorelines along the Barents Sea Platform. An intensified crustal extension and associated volcanism occurred from the Middle to Late Jurassic, creating a N-S striking rift system. As a part of the arctic North Atlantic rift system, this formed rift basins on both sides of the North Atlantic margins (Dallmann, 2015). As a result of faulting and widespread magmatic activity in Svalbard during Late Jurassic and Early Cretaceous, magma intruded the sedimentary successions and left dolerite sills up to 100 m thick (Worsley, 1986; Hjelle, 1993).

The Cretaceous is characterised as the warmest period in Earth's history (Dallmann, 2015). The warm climate was a consequence of massive volcanism related to the Pangea break-up and the seafloor spreading of the Atlantic Ocean. In combination of melted polar ice caps, the global sea level was exceptionally high (Worsley, 1986). Svalbard was situated between 60 and 70°N (Figure 2.6) and positioned on a large Arctic platform area that was partly covered by a shallow, epicontinental sea (Dallmann, 2015). The archipelago was subjected to a great extent of uplift and erosion during the Cretaceous, particularly in the northern region. This resulted in the largest continuous break in deposition that has occurred in Svalbard. It is believed that the northern uplift produced cross-cutting E-W faults that represent the present fjord lines (Worsley, 1986).

Figure 2.6: Global palaeogeography during the Late Carboniferous. Svalbard is encircled in red. Modified from Dallmann (2015).

2.2.4 Cenozoic

The Palaeogene started off warm and humid, and then became gradually cooler and drier. The start of the Cenozoic was dominated by lateral fault movement in Svalbard. The opening of the Norwegian-Greenland Sea introduced a strike-slip regime in the Barents Sea during the Palaeocene and Eocene, with the continental Greenland plate and the Eurasian plate (with Svalbard) moving in opposite directions. The curved plate boundary exposed Svalbard to significant transpression along the west coast, creating the West-Spitsbergen Fold-and-Thrust belt (WSFTB) (Hjelle, 1993; Fookes, 2008). A reconstruction of the formation of the WSFTB is given in Figure 2.7. This belt is 100-200 km wide and 500 km long (Bergh et al., 1997). East of the new mountain range, from Isfjorden and southwards, the land subsided and formed a N-S directed depression, known as the Central Tertiary Basin (CTB) (Fookes, 2008). The WSFTB served as the main sediment source of the CTB, which accumulated a thick succession of eroded Upper Palaeozoic and Mesozoic sedimentary rocks, including coal deposits (Worsley, 1986; Hjelle, 1993; Dallmann, 2015).
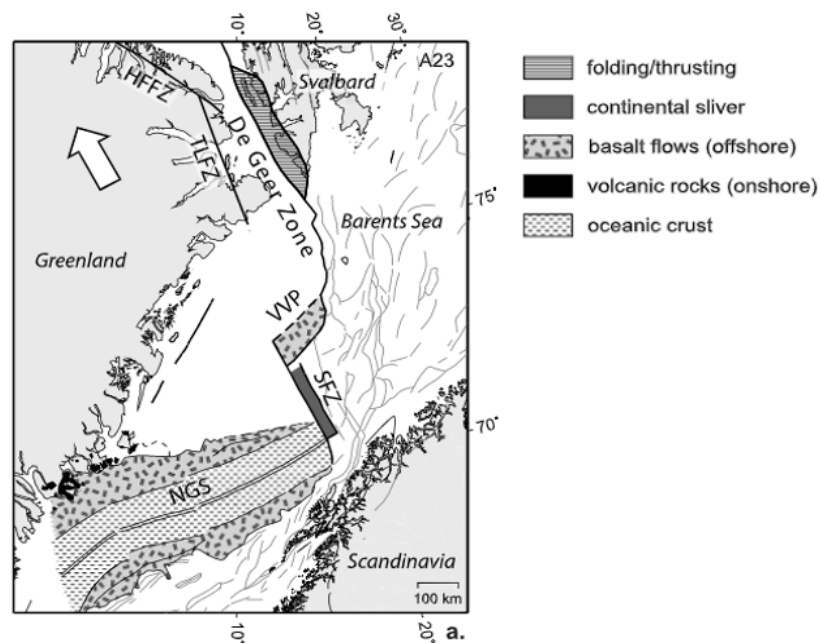
Figure 2.7: A reconstruction of the plate tectonics in the North Atlantic during the Palaeocene and Eocene. The relative plate motion is indicated by the arrow. The opening of the Norwegian-Greenland Sea induced a shear regime in the Barents Sea. Transpression occurred along West-Spitsbergen and formed the WSFTB (indicated by hatching). Senja Fracture Zone (SFZ), Vestbakken Volcanic province (VVP), Norwegian Greenland Sea (NGS), Harder Fjord Fault Zone (HFFZ), Trolle Land Fault Zone (TLFZ). Modified from Faleide et al. (2008).

The seafloor spreading continued throughout the Neogene and Quaternary, and Svalbard experienced episodes of volcanism (Worsley, 1986). The climate continued to cool. Svalbard was repeatedly covered by ice-sheets, with intervening warmer episodes, and was subjected to a high rate of erosion and denudation (Hjelle, 1993; Dallmann, 2015). The WSFTB developed as an erosional relief, while the eastern parts of Svalbard acted as low-relief plateaus (Dallmann, 2015). The present landscape of Svalbard was largely formed during the Quaternary, as glaciers have been extremely active in shaping the landscape (Hjelle, 1993).

2.3 Deformation structures

This subchapter will give a general overview of the most important deformation structures that form in contractional and extensional regimes. In a contractional regime, rocks are shortened by tectonic or gravitational forces. This results in thickening and deformation of the crust and the development of reverse and thrust faults. In an extensional regime, the lithosphere is exposed to regional horizontal stretching and thinning, forming normal faults and graben structures. Contractional and extensional structures may also form in strike-slip fault systems by transpression or transtension deformation (Van der Pluijm & Marshak, 2004; Fossen, 2010). The style of deformation depends on the mechanical strength of the rocks involved and location at time of deformation (Fossen, 2010). While ductile material commonly responds to stress by folding, brittle material will undergo faulting. Reverse faults (>30°) or thrust faults (<30°) are common in contractional regimes, in which the hanging wall has moved up relatively to the footwall. In this way, older rocks may be emplaced above younger strata. Normal faults are common in extensional regimes, as the hanging wall moves down relatively to the footwall (Fossen, 2010).

Fold-and-thrust belts form in response to compressional forces. The belts are divided into sections in which distinct deformation structures form (Figure 2.8). Fold-and-thrust belts have an overall wedge-shaped geometry in cross-section view. The load of the thick hinterland pushes the surface of the crust down and the foreland gets progressively thinner away from the collision zone. A foreland-basin, a wedge of sediments eroded from the orogen, develops in the depression of the foreland (Van der Pluijm & Marshak, 2004). The central part of the collision zone is called the hinterland, commonly denoted as the "thick-skinned" section. This is a complex zone of more intensely deformed and metamorphosed rocks. The hinterland

involves basement-penetrating reverse faults, which causes uplift of the basement (Van der Pluijm & Marshak, 2004). The foreland typically forms the "thin-skinned" part of an orogenic contractional zone and is the marginal parts of the collision zone. Imbrication and duplex structures above a detachment are characteristic of this regime. A duplex is a series of similar oriented reverse faults or thrusts ("horses") that branch upwards. The horses are formed during progressive sliding, enabling ramps and anticlinal folds. They are attached along a lower low-angle floor thrust or sole thrust and merge with a higher detachment or roof thrust. A detachment layer, also called a décollement, is a term used for a thrust fault that separates an entire stack of horses from a basement (Fossen, 2010). These commonly form in weak lithologies, such as shale and evaporites (Van der Pluijm & Marshak, 2004). This deformation structure is illustrated in Figure 2.9. Foreland deformation structures may be complex in the case of several tectonic events.
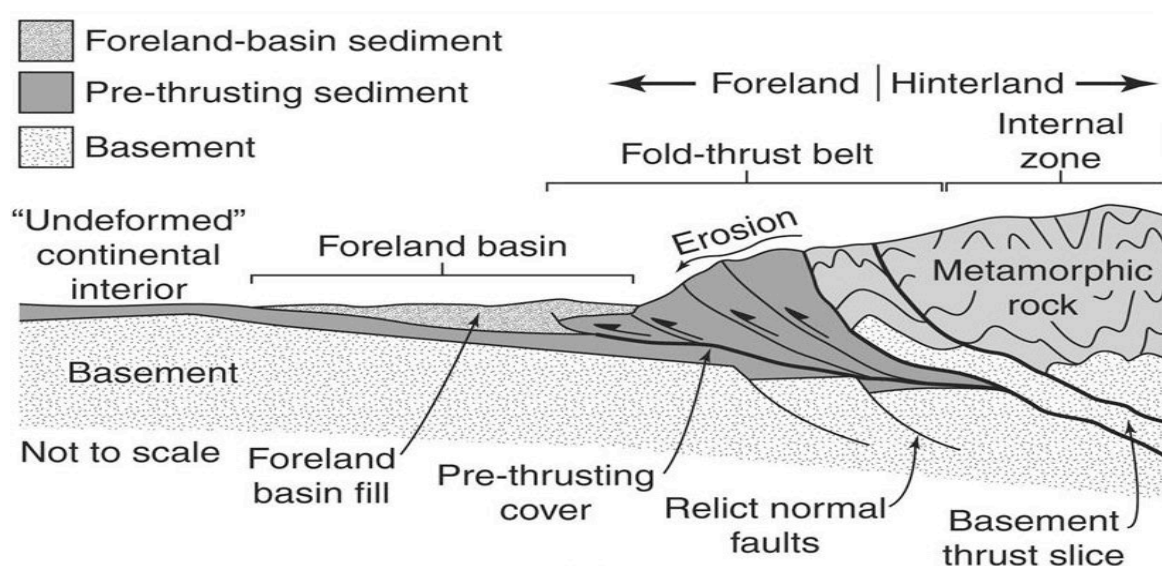
Figure 2.8: A schematic cross-section of a fold-and-trust belt and its major features. Illustration by Van der Pluijm & Marshak (2004).
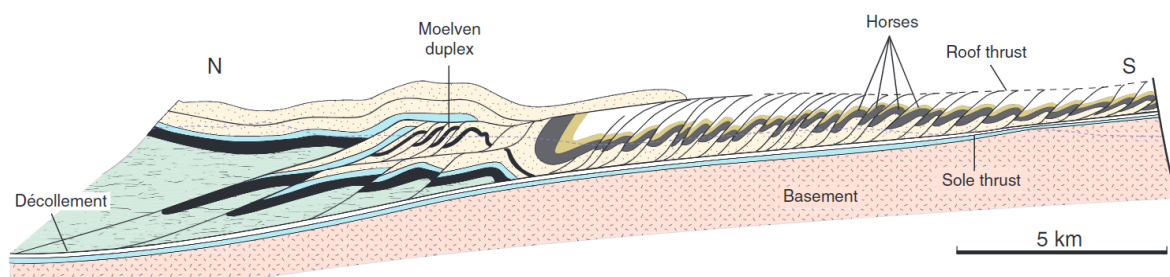
Figure 2.9: A cross-section view of typical foreland structures. A duplex of horses develops along a décollement or sole thrust and are bounded by a roof thrust. Illustration by Fossen (2010).

Extensional regimes are commonly influenced by normal faulting, formed in response to tectonic forces. In active rifting, mantle plumes may induce doming and tensile stresses to an area, while passive rifting is controlled by plate tectonic stresses. Rifts form in zones of weakness in the lithosphere, commonly along contractional structures of former orogenic zones (Fossen, 2010). In rift systems, normal faults may be classified as planar or listric. Planar faults have a constant dip with depth, while listric faults have a decreasing dip with depth. Tilted fault blocks commonly underlie half-grabens, which are filled with sediments. If the deposition occurred during active faulting (syn-rifting), the strata are tilted and thicken towards the fault. These are called growth faults (Van der Pluijm & Marshak, 2004). Figure 2.10 illustrates the formation of these common extensional structures. Similar to contractional regimes, imbrication zones and duplexes may form in extensional fault systems (Fossen, 2010).
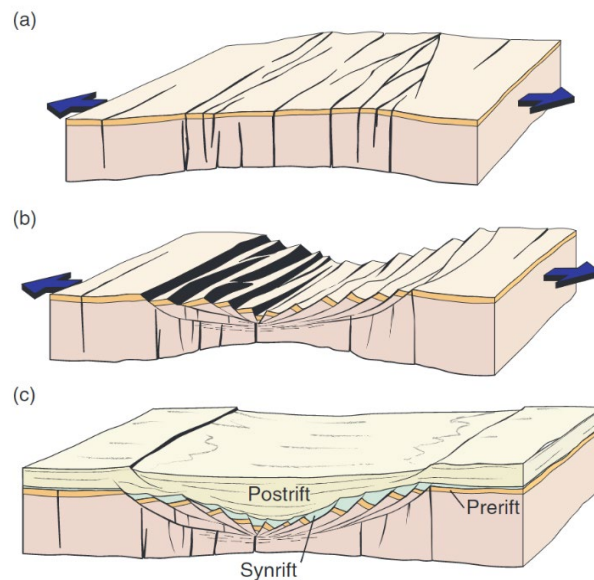
Figure 2.10: Stages of the development in passive rifting. Extensional forces are introduced to an area of lithospheric weaknesses (a), which is stretching and thinning the crust while forming extensional structures (b). Model (c) illustrates post-rift extensional deformation structures of tilted listric normal faults that underlie half-graben structures filled with syn-rift sediments. Figure by Fossen (2010).

An orogeny may endure an extensional collapse, driven by gravitational forces (Figure 2.11) Zones of extreme crustal thickening have been subducted and exposed to heating, which in turn has weakened the crust. When the crust becomes too thick to support its own weight, it collapses and forms zones of extension (Van der Pluijm & Marshak, 2004). This commonly reactivates thrusts as extensional detachments (Fossen, 2010).
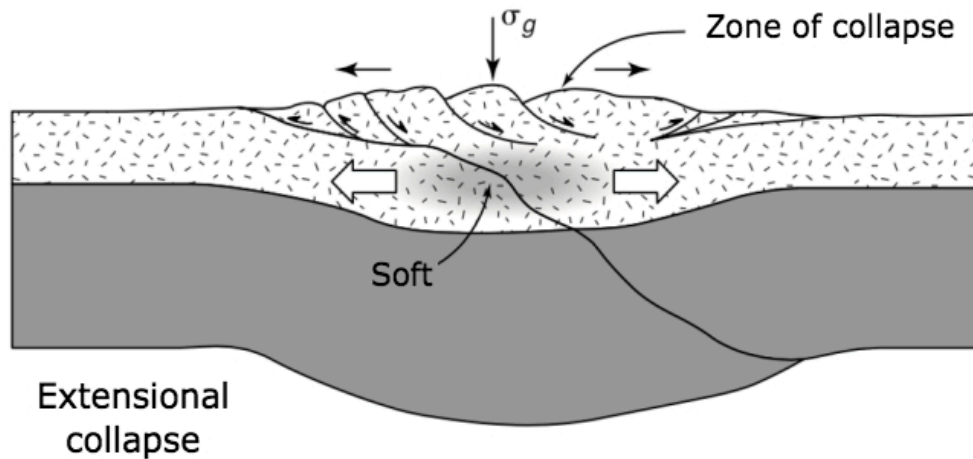
Figure 2.11: An orogenic collapse of thickened and weakened crust, driven by gravitational forces. The light area represents the continental crust, while the dark area represents the uppermost solid mantle of the lithosphere. Figure by Van der Pluijm & Marshak (2004).

Contractional and extensional deformation structures can also form in strike-slip faults that deviate from a simple shear. Depending on the sense of slip and stepping of the fault, a releasing bend (transtension) or restraining bend (transpression) forms (Figure 2.12) (Fossen, 2010). Transtension deformation forms in response to extensional forces, developing pull-apart basins bounded by normal faults. Transpression deformation occurs due to contractional forces, resulting in shortening, uplift and thrusting of the fault zone (Van der Pluijm & Marshak, 2004). Large-scale transtension and transpression may lead to the formation of basins and local orogeneses of complex structures, involving numerous strike-slip faults, normal and reverse faults and folds (Van der Pluijm & Marshak, 2004; Fossen, 2010).

(a) Releasing bend (transtension) forming normal faults in a pull-apart basin

(b) Restraining bend (transpression) forming thrust faults
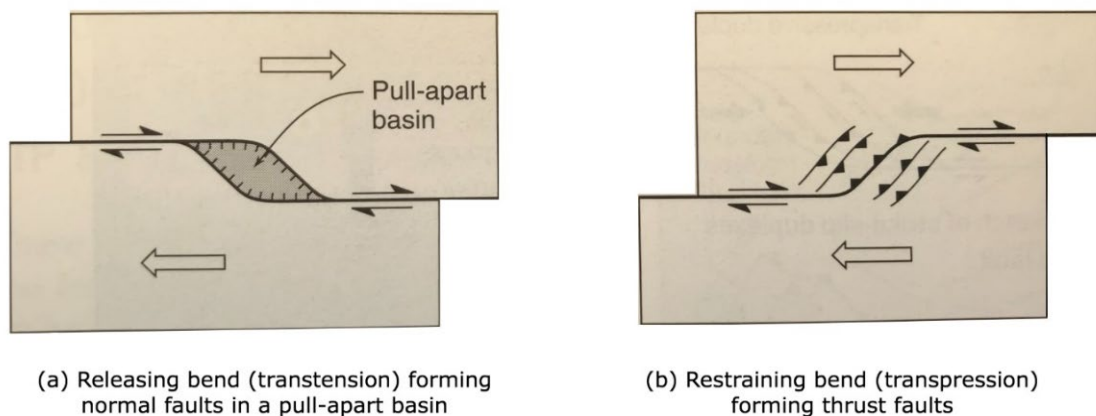
Figure 2.12: Schematic illustration of the formation of transtension (a) and transpression deformation (b). Modified from Van der Pluijm & Marshak (2004).

Strike-slip faults are associated with flower structures in cross-sections, which split and widen upwards (Fossen, 2010). Positive flower structures develop in a restraining bend and commonly form thrust and reverse faults, while negative flower structures are associated with a releasing bend and normal faulting. These structures are illustrated in the figure below.

(a) Positive flower structure   (b) Negative flower structure
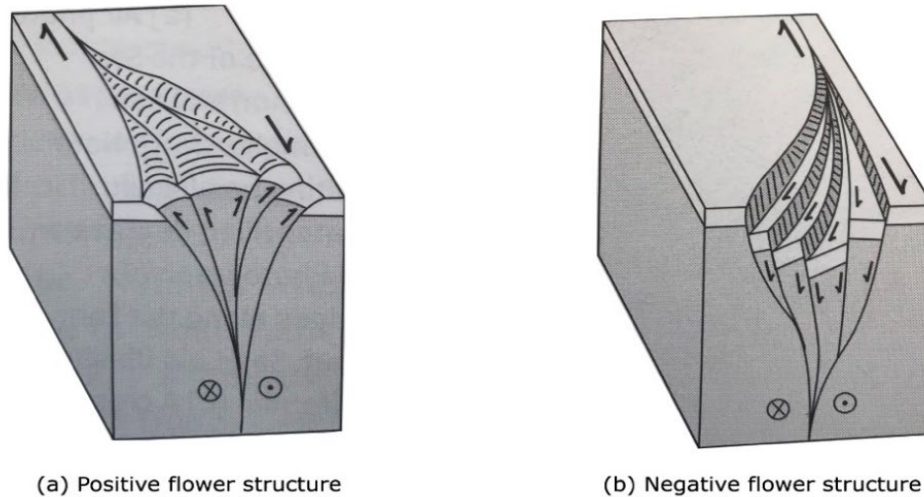
Figure 2.13: Schematic cross-section view of a positive (a) and negative (b) flower structure that forms in a strike-slip fault which deviates from a simple shear. Modified from Van der Pluijm & Marshak (2004).

2.4 Stratigraphy

This chapter will describe the stratigraphy of Svalbard, which extends back to the Precambrian. The great change in latitude, from the southern hemisphere in the Cambrian to the present location in the northern hemisphere, has resulted in a highly varying depositional environment. This is reflected in the stratigraphic sequence of Svalbard, which shows a great diversity of sedimentary deposits. The following figure (Figure 2.14) gives an overview of the stratigraphic units found in western Svalbard, including their thickness, stratigraphy and structural role.
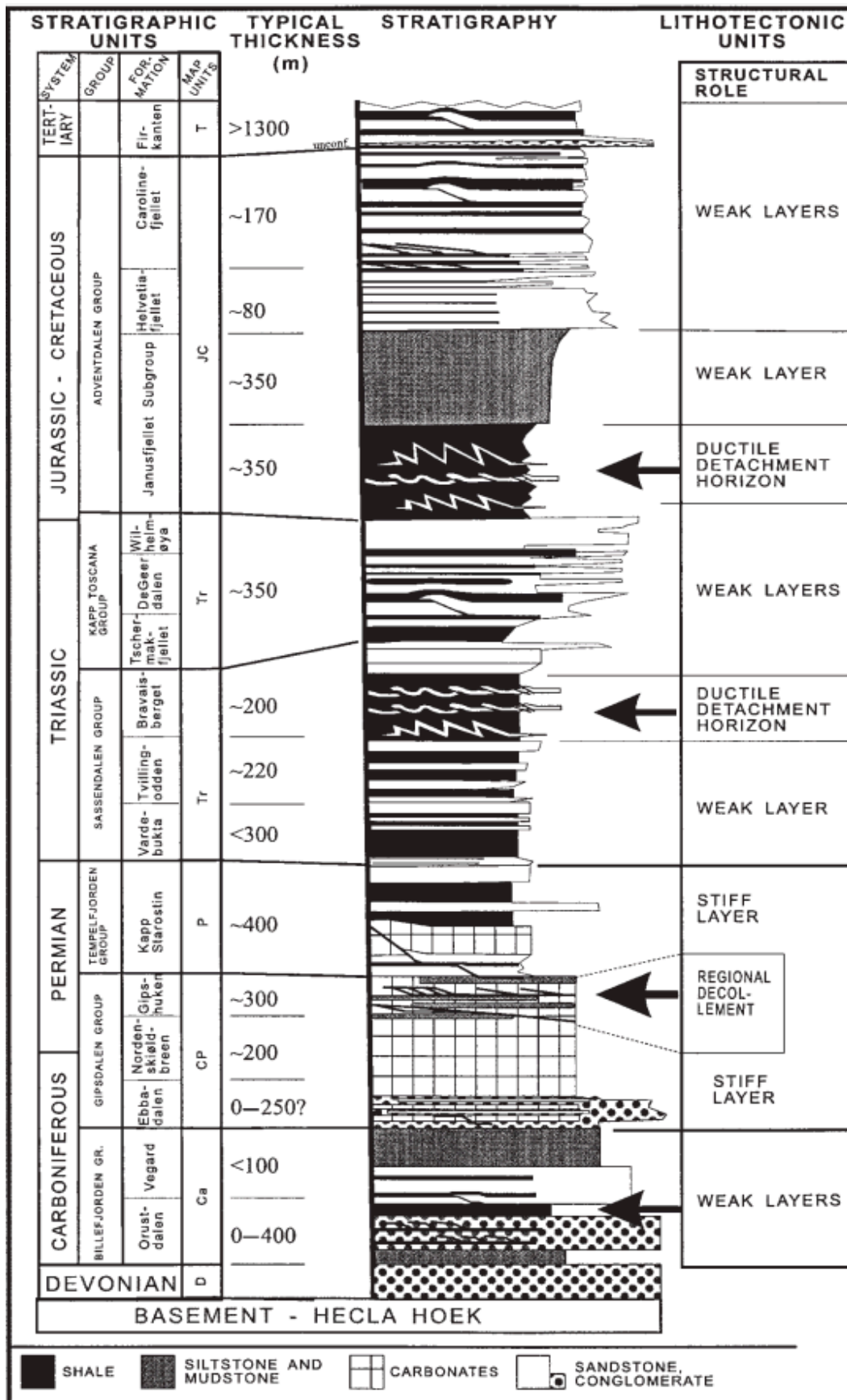
Figure 2.14: The stratigraphic scheme for western Nordenskiöld Land, Svalbard includes the name, thickness and structural role of the stratigraphy. The figure is extracted from Braathen et al. (1999).

2.4.1 Tertiary

The most recent groups, including the Van Mijenfjorden Group, were deposited in the Tertiary. These consist of sandstones, siltstones and shales, interbedded with coal and conglomerate. The base was deposited in coastal to shallow-marine environments, while the middle part consists of fluvial and continental to shallow-marine deposits. The top consists of pyroclastics and lavas (Dallmann, 2015).

2.4.2 Adventdalen Group

This group was deposited in an epicontinental basin, during the Late Jurassic to Middle Cretaceous. The base is of organic-rich mudstone, accumulated on a marine outer shelf, while an open-marine, inner shelf deposited shale is found above. The upper part consists of coarse-grained sediments of conglomerates, sandstones and shales with coal beds. A great extent of uplift and associated erosion during the Late Cretaceous resulted in a sedimentary hiatus, and Upper Cretaceous deposits are therefore not present in Svalbard (Dallmann, 2015).

2.4.3 Kapp Toscana Group

This Upper Triassic and Lower Jurassic group consists of shales, siltstones and sandstones, interbedded with thin layers of coal and scattered appearances of carbonate material. The succession was deposited in shallow-marine, alluvial and deltaic environments. Regional uplift and slowing down of basin subsidence during very Late Triassic to Middle Jurassic resulted in condensed inner-shelf to shallow marine deposits, followed by non-sedimentation and erosion (Dallmann, 2015).

2.4.4 Sassendalen Group

The Sassendalen Group is of open marine, cold-water clastics, deposited in a low-relief, deep shelf embayment. The Lower to Middle Triassic succession is high in organic content. The dominant rock-type is shale, with intervals of siltstones and sandstones (Dallmann, 2015).

2.4.5 Tempelfjorden Group

The Tempelfjorden Group (Middle to Late Permian) is of highly variable temperate to cold-water deposits. It consists of both shallow-marine chert and carbonates, rich in invertebrate remains, as well as deeper marine offshore clastics (Dallmann, 2015).

2.4.6 Gipsdalen Group

The lower part of this group, deposited in the Middle Carboniferous, is of clastic beds, including conglomerate, sandstones, siltstones and shales. The middle to upper part (Late Carboniferous to Early Permian) consists of evaporates and carbonates. This succession was deposited during progressive flooding, as the environment was transitioning from a terrestrial, desert-like environment, to a warm and dry shallow-marine environments of coastal plains, tidal flats and lagoons. This created a platform for carbonates (Dallmann, 2015).

2.4.7 Billefjorden Group

The Billefjorden Group was deposited during Early Carboniferous and is a succession of conglomerates, sandstones and shales with local coal seams. The group is of terrestrial lowland origin, deposited in alluvial fan, fluvial, lacustrine and alluvial environments in a warm and humid climate. An abundance of unevenly distributed coal seams and plant remains indicate organic-rich environments of swamp forests and wetlands (Dallmann, 2015).

2.4.8 Devonian

The "Old Red" sandstone of Svalbard is characteristic of the Devonian. The unit was deposited in a continental molasse basin and represents fault-controlled sedimentation. The distinctive red colour of the fining-upward sandstone is linked to a dry, desert-like climate, with depositional environments of alluvial fans and braided rivers (Dallmann, 2015).

2.4.9 Basement – Hecla Hoek

The basement rock of Svalbard consists of strongly folded and metamorphosed rocks (Braathen et al., 1999). The Hecla Hoek formed during Precambrian to Silurian times, which makes the bedrock older than 400 Ma. It generally consists of gneiss, granite, phyllite, limestone, quartzite and volcanic rocks (Hjelle, 1993).

3 Methods

This chapter will give an overview of the seismic reflection data acquisition method. The raw data of this study was acquired using an airgun array and a streamer of hydrophones, in which the fundamental principles of these will be further elaborated in this chapter. Next, the methods that have been used throughout the processing and interpretation part will be presented.

3.1 Seismic reflection data acquisition

Seismic reflection is a geophysical method used for studying subsurface geological conditions. Seismic data is collected for three fundamental purposes: Identifying structural elements, stratigraphic features and rock/sediment properties of the subsurface. The goal is to produce the most accurate image of the earth. Throughout its history, this has been fundamental for the petroleum industry and for identifying hydrocarbons (Hart, 2000; Gelius & Johansen, 2010).

Seismic reflection surveys record ray paths of seismic waves between a source and receiver. An energy source is used to generate an acoustic pulse with an expanding wavefront that travel through the earth. When the expanding wavefront reaches some interface of changing physical parameters, the acoustic energy will be split. Some will be reflected back to the surface and recorded by receivers, while some will be transmitted to the underlying bed (Hart, 2000). The information from the seismic survey is captured by the surface receivers. These record the strength of the reflected energy (reflection amplitude), which depends on differences in physical parameters between adjacent rocks, and the two-way travel time (TWT). This may be displayed in a t-x plot as traces with variations in amplitude as a function of time. Time in seconds is positioned on the y-axis, while offset (source and receiver distance) is plotted along the x-axis. This enables the interpreter to study how physical parameters change in the subsurface and to identify geological conditions (Hart, 2000).

There are several types of seismic waves that appear in a seismic section. Primary waves (p-waves) are usually of greatest interest. These produce first order reflections from layer boundaries, and therefore convey true information about the geological conditions of the subsurface (Gelius & Johansen, 2010). However, seismic sections usually suffer from various

types of noise that have a degrading effect on the seismic image. Noise is defined as any seismic signal but the primary reflections (Gadallah & Fisher, 2009), which includes the direct wave, surface waves, refractions, diffractions and multiples. Noise is further divided into coherent- and incoherent noise. Coherent noise appears in a consistent manner in the traces, while incoherent (random) noise will not a have a uniform pattern. The latter includes wind, waves, instrumental noise or noise from platforms and other boats (Gelius & Johansen, 2010). It is essential to suppress noise through processing to avoid misinterpreting geological features in the seismic image.

A multiple is defined as seismic energy that has undergone more than one reflection (Gadallah & Fisher, 2009). These occur as internal reflections in a layer when the R_c is particularly large. Different types of multiples are illustrated in Figure 3.1. Water-bottom multiples commonly dominate in marine seismic due to the large contrast in physical parameters between the sea and the subsurface. A periodic relationship is established between primaries and multiples. This means that shallow marine seismic data will suffer from multiples of short intervals (Gelius & Johansen, 2010). The source ghost is a short-path multiple that occurs when energy travels up-wards from the source and is reflected back from the sea-surface (Kearey et al., 2002). The impedance contrast between the water and air makes it an almost perfect reflector, and the ghost will therefore appear with an opposite phase at a short time later compared to the down-going wave. The depth of the airgun array and receiver is chosen to ensure a constructive interference with the ghost (Gelius & Johansen, 2010; Mjelde, 2011).
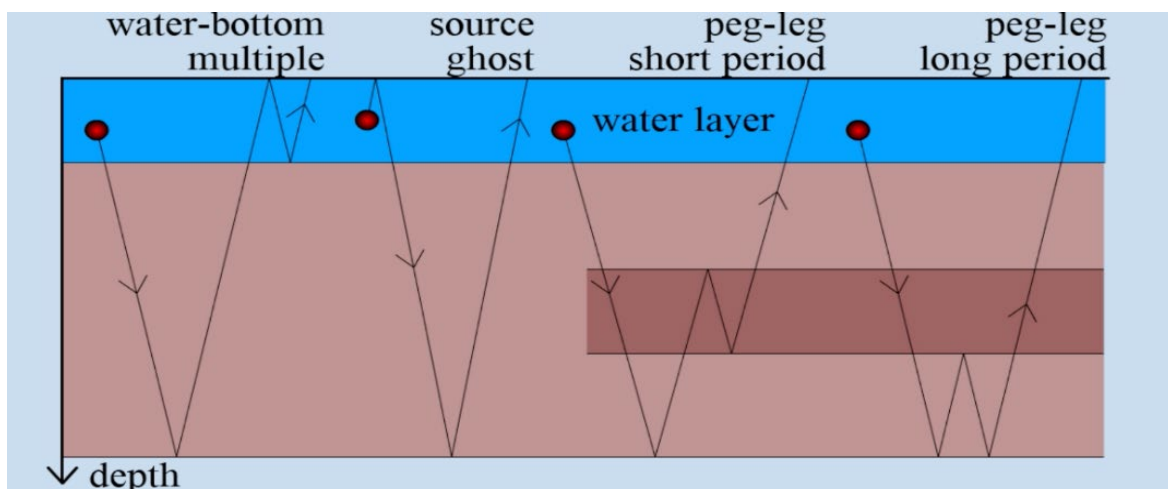
Figure 3.1: Illustration of different types of multiples. Water-bottom multiple and source ghost is classified as surface multiples, while peg-legs are multiples within a layer. The figure is extracted from Gelius & Johansen (2010).

There are several types of seismic reflection surveys, including 2D, 3D and 4D surveys. In 2D surveys, the vessel is only towing a single streamer. The resulting seismic image will therefore only contain information from the section below the line. 2D data often suffers from diffractions and noise caused by offline geological structure and will therefore produce a less clear seismic image. A 3D survey will take the entire wavefield into account and produce a better seismic section. During acquisition, the vessel is towing many streamers at the same time and has multiple arrays of airguns. By using multiple points of observations for subsurface locations, a better seismic image is produced. 4D seismic is a time-lapse of several 3D seismic surveys over time. This is used to monitor reservoir properties (Gelius & Johansen, 2010).

The seismic survey for the SVALEX 2002 project is a 2D marine multichannel survey. This survey utilises an airgun array as source, while a single streamer of hydrophones is towed behind the ship to record each shot. A schematic illustration of this type of survey is given in the figure below.
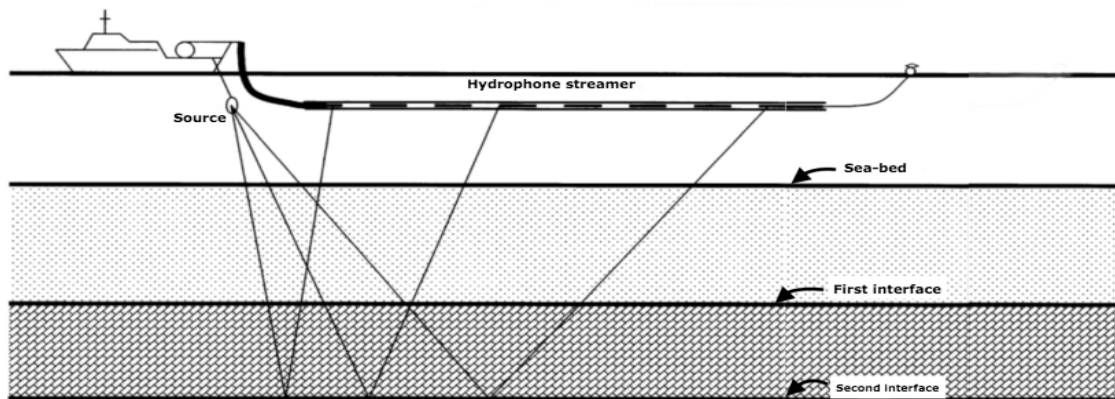
Figure 3.2: Schematic illustration of a 2D marine multichannel seismic survey, modified from Bacon et al. (2003).

3.1.1 Source

An airgun array is the most common source used in marine seismic surveys. An airgun fires rapidly and at constant intervals. At the same time, it generates a powerful pulse, is simple to operate, dependable and does not severely affect marine life. Airguns are maintained at a constant depth and produces minimum drag during towing (Gadallah & Fisher, 2009).

Airguns generate pressure waves by releasing high-pressured air into the water (Sheriff & Geldart, 1995). The air is generated from a compressor on the ship and stored in two chambers

in the airgun. When all the air is released instantaneously from the lowermost chamber, this creates a pressure-wave that will travel through the subsurface. Figure 3.3 illustrates the main features of an airgun. A navigation system via a gun controller will ensure correct timing of the shots (Mjelde, 2010).
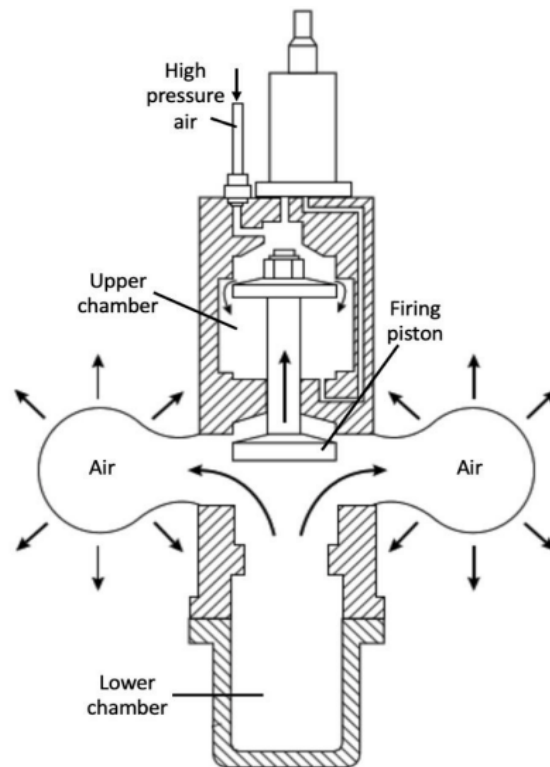
Figure 3.3: The main elements of an airgun. High-pressured air is stored in the lower chamber and released instantaneously to create a pressure-wave. Modified from Kearey et al. (2002).

It is necessary with several airguns to generate adequate seismic energy and a satisfactory pulse. The signal from one airgun will be contaminated by bubble pulses. These are generated as a bubble from an airgun that expands and contracts outward in all directions after the high-pressure air has been released due to differences in hydrostatic pressure between the bubble and the surrounding water. Successive expansions and contractions will continue until all the energy is dissipated, which creates strong repeating bubble pulses in the signal that weakens with time (Gadallah & Fisher, 2009). Figure 3.4 illustrates this principle.
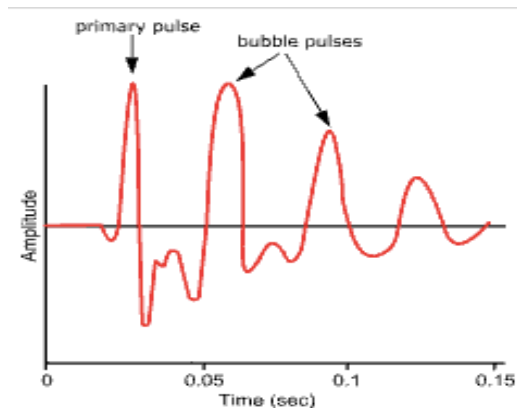
Figure 3.4: The seismic pulse from airgun is contaminated by bubble pulses that occur due to successive contractions and expansions of the pressure-bubble. The figure is derived from Mjelde (2010).

There are two ways to increase the signal from an airgun. First, an increase in airgun volume will proportionally increase the air bubble period. Second, an increase in number of airguns will increase the pressure and signal amplitude. A combination of these will solve the bubble pulse problem. A tuned airgun array is a cluster of several airguns of different volumes. As these are fired at the same time, the total amount of generated energy increases. Airguns of different chamber volumes create a deconstructive interference of the bubble pulses in the combined array signature, since the bubble effects occur out of phase from one another (Figure 3.5). This also provide directivity of the seismic signal. The resulting seismic signature is much closer to an ideal source and has an increased signal-to-noise ratio (SNR) (Gadallah & Fisher, 2009; Gelius & Johansen, 2010; Mjelde 2011).
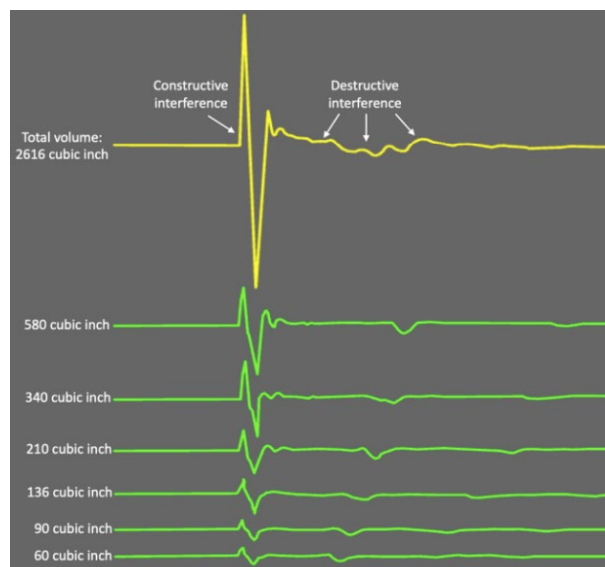
Figure 3.5: Airguns of different chamber volumes attenuate the bubble pulse and increase the SNR, as the smaller guns reach maximum expansion at an earlier time than larger guns. The figure is derived from Mjelde (2011).

3.1.2   Receiver

Hydrophones are commonly the recording instrument in seismic marine surveys. They consist of two circular Piezo-electric plates mounted on the ends of a hollow brass cylinder, that measure variations in pressure and converts it to a voltage. The plates have opposite polarities, which gives hydrophones the ability to record stresses from pressure waves that cause over- or under pressure, whilst cancel out stresses from one-direction acceleration (Figure 3.6). This minimises the influence of currents and wave acceleration on the signal (Gelius & Johansen, 2010; Mjelde, 2010).

Hydrophones are mounted on a neutrally buoyant streamer of several kilometres length that is towed behind a ship, usually at a depth between 10 – 20 m (Sheriff & Geldart, 1995). They are coupled in series or parallel to increase the sensitivity. The group length between hydrophones are commonly 12.5 or 25 m. The signals from the hydrophones in one array are added in order to increase SNR and reduce the total amount of data (Gelius & Johansen, 2010). Modern 3D vessels can tow up to 20 streamers at the same time, usually with 25 – 100 m spacing, while 2D vessels is only able to tow one. Birds with compass are attached to the streamer, and measure and adjust the depth if it deviates from the pre-set depth (Gadallah & Fisher, 2009).
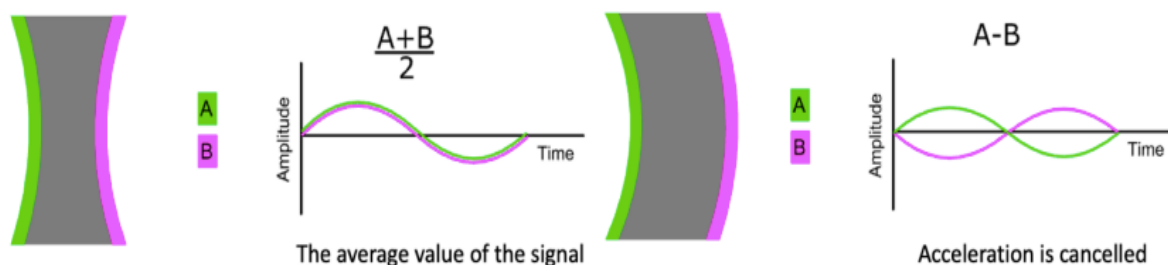
Figure 3.6: The construction of two Piezo-electric plates (A and B) with opposite polarities enables the hydrophone to record stresses from P-waves, whilst cancel out stresses from one-direction acceleration. The left figure shows the generated average value of the signal, as the under- and overpressure add up. The right figure illustrates how acceleration is cancelled out when A and B have opposite polarities. Modified from Mjelde (2010).

3.2 Seismic processing

Pre-processed seismic data suffers from various types of noise which degrades the quality of the seismic image. In turn, this makes it difficult to interpret geological features. The ultimate goal of seismic processing is to increase the SNR and improve seismic resolution so that the resulting seismic section represents a clear and accurate image of the subsurface geology (Gelius & Johansen 2010). The following subchapters include processing steps that contribute to this.

3.2.1 Editing

Editing involves removal of bad traces, which are substituted by interpolated traces. This includes noisy traces, traces with transient glitches or monofrequency signals. These traces may be partly or completely destroyed due to technical complications during the acquisition process and could have destructing effects on the SNR (Yilmaz, 2001). Editing also involves removal of traces with anomalously high or low amplitudes, which are likely to represent noise (Sheriff & Geldart, 1995).

3.2.2 CMP sorting

Traces are sorted into groups of commonalities. During acquisition, traces are usually grouped in common shot-gathers. A common-mid-point (CMP) gather, also denoted as a common-depth-point (CDP), is commonly used during processing (Figure 3.7). This is an assemblage of traces with the same mid-point in the subsurface, but with different distances between source and receiver. In a CMP-gather, the mid-point in the subsurface is assumed to lie vertically under the surface mid-point between the shot and receiver (Kearey et al., 2002).
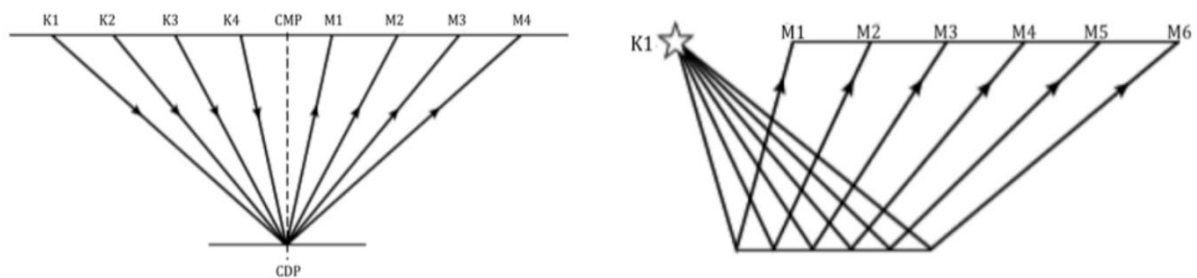
Figure 3.7: Illustration of a CMP-gather (left) and a shot-gather (right) by Kearey et al. (2002).

3.2.3 Amplitude recovery

Amplitude recovery is a means to compensate for amplitude decay with depth. Energy attenuation occurs as a result of spherical spreading, absorption and portioning of the energy at interfaces. Spherical spreading is a result of the wavefront increasing steadily in size with distance. Increasing velocity causes further divergence of the wavefront and the amplitude will therefore decay more rapidly with distance (Yilmaz, 2001). The earth works as a filter on the seismic signal, as imperfect elasticity in the subsurface causes friction and absorbs energy. This is frequency-dependent, meaning that higher frequencies will be attenuated more rapidly than low frequencies as the wave propagates (Yilmaz, 2001). When the signal reaches an interface, some energy will be reflected and some will be transmitted, causing energy losses. Additionally, the P-S conversion will decay the energy (Austegard, 2013). Amplitude recovery is performed to compensate for these amplitude losses. However, it may also strengthen ambient noise and have the potential of destroying the signal character if not used with caution (Gadallah & Fisher, 2009; Gelius & Johansen, 2010).

3.2.4 Frequency filtering

The aim of frequency filtering is to improve the SNR by removing band of frequencies from the data. Frequency filtering aims to suppress any coherent or incoherent noise events that have a different dominant frequency than the primary energy (Kearey et al., 2002). In order to apply frequency filtering, the signal must be transformed from the time domain, in which it is recorded, to the frequency domain through the two-dimensional Fourier-transform. Various types of frequency filters are illustrated in Figure 3.8. The application of a high-pass (HP) filter will cut out low frequency noise, such as from swell noise, and retain frequencies higher than the specified cut-off frequency. A low-pass (LP) filter will remove frequencies that are higher than the cut-off frequency, such as electric noise. Frequency filtering can also be carried out as an anti-aliasing filter to avoid aliasing in time. This is a low-pass filter with a steep slope (usually 70 dB/octave). A band-pass (BP) filter will retain frequencies within a certain frequency band and remove the energy outside. Opposite, a band-reject (BR) or band-stop filter will remove frequencies inside the specified frequency interval and keep what is outside. A notch-filter is a very sharp band-stop filter that removes a certain frequency, such as electrical noise. When the signal is transformed back to the time domain by inverse Fourier transform, it creates "ringing" in the signal. This is called Gibbs phenomenon and are unwanted oscillations caused by discontinuities in the signal or filters. These unwanted effects are avoided by

tapering the signal, which is created by a gradual decrease in amplitude to zero towards the edge of the filter, rather than a sharp cut-off (Sheriff & Geldart, 1995). The transition-band in Figure 3.8 illustrates how this is applied.
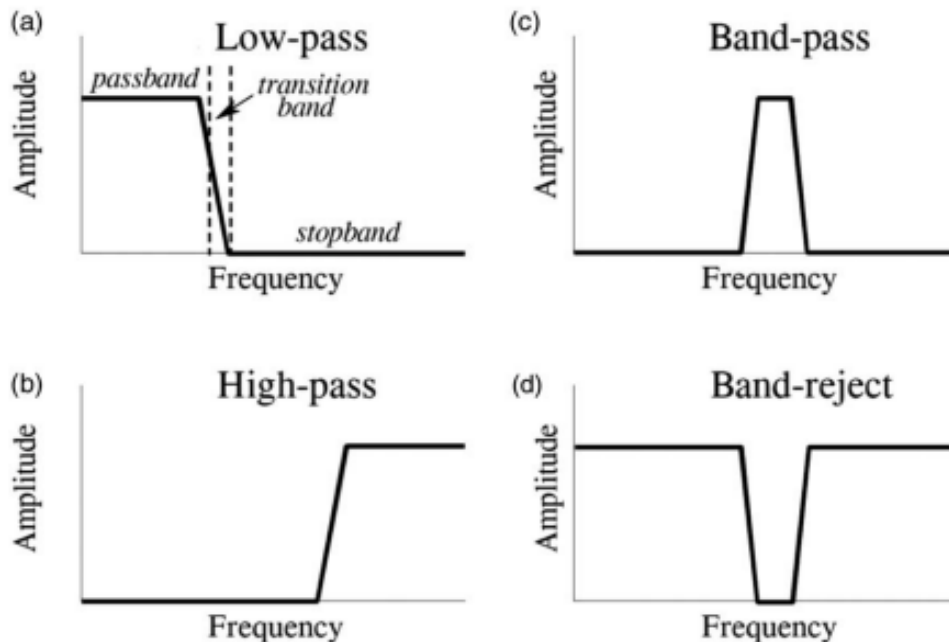
Figure 3.8: Illustration of a low-pass filter (a), high-pass filter (b), band-pass filter (c) and band-reject filter (d) by Obeid et al. (2017). The transition-band are frequencies that plots between the passband (frequencies that are kept) and the stopband (frequencies that are suppressed), which represent a gradual decrease or increase in amplitude.

Frequency filters will normally vary as a function of reflection time, since the dominant frequency of reflected arrivals decrease with increasing length of travel (Kearey et al., 2002). This is linked to absorption of higher frequencies, peg-leg multiples and other natural filtering processes. The band-pass filter should therefore shift towards lower frequencies for later arrivals of the records (Sheriff & Geldart, 1995).

3.2.5   Deconvolution (inverse filtering)

Deconvolution acts to remove the effect of previous filter or convolution operations by convolving the signal with an inverse filter (Kearey et al., 2002). It removes adverse filtering effects (lengthening of the pulse) that occurs when seismic waves travel through the ground. By shortening the pulse, deconvolution improves vertical resolution (Kearey et al., 2002; Gadallah & Fisher, 2009). The general aim of deconvolution is to compress every occurrence of a composite waveform to form a spike output, and in turn reproduce the reflectivity function

28

of the subsurface layering (Kearey et al., 2002). There are several applications of an inverse filter, such as the removal of reverberations in the signal and deghosting. Deconvolution is also able to remove significant parts of the multiple energy in seismic sections (Austegard, 2013). Predictive deconvolution attempts to predict the arrival time of multiple energy from the knowledge of primary energy arrival times (Kearey et al., 2002).

3.2.6 Velocity filtering

Velocity filtering, also called f-k filtering or dip filtering, acts to remove coherent noise based on particular dip angles of seismic events. This is determined from the apparent velocity v_a of which it propagates across a spread of detectors, expressed in equation 3.1. v_a is calculated from frequency f and wavenumber k_a, which equalise a wave travelling at velocity v at an angle a.

(eq. 3.1)

$$v_a = \frac{v}{\sin a} = \frac{f}{k_a}$$

To perform f-k filtering, the data is transformed from the t-x domain to the f-k domain by the two-dimensional Fourier transform, before it is transformed back again after filtering. Frequency f is plotted against wavenumber k_a with a gradient of the v_a. This forms wedge-shaped zones that fit different types of seismic events (Figure 3.9). In this way, it is possible to separate particular unwanted seismic events on the basis of their apparent velocities. Events that plot in the positive wavenumber field will appear to travel away from the source, while events that plot in the negative field will travel towards the source. The aim in f-k filtering is to define a negative and positive cut-line that includes the primary reflections and rejects everything else. It can filter out events of anomalous dip in portions of the seismic record sections, such as diffraction patterns, or be applied to individual shot-gathers to remove high-velocity noise, for instance. F-k filtering enables a better estimation of stacking velocities and then also a better suppression of multiples (Kearey et al., 2002). The filter is usually applied several times throughout the processing sequences, first in a very early stage to remove obvious noise, then later to remove artefacts caused by other processing stages (Kearey et al., 2002).
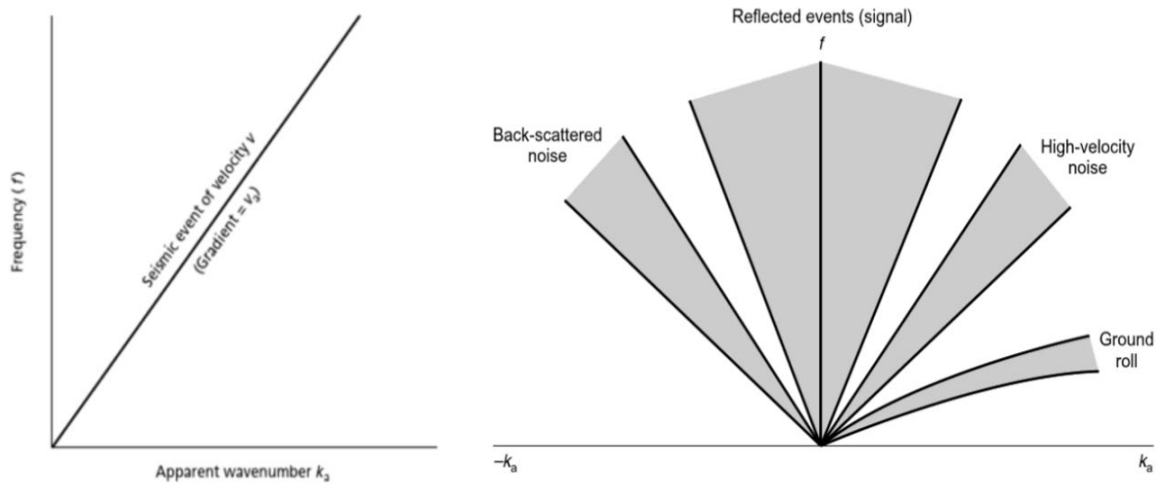
Figure 3.9: Illustration of velocity filtering of a shot-gather that contains primary reflection events and noise, displayed in a f-k plot. Based on the apparent velocity of events, it is possible to suppress unwanted noise (Kearey et al., 2002).

3.2.7 Static correction

Local variations in water depth cause unwanted "pull-up" (local highs) and "pull-down" (local lows) effects for the reflectors under the seabed. The larger the velocity differences are between the water and seabed, the greater these effects turn out (Ruud, pers. comm). Marine surveys close to shores or in fjords are particularly prone to this problem, as they commonly have large local variations in water depth over a small area (Kearey et al., 2002). Local variations may severely degrade the quality of the seismic data, due to wrong stacking velocities. Seismic reflections will be delayed by dissimilar times caused by velocity differences between the water and subsurface. In turn, this will result in distortion in the hyperbolic trajectory of the NMO and wrong stacking velocities (Kearey et al., 2002). Static correction must therefore be applied before NMO-correction to enable a common height datum (Yilmaz, 2001).

3.2.8 Velocity terminology

Seismic energy pulses are reflected from interfaces in the subsurface and recorded by detectors at the surface. Due to different physical properties in the subsurface, velocities vary as a function of depth. The velocity will normally increase with depth due to increasing compaction. The average velocity $\bar{V}$ is given in equation 3.2, where Z_n is the total thickness of the top n layers, while T_n is the one-way travel time through n layers.

(eq. 3.2)

$$\bar{V} = \frac{Z_n}{T_n}$$

Root-mean-square (RMS) velocity (eq. 3.3) takes different travel times in different layers into account and produces a closer approximation of an average velocity compared to $\bar{V}$ given in equation 3.2. It is a velocity estimation of the layers overlying the *n*th reflector, as a multi-layered ground creates a complex travel-path with inclined rays (Kearey et al., 2002). In the following equation, v_i is the interval velocity of the i*th* layer and t_i is the one-way time of the reflected ray through the *i*th layer.

(eq. 3.3)

$$V_{rms,n} = \left[\sum_{i=1}^{n} v_i^2 t_i \Big/ \sum_{t=1}^{n} t_{i1} \right]^{1/2}$$

3.2.9   NMO and velocity analysis

Accurate velocity models are crucial to produce a correct seismic image of the subsurface. A velocity analysis is performed on selected CMP-gathers to find accurate stacking velocities that correct for the normal-move-out (NMO). This is an effect that occurs due to the increasing distance between shot and receivers, which increases the travel-time for reflections. The NMO for the *n*th reflector is given by equation 3.4, where *x* is the offset and *t* is the total travel time.

(eq. 3.4)

$$\Delta T_{nmo} \approx \frac{x^2}{2V_s^2 t_0}$$

A velocity analysis aims to identify the NMO by obtaining velocity picks that give the closest representation to the observed hyperbola, over the entire spread length of the CMP-gather (Figure 3.10) (Yilmaz, 2001). To find optimal stacking velocities as a function of arrival time, CMP-gathers are displayed side-by-side in a velocity spectrum (Kearey et al., 2002). These spectrums usually display contour plots, which is a measure of signal coherency. Peak power

is assumed to represent optimal stacking velocity (V_s). Velocity normally increases monotonically with depth for primary reflections. Peaks in the contour plots may also represent multiples, but these are usually associated with lower velocities since they spend more time in the water layer (Sheriff & Geldart, 1995).
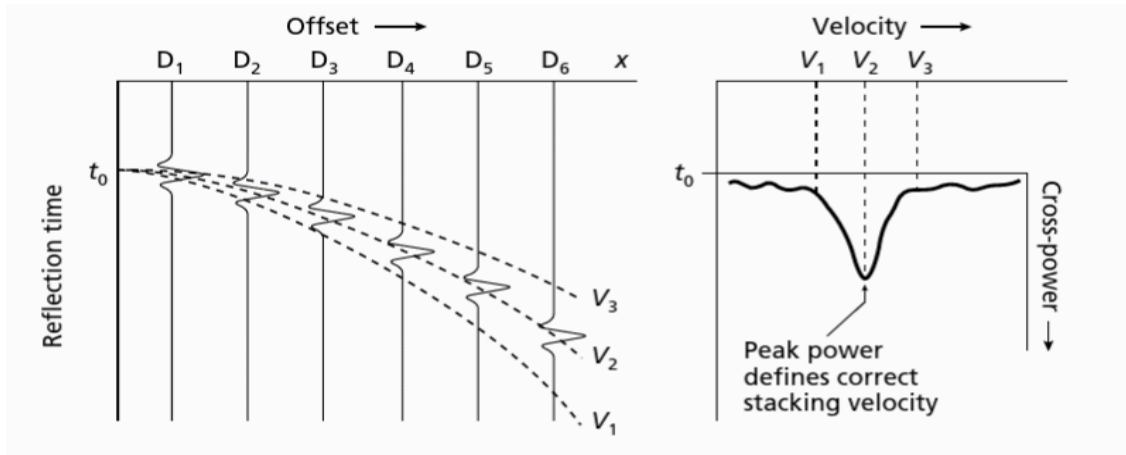
Figure 3.10: Hyperbolic events for traces in a CMP-gather. Optimal velocity is V_2 since this velocity approximates the hyperbola and fits the peak power. The figure is derived from Kearey et al. (2002).

3.2.10 NMO-correction

NMO-correction is applied after velocity analysis. A successful velocity analysis will flatten out the hyperbolas in the CMP-gathers and simulate a zero-offset response (Figure 3.11) (Yilmaz, 2001). If the NMO-corrected traces instead curve upwards, this indicates that the traces are overcorrected and that the picked velocities are too low. Opposite, if the traces bend down-ward, they are undercorrected and the picked velocities are too high.
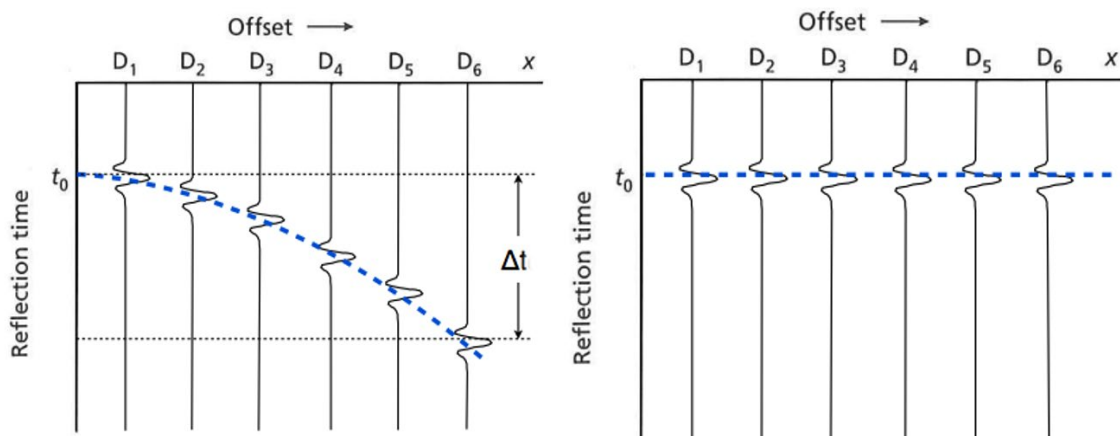
Figure 3.11: Correct velocity will flatten out the hyperbolic moveout during NMO-correction. Modified from Kearey et al. (2002).

3.2.11 Muting

In order to optimise the seismic data quality, it is necessary to exclude traces of poor quality. Muting is used throughout several stages in the processing to enhance seismic resolution and will set traces within a specified range to a value of 0 to completely cancelled out the energy. This is usually applied to the first-breaks and the refraction wave trains that follow them, since they are so strong that they may degrade shallow reflection quality during stack (Sheriff & Geldart, 1995). Reflections at shallow times and far-offset arrivals commonly suffer from large stretching due to rapid changes in the NMO. This changes the frequency spectrum of the wavelet and attenuates higher frequencies during stacking. Stretched traces are therefore muted to avoid degradation of seismic quality (Sheriff & Geldart, 1995).

3.2.12 DMO-correction

A dipping surface will have the reflection points in a CMP-gather spread out along the reflector, as illustrated in Figure 3.12. This creates what is called a dip-move-out (DMO), which changes the offset and decreases the zero-offset travel time. This is particularly the case in areas of structural complexity, such as folds and fault, as the moveout from steeply dipping fault plane reflections will be in conflict with the moveout from gently dipping or near-flat reflectors during stacking. This will cause wrong stacking velocities and smearing in the seismic unless it is corrected for (Sheriff & Geldart, 1995). DMO-correction is applied after NMO-correction to correct for dipping effects on stacking velocities, and thus preserve conflicting dips during stacking. DMO-correction in combination with post-stack time migration is a robust method for imaging complex geological structures (Yilmaz, 2001).
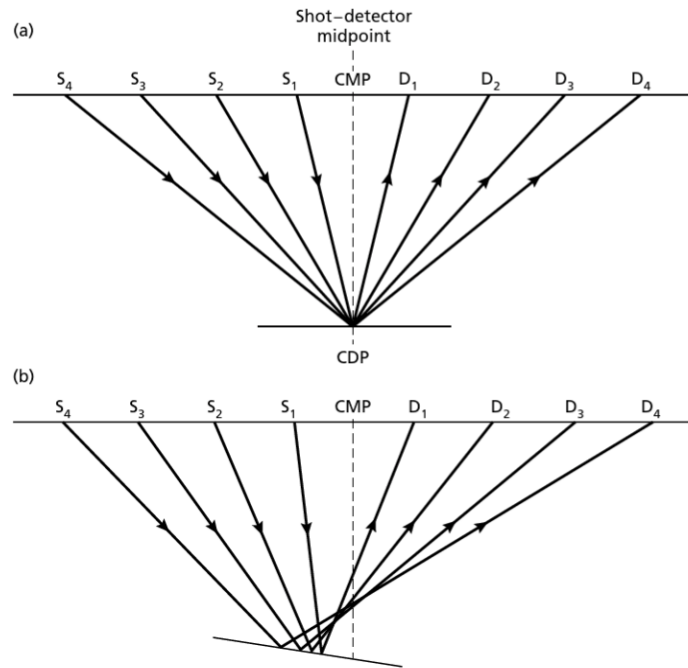
Figure 3.12: A common depth point is not achieved when a dipping reflector is present (figure b), as it is for a horizontal reflector in figure (a). Rather, the reflection points are spread out along the reflector. Illustration by Kearey et al. (2002).

3.2.13 Stacking

Stacking sums all NMO-corrected traces in a CMP-gather (Figure 3.13). If correct stacking velocity is applied, this considerably increases the SNR as the primary energy will have a constructive interference. Multiple energy and noise will have a destructive interference, and therefore be attenuated during stacking (Yilmaz, 2001). Stacking gives one response for a CMP and is often regarded as a zero-offset section (Sheriff & Geldart, 1995).
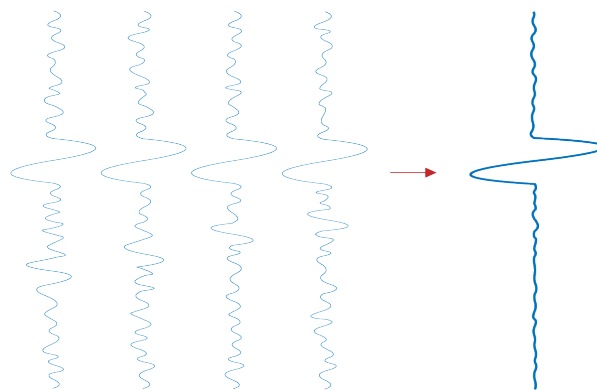
Figure 3.13: Stacking of a CMP-gather. Primary energy is amplified relatively to noise. The figure is extracted from Gelius & Johansen (2010).

3.2.14 Migration

Non-migrated seismic images suffer from diffractions and misplaced events that occur from non-horizontal interfaces. Point sources yield hyperbolic patterns in the seismic image, while dipping events are displayed with a shallower dip (Figure 3.14). Synclines appear as "bow-tie" events, resulting from the presence of three discrete reflection points for any surface location (Figure 3.15). The reflection point of a seismic event with a given reflection time may be anywhere on the arc of a circle, centred on the source-detector position. This arc represents a locus of all reflection points with equal travel times. Prior to migration, this point will be imaged vertically below the source-detector position, as displayed in Figure 3.14 (Kearey et al., 2002). In turn, this creates an incorrect image of the subsurface.

Migration is the process of repositioning seismic events back to their supposedly true subsurface locations, at a corrected vertical reflection time. It increases spatial resolution by focusing the energy in the Fresnel Zone, correlates dipping reflectors and collapses diffractions (Kearey et al., 2002). However, 2D migration is an imperfect process. It does not provide information on cross-dips and limits the reflection points to lie within the plane of the section. In the presence of cross-dips, the seismic image will not provide a true representation of the subsurface structures, as true reflection points then lie outside the vertical section (Kearey et al., 2002).

Migration may be performed in time or depth, and before or after stacking. Complex models with large dips and strong lateral velocity variations usually require pre-stack migration. Post-stack migration in combination with DMO-correction also provide a robust method to solve for complex geological models and is more computational-efficient (Yilmaz, 2001).
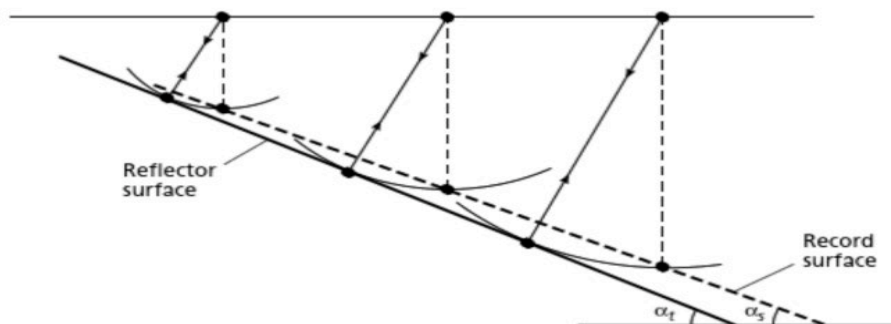
Figure 3.14: A dipping reflector is shallower in non-migrated sections and plotted vertically below the source-detector position (Kearey et al., 2002).
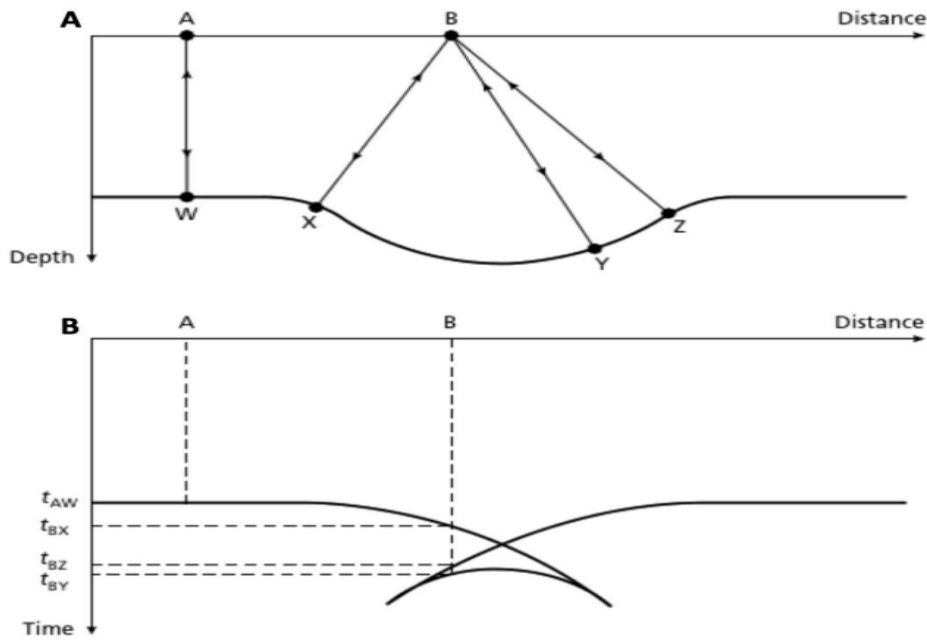
Figure 3.15: Synclines create a "bow-tie" appearance in the non-migrated section (figure B). The upper figure (A) represents the migrated section. Illustration by Kearey et al. (2002).

3.3 Seismic interpretation

When processing is complete, the data is ready for interpretation. The relationship between lithology, acoustic impedance (AI), reflection coefficient (R_c) and the seismic response is given in Figure 3.16. The seismic response is measured by the reflection that is created at an AI boundary, in cases when the physical properties are different for two adjacent layers (Herron, 2011). The AI is given by the following equation:

(eq. 3.5)

$$AI = \rho \, v$$

The R_c for normal incident ray paths at an AI boundary is expressed in equation 3.6, which is the ratio of the amplitude of the reflected wave relatively to the incident wave. The stronger the AI contrast, the higher the amplitude of the reflection. The R_c ranges from -1 to +1 (Hart, 2000).

(eq. 3.6)

$$R_c = \frac{\rho_2 v_2 - \rho_1 v_1}{\rho_2 v_2 + \rho_1 v_1} = \frac{Z_2 - Z_1}{Z_2 + Z_1}$$

36
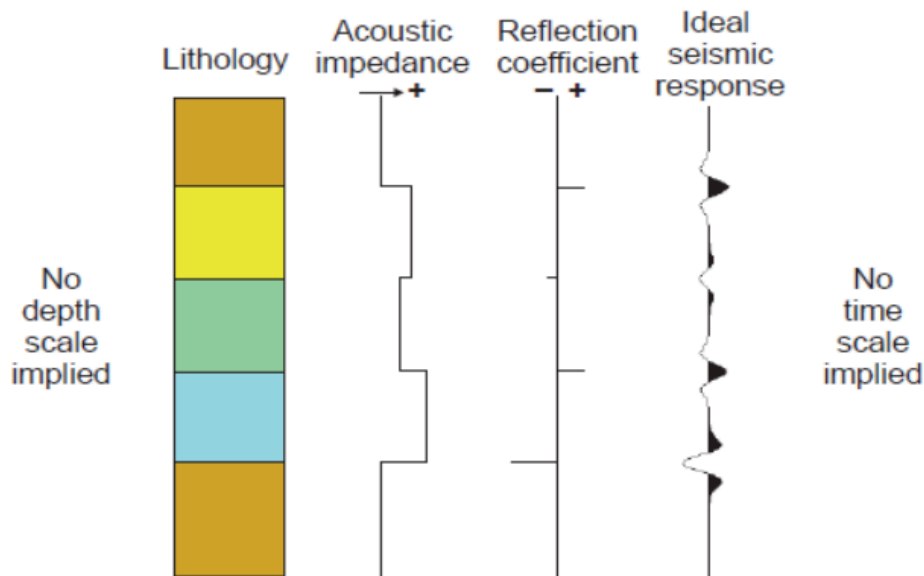
Figure 3.16: A seismic response is generated at an acoustic impedance boundary with a positive or negative reflection coefficient. Illustration by Herron (2011).

Seismic display

After CMP-gathers are stacked as a function of time, the seismic section can be displayed in various ways. The following displays in Figure 3.17 have a vertical axis that represents depth as time, while the horizontal axis represents the distance. Traces may be displayed as a continuous curve (Figure 3.17, A) or as variable wiggle display (Figure 3.17, B), where the peaks are filled with black. A variable density display (Figure 3.17, C) has a user-defined or customised colour scheme assigned to the amplitudes, commonly in the colours red, blue and white. Red and blue represent a peak and trough, while white indicates near-zero amplitudes. The variable wiggle and density display may be combined (Figure 3.17, D), which commonly serves the purpose of deriving more information from the data display. This is because peaks and troughs in the variable density are presented with equal weight visually (Hart, 2000).
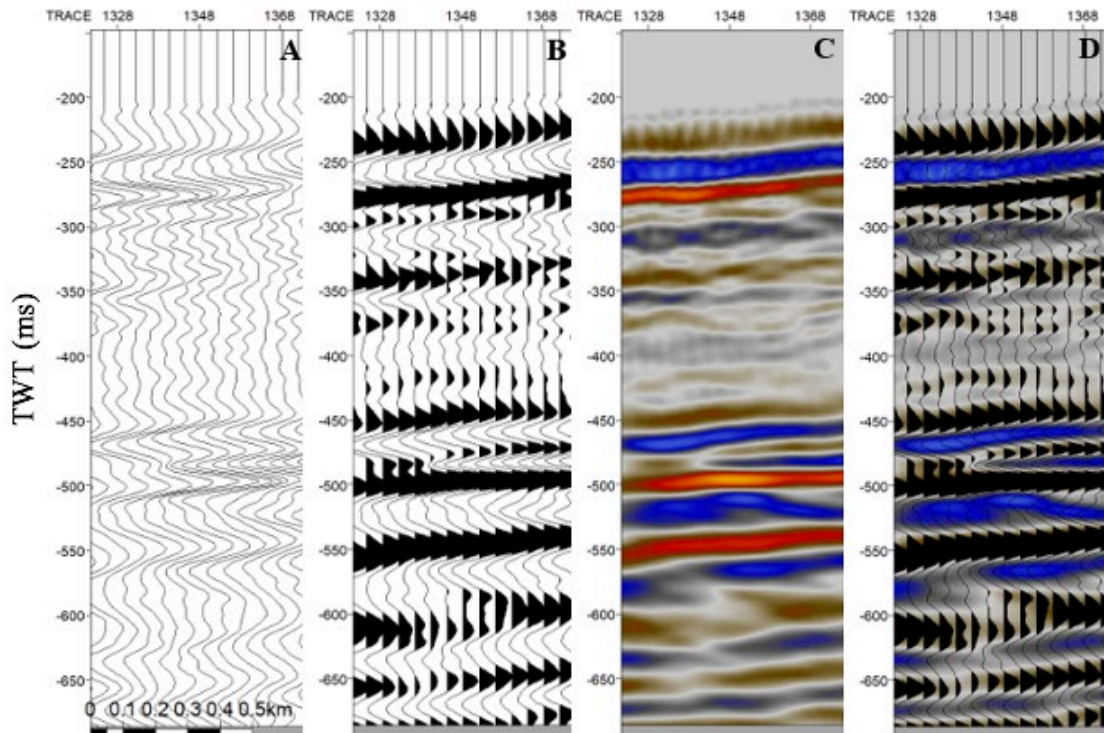
Figure 3.17: Variable ways to display the seismic sections: A) traces only, B) wiggle display, C) variable density display and D) a combination of B) and C). The scale is given in figure A and is the same for all. The figure is derived from line 4.

Polarity

Seismic polarity describes the way the seismic wiggle is visualised in a seismic section, whether the positive R_c will be displayed as a peak or a trough (Hart, 2000). The Society of Exploration Geophysicists (SEG) standard polarity convention, also called the American polarity, displays a positive increase in AI as a peak. Opposite, the European normal polarity displays this as a trough. This study displays the seismic data as European normal polarity, where an increase in AI is displayed as a trough in the colour blue. To find the polarity of a seismic section, one option is to display the combined wiggle and density display and then identify the strong and dominating sea-bottom reflector, which has a positive increase in AI.

Phase

The phase of a seismic signal is the position of a point in time on a waveform cycle. This tells us where the maximum amplitude of the signal will be located relatively to time 0. A zero-phase wavelet is represented by a central peak that is symmetric at t = 0, meaning that the particle motion starts before t = 0. This wavelet is more commonly used in processing, since

its maximum occurs exactly at the position of the reflection interface (Herron, 2011). A minimum phase wavelet will have particle motion only after t = 0, which is usually how the data is recorded at acquisition. Most sources will have a fast build-up of energy after time 0 (Sheriff & Geldart, 1995). An illustration of a zero-phase and minimum-phase wavelet is provided in Figure 3.18.
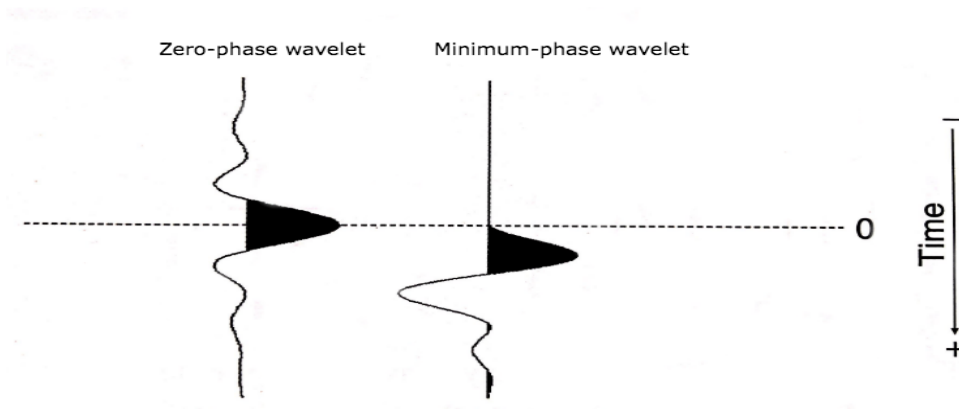
Figure 3.18: A zero-phase and minimum phase wavelet. Modified from Herron (2011).

3.3.1   Stratigraphic interpretation

To interpret seismic data in an efficient way, it is necessary to collect and analyse data and reports from the specific study area. This will give the interpreter an understanding of what to look for and to more quickly identify structural and stratigraphic features (Hart, 2000). Seismic stratigraphic interpretation is subdivided into three steps, which moves from large to small features of interest (Sheriff & Geldart, 1995):

1. Seismic-sequence analysis: The separation of major stratigraphic packages. These represent time-limes in the deposition and are identified based on unconformities or changes in seismic pattern.

2. Seismic facies analysis: The establishment of different depositional environments within a discrete stratigraphic package. This is defined based on a variability of the seismic reflection character.

3. Reflection-character analysis: The identification of changes in the stratigraphy and their nature, based on lateral variation of individual reflection events. This method is commonly performed by modelling of synthetic seismograms or seismic logs.

The seismic-sequence analysis involves subdividing the data into discrete stratigraphic packages. These are identified from unconformities, flossing surfaces or sequence boundaries which generally represent timelines in deposition (Hart, 2000). Sequence boundaries are often recognised by seismic reflection terminations, such as downlap, toplap, onlap and erosional truncation (Figure 3.19). These represent stratal discontinuities in the seismic section that separate conformable sedimentary units from non-conformable units. The surface of a stratigraphic package is then defined by tracing along peaks or troughs.
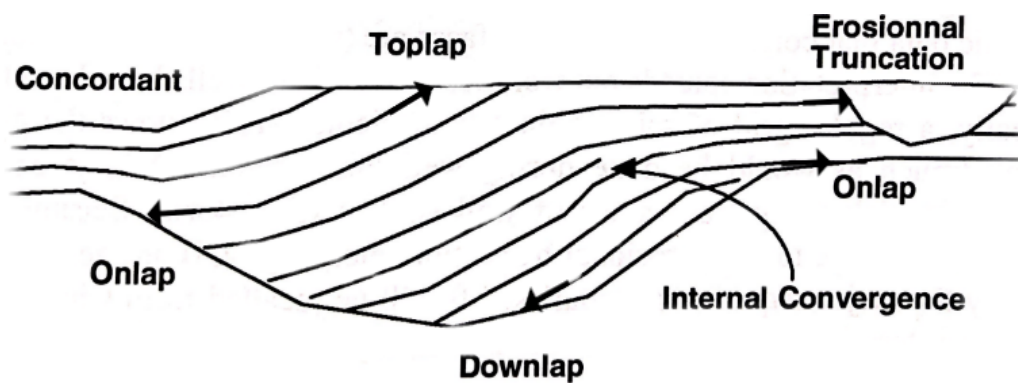
Figure 3.19: Illustration of reflection terminations observable in seismic data. Onlap are horizontal or dip away from their terminations, while downlap dip towards their terminations. Erosional truncation is a termination where a stratal package has been removed by erosion. Toplap is termination of strata against an overlying package, representing non-deposition or minor erosion (Sheriff & Geldart, 1995). Modified from Mitchum et al (1977).

Next, the seismic facies analysis involves distinctive characterisation of one group of reflections that differentiates from nearby reflectors. This step includes establishing facies, which are features that characterise a depositional environment (Sheriff & Geldart, 1995). Classifications of sequences are defined based on reflection terminations, reflection characteristics, stratal patterns and the external shape. The reflection characteristics are examined by their frequency content, amplitude and continuity (Hart, 2000). Following, stratal patterns are identified from the abundance and continuity of the reflectors, including the consistency of the amplitude. Figure 3.20 illustrates different reflection characteristics. Parallel reflections propose uniform deposition in a stable environment, on a steady or uniformly subsiding surface. A variation in the rate of deposition across an area or gradual tilting is likely to result in divergent reflectors. If the reflectors are chaotic, this indicates high depositional energy, changing conditions during deposition or disruption after deposition, such as slumping, sliding or turbidity-current flow. A sequence that is reflection free indicates the presence of a uniform lithology (Sheriff & Geldart, 1995).
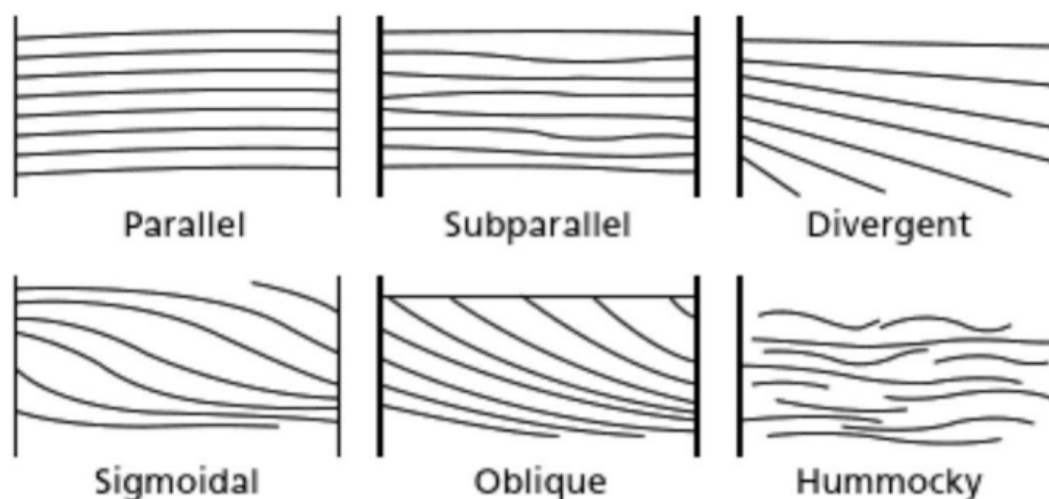
Figure 3.20: Illustration of reflection characteristics (Kearey et al., 2002).

A reflection character analysis is performed to better understand the relationship between seismic reflections and the physical properties of rocks (Hart, 2000). This is a detailed study of trace-to-trace changes in the waveshape of an area of interest and how this relates to the stratigraphy or fluid in the pore spaces (Sheriff & Geldart, 1995). The analysis is commonly performed by modelling of synthetic seismograms or seismic logs (Hart, 2000).

3.3.2 Structural interpretation

Structural analysis is centred around defining geometry patterns in the seismic profile. First, structural deformation style depends on the tectonic setting, whether the study area has been subjected to divergent (separating), convergent (coming together) or transform (sliding past each other) plate boundary forces. Depending on the magnitude, duration of stresses, strength of the rock, adjacent rocks etc, this will produce a variety of structural features (Sheriff & Geldart, 1995). Major patterns should be defined first, followed by more detailed interpretation. Faults are defined as a "displacement of rocks along a shear zone" (Sheriff, 2002). The signature of faults in the seismic is highly variable but they are generally recognised by sharp terminations in reflections, that resume again in displaced positions on the other side of the fault (Sheriff & Geldart, 1995). Complex fault zones require stratigraphic and structural interpretation to be closely correlated. Isopach maps are a tool for structural interpretation, which display thickness variations between two subsurface horizons. In this way, they form a time-variant map that can display paleo structures of a horizon, before the upper horizon was deposited (Gadallah & Fisher, 2009).

3.3.3 Seismic resolution

Seismic resolution is separated into vertical and horizontal resolution. Vertical resolution is defined as the ability to separate two discrete features (Sheriff, 2002; Gelius & Johansen, 2010). It is dependent on the AI contrast and the thickness of the beds relatively to the dominant wavelength of the acoustic pulse. The bed must be at least ¼ λ to produce separate reflections in the seismic section. ¼ λ is known as the tuning thickness of a bed, in which reflections from the upper and lower surfaces have a maximum constructive interference and amplitude response. Vertical resolution gradually decreases with depth. Higher velocity and decreasing average frequency with depth increases the average wavelength, which in turn lowers the ability to resolve fine-scale stratigraphic details in deeper sections (Hart, 2000; Austegard, 2013).

Horizontal seismic resolution is a measure of the lateral spacing between two points in order to be distinguishable. This is expressed by the Fresnel Zone, which is defined as "the portion of a reflector from which reflected energy can reach a detector within one-half wavelength of the first reflected energy" (Sheriff, 2002). Waves that have this arrival time will interfere constructively and be detected as a single arrival. Distances that are smaller than the Fresnel Zone will interfere destructively and therefore not be possible to observe individually (Kearey et al., 2002). In such, a smaller zone will generate a better horizontal resolution. The radius of the Fresnel Zone (R_f) is given in equation 3.7.

(eq. 3.7)

$$R_f = \sqrt{\frac{\lambda Z}{2}} = \sqrt{\frac{vZ}{2f_c}}$$

The Fresnel Zone is a measure of depth Z, the average wave propagation velocity v and the dominant frequency f. The Fresnel Zone is measured with respect to unmigrated seismic data. Migration is therefore a tool for enhancing horizontal resolution by collapsing these zones (Herron, 2011). However, 2D migration only collapses the Fresnel Zone in the in-line direction, which limits the spatial resolution (Cartwright & Huuse, 2005). An illustration of the Fresnel Zone is given in the figure below.
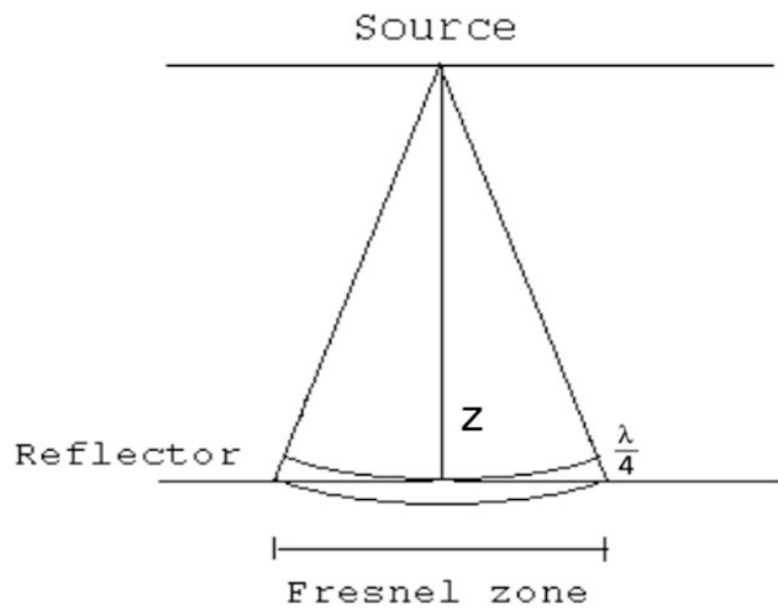
Figure 3.21: An illustration of the Fresnel Zone, modified from Austegard (2013).

4 Data acquisition

Several 2D multichannel reflection seismic lines were acquired in Isfjorden, Spitsbergen in the period between August 31st to September 3rd in 2002. This was acquired by the vessel R/V Håkon Mosby and performed as a part of the 2002 SVALEX student project, a cooperation between UiB, NTNU, Statoil and the Norwegian Petroleum Directorate. A total of 14 seismic lines were collected. This study will process and interpret four of these. An overview of the relative locations of the lines is given in Figure 4.1, while the acquisition parameters are listed in Table 4.1. No downtime due to bad weather conditions was recorded, nor severe errors in the seismic. A recording filter with a low-cut of 3 Hz (18 dB/octave) and high-cut of 180 Hz (72 dB/octave) was applied during acquisition. This acts as an anti-aliasing filter and removes low-frequency noise occurring from waves and drag in the streamer.

Vessel	R/V Håkon Mosby
Speed	4.5 knots
Streamer	3 km Nessie 3 of WesternGeco
Recording system	Tracq by WesternGeco
Source	5 airguns (GEO, UiB airgun string) + 1 additional airgun (580 cubic inches)
Shot-point interval	50 m
Sampling interval	2 ms
Group length	12.5 m
Record length	12 s (TWT)
Airgun depth	7 m
Streamer depth	10 m
Channels	240
Distance from GPS antenna and centre of source	72 m
Distance from GPS antenna to first active channel	150 m
Recording filter	Low-cut: 3 Hz (18 dB/octave) High-cut: 180 Hz (72 dB/octave)

Table 4.1: Acquisition parameters during the 2002 SVALEX project in Isfjorden. All values are extracted from Mjelde (2003).
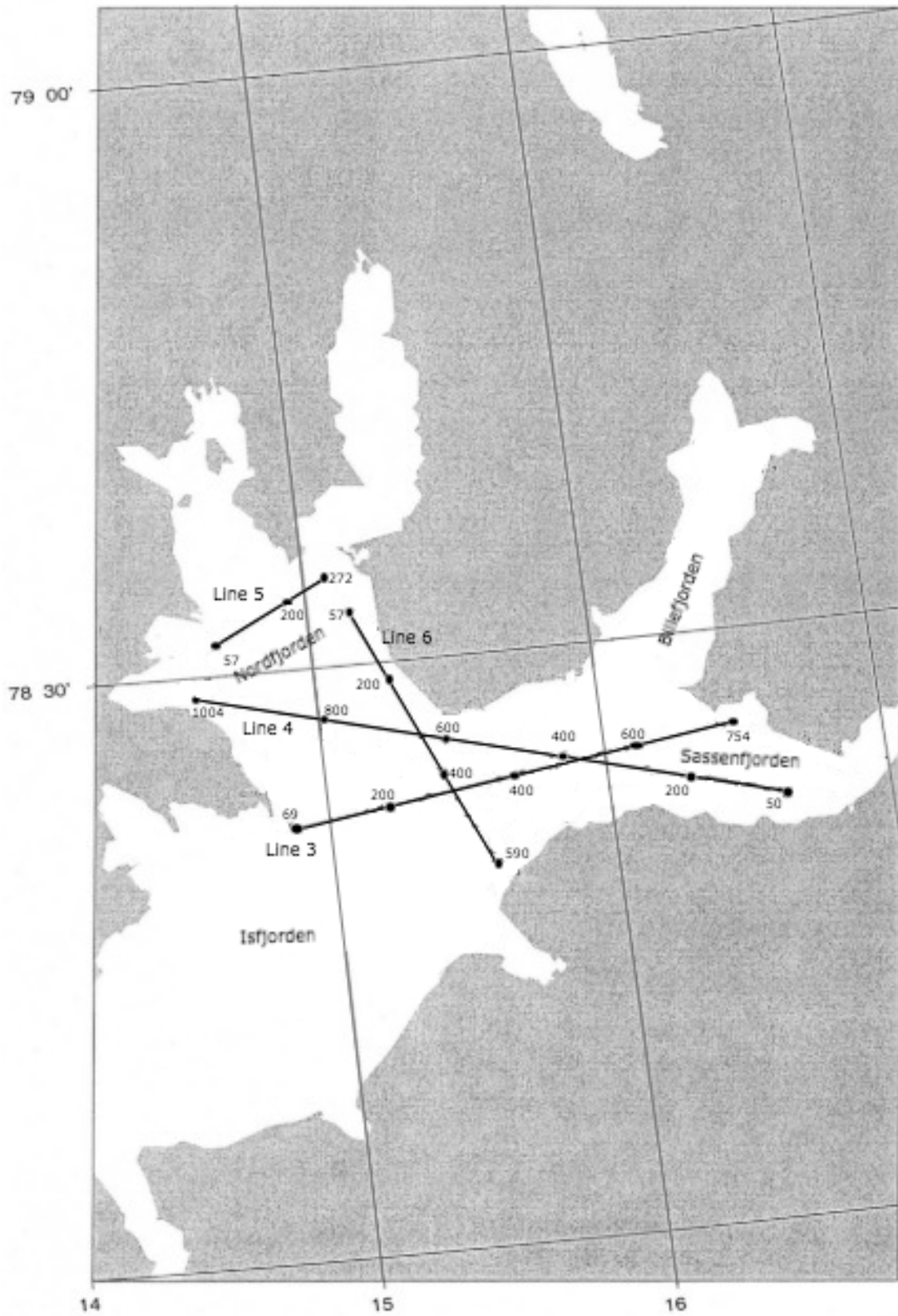
Figure 4.1: An overview of the study area and four 2D multichannel seismic lines that were collected during the 2002 SVALEX project. This figure displays line 3, 4, 5 and 6. The shotpoints are plotted along the lines. Modified from Mjelde (2003).

The geographical positions of the lines are listed in Table 4.2. These are recorded in UTM-datum, zone 33X. The lines cover areas in Nordfjorden, Sassenfjorden and inner Isfjorden. Line 5 was collected in Nordfjorden and does not cross any of the other lines that will be used in this study. This line was shot in a NE direction. Line 6 was acquired along the NE part of Nordfjorden, extending across Isfjorden in a SE direction. Line 3 was shot in an ENE direction, starting in the NW part of Isfjorden and was completed in Sassenfjorden. Line 4 was shot in the other direction (WNW), starting in Sassenfjorden and ending in the SW part of Nordfjorden.

Line no.	Event no.	Northing	Easting	°N	N_{min}	°E	E_{min}	Length (km)
Line 3	69	Ca. 8728200	Ca. 764520	78	Ca.23	14	Ca. 55	37.2 km
	745	Ca. 8741680	Ca. 789590	78	Ca. 27	16	Ca. 27	
Line 4	50	8733954.53	803710.43	78	21.558132	16	36.069328	49.9 km
	1004	8737618.85	756156.56	78	28.938126	13	33.856584	
Line 5	57	8742716.84	757183.31	78	31.513938	14	39.280308	12.7 km
	272	8750028.13	765064.58	78	34.507026	15	4.153428	
Line 6	57	8747092.05	767386.70	78	32.707032	15	8.670912	29 km
	590	8724744.62	781907.91	78	19.334208	15	34.13874	

Table 4.2: The geographical positions of the four seismic lines of this study. These are recorded in UTM-datum, zone 33X. All values are collected from the 2002 SVALEX cruise-report by Mjelde (2003).

Some problems occurred during the acquisition of line 3 and 6. For line 3, the streamer was not straight until shotpoint 69, and was up to 100 m offline to the south at shotpoint 160. This occurred due to GPS problems. For line 6, there was some problems related to bird 1 and 2. These had a depth of ca. 11.5 m and 12.5 m for most shots from around shotpoint 335. During processing, it was found that the navigation data for line 3 was lost. For these reasons, this line was drawn manually on the map in an editing program. The positions were plotted based on the information from the planned survey and the field logs (Mjelde, 2003). The other two lines, line 4 and 5, were acquired without incidents.

The airgun configuration (Figure 4.2), far-field signature (Figure 4.3) and the amplitude spectrum (Figure 4.4) are displayed in the following three figures. The geometry of the source

is an airgun string with 5 guns, including an additional 580 cubic inch airgun. The long-array is towed in the same direction as the vessel, with a decreasing size of the airgun volume backwards. The differences in volume sizes have the purpose of attenuating the bubble pulse, as discussed in subchapter 3.1.1. The additional airgun, which is placed 10 m directly to the left from the first airgun in the array, holds the largest volume. The airgun configuration has a total volume of 2615 cubic inches and is a simple areal array. The energy is focused in the in-line direction, vertically downwards. The additional airgun limits the energy to transmit side-ways and cause sideswipes. This is necessary especially in fjords, sine these areas are prone to sideswipes from the sides of the fjord (Gelius & Johansen, 2010). The far-field signature is an overview of how the signal will be registered at a distance of 9 km behind the vessel with an incident angle of 0 degrees. The signature of the amplitude spectrum is shown with the same distance and incident angle.
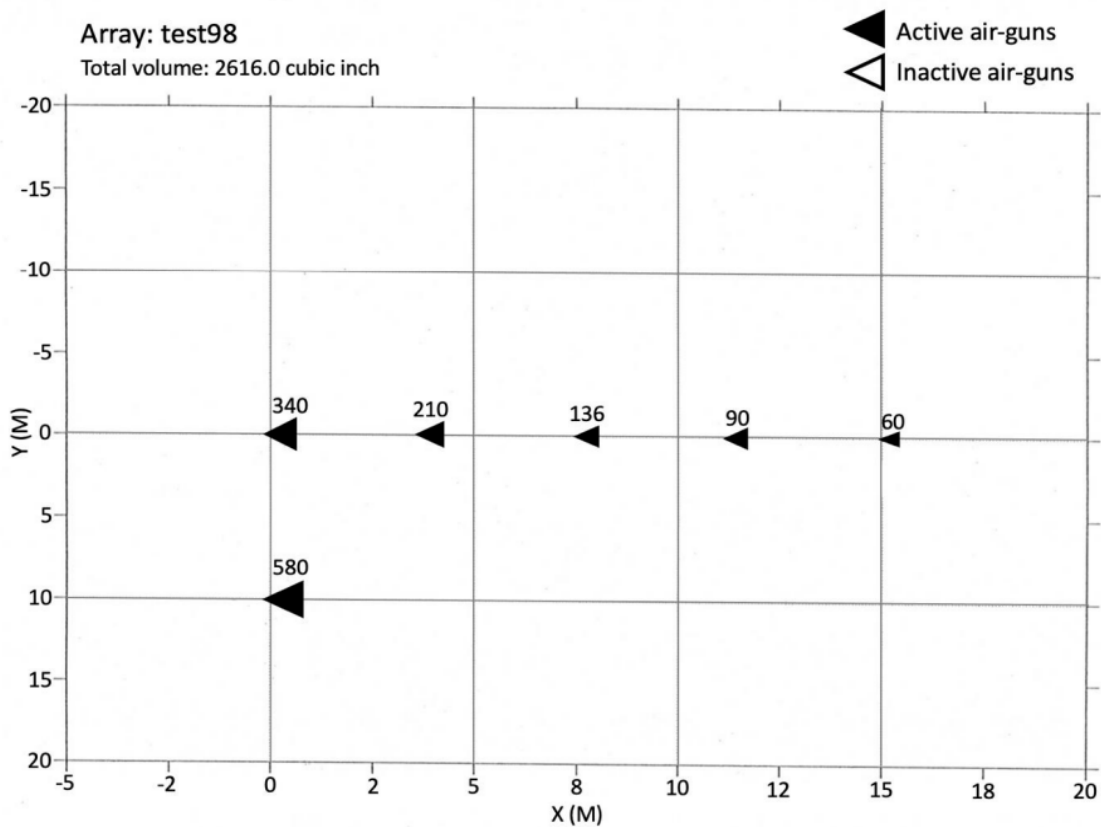
Figure 4.2: The geometry of the airgun configuration during the acquisition, showing their position and volume. The volume number over each airgun is given as cubic inches (Mjelde, 2003).

Far-field signature of array: test98

Distance: 9000 m   Azimuth: 0 deg   Angle of vertical: 0 deg

Primary : 17.0 barm	Source depth : 10.00 m
Peak-peak : 38.9 barm	Streamer depth : 0.00 m
P/B ratio : 7.8	Filter: out - 128.0/72 DFS V
Period (+/-) : 146.0/ 147.5 msec	Volume : 2616 cu.in.
	Pressure : 2000 psi
	Ghost strength : -1.00
	Sea temperatur : 7.00 C

bar m
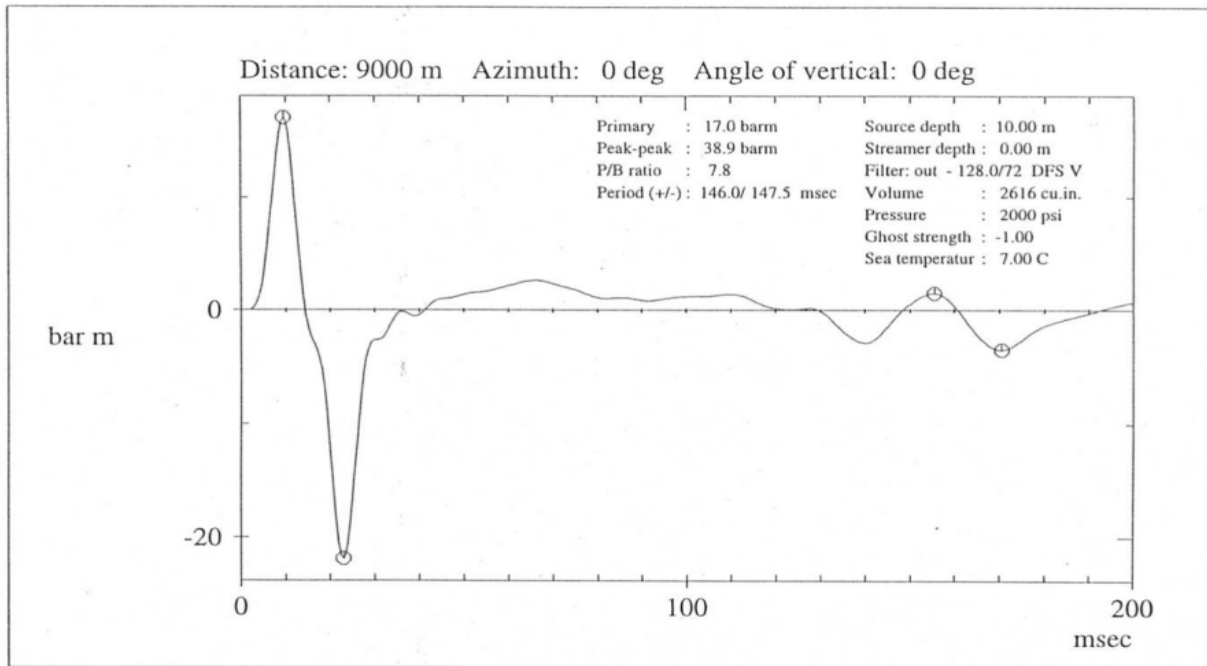
1200,580 10m

Figure 4.3: The far-field signature of the source array at 0 degrees incident angle (Mjelde, 2003).

Amplitude spectrum of far-field signature of array: test98

Distance: 9000 m   Azimuth: 0 deg   Angle of vertical: 0 deg

dB
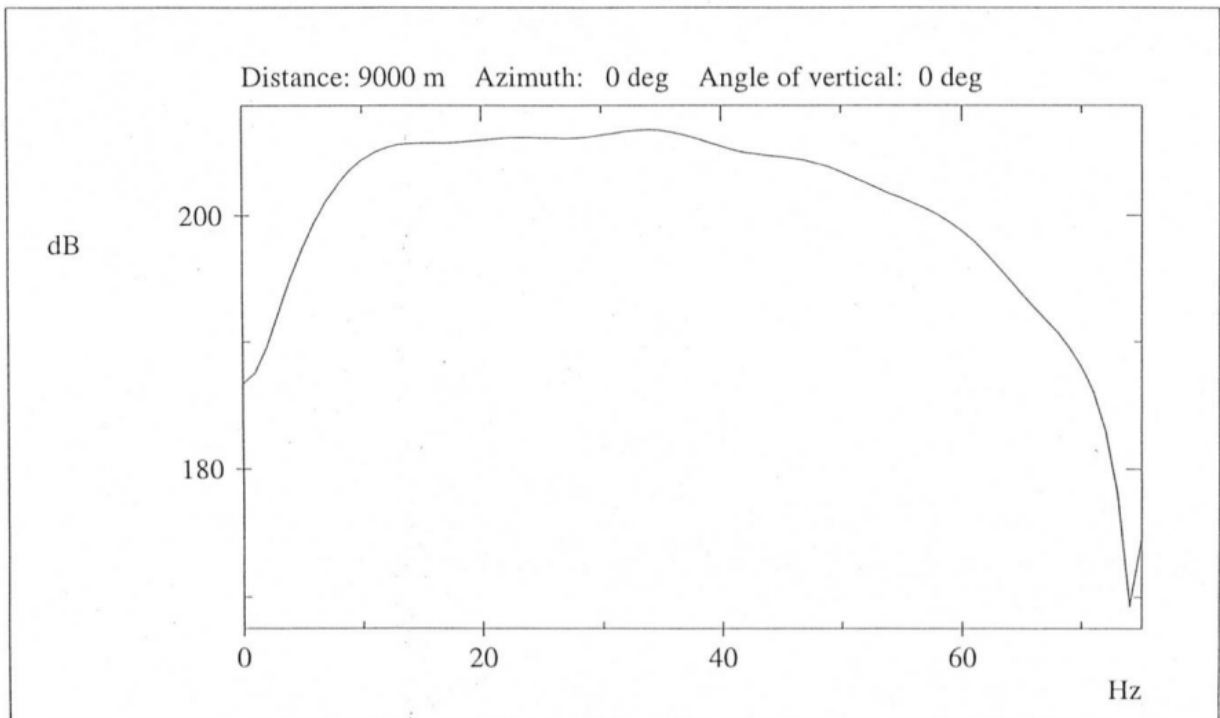
1200,580 10m

Figure 4.4: The amplitude spectrum of the far-field signature of source array at 0 degrees incident angle (Mjelde, 2003).

5 Processing

This chapter will first present the Geocluster software that has been used for processing of the seismic data. Next, the processing sequences will be presented, as well as the effect of various processing modules on the data.

5.1 The software – CGG Geocluster

Geocluster is a seismic processing software developed by CGG (Compagnie Générale de Géophysique). The processing of this study was executed using the Geocluster 5.0, 2008 version. Geopad is the main application of the software, which works as a platform and file manager for the processing sequences of the project. Other applications and tools will also be accessible from Geopad. The following subchapters will briefly discuss the main applications used in this study.

5.1.1 Xjob

This application is used to build and execute processing sequences. An Xjob consists of a workflow, which is a set of processing modules that will be run after another. The individual parameters of each module are defined and adjusted by the user.

5.1.2 Geovel - Chronovista

Geovel is a part of Chronovista, which is an application used to perform velocity analysis in the time domain and for quality control. The "Velocity Analysis Viewer" offers a range of graphical tools to optimise the picking of stacking velocities. The velocities derived from the velocity analysis may then be quality checked in Isovel. This application allows the user to visualise the correlation of RMS and interval velocities across the CMP-gathers and correct them in cases where they deviate in a small area. The stacking velocities may be altered and saved in both the velocity analysis and Isovel.

5.1.3   Xps

Xps works as a database library that stores auxiliary data used in the processing sequences. This includes stacking velocities derived from the velocity analysis, sea-bottom depths or mute functions created in Teamview. The data is given an "ident" and a "version", which makes the data possible to identify during processing sequences. The ident is constant for one project, while the version defines the specific dataset. The values of the library may be edited directly in Xps.

5.1.4   Teamview

This application displays the seismic data that is created from the processing sequences. This enables the user to study the effects of the processing modules on the data and decide whether the results are satisfactory. Seismic images can be displayed and compared side-by-side. In such, scaled stacking velocities may be visualised in Teamview to find the optimal values. Teamview has several additional tools, including displaying the frequency content and f-k spectrum of the seismic images. Manually picking of seabed and mutes are also performed in Teamview. The seismic data may be plotted with different types of amplitude scaling, the scaling of axes may be altered and the data can be shown with different colourmaps and seismic displays. This study will display the data with RMS amplitude scaling and use the colourmap "BlackWhite31". The "BluWhiteRed31" will be used to display the f-k spectra.

5.2   Processing sequence

This chapter will present the processing of the data, which includes 10 processing sequences. These are performed with the intention of removing the strong multiples and noise in the seismic sections without removing the primary energy. To optimise the sequence parameters and achieve the best seismic images, some sequences are run several times. This was the case for the velocity analysis, stacking and migration sequence. Teamview is actively used to assess which processing values that provides the desired seismic results. The velocity model is updated and run in the DMO-correction, vespa, velocity analysis and stacking sequence until the stacking does not further improve. Line 4 will be used as example throughout this chapter. Same procedure is performed for all lines, unless else is specified. The workflow is displayed in Table 5.1.

Editing	
SEGIN	Read SEG-Y file to CGG format
QCTRL	Quality control
HISTA	Reduce trace length
FILTR	Band-pass filter
RSAMP	Resample from 2 to 4 ms to reduce amount of data
SPASM	Remove noise bursts
MODET	Update header words
OUTBD	Main output; Write CGG tape format

↓

Signature deconvolution	
INPTR	Read CGG tape format
DESIG	Signature deconvolution, removal of bubble pulse
SPARN	Remove incoherent noise
REFOR	Spherical spreading correction
SPASM	Spatial amplitude smoothing
FKFIL	Velocity filtering
OUTBD	Main output; Write CGG tape format

↓

FK-filter	
XPSID	Xps identifier
INPTR	Read CGG tape format
FKFIL	Velocity filtering of shot-gathers
BSORT	Sort to receiver-gathers
FKFIL	Velocity filtering of receiver-gathers
BSORT	Sort to receiver-gathers
RECOV	Amplitude recovery
DECSC	Surface consistent predictive deconvolution
OUTBD	Main output; Write CGG tape format

↓

Static correction	
XPSID	Xps identifier
INPTR	Read CGG tape format
HABIL	Receiver water depth (W47)
MODET	Receiver side statics (W48)
HABIL	Shot water depth (W47)
MODET	Shot side statics (W49)
MODET	Total statics (W51)

HEDFI	Remove average statics for each CDP
HISTA	Apply statics (W45)
OUTBD	Main output; Write CGG tape format

Velocity model	
XPSID	Xps identifier
DAGEN	Generate traces with zero amplitude
MODET	W25 (interval velocity) = V2 – V1
EVERY	Set all amplitudes to W25
MUTES	Mute above water-bottom
MODET	W25 = V1
EVERY	Add W25 to all amplitudes
MODET	Set line nr.
VI2VR	Compute V_{rms} from V_{int}
TRVEL	Save V_{rms} library

DMO-correction	
XPSID	Xps identifier
INPTR	Read CMP-gathers
MUTAN	External mute from indecent angle
FILTR	Band-pass filter
FANMO	(Dynamic) NMO-correction
KIDMO	Kircchoff 2D DMO-correction
FANMO	Inverse NMO
OUTBD	Main output; Write CGG tape format

Velocity analysis preparation	
XPSID	Xps identifier
INPTR	Read CMP-gathers
FILTR	Band-pass filter
VESPA	Prepare data for velocity analysis, option variable velocities + trace output

Velocity analysis	
Chronovista → Geovel	Velocity analysis
Chronovista → Geovel	Quality control

Stack	
XPSID	Xps identifier

INPTR	Read CMP-gathers
MUTAN	External mute from incident angle
FANMO	Dynamic NMO-correction
STAPA	Trace stack
FILTR	Time variant band-pass filter

Post-stack migration	
XPSID	Xps identifier
MNGTY	Merge traces into one gather
MODET	W6 = 1, Amplitude set to 1ms
MUTES	Mutes above water-bottom line
FILTR	Band-pass filter
FKFIL	Dip filtering in f-k domain to remove spatial aliasing
SCALE	Gradual downscaling of traces in both ends of the line
FXMIG	2D migration in the f-k domain
SELTR	Trace selection of CDP

Write SEG-Y	
MODET	W5 = 4xCDP
HABIL	Get UTM coordinates (UTM zone 33)
MODET	Copy coordinates
BSORT	Invert plot (only for line 4)
SEGOU	Write SEG-Y format

Table 5.1: Processing workflow of this study.

5.2.1 Editing

In this first processing step, the raw data is formatted from SEG-Y format to the intern Geocluster format called CGT. A quality control of the traces is performed, in which noisy traces are removed or replaced with interpolated values of surrounding data. It is applied for traces with anomalously high amplitudes, which are likely to represent noise (Sheriff & Geldart, 1995). The initial trace length is 12 288 ms with a sample interval of 2 ms. Very little seismic information will be possible to extract at this depth, and it is therefore reduced to 6144 ms. This will also speed up computational time and make processing more efficient. A band-pass filter is applied to remove obvious noise that has occurred during acquisition. The high frequency limit is set to 90 Hz with a slope of 48 dB/octave, and low frequency limit to 8 Hz with a slope of 24 dB/octave. Raw marine data is contaminated by noise, such as swell and cable noise. This type of noise has a very low frequency and very high amplitude, which will

be removed by the low-cut of the band-pass filter (Yilmaz, 2001). Deconvolution will also remove this type of noise. Other types of noise, such as wind, wave motion and electrical noise from recording instruments etc. that have a very high frequency, will be removed by the high end of the band-pass filter.

The data is resampled from 2 ms to 4 ms for all traces, which halves the data. The resampling gives a Nyquist frequency of 125 Hz, which is a reduction from the prior 250 Hz. The high-cut of the band-pass filter of 90 Hz will prevent the signal to alias. A spatial amplitude smoothing is applied to remove noise bursts that cause unwanted noise. This will smooth out amplitudes that are anomalously high with surrounding traces within a specific window. Header words are defined in the module MODET for CDP number, offset etc. These will be used throughout the processing and contain important information about the traces. Values are acquired from the acquisition parameters which are stored in the imported SEG-Y file, given in Table 4.1. The output from this pre-processing stage is then saved and stored in a tape library.

The results after editing are plotted in the visualising tool Teamview and quality checked. Figure 5.1 shows some randomly selected shot-gather for line 4, displayed in a draped fashion at the time of field recording. The seismic traces of each shotpoint are plotted in their correct relative position and are displayed side-by-side to other traces. Common shot-gathers may display any particular shot of interest and are utilised as a tool to check if the recordings are satisfactory (Kearey et al., 2002). The figure clearly shows what waves the shots contain. The first wave is the direct wave (white arrow), while the second is the direct wave's bubble pulse (black arrow). The green arrow represents the critically refracted wave, which appear weak and linear. The first most obvious curved reflector is the sea-bottom reflection (red arrow), followed by several strong seabed multiples. The first four sea-bottom multiples are pointed out by the blue arrows. These are very strong and dominating in the shallow part. The main object of this project will be to attenuate the multiples as much as possible, so that the primary reflectors and subsurface geology may be interpreted.
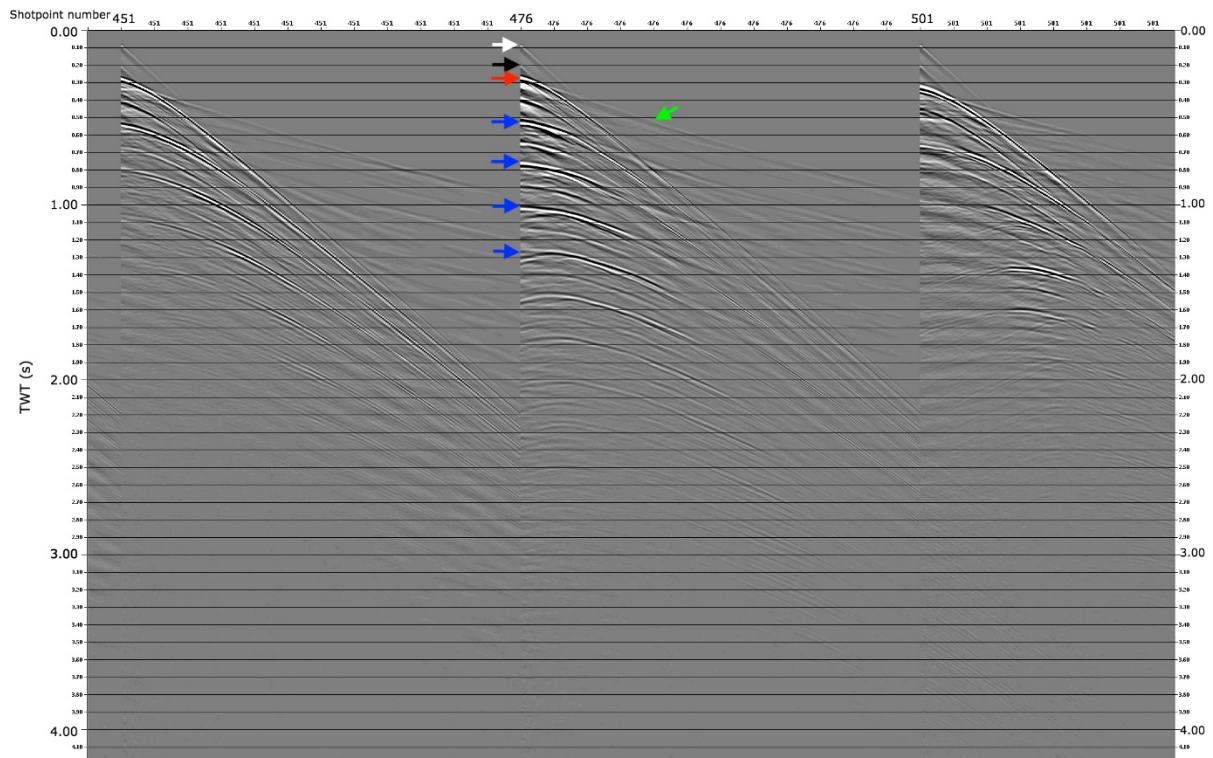
Figure 5.1: A randomly selected shot-gather for line 4. The arrows are pointing out the direct wave (white), bubble pulse of the direct wave (black), the seabed reflection (red), multiples of the seabed (blue) and the critically refracted wave along the seabed (green).

A near-trace plot displays the shortest-offset trace for each shot-record (Sheriff & Geldart, 1995). This gives a quick overlook of the profile and is used to analyse problems that may occur at later stages during processing. There is clear evidence of strong sea-bottom multiples in the near-trace plot of line 4, displayed in Figure 5.2. The energy from the sea-bottom multiples is dominating the profiles and are so strong that they overshadow real geological structures, particularly in the shallow part. The multiples are pointed out by blue arrows in the near-trace plot. With increasing depth, there is a weakening of the multiple energy. This is caused by partitioning of reflection energy at interfaces in the subsurface. Assuming that the seabed has a velocity of 4500 m/s and a density of 2 g/cm^3, this gives it a R_c of 0.72 for a vertical incident angle (see Appendix A: Estimations). The following multiples are given by -R^2, R^3, -R^4 etc., which is valid after correction for spherical spreading (Ruud, pers. comm). The topography of the sea-bottom in the near-trace plot is used for muting and multiple attenuation in later processing sequences. Figure 5.3 shows how points along the seabed of line 4 are picked in Teamview and then saved as a file in Xps.
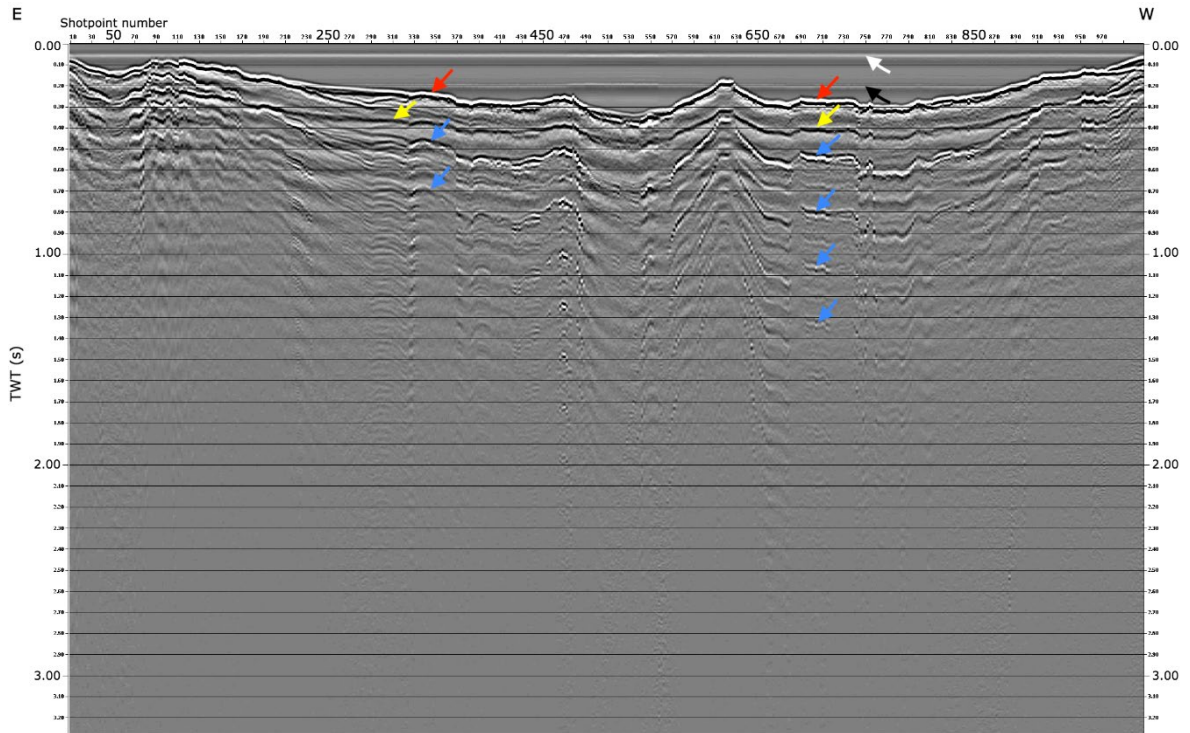
Figure 5.2: Near-trace plot for line 4. The strong sea-bottom multiples dominate and hide the energy from the primary reflections. The direct wave (white), direct bubble-pulse (black), sea-bottom reflector (red), sea-bottom bubble-pulse (yellow) and first four sea-bottom multiples (blue) are pointed out by the arrows.
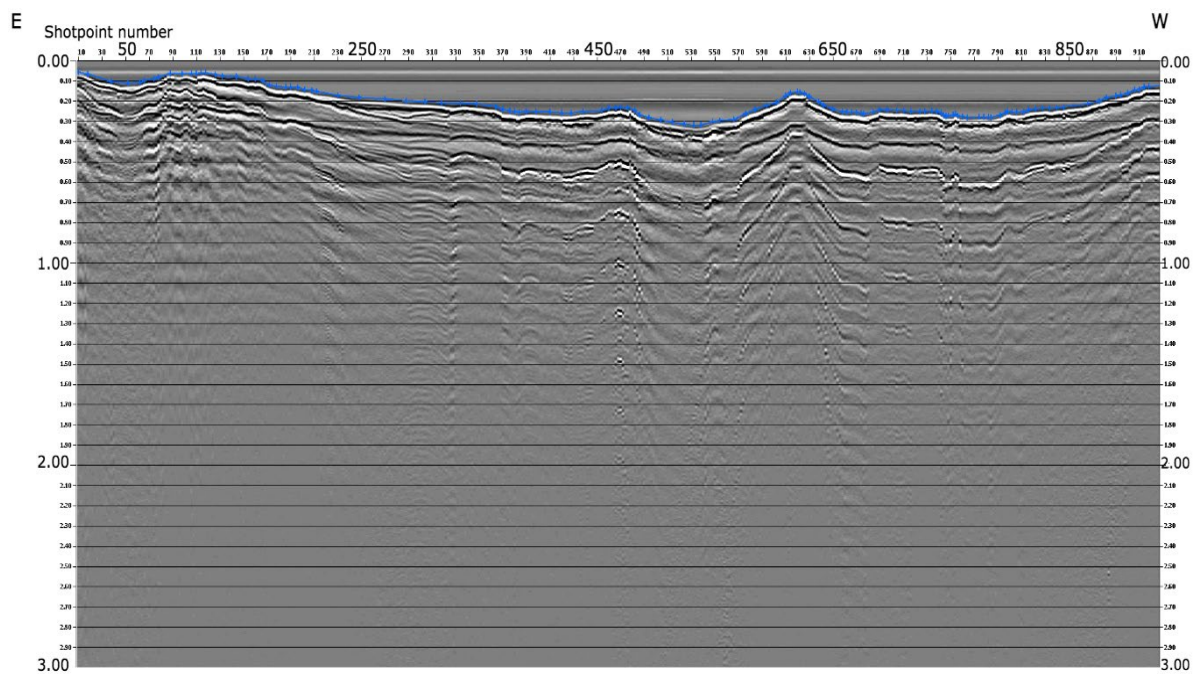
Figure 5.3: The picked sea-bottom (blue) in line 4 was saved as a mute library in Xps.

5.2.2 Deconvolution and filtering

The main issue in this study is to attenuate the dominant sea-bottom multiples. Due to abnormal high velocities under the seabed in Isfjorden, the multiples appear particularly strong in the seismic profiles. Since the seismic survey is acquired in a shallow area (ca. 70 m at the shallowest), the multiples to appear at short intervals. These factors combined create challenging seismic processing conditions. Deconvolution and filtering will be essential in order to attenuate the multiples. Filtering for instance, will be applied at several stages throughout the processing sequences.

Figure 5.4 shows the f-k spectre of a randomly selected shot-gather in line 4 prior to deconvolution and f-k filtering. This spectre illustrates how the energy of a shot-gather is portioned. Much of the wanted primary energy is hidden by dominating multiple energy and linear noise. There is also aliasing present, which occurs at high wavenumber and high frequencies.
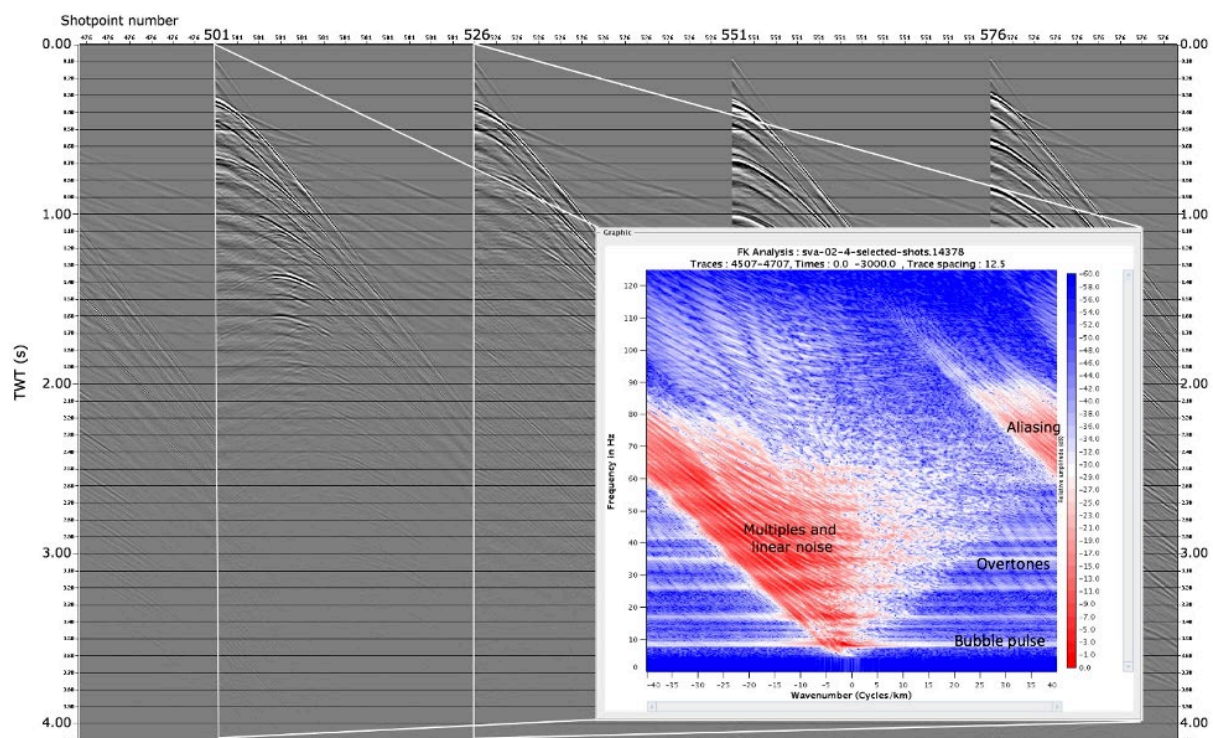
Figure 5.4: F-k plot prior to deconvolution and f-k filtering of a selected shot-gather in line 4. Multiples and linear noise are dominating over the primary energy, and aliasing appears at high wavenumber and high frequencies. The horizontal lines represent the bubble pulse (8.5 Hz) and overtones (17 Hz, 25.5 Hz, 34 Hz etc.).

It is applied a statistical, data-dependent, airgun signature deconvolution for every trace in the shot-gathers. The objective is to shape the wavelet to a target output wavelet of a minimum phase, to improve temporal resolution. Convolution convolves the signal with a filter that attempts to recover the reflectivity series (earth's response) from the recorded seismic. An inverse filter is then calculated and applied to all traces recorded at a shotpoint to attain the wanted minimal phase signal. This will compress significant reflections, while attenuate the bubble pulse and reverberations (Yilmaz, 2001).

Since deconvolution has a boosting effect on both the signal and low and high- frequency noise (Yilmaz, 2001), it is necessary to add a band-pass filter afterwards. This is specified with the low-cut frequency of 8 Hz and high-cut frequency of 90 Hz. Random noise attenuation is then applied, which carries out projective filtering in the f-x domain and separates the signal from the non-predictable noise. This ensures preservation of the signal, whilst optimising attenuation of random noise (CGGVertias, 2008). The minimum frequency is set to 7.5 Hz, while the maximum frequency is set to 50 Hz. An amplitude recovery module is added to correct for spherical spreading. This module applies a gain proportional to a power of time (CGGVertias, 2008), and is specified with the value of 1. This corrects for spherical spreading and restores amplitudes from the deeper part of the section. A spatial amplitude smoothing is again added, which attenuates spikes by smoothing out the input seismic trace with respect to neighbouring traces (CGGVertias, 2008).

Several f-k filters are applied with the intention to remove unwanted noise from the signal, such as multiple energy, back-scattered noise etc. Apparent velocity limits define what seismic energy will be kept, forming a wedge-shaped zone in the f-k plot. The energy outside will then be suppressed. In order to set the limits, the shallow refracted velocities are measured in Teamview. All the lines are found to have velocities of around 4.5 – 5 km/s. The velocity limits are set slightly higher to remove the direct wave, and to make sure all primary reflections are kept. Since all lines are measured with about the same velocity, limits are set to – 6 km/s and + 6 km/s. The apparent velocity limits form an opposite triangle in the f-k spectra that retains the energy that plots inside, while suppresses the outside energy. The figure below shows the f-k spectra prior and post f-k filtering and deconvolution for a shot-gather in line 4.
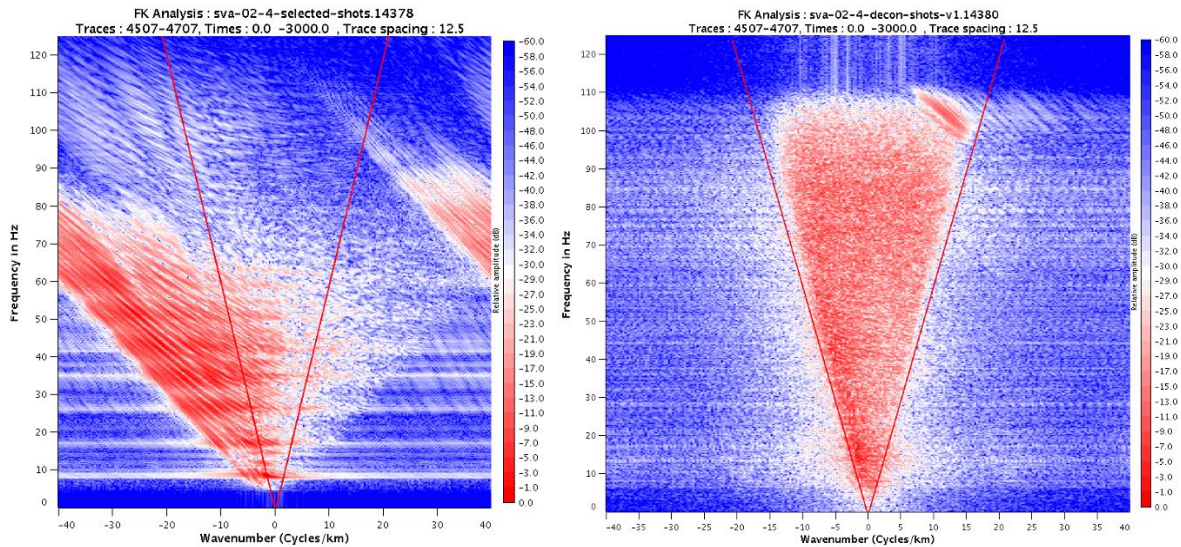
Figure 5.5: Comparison of the f-k spectra before (left) and after (right) f-k filtering and deconvolution, for a shot-gather in line 4. The red lines represent the apparent velocity limits, set to – 6 km/s and + 6 km/s. Energy that plots inside this limit is kept, while outside energy is suppressed. The bubble pulse and overtones are removed during this process.

The f-k filter is applied to the shot and receiver-gathers separately. Since the sea-bottom is irregular, this will affect the f-k filters differently depending on the shooting direction. To avoid an asymmetrical effect, these are applied individually, followed by sorting of the CMP-gathers. An amplitude recovery module then attempts to correct for spherical spreading and regain seismic energy from the deepest reflections (Yilmaz, 2001). This is an "AGC"- type of recovery method, which is applied within a window length. It gives a constant gain according to the average of that window (CGGVertias, 2008). This enhances weak reflectors and averages out anomalies, but also has the potential of enhancing noise (Yilmaz, 2001).

Predictive deconvolution is able to attenuate multiple energy by predicting its periodicity. This type of deconvolution is surface-consistent, meaning that it calculates different filters for each shot and receiver position. It removes the predictive parts of the signal (multiples) from the seismic dataset. Predictive deconvolution is especially effective in supressing short-period multiples and reverberations (Yilmaz, 2001; Recept et al., 2019).

Figure 5.6 shows the same shot-gathers as displayed in Figure 5.4, but after filtering and deconvolution. In comparison, there is a clear improvement in reducing the unwanted noise. The direct wave, bubble pulse and refracted wave are removed from the seismic section. The f-k spectre shows that the multiple energy, linear energy and aliasing are almost removed.

However, there has been an increase in noise in the deeper section. This will be removed in later processing sequences.
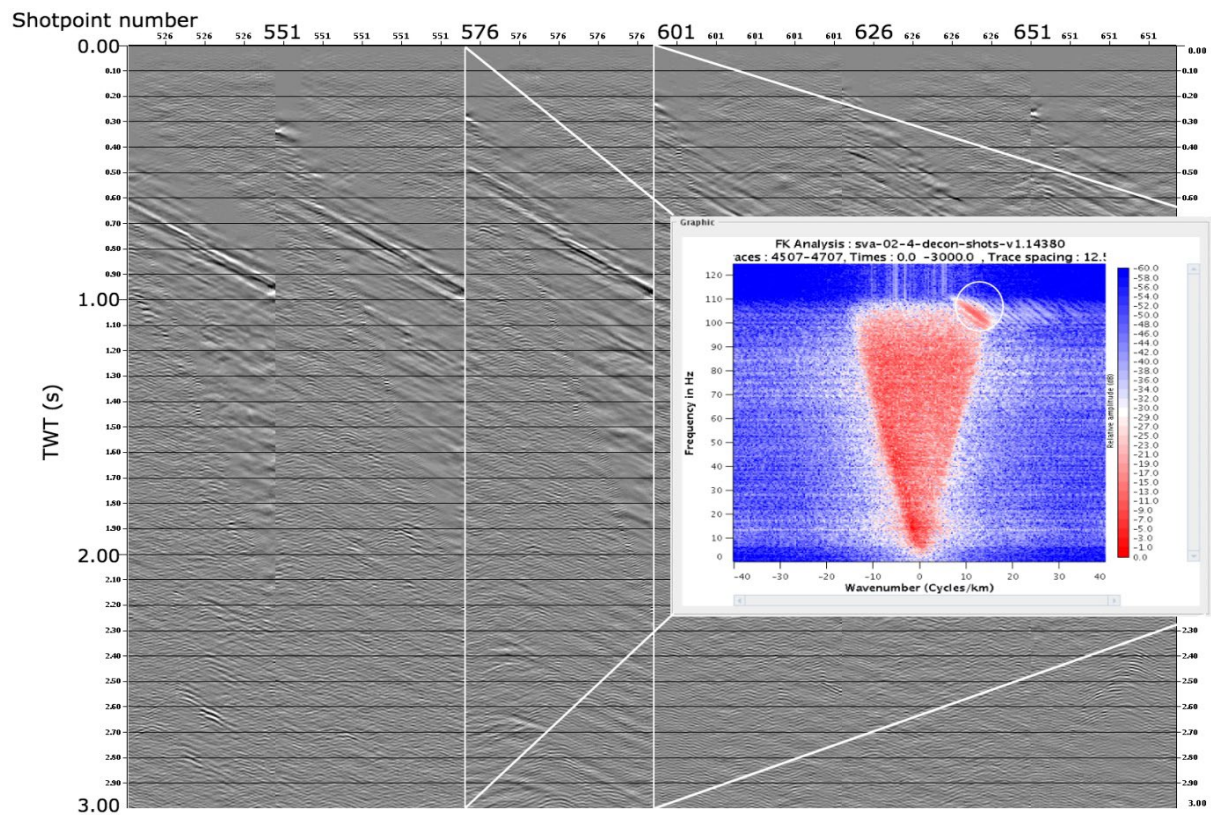
Figure 5.6: Shot-gathers of line 4 after filtering and deconvolution. The f-k spectre, from shot-gather 576, is significantly improved as most of the unwanted energy is suppressed. There is still some aliasing present (encircled in white), for high frequency (100 – 110 Hz) and high wavenumber (12 cycles/km).

There is still some aliasing present in the dataset, which is visible in the top right corner of the f-k plot. This has a frequency of 100 – 110 Hz and a high wavenumber of about 12 cycles/km. A higher velocity limit in the f-k filter could remove this, but this also has the potential of removing primary reflections.

5.2.3 Static correction

There are areas of large local variations in water depth in Isfjorden. The near-trace plot (Figure 5.2) shows that the elevation of the water-bottom changes rapidly over a relatively small area. In addition, there are found abnormal high velocities under the seabed. This increases the "pull-up" and "pull-down" effect in the seismic due to travel-time differences for rays that spend more time below the seabed opposed to the water layer (Samson & West, 1992). The static correction sequence attempts to correct for these effects. The method assumes a near-vertical

ray path of the water layer, and a known and near-constant seabed velocity (Ruud, pers. comm). The incident angle is already muted with a maximum of 45 degrees. By using Snell's law, this means that the incident angle in the water layer will be less than 15 degrees (see Appendix A: Estimations). The resulting seismic section is displayed in Figure 5.7. Water-bottom picking is performed on the resulting near-trace plot in Teamview, which will be used for further processing.
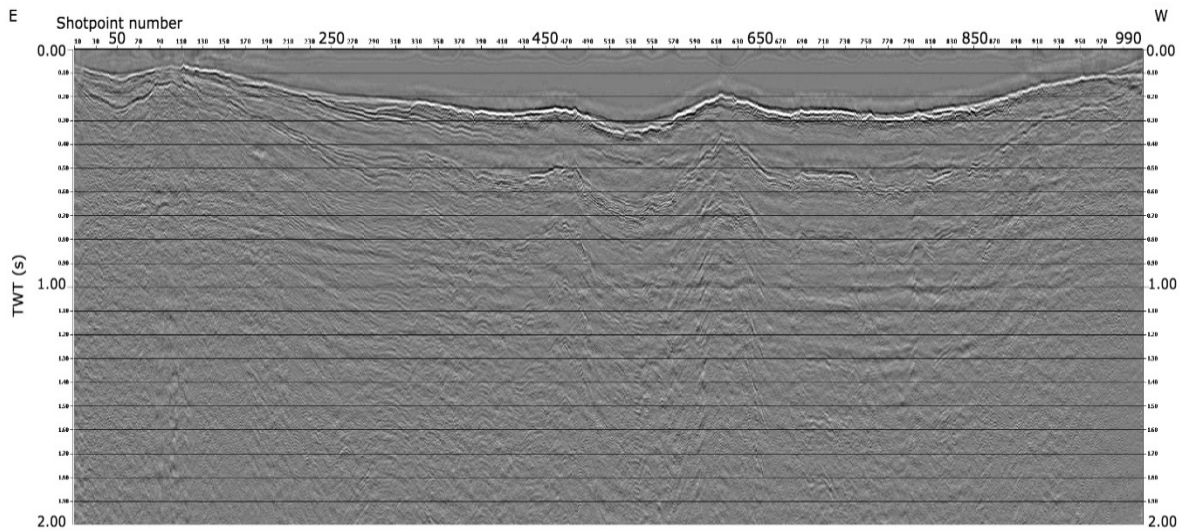
Figure 5.7: The near-trace plot of line 4 after static correction, displaying up to 2 s. There is a clear improvement from the near-trace plot in Figure 5.2, as multiples are reduced and some real reflections are visible. The sea-bottom, which is now corrected for traveltime-differences, is once again picked and saved as a library in Xps.

5.2.4 Velocity model

Velocity models are estimations of the subsurface velocity and are established to generate a clearer seismic image. This specific processing sequence creates a simple velocity model that will be used as a platform and reference in the first velocity analysis. Velocities above the seabed are set to 1500 m/s, while velocities below are 5000 m/s. Finally, there is a computation of RMS velocities from the interval velocities. This generates a model that gradually increases in velocity with depth below the seabed, from 1500 m/s to 5000 m/s (Ruud, pers. comm). The model is then saved to the V_{rms} library.

5.2.5 DMO-correction

Before the seismic data is imported to Geovel for velocity analysis, it is necessary to correct for dip-move-out (DMO). A dipping surface will have the reflection points in a CMP-gather spread out along the reflector. In turn, this will cause wrong stacking velocities. To avoid this effect and smearing in the seismic, the DMO-correction sequence is applied to preserve conflicting dips during stacking (Yilmaz, 2001).

First, an external mute from incident angle of maximum 45 degrees is applied to mute any signals coming from a higher angle, which mainly represent wide-angle reflections and refractions. A band-pass filter (Table 5.2) excludes high- and low-frequency noise that may have been introduced to the dataset during the processing sequence. This filter maintains a constant and maximum amplitude between 15 and 75 Hz, while frequencies lower than 5 Hz and higher than 100 Hz are removed (CGGVertias, 2008).

Band-pass filter limits (Hz)			
5	15	75	100

Table 5.2: Band-pass filter values used during DMO-correction.

In order to perform DMO-correction, the traces must be NMO-corrected. A dynamic NMO-correction module is therefore applied to the dataset, using the velocity values obtained from the velocity model. This module applies linear interpolation between velocity values to obtain velocities for all points in time (CGGVertias, 2008). A Kirchhoff 2D DMO-correction module then corrects for dipping effects for all traces, using a Kirchhoff integral method. In combination with post-stack migration, this DMO-correction provides a robust solution that may be compared to pre-stack migration (Ruud, pers. comm). The water-bottom library is included to mute all traces above the seabed. An inverse dynamic NMO-correction then removes the NMO-correction, which is necessary to make the dataset ready for the velocity analysis.

5.2.6 Velocity analysis

Prior to the velocity analysis, another set of band-pass filter is applied with the values presented in Table 5.2. This ensures that no low or high frequency noise has been introduced to the dataset. The dataset is then arranged into CMP-gathers of 80 CMPs for all lines except for line 4, which is arranged into 90 CMPs. This is the longest line in this study, and a higher number

of CMPs in the CMP-gather will make the velocity analysis more efficient. This number represents the distance between every CMP-gather that appears in the velocity analysis. Finally, the velocity spectrum is calculated and the data is formatted into a velcom output. This makes it possible to import the data into Geovel, where the velocity analysis will be performed.

The velocity analysis is executed in The Velocity Analysis Viewer, displayed in Figure 5.8 for a randomly selected CDP in line 4. Tools allow for velocity picking of CMP-gathers from the velocity spectrum or the mini-stack window. The velocity spectrum displays NMO-velocities between 1000 – 7000 ms on the horizontal axis, and TWT values on the vertical axis, ranging from 0 to 6000 ms. The velocities are picked from maximum coherency peaks that appear in the spectrum, which are associated with primary reflections. The stronger the coherency, the stronger yellow it will appear in the spectrum. Red in the shallow part indicates low velocities, while blue in the deep part signalises high velocities (Yilmaz, 2001). The correlation between the picked interval velocities in a CMP-gather is displayed in the interval velocities window adjacent to the velocity spectrum. This provides a means of picking velocities that are within a reasonable increase or decrease in respect to neighbouring velocities. Interval velocities should in general increase with increasing TWT. However, some exemptions occur, such as sill intrusions that yield abnormal high velocities. Additionally, unusually high seabed velocities may result in decreasing interval velocities just under the seabed (Ruud, pers. comm). The Velocity Analysis Viewer also displays a central gather window, in addition to a corrected gather window. The main objective is to pick velocities that flatten out the reflector of a primary event. If the NMO-corrected reflector instead curves upwards, this indicates that the picked velocity is too low, while a downward-curvature indicates that the velocity is too high. Only primary reflections must be picked in order to enhance the SNR. If multiples are picked, their reflection in the seismic will appear stronger and create an unrealistic seismic section.
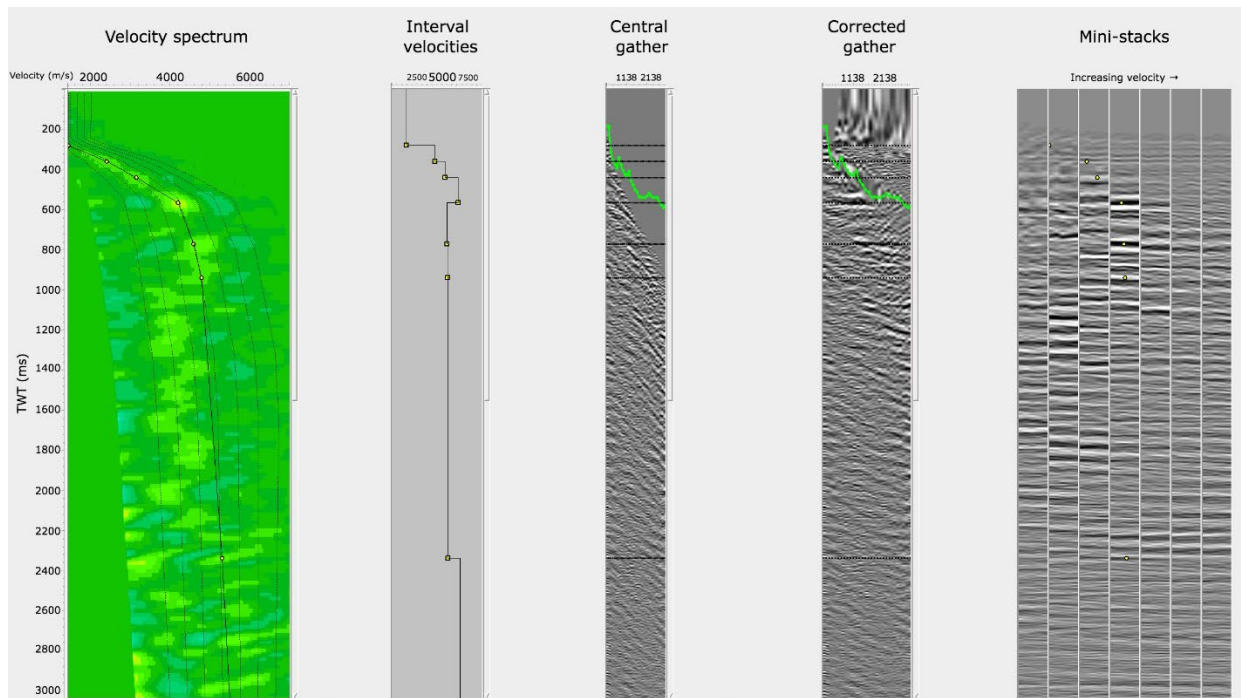
Figure 5.8: A section of the velocity analysis performed for CDP 3464 of line 4 in Geovel. The left window displays the velocity spectrum of the selected CDP-gather and the picked velocities (yellow dots). The second window shows the interval velocities. The third and fourth window show the CDP-gather, with and without NMO-correction. Everything above the green line will be muted. The yellow dots in the mini-stacks window indicate where the velocities have been picked.

Velocity picking is performed for every second CMP-gather, except for the 2-3 first and last gathers. This is because these contain few and often distorted traces due to streamer noise and will therefore not give sufficient information to successfully perform a velocity analysis. The increment between the CMPs in the velocity analysis is 80, meaning that a velocity picking of every second gather will have a distance of 160 CMPs. The distance between each CMP-gather is 6.25 m, which gives a total distance of 1 km between picked CMPs. For line 4, the total distance is 1,125 m, due to an increment of 90 CMPs. When the velocities are picked at a location, this enables calculation of a velocity function. Values are interpolated between picked locations to form a velocity field (Yilmaz, 2001). The water velocity is estimated to 1500 m/s, which represent the first picked seabed velocity. Under this point, there is a steep increase in the velocity, ranging from 4500 – 6000 m/s, followed by a minor reduction. Finally, the velocity increases steadily with depth.

A quality control is performed in Isovel (Figure 5.9), where the full velocity model is displayed. This makes it possible to get an overview and evaluate how the picked velocities correlate across the whole profile. In general, there should not be any drastic changes. The velocities

should rather have a smooth transition (Ruud, pers. comm). In case of any anomalies, this is checked in the velocity analysis. Changes to the velocity model can also be done in Isovel and then saved.
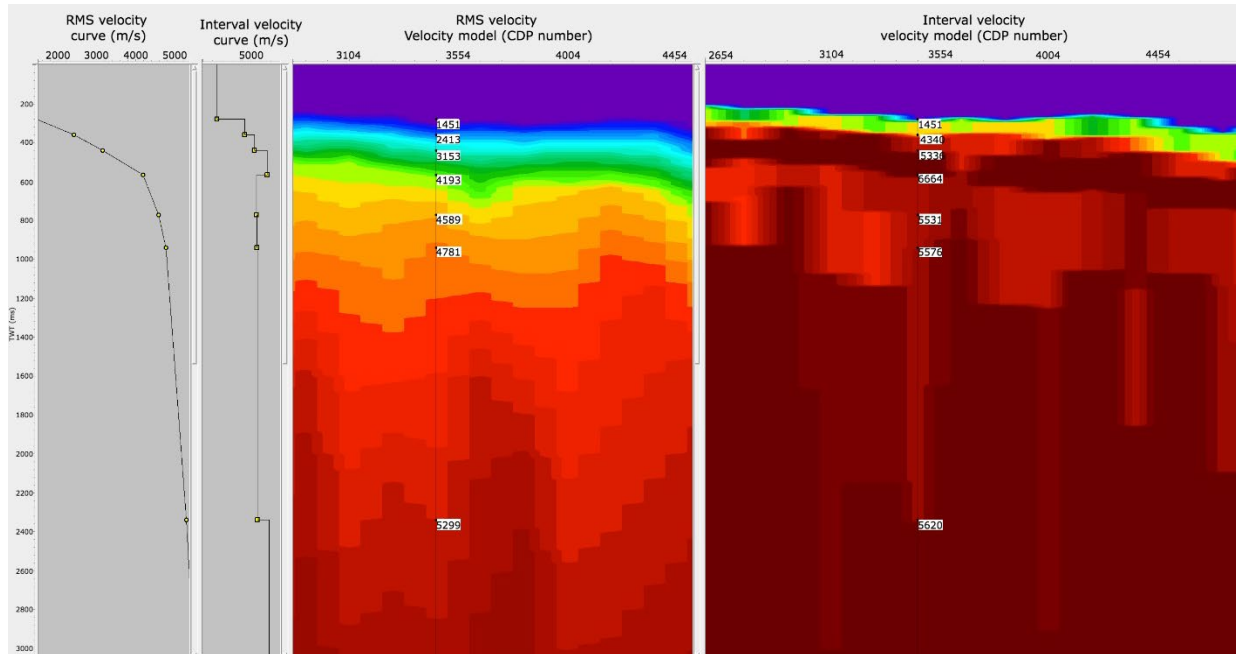
Figure 5.9: The section displays CDP 3464, line 4 in Isovel. The first and second window represent the RMS-velocity and interval velocity for the selected CDP-gather. The picked velocities appear with yellow dots. The third and fourth window display how interpolated RMS-velocities and interval velocities vary across the profile, including the positions and values of the picked velocities. The blue/purple colour in the velocity model corresponds to low velocities of around 1500 m/s, while dark red indicates high velocities of around 6000 m/s.

After the velocities are checked and approved in Isovel, they are exported to the Xps database as a velocity library. The output from the velocity analysis form table of numbers, which is a function of CMP-number and TWT. The result of the velocity analysis is a new and updated velocity field, which will be used in subsequent processing sequences.

5.2.7   Stacking

Prior to stacking, an external mute from incident angle is applied to a maximum angle of 42 degrees. This is to ensure signals of higher incident angle are excluded, since these will mainly represent noise. The new velocity field obtained from the velocity analysis is included in a dynamic NMO-correction module. This is an attempt to remove the last remaining multiples in the dataset. Since multiples have a larger moveout than primaries, they will be over-corrected

during stacking. A preserved amplitude stacking module stacks the trace gathers and gives an output which contains the total weighted stack (CGGVertias, 2008). During stacking, stretching is limited to 200%. This attempts to attenuate the frequency distortions that commonly occur with large-offset and shallow times (Yilmaz, 2001). The last step involves applying a time variant band-pass filter that removes high and low-frequency noise within an application window. The values of the filter is displayed in Table 5.3, which have progressively decreasing cut-values with depth. Due to attenuation, the bottom of the section is assumed to contain more of the low-frequency energy and the filter must therefore be adjusted accordingly. This band-pass filter works as an anti-aliasing filter that indicates the highest frequencies that will be present in the dataset before stacking and migration. The highest frequency in this dataset is 110 Hz.

Band-pass filter				Application window
10	20	90	110	0 - 300
8	16	80	95	600 - 900
7	14	60	75	1200 - 1700
6	12	45	60	2000 - 2500
5	10	30	45	3000 - 6000

Table 5.3: The values of the time variant band-pass filter used during stacking.

The output from the stacking sequence gives an overview of the seismic section. In this way, it is possible to quality check the seismic prior to migration and make adjustments if necessary. Scaling of the velocity field was an essential tool used to obtain the best possible velocity model. The velocity field obtained from the velocity analysis was scaled up and down by 10% in Xps, and then run in the stacking sequence (Figure 5.10). If subsurface geological events were better imaged in any of the scaled models, this signalised that the velocities should be adjusted accordingly. This may be done in the velocity analysis or in Isovel. This procedure was performed until satisfactory results were obtained, when the final velocity model gave the clearest image of the subsurface compared to the scaled models.
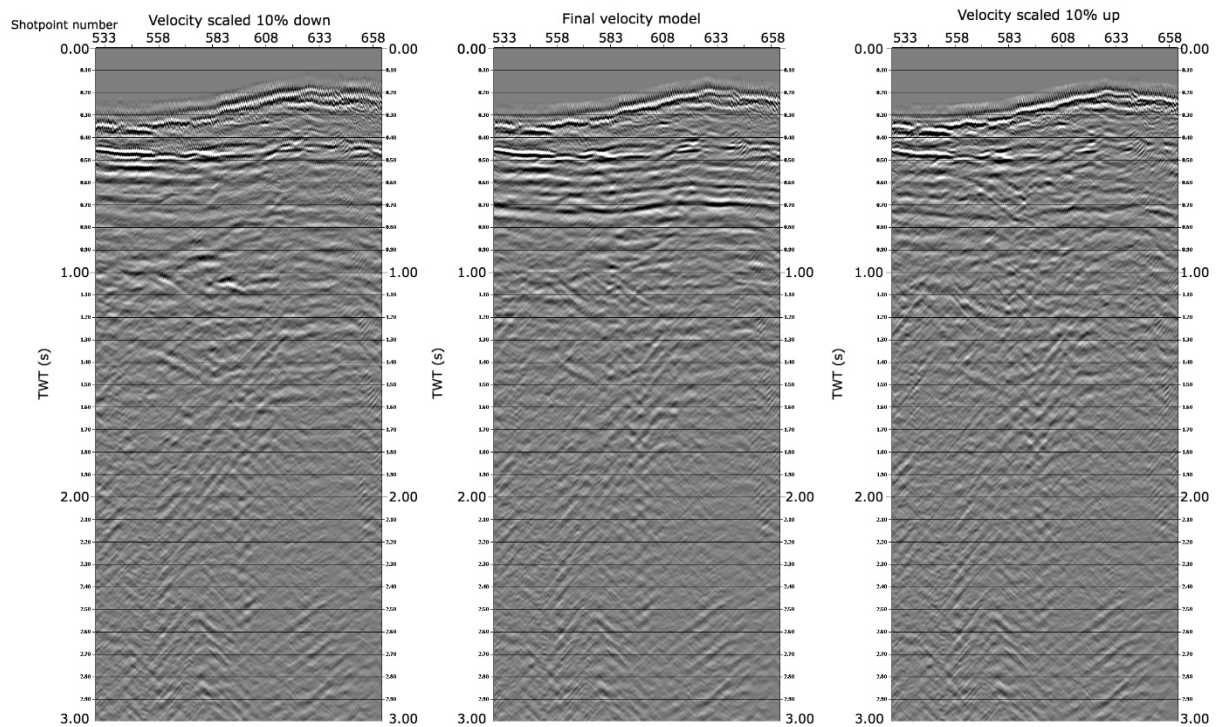
Figure 5.10: A comparison of different stacking velocities for line 4. The velocities in the left figure are scaled 10% down relatively to the middle figure, while the velocities in the right figure are scaled 10% up. The middle figure represents the final velocity model, which clearly images the subsurface structures the best.

Another quality check is performed using the CMP-gather output from the stacking sequence, which displays the NMO-corrected traces in a gather prior to stacking. Correct velocity values will flatten out the reflections. If undercorrected (velocity is too high) or overcorrected (velocity is too low) reflections are detected, this is checked and altered in the velocity analysis or Isovel. The CMP-gathers are also used to check if outer traces of long offsets suffer from stretching compared to the inner traces. Stretching increases for long-offset traces and have the potential of reducing the stack (Austegard, 2013). This may be muted by picking muting lines for CMP-gathers in Teamview, which will zero out the amplitudes of the distorted zones before stacking (Yilmaz, 2001). This is not done during this study, since the CMP-gathers did not show significant stretching at this point.

Figure 5.11 compares the different velocity libraries for line 4. The procedure of creating a new and improved velocity model is executed three times. This procedure should be repeated until the resulting stacked section is not showing further improvement (Ruud, pers. comm). There is a clear improvement in the seismic image when comparing the velocity model to the models

obtained from the velocity analysis, and some minor improvement from the first to second velocity analysis. The subsurface structures are better imaged in the last velocity model, but the seabed reflector is slightly degraded. Since the deeper structures represent the target area of this study, the output from the second velocity analysis is used in the final results.
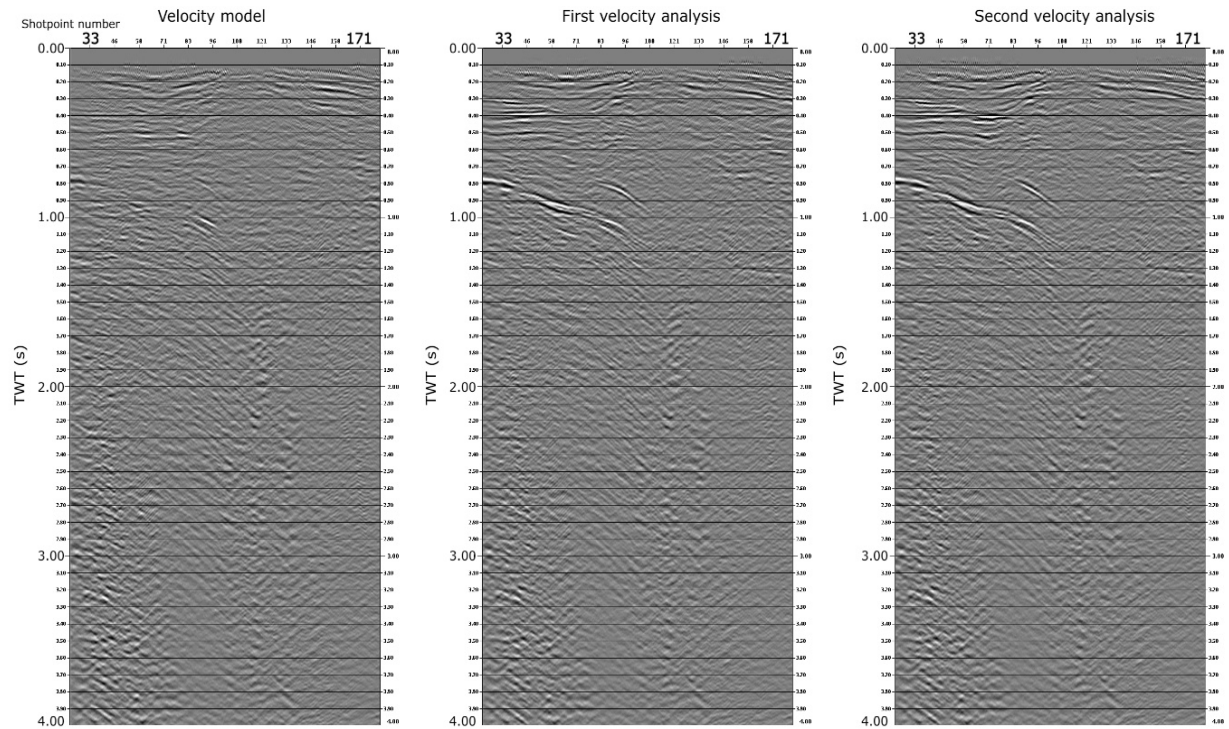
Figure 5.11: Stacked sections of line 4 using the velocity model (left image), first velocity analysis (middle figure) and second analysis library (right image). The latter model displays the best seismic image of the subsurface structures and is therefore used in the final results.

5.2.8   Migration

Post-stack migration, when run in combination with Kirchhoff 2D DMO-correction, provides robust seismic images and is computational-efficient (Yilmaz, 2001; Ruud, pers. comm). This processing sequence attempts to reposition seismic events back to their supposedly true subsurface locations, at a corrected vertical reflection time (Kearey et al., 2002).

Prior to post-stack migration, a MODET module is added as an attempt to enhance the seabed reflection. The upper part of the stacked seismic section completely lacked amplitude energy for every 4th trace, which signalised that this had most likely been muted in earlier processing sequences. The purpose of the MODET module is to remove previous mute-times that are saved in the trace headers. It is specified to remove prior mutes up to 1 ms, followed by an

added mute along the water-bottom. This regained most of the missing energy, displayed in Figure 5.12. However, this did not apply for the shallowest seabed areas, particularly for areas of less than 100 ms TWT.
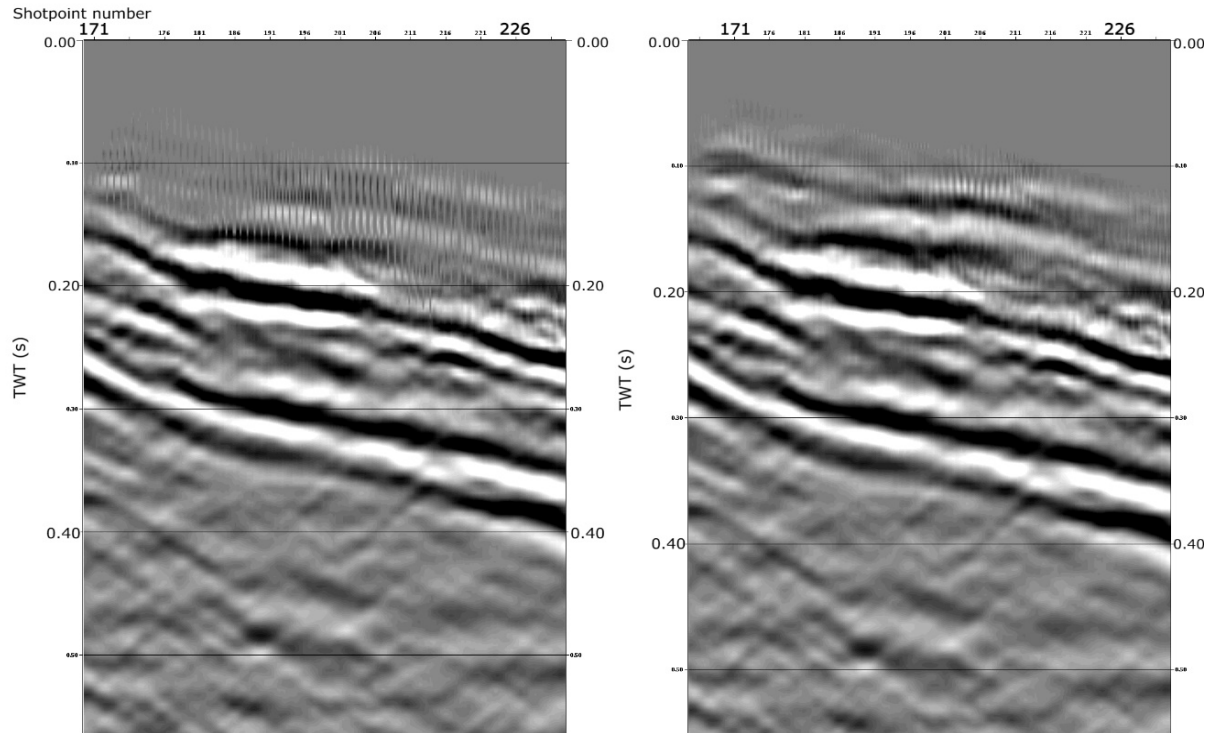
Figure 5.12: Most of the seabed energy was regained by adding a module which removed prior mutes, followed by a mute above the seabed. A section of the upper part of line 4 is displayed in the figures.

The application of an additional f-k filter prior to migration reduced the spatial aliasing in the seabed and shallow reflections, which causes "stripes" in the seismic image. Figure 5.13 displays how this gave a significantly clearer seismic section. The f-k filter also attenuated remaining noise still left in the dataset, such as diffraction patterns in the deeper section, shown in Figure 5.14. The f-k filter is specified with the values given in Table 5.4. This is a 4-velocity band-pass filter, also called a fan filter, in which the maxima and minima pair values define a transition zone. Zones that fit outside the maxima values are rejected, while zones inside the minima values are preserved (CGGVertias, 2008). Several different f-k filter values were attempted, but the values given in Table 5.4 gave the best results in attenuating noise without removing primary energy.

Velocity 1	- 8000	**Velocity 3**	8000
Velocity 2	- 10 000	**Velocity 4**	10 000

Table 5.4: The values of the 4-velocity band-pass filter used during migration.
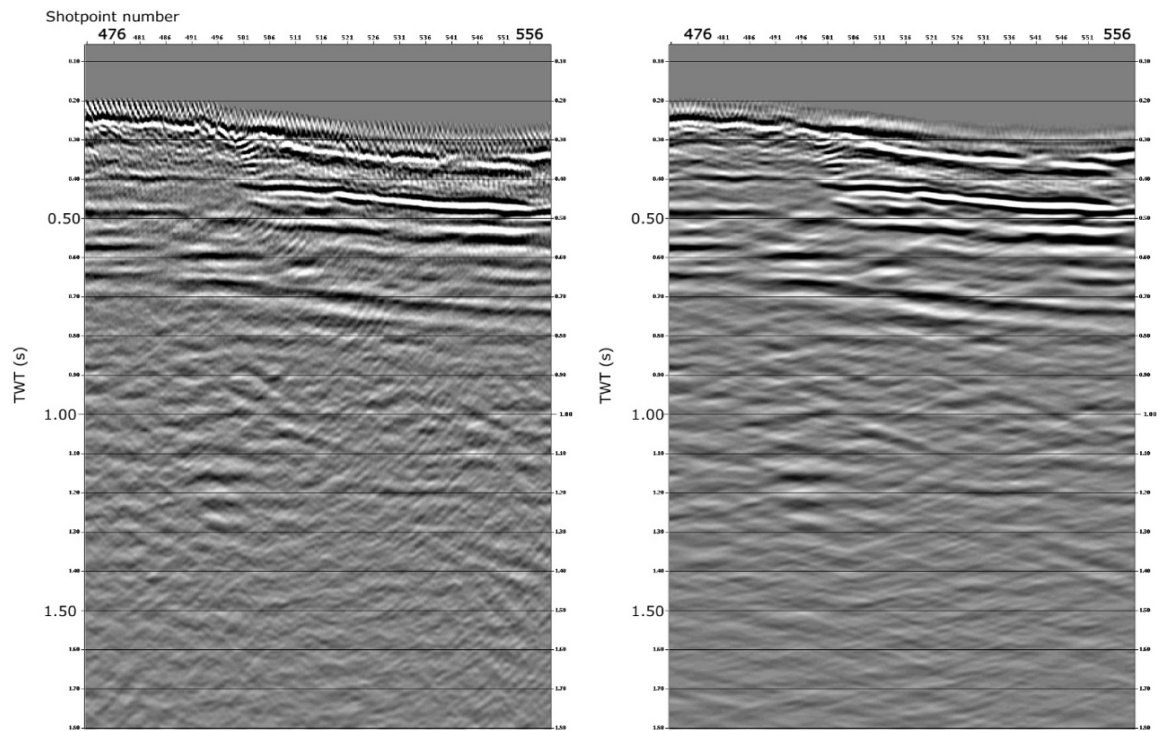
Figure 5.13: The application of an f-k filter reduces spatial aliasing that causes "stripes" in the seismic sections. These are present in the left image, prior to f-k filtering. The right image, after f-k filtering, is less noisy and has enhanced sea-bottom and shallow seabed reflections. The figures are derived from line 4.
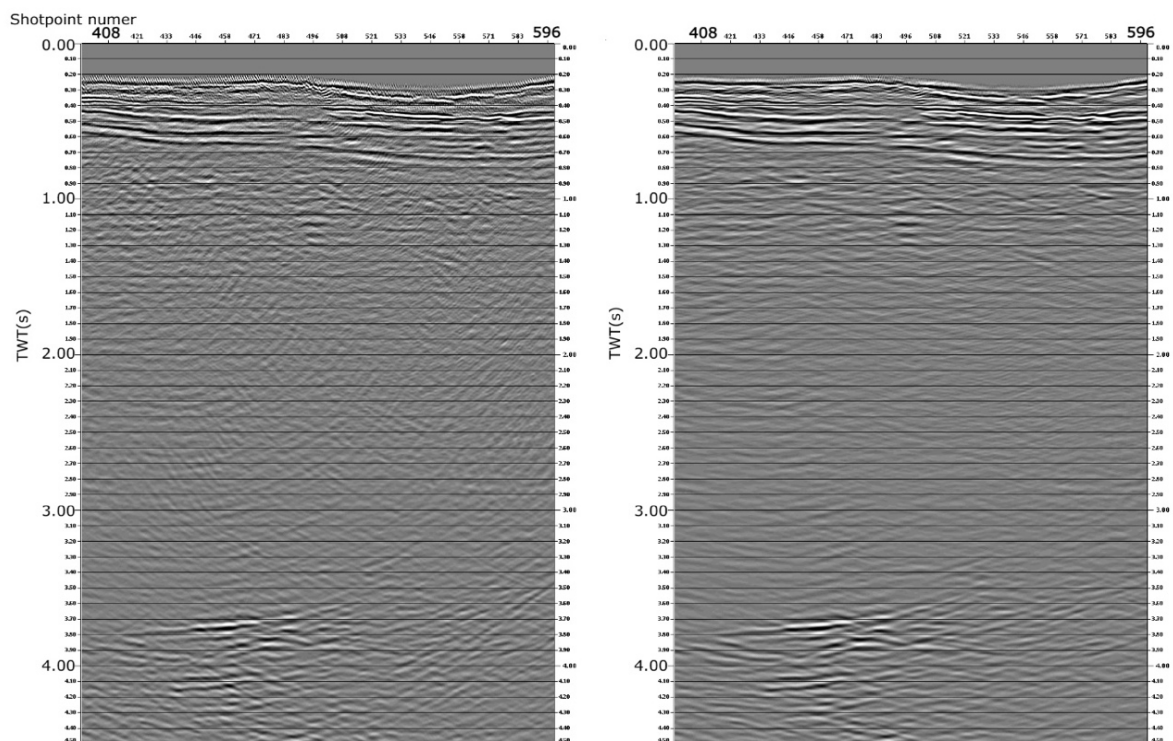
Figure 5.14: Diffraction patterns were dominating the deeper sections of the seismic profiles (left image) prior to the application of an f-k filter. The diffraction patterns are attenuated in the right image, after f-k filtering. The figures are derived from line 4.

An amplitude recovery module is added to create a better amplitude balance between the shallow and deeper part of the seismic sections. A power coefficient is specified to -0.3 in a time-gain method (CGGVertias, 2008), meaning that the amplitude is scaled by $t^{-0.3}$. The negative value has the effect of scaling up the amplitudes coming from shallow reflections, while amplitudes from deeper reflections are scaled down. The more negative this value is, the stronger the amplitudes from the shallow reflections in the seismic image will be. This specific value gave the best results. Several other values were attempted, but lower negative values caused the deeper reflectors to appear much stronger than the shallow reflectors, while higher values made the deeper reflectors fade.

A gradual downscaling of both ends of a seismic line attenuates unwanted energy from streamer noise. These parts of a line contain few traces that are commonly distorted. By scaling down the traces along the edges, unwanted edge-effects in migration will be reduced (Ruud, pers. comm). Next, a 2D post-stack migration performs a time migration on the dataset, using the final velocity model. This migration is based on the "finite difference" algorithm, that solves the acoustic wave equation in the space-frequency (X, T) domain (CGGVertias, 2008). A phase filter gives a small but favourable effect on the seismic image. This shifts the dataset from a minimum phase to a zero-phase wavelet, which is characterised by a maximum amplitude occurring at time = 0. The module attempts to sharpen the seismic reflections.

The f-k filter, which is not a causal filter, may generate some energy above the sea-bottom (Ruud, pers. comm). In the attempt of removing this energy, a water-bottom mute is added at the very end of the processing sequence. Some of the shallowest areas have strongly attenuated reflectors just under the water-bottom, which makes the energy from the f-k filter dominating. This is significant in the shallowest part of line 4, shown in Figure 5.15. Since the water-bottom mute lies above this area, it did not remove the f-k filter effects. This could have been removed by lowering the values of the sea-bottom library in the affected areas, but this could then potentially also remove some primary reflections. As the main object in study is the subsurface structures and not the seabed, these shallow f-k filter effects do not represent a problem for interpretation and was therefore unaltered.
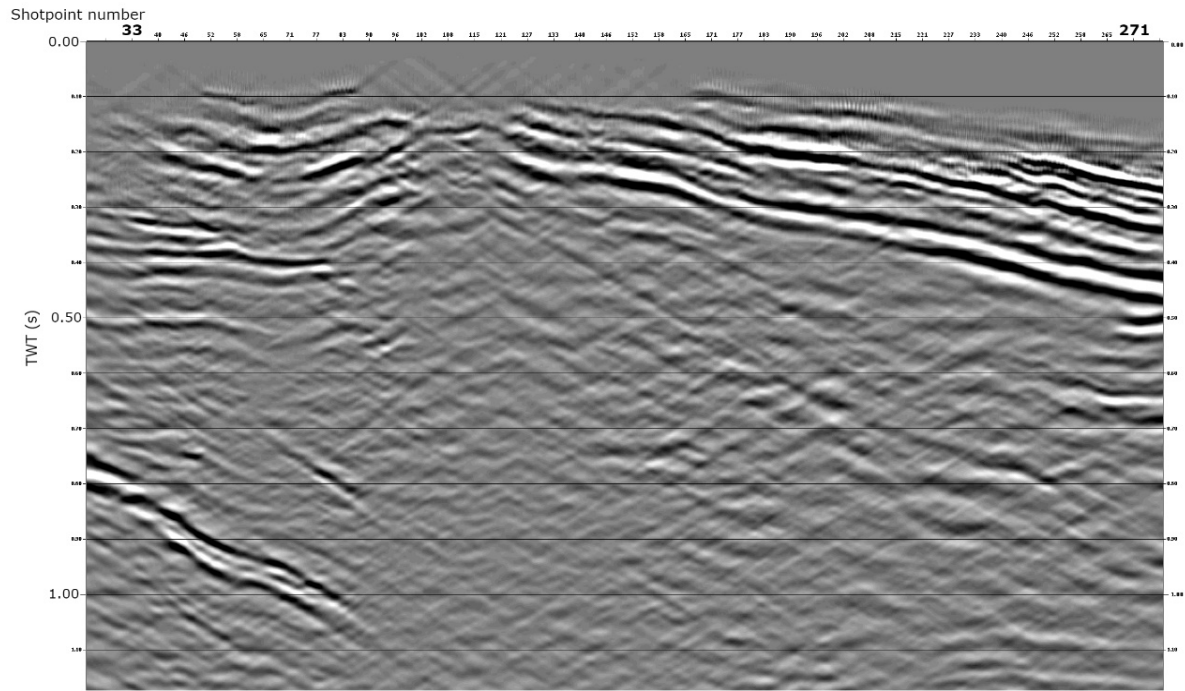
Figure 5.15: The energy from the f-k filter is dominating in the shallowest area of line 4, which is lacking reflectors.

The final migrated sections are plotted in Teamview and quality controlled one last time. Figure 5.16 is comparing the near-trace plot from the editing sequence with the final processed migrated section of line 4. There is a clear improvement in seismic quality between the two images. While the near-trace plot is dominated by multiples and noise, the final processed section displays clear subsurface geological structures and horizons.
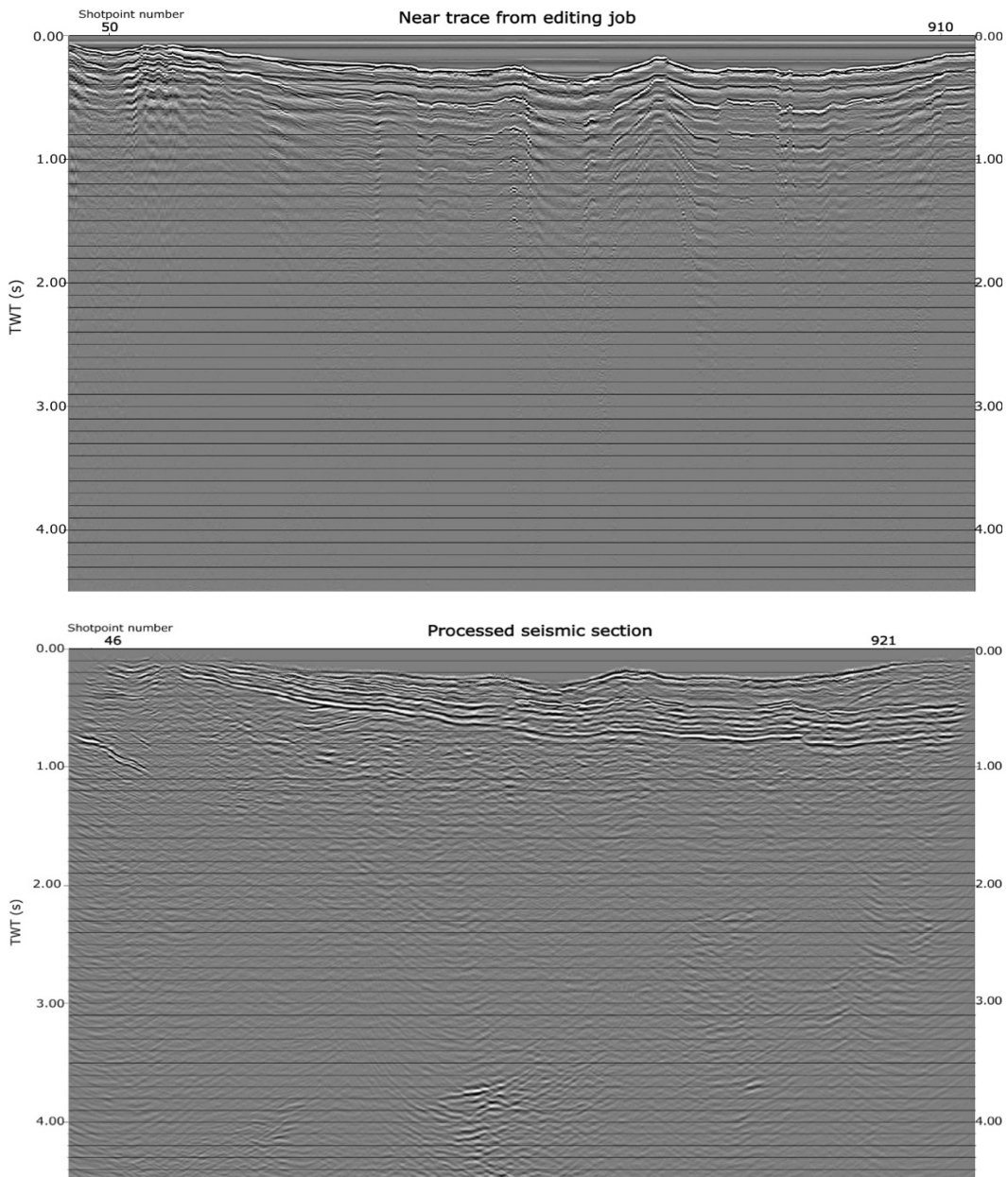
Figure 5.16: Comparison of near-trace plot obtained from the first editing sequence, versus the final processed seismic section of line 4 (upper 4 seconds). There is a significant improvement in seismic quality.

5.2.9 Converting to SEG-Y format

The very last step is to convert the intern Geocluster format CGT back to SEG-Y, which will be used in Petrel for interpretation. Before the files are converted, UTM coordinates for zone 33X are imported and added to the four lines. These are defined by their shotpoints and will therefore give exact location to all lines. In this way, they are correlated in relation to each other and the surrounding area. The final step writes the SEG-Y file. All final migrated lines are displayed in Appendix C: Processed lines.

6 Interpretation

This chapter will present the interpretation of the four seismic lines acquired in Inner Isfjorden, Nordfjorden and Sassenfjorden. The main target of the interpretation is to establish an understanding of the stratigraphic units and the dominant structural features in the area. The following subchapter will present the Petrel software that has been utilised to derive the interpretation in this study.

6.1 The software – Petrel

Petrel is a software developed by Schlumberger for geoscientists and engineers to analyse subsurface data. The software is well-recognised in both academia and in the petroleum industry, where it is utilised in both exploration and production (Schlumberger, 2022). The software offers a range of tools to enable an enhanced geological understanding, including stratigraphic and structural interpretation of seismic data.

The processed lines were imported to Petrel as SEG-Y files in the coordinate system ED50-UTM33. The seismic data is displayed with the default colour "seismic", in which peaks appear in red and troughs in blue. The interpretation is performed in an "interpretation window", and then analysed and correlated across the different seismic lines in the "2D-" and "3D window". Manual interpretation was used in areas of weak and discontinuous reflectors, while continuous reflectors allowed for "Seeded 2D auto tracking". A surface map was generated for each interpreted horizon, followed by an isopach map that was generated using two surface maps. The isopach map displays the vertical thickness between two surfaces. These maps provide a tool for identifying large-scale or local variations between interpreted geological surfaces.

6.2 Basis for interpretation

6.2.1 Previous studies in the area

A range of previous research has been conducted on-shore and off-shore in Svalbard. Some of these have been important for the interpretations made in this study, which are listed below. The study by Blinova et al. (2013) served as a basis for identifying stratigraphic horizons, while

the study by Bælum & Braathen (2012) and Braathen et al. (2017) were important during the structural interpretation. The findings were also correlated with previous master theses by Skaara (2020) and Ågesen (2021), who interpreted seismic data from close-by lines.

- Bergh et al. (1997): *Interaction of Basement-Involved and Thin-Skinned Tectonism in the Tertiary Fold-Thrust Belt of Central Spitsbergen Svalbard*. Discusses the fold-and-thrust belt structures and the kinematic evolution on the basis of multichannel reflection seismic data from Isfjorden.

- Braathen et al. (2017): *The Keisarhjelmen detachment records Silurian-Devonian extensional collapse on Northern Svalbard.* Argues for the presence of a Devonian extensional collapse detachment in north-western Svalbard.

- Blinova et al. (2012): *Seafloor expression and shallow structure of a fold-and-thrust system, Isfjorden, west Spitsbergen.* Discusses shallow geological structures of Isfjorden based on multichannel reflection seismic data and bathymetric data.

- Blinova et al. (2013): *Analysis of structural trends of sub-sea-floor strata in the Isfjorden area of the West Spitsbergen Fold-and-Thrust Belt based on multichannel seismic data*. Discusses deep geological structures of Isfjorden.

- Bælum and Braathen (2012): *Along-strike changes in fault array and rift basin geometry of the Carboniferous Billefjorden Trough, Svalbard, Norway*. Discusses geological structures along the Billefjorden Fault Zone.

- Senger et al. (2013)*: Geometries of doleritic intrusions in central Spitsbergen, Svalbard: an integrated study of an onshore-offshore magmatic province with implications for CO2 sequestration*. Discusses magmatic sill and dyke intrusions in central Spitsbergen.

- Skaara (2020): *Prosessering og tolkning av refleksjonsseismiske data fra Isfjorden, Svalbard*. Discusses 2D multichannel reflection seismic data from Inner Isfjorden, Sassenfjorden and Billefjorden.

- Ågesen (2021): *Processing and interpretation of reflection seismic data from Isfjorden, Svalbard.* Discusses 2D multichannel reflection seismic data from Inner Isfjorden and Sassenfjorden.

6.2.2 Seismostratigraphic framework

A stratigraphic column derived by Blinova et al. (2013) in Isfjorden provides the basis for the seismic units identified in this study, presented in Figure 6.1. The seismic signature of these are described in the seismostratigraphic framework below.
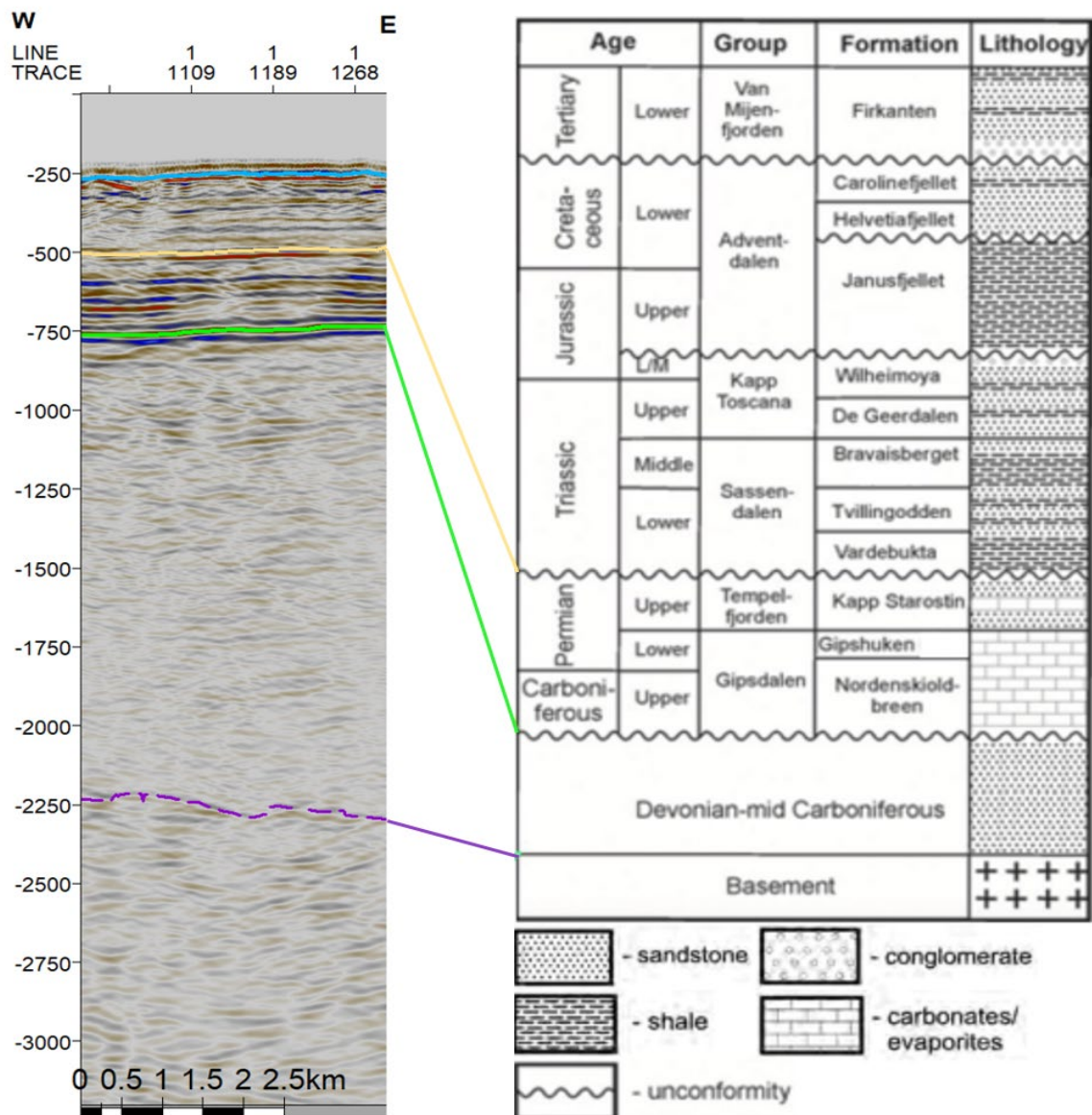
Figure 6.1: The stratigraphic column of Isfjorden tied with the seismic units of line 4. Modified from Blinova et al. (2013).

The Tertiary succession, including the Van-Mijenfjorden Group, contains the youngest sedimentary rocks found in Spitsbergen and includes sandstones, siltstones and shales. The group is separated from the underlying Adventdalen Group by an unconformity that formed in response to regional uplift in the Late Cretaceous. A thick sequence of Mesozoic sediments were deposited in a time of stable platform conditions and sea level fluctuations. The youngest subunit of the Adventdalen Group, the Carolinafjellet formation, comprises shale and sandstone successions of weak and laterally inconsistent reflectors. The boundary between the Carolinafjellet formation and the underlying Helvetiafjellet formation is transitional and therefore difficult to identify in the seismic. The high-velocity sandstone of the Helvetiafjellet formation displays sequences of strong and continuous reflections. The strong AI contrast to the underlying low-velocity shale of the Janusfjellet formation forms a sharp impedance contrast in the seismic. The Janusfjellet formation has a chaotic and discontinuous reflectivity pattern that is almost transparent in the seismic.

Another sharp impedance contrast forms at the upper boundary of the Kapp Toscana Group, a boundary recognised as a regional hiatus. The group consists of deltaic sandstones that appear with strongly folded and over thrusted reflectors. The marine shales of the Sassendalen Group have weak and discontinuous reflectors that are mostly transparent (Bælum & Braathen, 2012; Blinova et al., 2013). The Permian to Late Carboniferous units predominantly consist of carbonates and evaporites that generate strong, parallel and continuous reflectors. The upper and lower boundary are bounded by distinct unconformities. The Devonian "Old Red" sandstone has a scattered and weak reflectivity pattern, less pronounced than the underlying basement, the Hecla Hoek. The highly deformed Hecla Hoek has a chaotic and discontinuous seismic character (Blinova et al., 2013).

6.2.2.1 Décollements

Three main décollements are acknowledged in Isfjorden, formed in response to WSW–ENE shortening during the formation of the WSFTB (Bergh et al., 1997; Blinova et al., 2012). The term refers to faults that are basal and layer-parallel and is a detachment surface from which thrust faults splay (Blinova et al., 2012). Isfjorden comprises the "thin-skinned" foreland of the fold-and-thrust belt, in which décollements commonly form in weaker mechanical layers in response to stress (Fossen, 2010). Ramp-flat geometry structures tend to form above these sole

thrusts, including fault-bend folds and fault-propagation folds (Bergh & Andresen, 1990). The lowermost décollement (D1) is located in the Permian evaporites, the middle (D2) in the Triassic shale and the upper (D3) in the Jurassic-Cretaceous shales. The strata situated between D2 and D3 has undergone the most intense strain, whereas the lower sedimentary rocks between D1 and D2 have undergone relatively mild deformation (Blinova et al., 2013).

6.2.2.2 Igneous intrusions

Dolerites intrusions in Svalbard are predominantly identified within the Triassic shale, but also in the Permian successions (e.g., Bælum & Braathen, 2012; Blinova et al., 2013; Senger et al., 2013). In the seismic, igneous intrusions characteristically appear with high amplitude, abrupt terminations, saucer-shaped morphology and are locally transgressive (Planke et al., 2005). Due to a very high velocity (>6 km/s), they may appear so strong that they mask the underlying reflectors. The intrusions in Svalbard occur primarily as sills, typically less than 50 m thick, but extending over 10 km laterally (Senger et al., 2013). They are found to reach widths between 3 to 12 km, striking along two main trends in NW-SE and NE-SW directions. Igneous intrusions were emplaced during Late Jurassic and Early Cretaceous as a result of faulting and widespread magmatic activity in Svalbard (Worsley, 1986; Hjelle, 1993).

6.2.3 Data quality

	Depth (Z)	Velocity (v)	Dominant frequency (f)	Wavelength $\lambda = \dfrac{v}{f}$	Vertical resolution $\sqrt{\dfrac{\lambda}{4}}$	Horizontal resolution (Fresnel Zone) $\sqrt{\dfrac{\lambda Z}{2}}$
Seabed	250 ms	4800 m/s	24 Hz	200 m	50 m	158 m
Hecla Hoek	3700 ms	5500 m/s	15 Hz	367 m	92 m	824 m

Table 6.1: Calculation of the vertical and horizontal resolution for this study.

A calculation of the seismic data resolution of this study is given in Table 6.1. The abnormal high velocities in the seabed of Isfjorden has degraded the data quality, as it generates a very large R_c and a small critical angle (~18°). The critical angle, the angle at which no compressional energy will propagate into the lower medium (Poley, 1964), is given in equation 6.1. With a small critical angle, much of the energy will be reflected at the seabed and less will

be transmitted. In turn, this reduces the data quality and resolution of the subsurface structures. The presence of igneous intrusions also has the potential of preventing the propagation of seismic energy vertically downwards by masking underlying reflectors.

$$sin\theta_c = \frac{V_1}{V_2} = \frac{1500}{4800} = 18.2$$

The general data quality is displayed in Figure 6.2. The data quality of the seabed varies, but is particularly reduced for the shallowest areas, reaching about 50 ms depth, that completely lack seismic energy (Figure 6.3). This could have been resolved by considerably reducing the source and receiver-offset during acquisition. Generally, the data quality of the seabed has been reduced in the attempt to attenuate the initial strong and short-interval multiples. This will be further discussed in 7.1.2. Since this study focuses on the subsurface structures, a degraded quality of the shallow seabed is not a critical factor. Various processing sequences have successfully reduced the multiples and improved the overall seismic image, and in turn made it possible to execute a reliable interpretation.
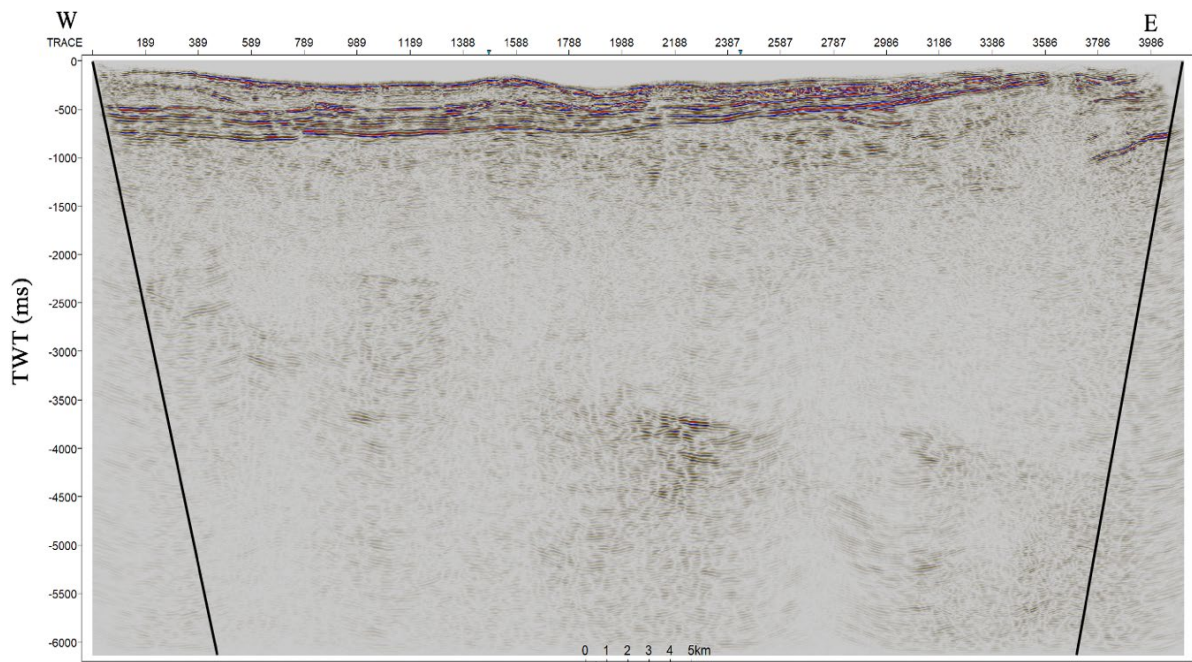
Figure 6.2: The general data quality of this study, displaying line 4. The streamer noise is indicated by the black lines.
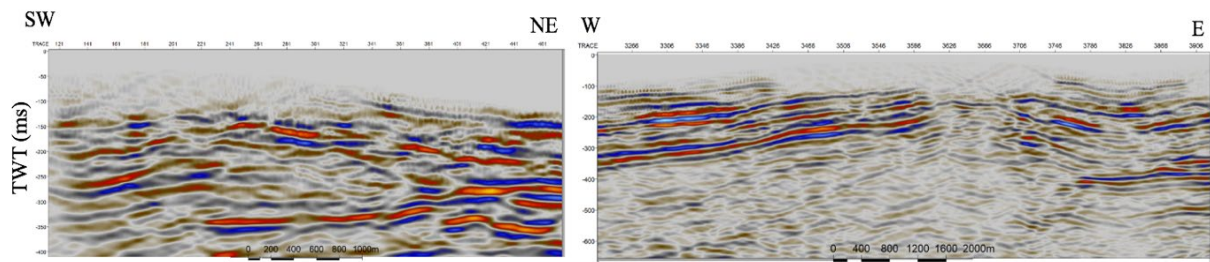
Figure 6.3: Missing or reduced sea-bottom reflectors. The left image shows the shallowest seabed area for line 5, located in the SW, while the right image is derived from the eastern part of line 4.

Streamer noise is present for all lines, which lowers the data quality along the edges. This occurs as the seismic vessel turns during acquisition and the streamer is not fully extended in the correct position behind the ship. The black lines in Figure 6.2 illustrate the zones of line 4 that are affected by streamer noise. The noise could have been removed by excluding shots that were acquired before the full streamer was in the correct position, but this would have resulted in shorter lines. The seismic sections also contain some local transparencies, shown in Figure 6.4, which indicate areas of low amplitude, incoherent energy or mission reflectors.
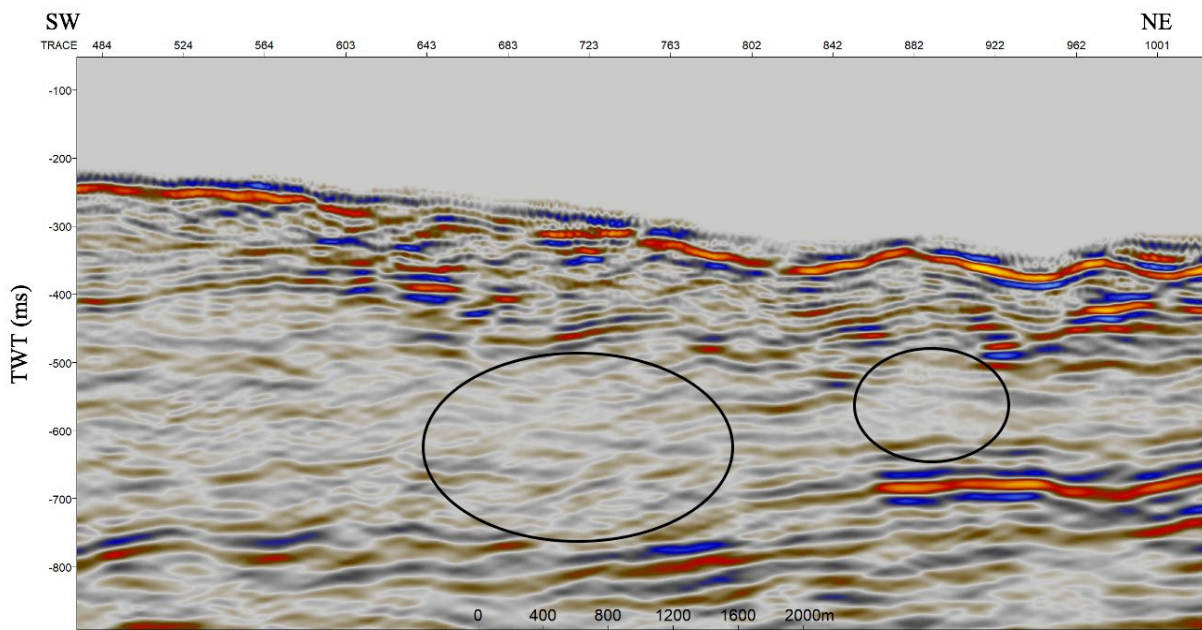
Figure 6.4: Areas of local transparencies in the seismic for line 3.
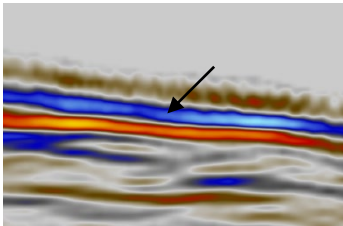
Imaging of dipping surfaces is affected by the shooting direction, whether the seismic is acquired up-dip or down-dip. This is the case for line 3 and 4, in which the data is acquired in different directions over the BFZ. In turn, these lines will image the same dipping surfaces slightly differently. This is related to the directivity of the receivers. Directivity does not imply to the source, since it was set up as a wide array (an additional airgun) (Mjelde, pers. comm).

It is also important to be aware of the vertical exaggeration present in seismic sections displayed in time. This gives certain advantages during stratigraphic and structural interpretation, such as the possibility to view long-wavelength structures, but will not display 100% accurately geological sections. It may cause distorting effects on geological structures, such as affecting dip and curvature (Stewart, 2012).

Another noteworthy deviation in the study is the loss of coordinates for line 3. The navigation data was lost during acquisition and had to be drawn manually based on the information from the planned survey and the field logs (Mjelde, 2003). This has caused a small mismatch in the correlation between the seismic profiles and thus a minor deviation in topography when surface and isopach maps are created.

6.3 Stratigraphic interpretation

This subchapter will describe the reflector characteristics that has been used to distinguish the stratal packages in this study. A total of six horizons are interpreted, of which five will be presented in this subchapter. The remaining BFZ horizon is heavily influenced by the fault zone and will therefore be presented during the structural interpretation. The reflector continuity differentiates between the horizons. The shallowest horizons generally have a more continuous reflector, whilst the top-basement horizon is weak and discontinuous. Table 6.2 gives an overview of the horizons that are interpreted, their seismic phase, reflector characteristics and seismic signature. The seismic signature image is derived from where the horizon is best displayed.

Horizon	Seismic phase	Reflector characteristics	Seismic signature
Seabed	Positive amplitude (trough)	Weak to strong amplitude, mainly continuous	
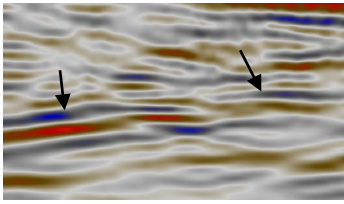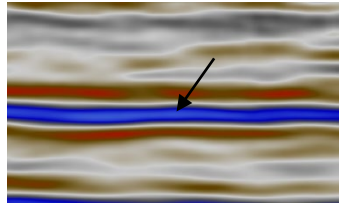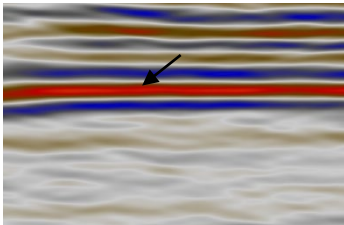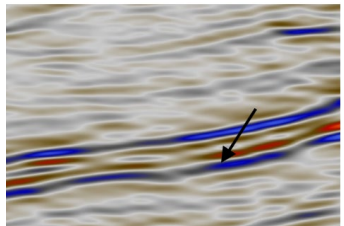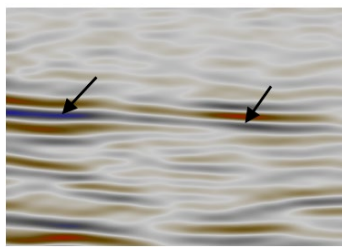
Base Jurassic	Positive amplitude (trough)	Weak to medium amplitude, continuous to discontinuous	
Top Permian	Positive amplitude (trough)	Medium to strong amplitude, mainly continuous	
Top mid-Carboniferous	Negative amplitude (peak)	Strong amplitude, continuous	
BFZ horizon	Positive amplitude (trough)	Weak to medium amplitude, mainly discontinuous	
Top Hecla Hoek	Positive amplitude (trough)	Weak amplitude, mainly discontinuous	

Table 6.2: The seismic phase, reflection characteristics and seismic signature of the interpreted horizons. The images are mainly derived from line 4, except for the base Jurassic horizon, which is only present in line 3.

The stratigraphic horizons that will be interpreted include the seabed, base Jurassic, top Permian, top mid-Carboniferous and top Hecla Hoek. The crystalline basement is overlain by

a thick Upper Palaeozoic to Tertiary sediment cover (Bergh et al., 1997). The youngest sedimentary package identified in this study is the Jurassic unit. Younger sedimentary units are likely not present in the study area, as they have been uplifted and eroded above the BFZ.

Surface maps and isopach maps are generated for interpretation purposes. A surface map is created from an interpreted horizon and will display how variations in depth correlates across the area. The shallowest areas are displayed in red, while purple represents the deepest. The data is interpolated between the seismic lines and will therefore only give rough TWT estimations in these areas. In turn, this may create false topography on the map. This is a result of the use of 2D seismic and the lack of densely covered seismic data in an area. Additionally, due to loss of navigation data for line 3, as discussed in 6.2.3, the topography will deviate to some extent along this line. An isopach map shows the vertical thickness of a stratal package between two interpreted horizons. All the maps are displayed in TWT and include an arrow that shows the direction of north, a legend and a scale.

The following figures (Figure 6.5 and Figure 6.6) display line 4 before and after the stratigraphic interpretation, respectively. The interpreted horizons are displayed with different colours, in which the upper light blue represents the seabed, blush is the base Jurassic (only present in line 3), orange the top Permian, green is the top mid-Carboniferous, pink is the BFZ horizon and purple is the Hecla Hoek. The dotted lines indicate uncertainty in the interpretation, which is the case for the BFZ horizon and Hecla Hoek.
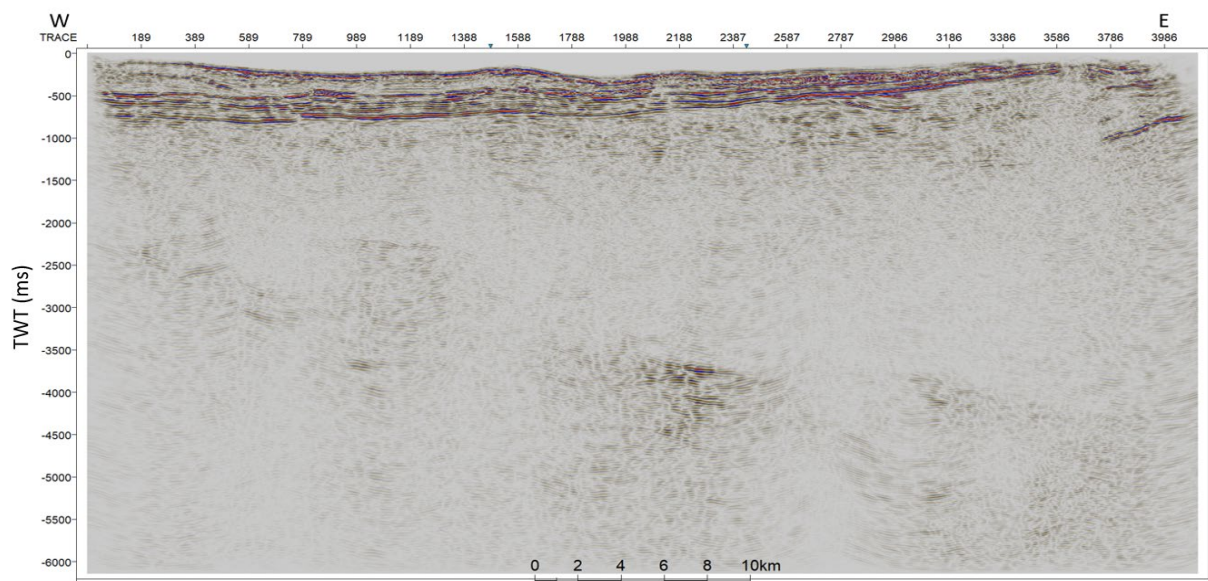
Figure 6.5: Line 4 prior to stratigraphic interpretation.
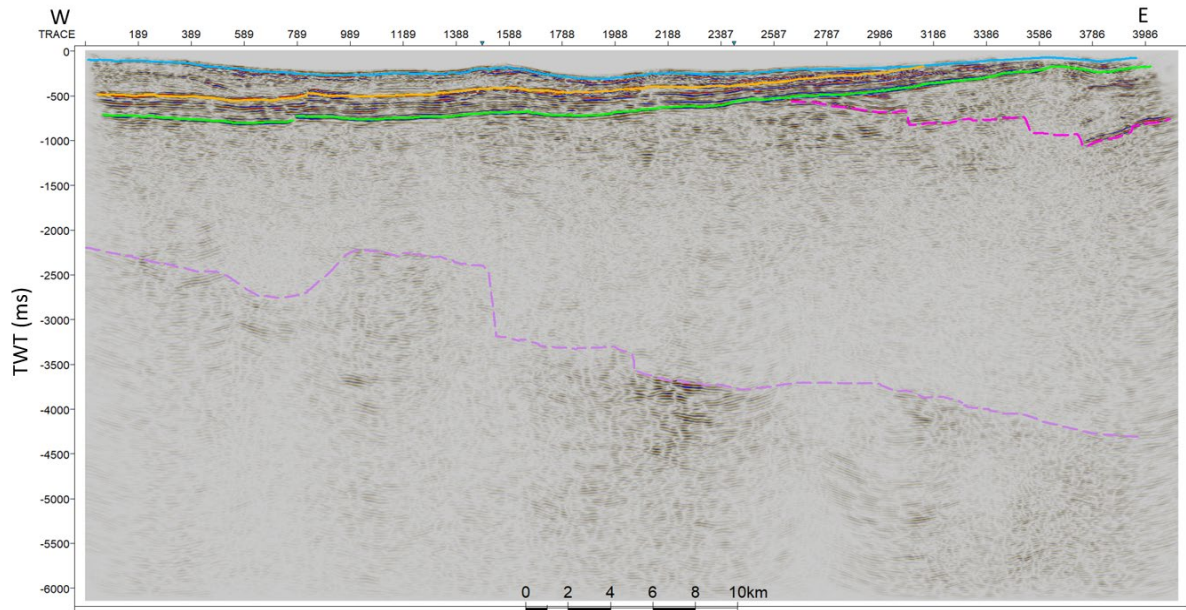
Figure 6.6: Line 4 after the stratigraphic interpretation. The stratigraphic horizons are the seabed (light blue), top Permian (orange), top mid-Carboniferous (green), BFZ horizon (pink) and Hecla Hoek (purple). The dotted lines indicate uncertainty in the interpretation. Note that the structural interpretation is not included.

6.3.1   Seabed

The seabed reflector is commonly the strongest reflector in a seismic section. However, the quality of the reflector was degraded in the process of removing the strong and short-interval multiples. Consequently, the seabed reflector varies between a weak and a strong amplitude. It is mainly continuous across the lines, except for in the shallowest areas of line 4 and 5, where the reflector is completely removed (Figure 6.3). In these areas, the horizon had to be interpolated. The increase in acoustic impedance between the water layer and the seabed generates a trough in the seismic, using the European Polarity standards. The horizon is thus interpreted as the first and most dominant trough in the image. The surface map in Figure 6.7 shows that the depth varies from 50 ms to 350 ms (TWT). The shallowest seabed is located in the eastern and NE part of the study area, in Sassenfjorden and Nordfjorden. The seabed reaches the deepest in the central part of the study area, in inner Isfjorden.
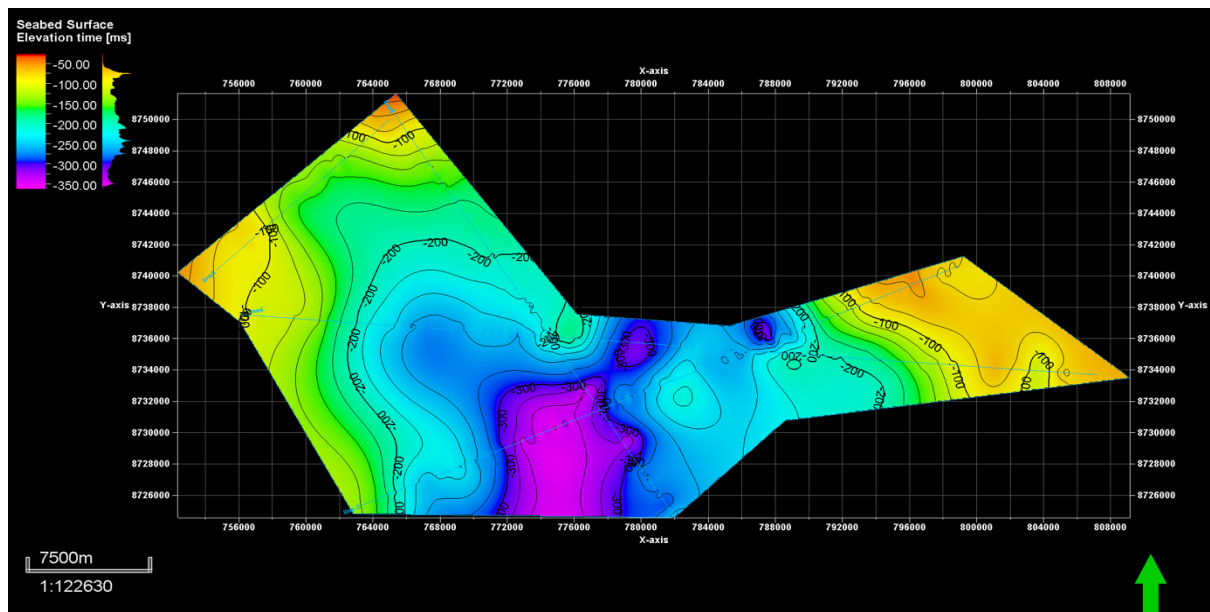
Figure 6.7: Surface map of the seabed horizon in TWT (ms).

6.3.2 Base Jurassic

This horizon is only identified in a small area in the SW of line 3. It is identified as a trough in the seismic, with a weak to medium amplitude. The low-velocity Jurassic shale is bounded by an underlying unconformity, separating it from the underlying sandstone/shale unit of the Kapp Toscana Group. The reflector is continuous to discontinuous, and therefore challenging to follow in some areas. Base Jurassic is shallowing to the NE, ranging from 175 to 350 ms (TWT). As the horizon is only present in a small area in line 3, a surface map is not generated.

6.3.3 Top Permian

The top Permian reflector is bounded by an overlying unconformity and characterised by the appearance of strong, parallel and continuous reflectors. The high-velocity Permian carbonites and evaporites create a strong impedance contrast to the overlying low-velocity shale/sandstone unit and is represented by a positive amplitude (trough) in the seismic section. In this study, the horizon appears continuous to discontinuous, in which it is abrupted in some locations, particularly for line 3. The surface map of the top Permian horizon is displayed in Figure 6.8. The surface is shallowing to the east and is truncated by the seabed in the eastern part of line 3 and 4, due to the uplift along the BFZ. This is also the case for the NW of line 6 and NE part of line 5, where the Blomesletta Fault is located. The surface varies from 50 to

850 ms (TWT). The shallowest area is located above the BFZ in the NE and the deepest is in the SW.
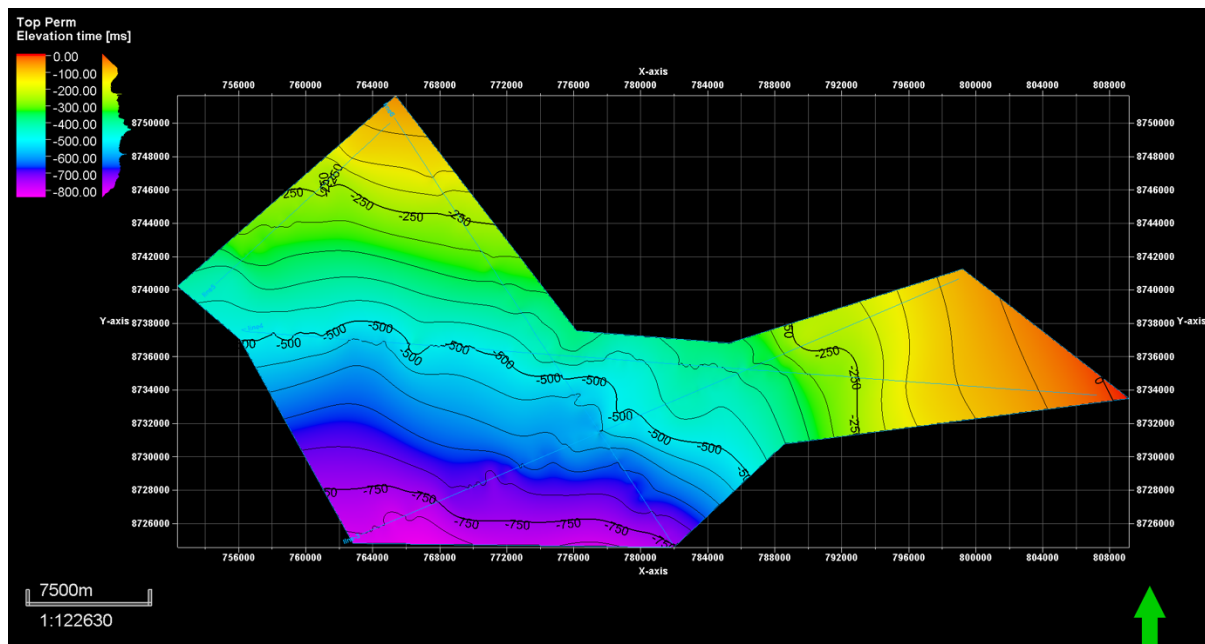
Figure 6.8: Surface map of the top Permian horizon in TWT (ms).

6.3.4 Top mid-Carboniferous

The top mid-Carboniferous horizon is strong and continuous, bounded by an underlying unconformity that is recognised by the presence of an angular unconformity. The horizon separates the overlying high-velocity carbonate unit of Gipsdalen Group from the underlying Devonian sandstone, which creates a strong AI contrast. The horizon is represented by a peak in the seismic. Like the overlying surfaces, the top mid-Carboniferous surface is shallowing to the east (Figure 6.9). It is deepest and shallowest in line 3, where it stretches from 1050 ms (TWT) in the SW to 150 ms (TWT) above the BFZ in the NE.
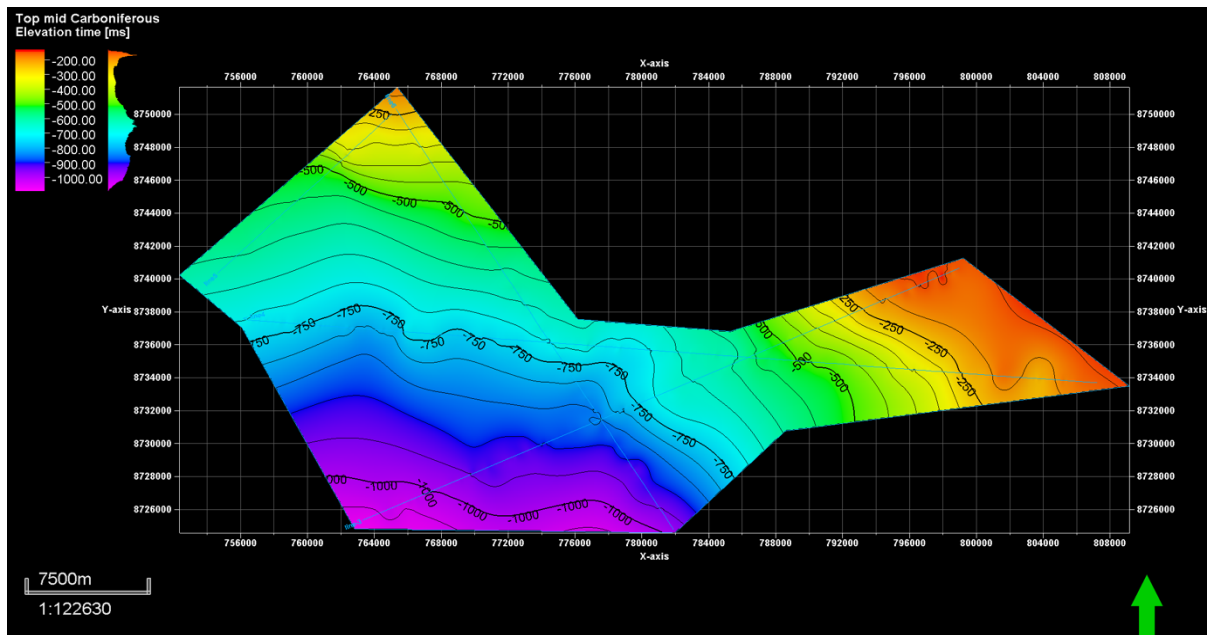
Figure 6.9: Surface map of the top mid-Carboniferous horizon in TWT (ms).

6.3.5 Top Hecla Hoek

The top Hecla Hoek is the deepest interpreted horizon in this study, interpreted between 4100 ms and 2200 ms (TWT). Due to a weak amplitude and mainly discontinuous reflector, it is challenging to interpret the horizon with confidence. The horizon is represented by a positive amplitude (trough), due to the higher density and velocity of the basement rocks. In contrast to the overlying surfaces, the top Hecla Hoek is shallowing to the west and is deepest in the east of the study area. The surface map of the horizon is shown in Figure 6.10. The surface includes several faults, displayed by an abrupt change in TWT. These will be further discussed in chapter 7.2.2.4.
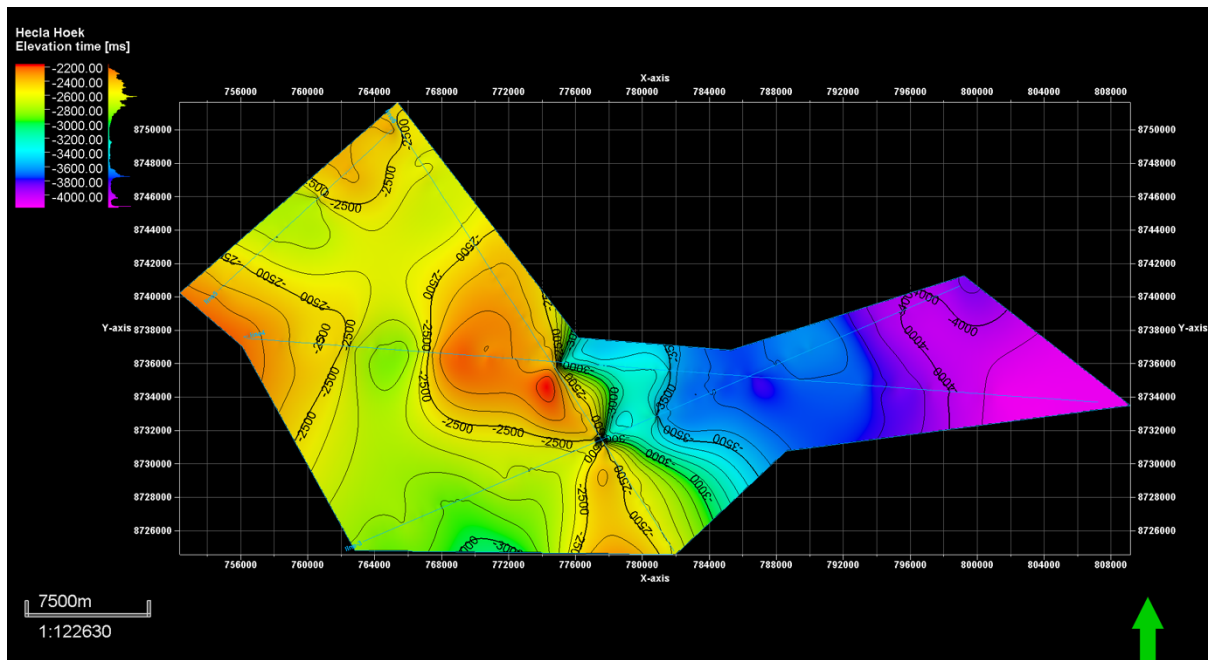
Figure 6.10: Surface map of the top Hecla Hoek horizon in TWT (ms).

6.3.6 Stratigraphic units

It can be useful to study the stratigraphic units between two surfaces to derive more geological information. Thickness variations between surfaces are displayed in isopach maps. These may help to understand what geological processes a stratigraphic package has been exposed to, such as erosion, uplift and deformation, and how the sedimentation varies across the area. Five stratigraphic units will be discussed in this subchapter, while the remaining BFZ horizon will be included in subchapter for structural interpretation.

6.3.6.1 Unit 1: Jurassic

This unit includes the organic-rich shales of the Janusfjellet Formation, the lower Adventdalen Group, and has a chaotic, discontinuous and generally weak reflectivity pattern. It is only identified in the SW of line 3. The unit reaches the maximum thickness of 175 ms (TWT) in the SW, while is gradually thinning towards the NE, before it is truncated by the seabed. The unit is distinguished based on an apparent unconformity against the underlying sandstone of the Kapp Toscana Group, with some evidence for onlaps onto the base-Jurassic horizon (Figure 6.11). The unit is also identified and separated from the underlying section by the apparent change in reflectivity characteristics. Unit 1 seems to have a more chaotic reflectivity package

of NE-tilted reflectors, which contrasts to the underlying horizontal or slightly SW-tilted reflectors. An isopach map is not generated for this unit, as it is only present in line 3.
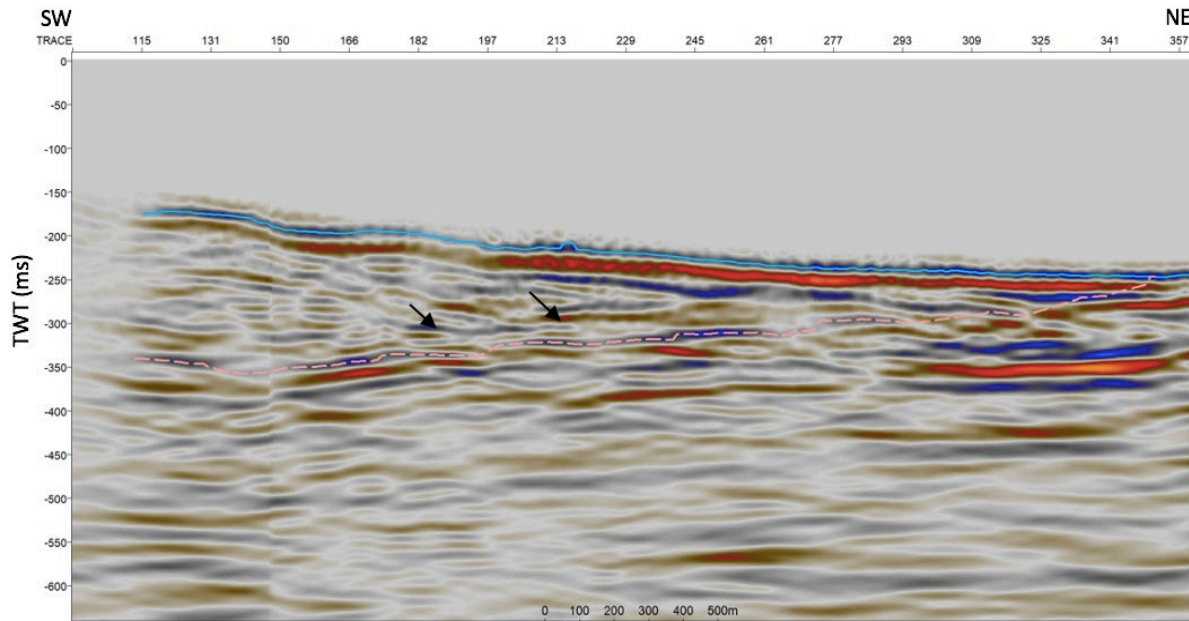
Figure 6.11: The seismic character of unit 1, which is only present in line 3. Onlaps are pointed out by the black arrows.

6.3.6.2 Unit 2: Triassic

This unit includes the Sassendalen Group and Kapp Toscana Group, sandstone and shales successions deposited between the Triassic and Early Jurassic. The unit is bonded by the seabed and the top Permian reflector. The reflectivity pattern generally appears weak and discontinuous, but displays zones of stronger amplitude and continuity, as indicated by arrows in Figure 6.12. The reflectivity pattern appears the weakest in the deeper sections, while contain medium amplitudes in the shallower parts. The isopach map in Figure 6.13 reveals that the stratigraphic package is thickest in the SW and thinnest in the NE. It is not exposed in the eastern parts of line 3 and 4, over the BFZ, nor in the NE of line 5, over the Blomesletta Fault. In line 6, it is exposed across almost the full line, except for in the NW. The unit ranges from 750 ms to 0 ms (TWT) thickness, in which 0 ms represents where the top Permian reflector is truncated by the seabed.
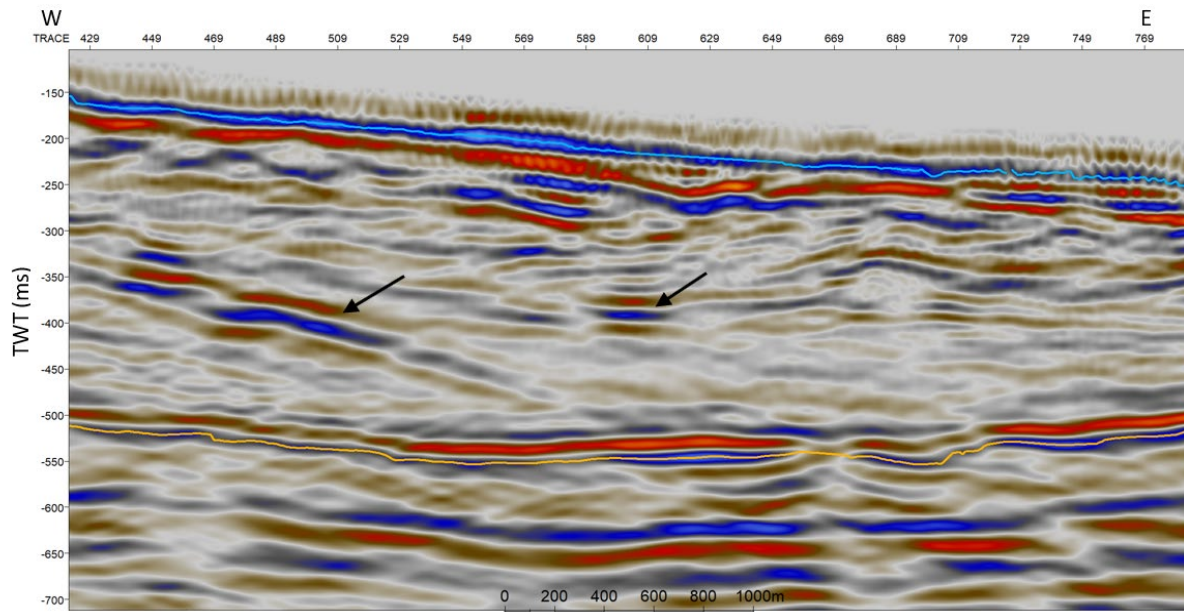
Figure 6.12: The seismic character of unit 2, displaying line 4. The black arrows point at stronger reflectors within the unit between the seabed (blue) and top Permian reflector (orange).
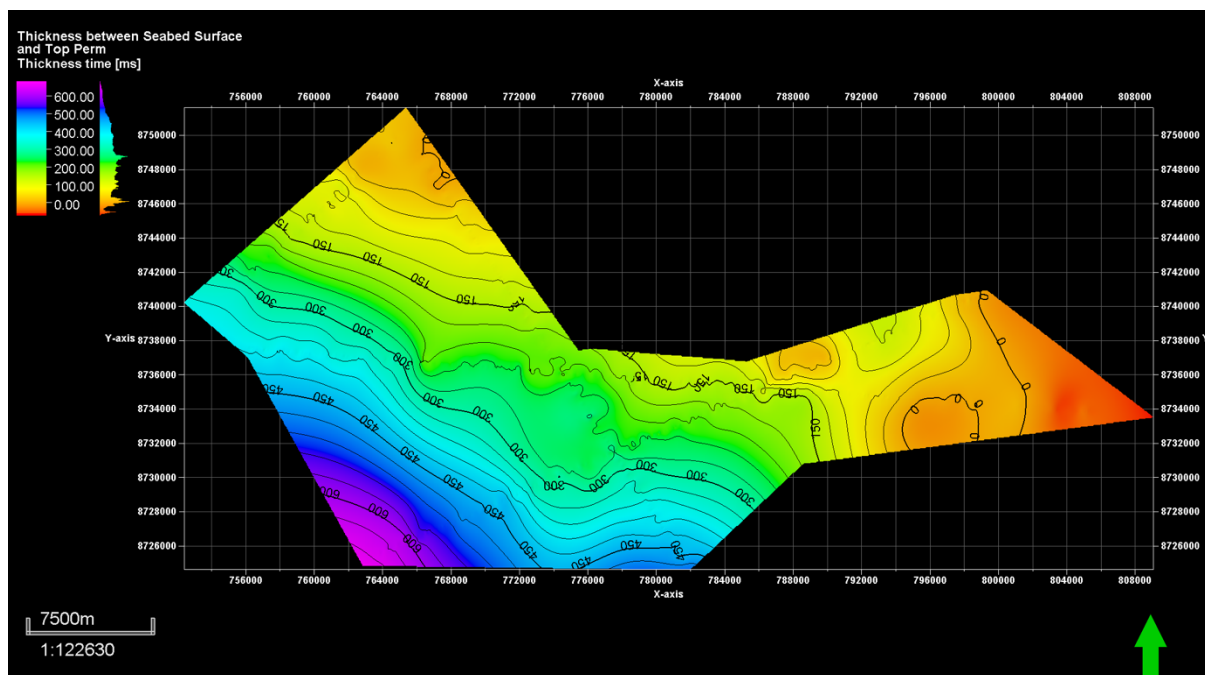
Figure 6.13: Isopach map between the seabed and top Permian surface in TWT (ms).

6.3.6.3 Unit 3: Top Permian to top mid-Carboniferous

This unit includes the sedimentary packages of the Tempelfjorden Group and Gipsdalen Group, deposited between the Permian and mid-Carboniferous period. These are characterised by the

accumulation of carbonates and evaporites, deposited in a shelf setting (Blinova et al., 2013). In the seismic, the reflectors are strong, parallel and continuous (Figure 6.14). There are some local discontinuities in the reflectors, which is particularly evident in the SW of line 3 and the NE of line 5, above the Blomesletta Fault. The stratigraphic unit is present in all lines, but gets thinner towards the NE, reaching 75 ms (TWT), as the unit is partly eroded and truncated by the seabed over the BFZ. The isopach map in Figure 6.15 shows that the unit keeps approximately the same thickness across the study area, about 250 ms thickness (TWT), but is slightly thicker in the central part, where it reaches 275 ms (TWT).
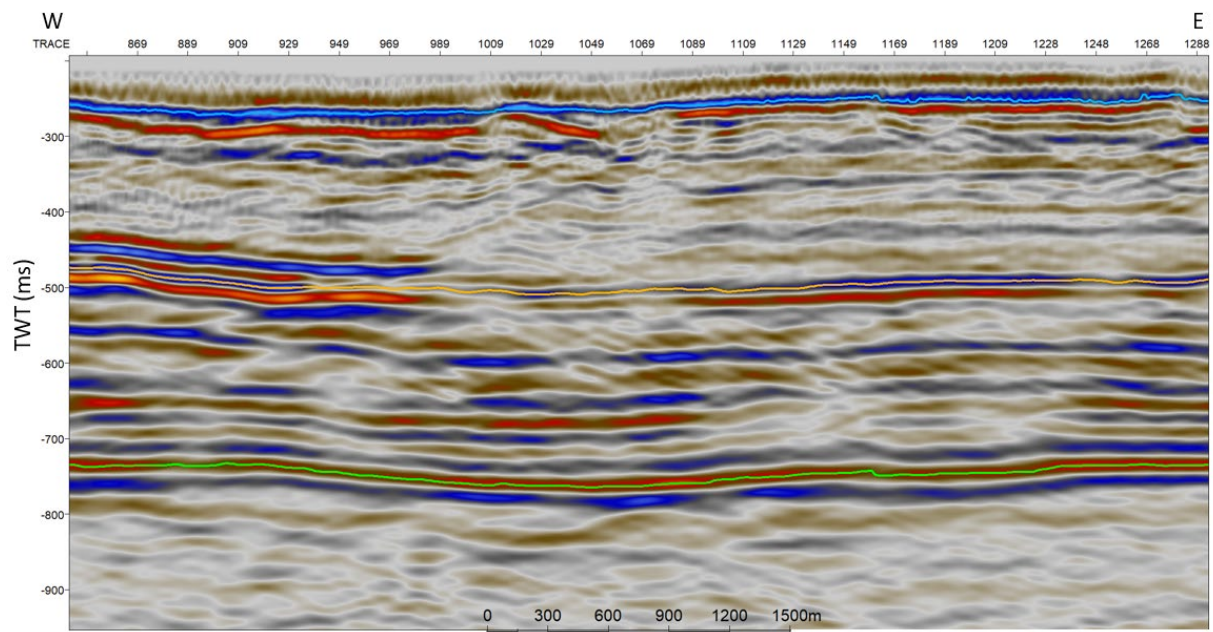
Figure 6.14: The overall typical seismic character of unit 3, present between the top Permian (orange) and top mid-Carboniferous reflector (green). The figure is derived from line 4.
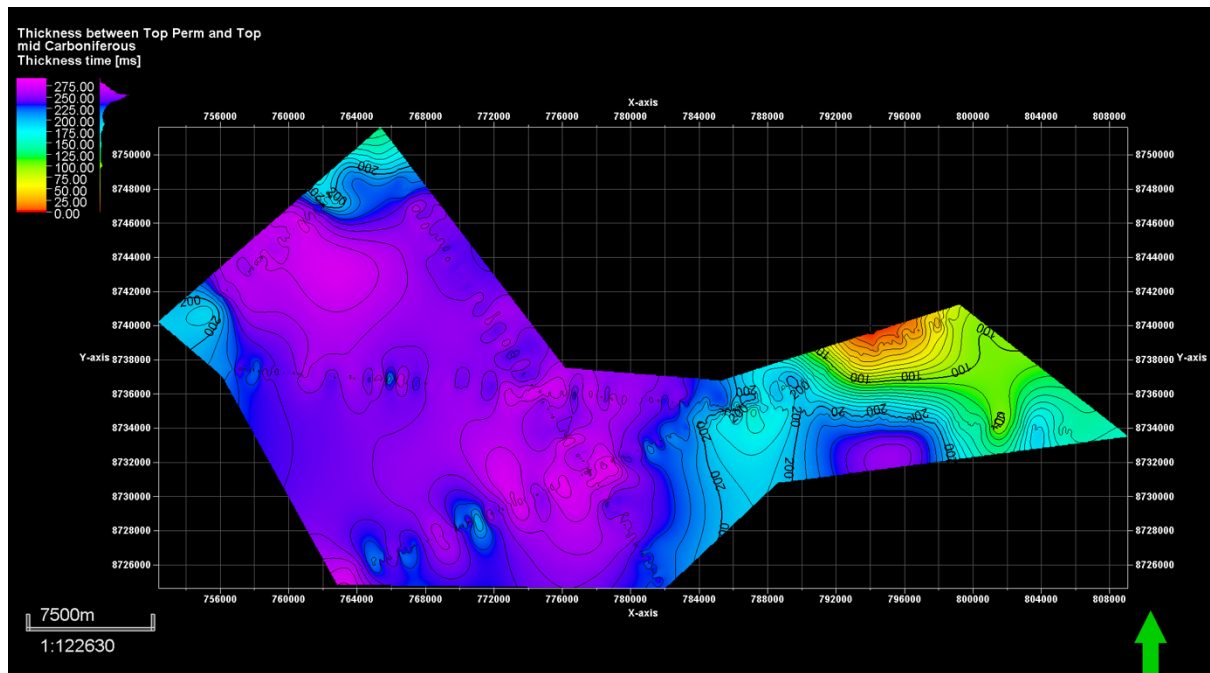
Figure 6.15: Isopach map between the top Permian and the top mid-Carboniferous surface in TWT (ms). The thickness is concentrated around 250 ms, but varies from around 75 ms in the NE to 275 ms in the central part of the study area.

6.3.6.4 Unit 4: Devonian

This sedimentary package was deposited in the Devonian period. The seismic character varies between the lower and upper part of the unit. The lower part of the unit has a scattered, chaotic and weak seismic reflectivity pattern with almost transparent zones. This is characteristic of the "Old Red" sandstone (Blinova et al., 2013). The upper part of the unit is also chaotic but contains some higher amplitude reflections, pointed out in Figure 6.16. This unit comprises a large section of the seismic profiles and is present across all lines. The TWT varies from 1500 ms to 4000 ms, as indicated in the isopach map in Figure 6.17.
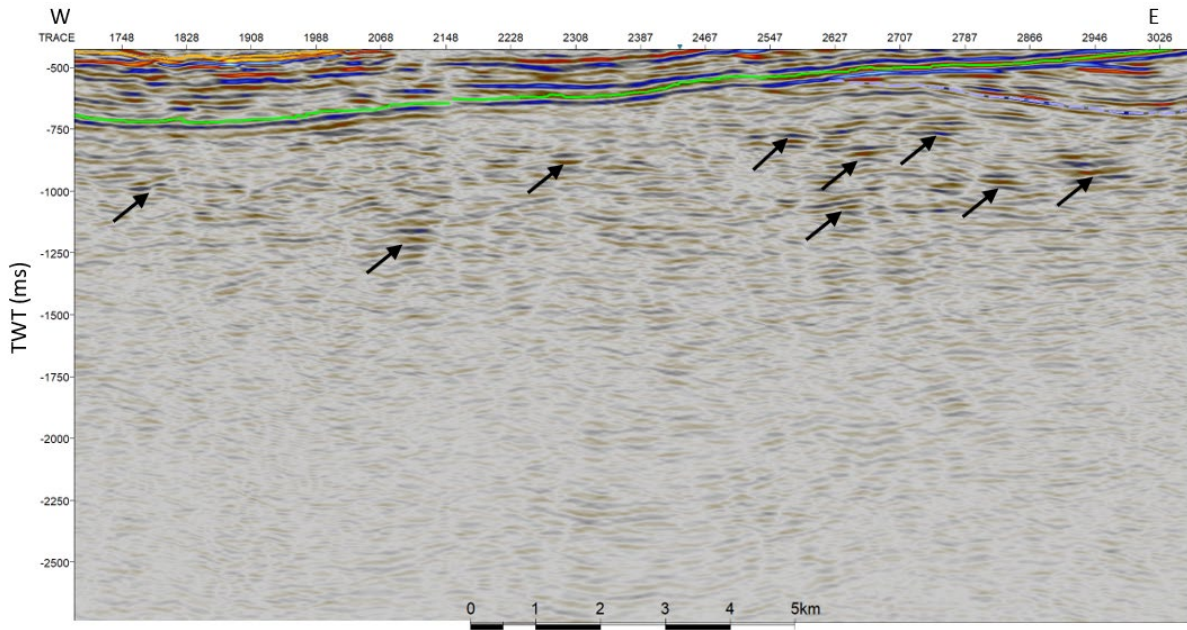
Figure 6.16: The seismic character of unit 4 from line 4, which overall appears with weak, scattered and chaotic reflectors. Stronger reflections appear in the upper part of the unit, as indicated by the black arrows. The green line indicates the top mid-Carboniferous horizon.
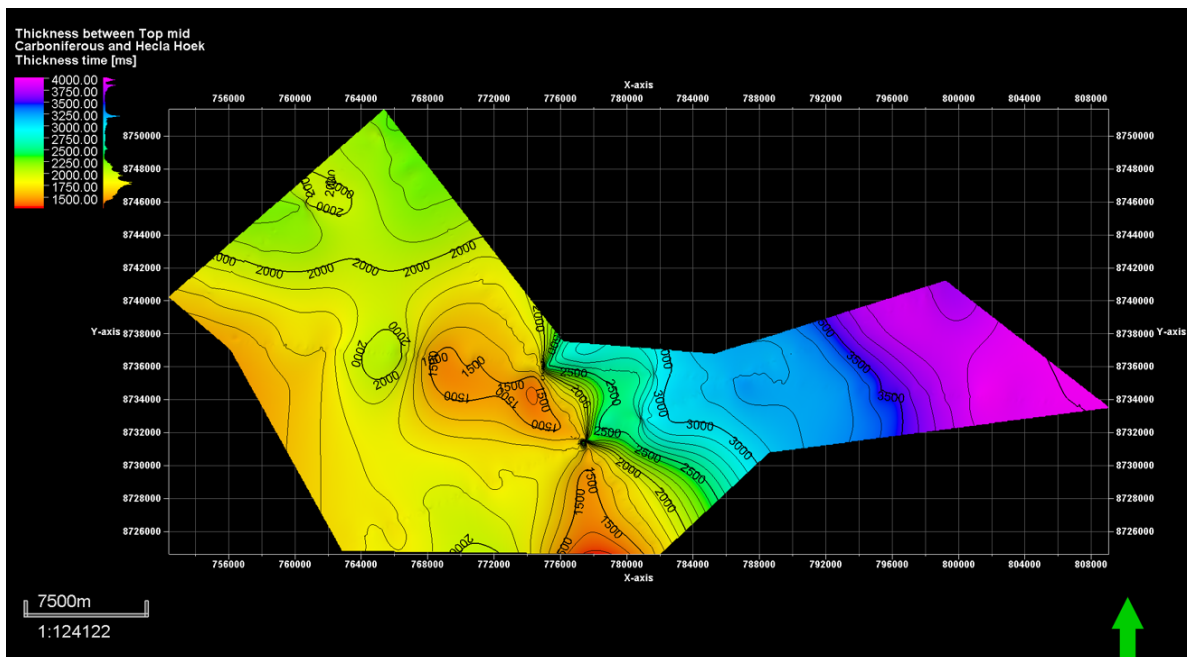
Figure 6.17: Isopach map between the top mid-Carboniferous and top Hecla Hoek surface in TWT (ms).

6.3.6.5 Unit 5: Hecla Hoek

The basement rock of Svalbard comprises igneous and metamorphic rocks that were deposited from Late Proterozoic to Silurian Age (Blinova et al., 2013). The impedance contrast to the overlying Devonian sandstone generates some areas of stronger amplitude for the top reflectors. The reflectivity pattern is generally chaotic, weak and discontinuous, resulting from high deformation during the Caledonian Orogeny (Hjelle, 1993; Blinova et al., 2013). Figure 6.18 displays the overall seismic character of the Hecla Hoek.
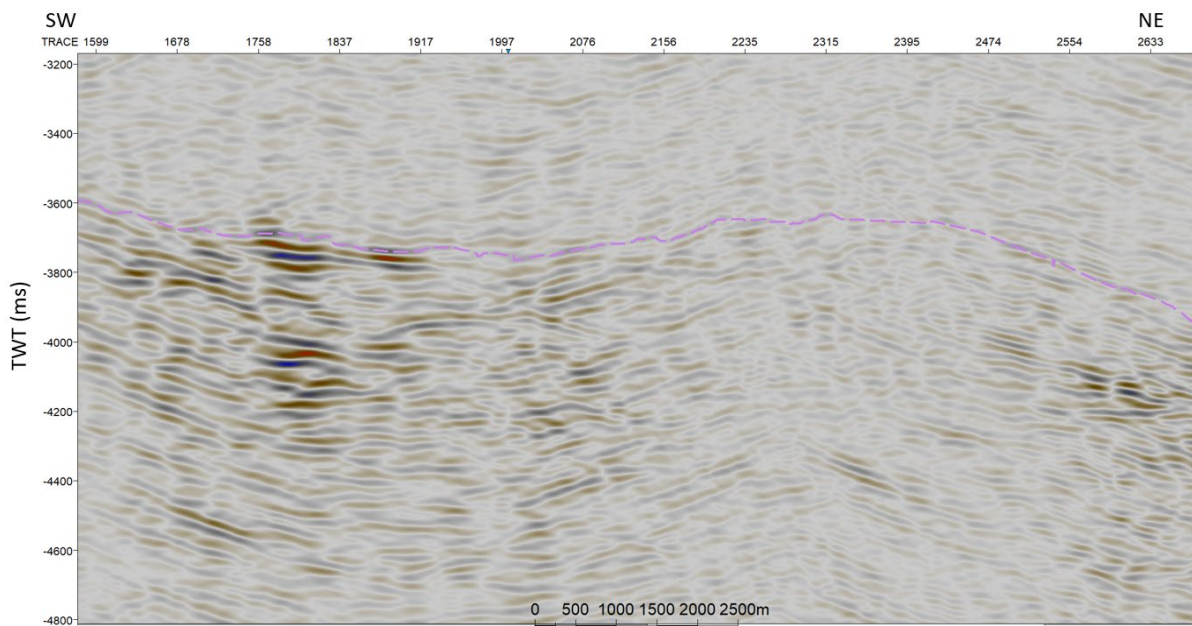
Figure 6.18: Seismic character of unit 5, displayed for line 3. The top Hecla Hoek horizon (purple dottle line) appears distinctive with stronger reflections in some areas, while is challenging to pinpoint in other areas, such as NE in the figure.

6.4 Structural interpretation

This subchapter will focus on the main structural features that have been interpreted in the BFZ, the Blomesletta Fault and the Hecla Hoek. The structural interpretation is based on terminations and displacements in the seismic reflections, which was particularly challenging for the poorly imaged BFZ. The horizon identified along the fault zone, named the BFZ horizon, will be presented in this chapter due to high uncertainty attached to the interpretation.

6.4.1 Fault structures in the BFZ

The interpretation option of the BFZ considered the most likely is displayed in Figure 6.19 (line 4) and Figure 6.20 (line 3). The fault zone is present in the east of line 3 and 4, but only partly included in line 3. The BFZ model includes two steep east-dipping faults, a western major reverse fault and an eastern normal fault. The western fault stand has displaced the metamorphic basement in the east against the half-graben Devonian basin in the west, while normal fault movement simultaneously to sedimentary deposition has left a pronounced half-graben structure east of the BFZ. A west-dipping normal fault is interpreted within the half-graben. On the western side of the BFZ, an east-dipping normal fault is interpreted in line 4, while a normal and reverse fault is interpreted in line 3.
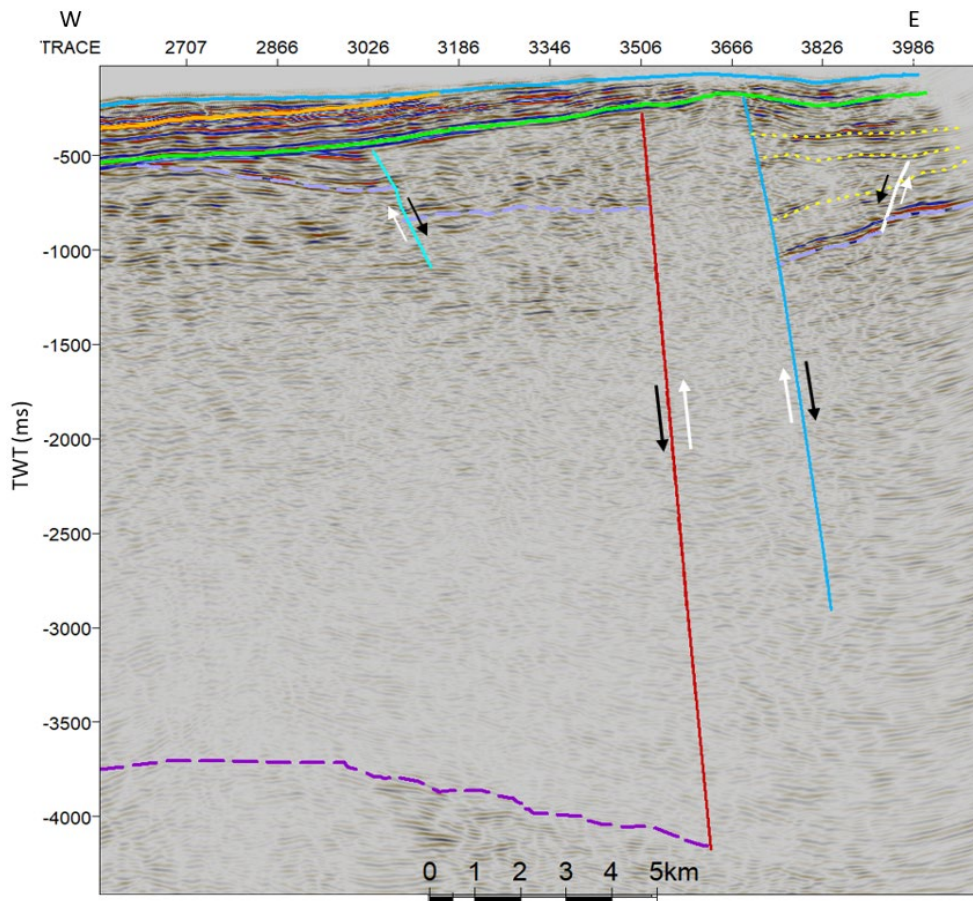
Figure 6.19: The interpretation of the BFZ (showing line 4) includes a western reverse fault (red) and an eastern normal fault (blue), both dipping steeply to the east. A pronounced half-graben structure is identified along the normal fault, in which a minor west-dipping normal fault (white) is interpreted. An east-dipping normal fault (turquoise) is interpreted west of the BFZ.
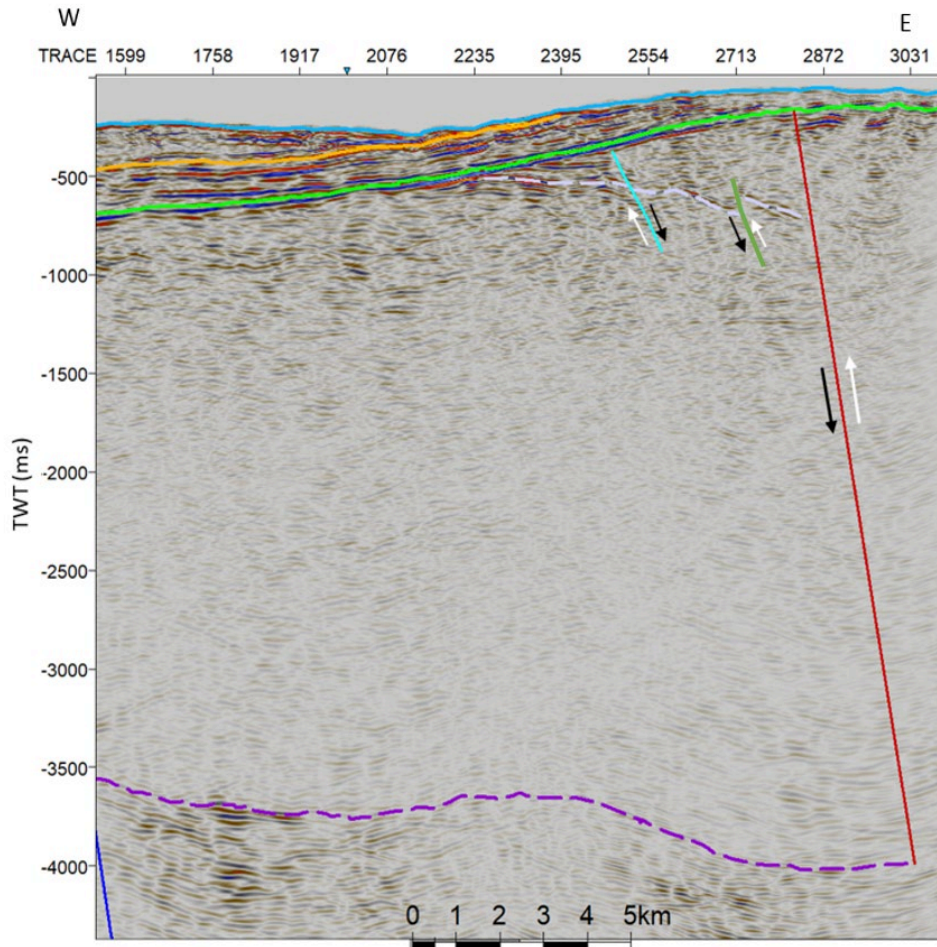
Figure 6.20: The BFZ interpretation for line 3 shows the major reverse fault (red) dipping steeply to the east. Two minor faults, one normal (turquoise) and one reverse (green) are identified in the western basin.

6.4.2 Stratigraphy of the BFZ

One horizon is interpreted across the BFZ, denoted as the BFZ horizon. It is present in both line 3 and 4, but only the western part is included in line 3. The BFZ horizon is interpreted along a trough of weak to medium amplitude reflection. It is displayed with a dotted line due to the uncertainty attached to the interpretation, caused by weak, chaotic, discontinuous and almost transparent reflectors across the main fault zone. However, on each side of the fault zone, the continuity and strength of the reflector is considerably enhanced. A surface map of the BFZ horizon is displayed in Figure 6.21. The surface is interpreted deepest in the east, reaching 1050 ms (TWT), and shallowest in the west with an elevation time of 500 ms (TWT). The surface has a bowing appearance, and shallows to the east and west of the deepest section. Additionally, the presence of faults creates a varying topography. The derived BFZ surface is using the BFZ horizon of the scoop-model, as this extends across the fault zone.
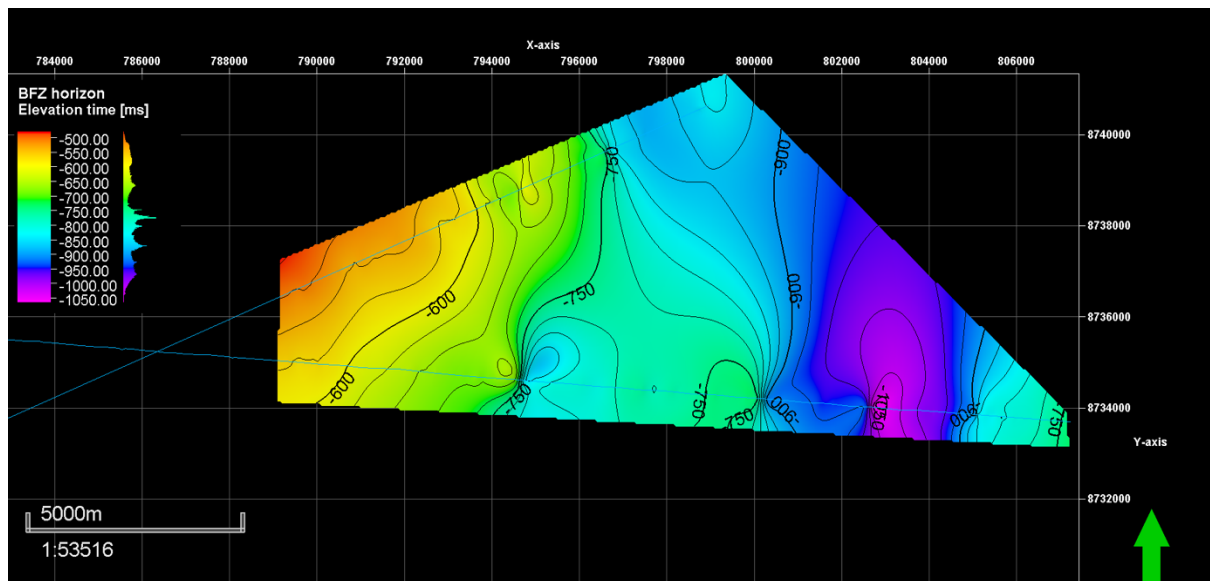
Figure 6.21: Surface map of the BFZ horizon in TWT (ms).

6.4.2.1   Unit 6: The Billefjorden Trough

This stratigraphic unit is denoted as the Billefjorden Trough due to its presence along the BFZ. It is bounded by the lower BFZ horizon and upper top mid-Carboniferous unconformity. The eastern side of the stratigraphic unit is largely of medium amplitude and continuous reflectors, while the central part has weak, chaotic and discontinuous reflectors that are almost transparent in the seismic. The western side appears with some reflectors of medium amplitudes that are continuous, but are otherwise dominated by a chaotic and discontinuous reflectivity pattern. The isopach map in Figure 6.22 between the BFZ surface and top mid-Carboniferous surface shows that the thickness varies between 800 ms to 0 ms (TWT). The thickest part is along the main fault zone in the east, caused by faulting, while the thinnest part is in the west where the BFZ horizon is truncated by the unconformity.
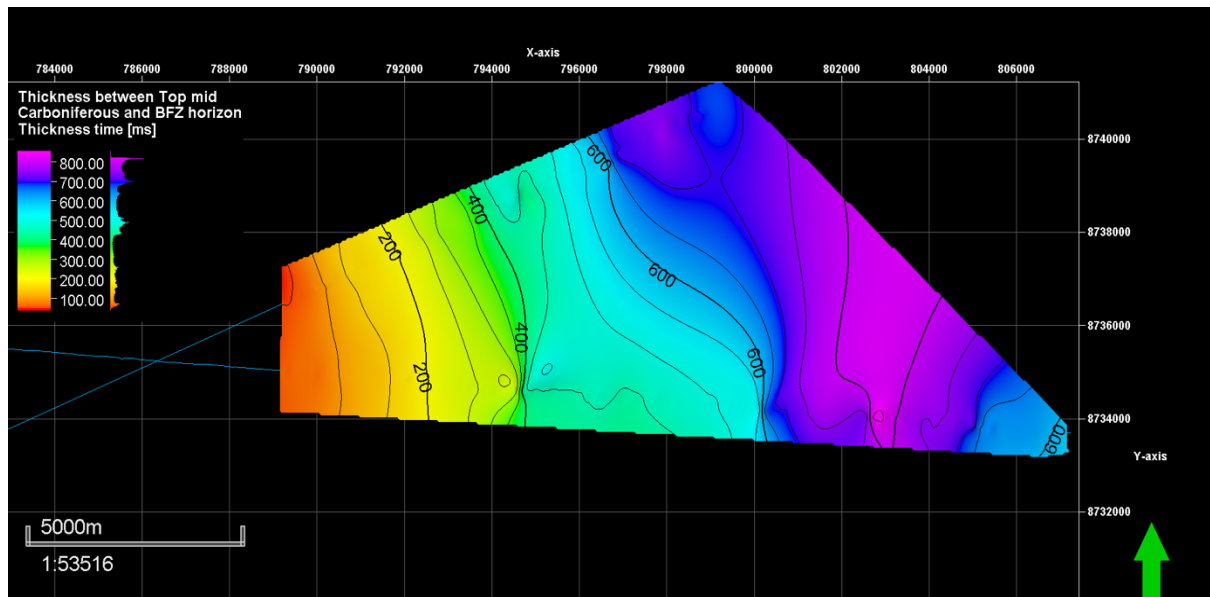
Figure 6.22: Isopach map between the BFZ surface and top mid-Carboniferous surface in TWT (ms), denoted as the Billefjorden Trough unit.

6.4.3   Structures in Blomesletta Fault

The Blomesletta Fault is only present in the NE part of line 5, which covers Nordfjorden. An east-dipping reverse fault springs out to two minor branches that seems to terminate in a décollement (D1) in the Permian-Carboniferous unit. The magnitude of vertical throw is ca. 100 ms. Three west-dipping thrust faults are present above the major Blomesletta Fault and attach to the underlying sole thrust of D1. The interpreted structures of the Blomesletta fault is shown in the figure below.
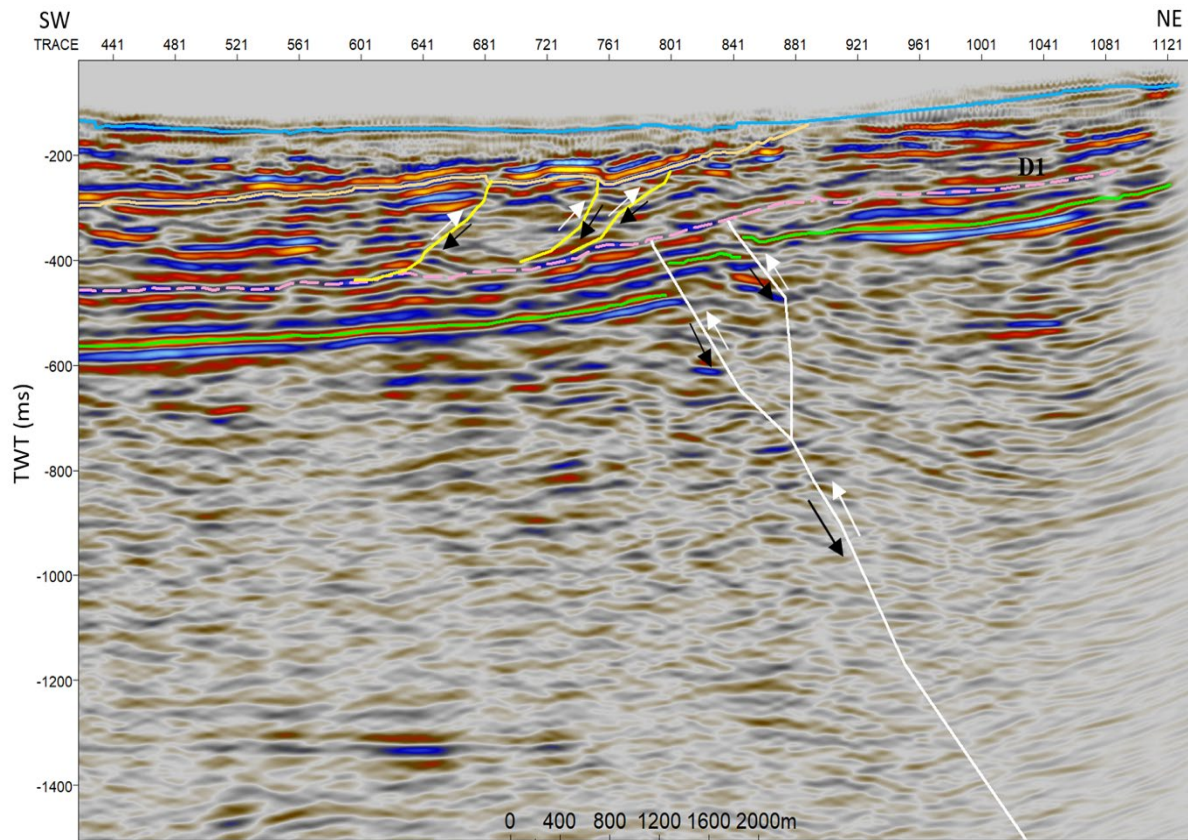
Figure 6.23: The Blomesletta Fault is interpreted as a steep east-dipping reverse fault (white), overlain by three west-dipping thrust faults (yellow) that attach to the D1 décollement along the Permian-Carboniferous strata (pink dotted line). The figure is derived from line 5.

6.4.4 Structures in Hecla Hoek

Due to an overall weak and discontinuous reflectivity pattern of the Hecla Hoek, the structural elements of the unit may be interpreted in different ways. These will be further discussed in chapter 7.2.2.4. The most likely option suggests that the basement rock is both folded and faulted. The undulating appearance of the top Hecla Hoek is interpreted as folding. Two steep east-dipping normal faults are interpreted in line 3 and 4 (Figure 6.24) with a vertical throw of ca. 600-800 ms (TWT) for the largest displacement in the SW, and ca. 250 ms (TWT) for the displacement in the NE. One reverse fault with a vertical throw of ca. 170 ms (TWT) is interpreted in line 5, displayed in Figure 6.25.
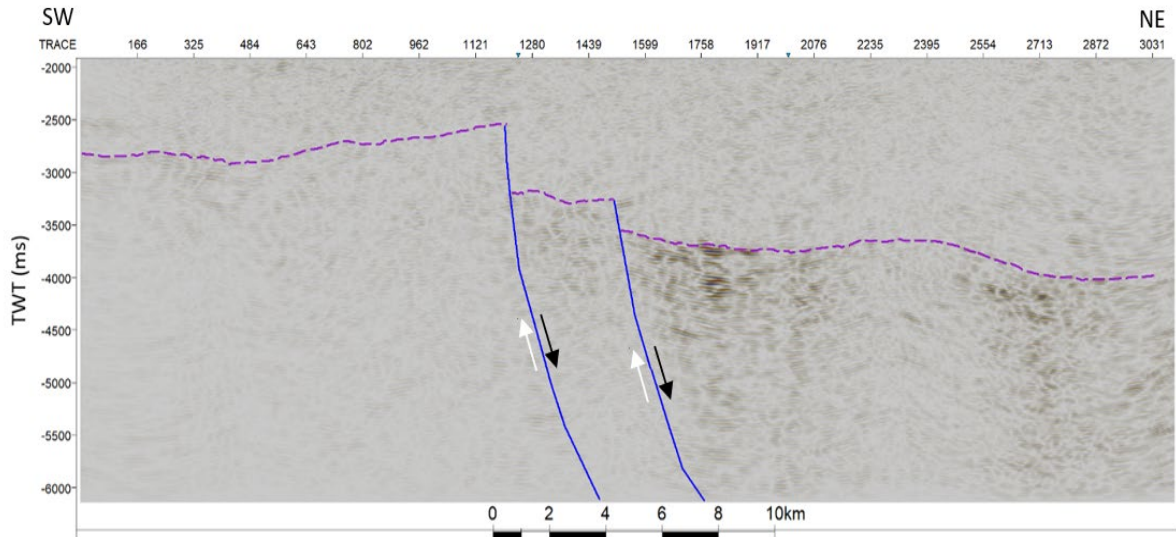
Figure 6.24: The undulating appearance of the top Hecla Hoek is interpreted as folding. Two steep east-dipping normal faults are interpreted in line 3 and 4. This figure displays the interpretation for line 3.
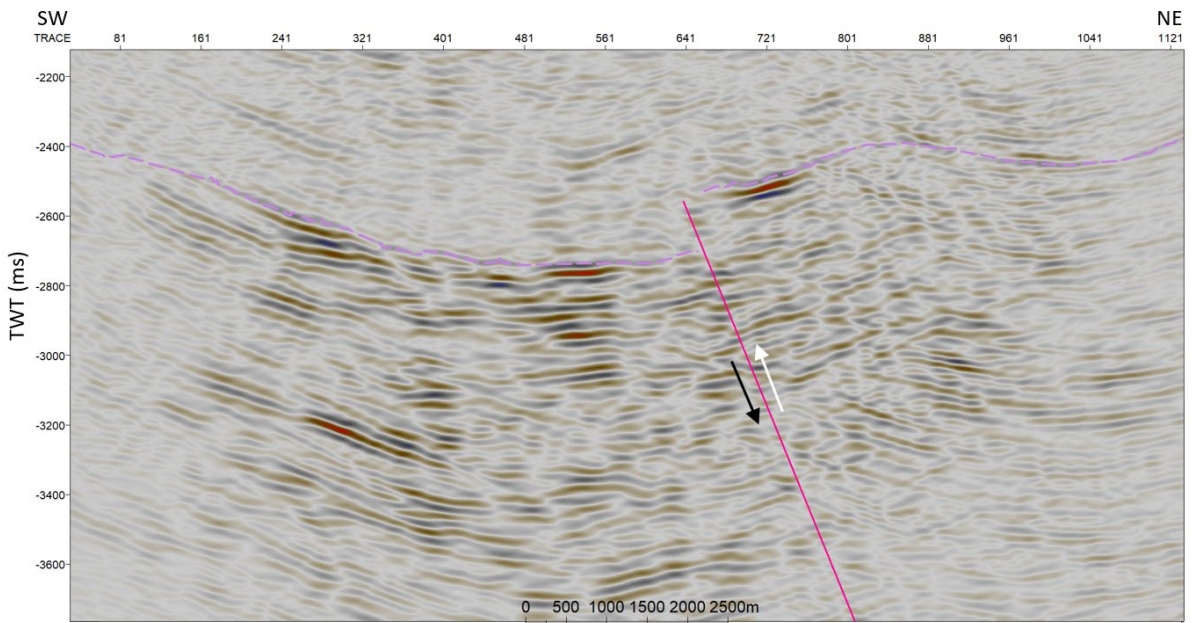
Figure 6.25: One steep reverse fault dipping in an NE direction is interpreted in the Hecla Hoek for line 5.

7 Discussion

This chapter will discuss results from the processing and interpretation separately. First, the processing will be discussed in terms of problems that were encountered, how these were resolved or how they could have been resolved. The findings from the interpretation will be discussed in relation to previous studies in the area.

7.1 Processing

7.1.1 Water-bottom multiples

Multiples are very common in marine reflection seismic and represent a challenge in processing. This is particularly the case for shallow marine data, in which the periodic relationship between primaries and multiples for small offsets give rise to short-interval multiples (Gelius & Johansen, 2010). When the seabed has abnormal high velocities, the multiple will appear stronger and more dominating in the seismic section due to the large change in AI. These two factors combined create particularly challenging seismic processing conditions, which is the case for Isfjorden. The raw data was initially dominated by multiples, and real reflection events were almost completely hidden by the strong noise and therefore not possible to deduce.

Several approaches were made to attenuate the water-bottom multiples. The process started with surface-consistent predictive deconvolution and velocity filtering. Since the multiples in the dataset appeared with a certain periodicity, the predictive deconvolution gave good results in attenuating the multiples. Some multiples were still left in the dataset, but these were largely removed by f-k filters that were applied at several stages throughout the processing sequences. F-k filters do have the potential of also removing primary reflections if the filter limits are set too high. Ultimately, this enables a "trade-off" in which some noise will be present to avoid losing real event reflections. The f-k filters were applied with the same values, except for the last filter applied just before migration. This was put with higher limits, which had a positive effect in attenuating more of the remaining noise, at the same time as it was carefully controlled that it did not remove real reflection events. All the filters were tested with several different

values to ensure that the final values gave the best results. However, to make sure that no primary reflection events had been removed from the seismic during the processing sequences, the f-k filters were not put with high limits at an earlier stage. Stacking, which exploits the velocity discrimination property, also contributed to attenuate multiples. The resulting seismic section is seemingly free from multiples and has a significantly enhanced seismic quality (see Figure 5.16).

7.1.2 Attenuated seabed reflector

Another problem encountered during the processing sequences, was a strongly attenuated seabed reflector. Prior to processing, this reflector was the strongest and most continuous in the seismic section due to the presence of total internal reflections. These are removed in processing as they cause unwanted phase shift and a large amount of NMO stretching. With a water depth of 50 m, all seabed reflections with an offset greater than 34.8 m will represent total internal reflections (see Appendix A: Estimations). These will be reduced by applying f-k filtering, but not completely removed as this filter is less effective for the smallest and largest offsets. The greater proportion of total internal reflection for the shallowest areas may hinder some seismic energy to travel through (Ruud, pers. comm). The total internal reflections may be further attenuated by NMO-stretch mute or by manual picking of muting in Teamview. If the limits of the f-k filter are reduced, this will let more of the shallow seabed reflections pass and thus enhance the reflector. However, this will also let a larger portion of refractions through (Ruud, pers. comm). Additionally, shallow areas initially suffered from the abundance of strong and short-interval multiples. When processing modules and mutes attempt to remove the noise, some real seismic events may also be removed. In turn, these areas may suffer from greater energy removal and leave a seismic section of poorer data quality.

Some traces of the shallowest seabed is completely removed. This is the case for line 4 between shotpoint number 71 and 171, which has a TWT of around 70 ms (Figure 7.1). Line 5 also suffers from this between shotpoint number 41 and 79, an area with a TWT of 80 ms (Figure 7.2). The reason for this is the lack of small-offset traces. To obtain good seismic data in shallow areas, the offset between the source and start of the streamer needs to be considerably reduced (Ruud, pers. comm). The lack of near-offset data is a common problem in conventional acquisition. A solution for this is a TopSeis acquisition survey, which incorporates an

additional source vessel that shoots directly above the middle of the towing streamers (CGG & Lundin Norway, 2017).

The energy from the seabed was tried to regain in several ways. First, an upscaling of the velocity library for the seabed reflector used in the module for external mute gave small but favourable effects (Figure 7.1). The maximum muting angle was kept to 42 degrees, as a lower angle did exclude some seabed energy, and the velocity of the sea-bottom reflector was set higher than the assumed sea velocity (commonly 1500 m/s) in the library. By using a higher velocity, the seabed reflector will not be "lifted" as much in the NMO-correction. The external mute will in this way let more seismic energy from the sea-bottom pass. This also results in less NMO-stretch, and ultimately less NMO-stretch mute. Despite a wrong stacking velocity in the NMO-correction, the seabed reflector will appear stronger since only a few traces with almost the same move-out will be stacked. A disadvantage of this method is that the sea-bottom may appear deeper than it really is (Ruud, pers. comm). The effect of this was investigated in Teamview, but did not show significant differences in depth compared to a seismic section of an unaltered water-bottom library. Since this application gave favourable effects on the seabed reflector, predominantly for the shallowest areas, it was applied for all external mute modules.
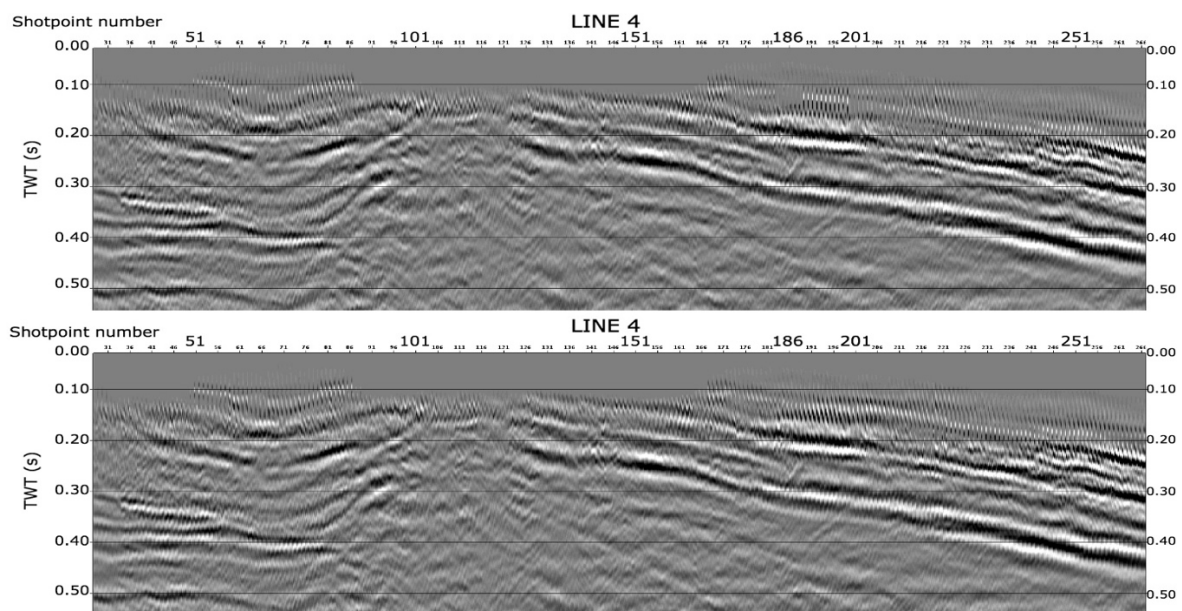
Figure 7.1: Stacked section of line 4. Higher velocities for the water-bottom reflector in the external mute module did give small but favourable effects, shown in the lower figure. The favourable effects are particularly noticeable around shotpoint number 186 in the lower figure, where the sea-bottom reflector is less "lifted up" and therefore appears stronger in the seismic section. The upper figure shows the stacked section using an unaltered velocity library for the external mute module.

Seabed energy was also restored adding a MODET module after stacking and prior to migration. This module regains seismic energy that has been lost in previous muting modules. A mute was applied afterwards to remove all energy above the water-bottom. This approach did result in improved seismic sections by restoring more of the previously missing seabed energy. However, this was not the case for the shallowest reflectors of line 4 and 5, which will suffer from the lack of small-offset traces regardless (Figure 7.2). Since this study focuses on extracting information from deeper geological structures, no more attempts were made to regain the seismic energy from the seabed.
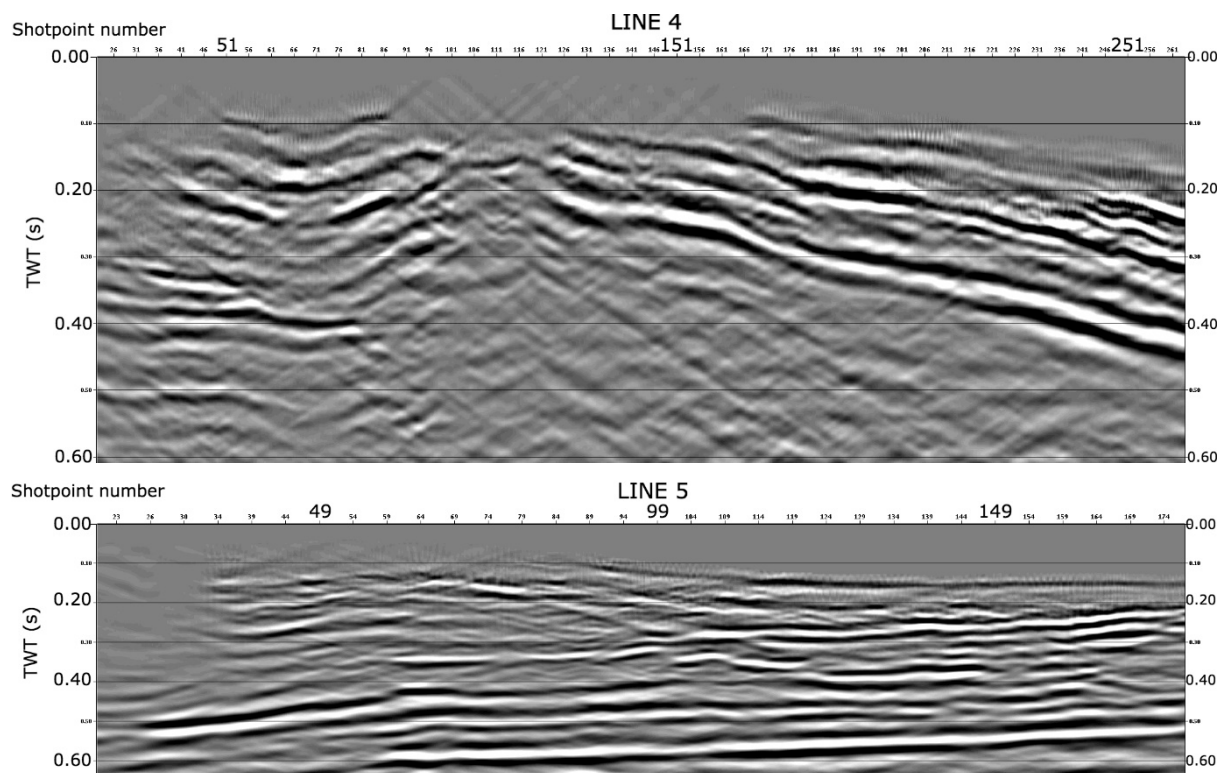
Figure 7.2: Parts of the final migrated section of line 4 (upper figure) and line 5 (lower figure), showing the seabed reflector. After several attempts to regain the seismic energy from the seabed reflector, it was not fully successful for the shallowest areas of these lines due to lack of small-offset traces.

7.1.3 Diffraction patterns

There is still some noise present in the seismic profiles after processing. Diffraction patterns appear more distinctive towards the lower part of the profiles. Several approaches have been made to attenuate this noise, including f-k filtering and amplitude recovery. Dip filtering was carefully applied to avoid removing primary seismic events, but to attenuate as much noise as possible. Due to this trade-off, the diffraction patterns are not completely attenuated in the

section, but are reduced (Figure 5.14). The filter application did however also reduce the overall sharpness of the reflectors at some minor extent. This is however not significant and will therefore not impact the interpretation process. An amplitude recovery module was applied just after migration to scale the reflectors. The bedrock reflectors were initially very strong compared to the shallow reflectors, which also amplified the diffraction noise in the deeper part of the profiles. A reverse amplitude recovery module was therefore implemented to scale down deeper reflectors opposed to shallow reflectors. This resulted in better balanced seismic sections and significantly reduced diffraction noise.

An area in the BFZ of line 3 and 4 was difficult to process, including an area in the Blomesletta Fault of line 5. For line 3 and 4, there are seismic events appearing at about 4 s that initially looked like diffraction noise. An example from line 4 is shown in Figure 7.3. Since these were identified in both lines and at about the same TWT, this is likely to represent real reflection energy. Likewise, the study by Skaara (2020) identified these seismic events in the BFZ appearing at around 3 s in a close-by seismic line. For these reasons, it is concluded that these seismic events represent real reflections that originate from a complex geological deformed zone. A similar seismic event appears at around 1 s and 3 s for line 5, which is the area of the Blomesletta Fault. These events are encircled in Figure 7.4. Since this diffraction-like noise appears similar to what is seen in line 3 and 4, these are also interpreted as real reflection events.
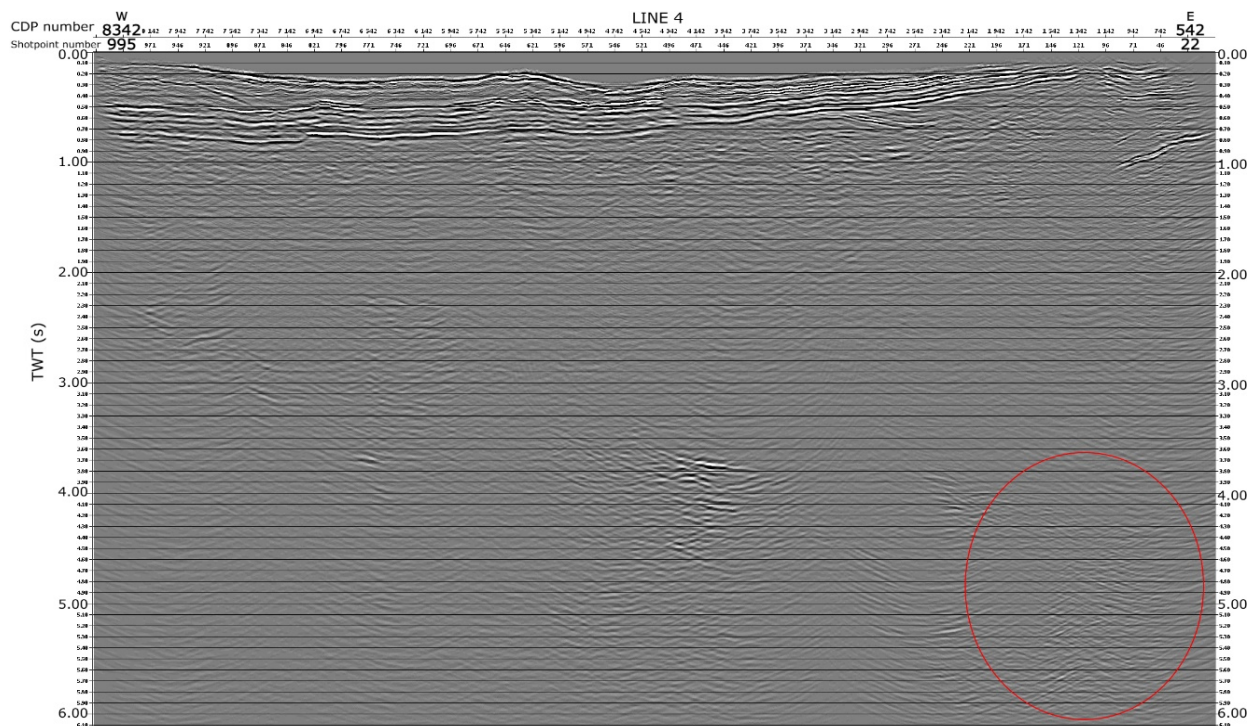
Figure 7.3: Seismic event appearing at around 4 s in the BFZ of line 4 (encircled in red) that looks like diffraction noise but is likely to represent a complex geological zone.
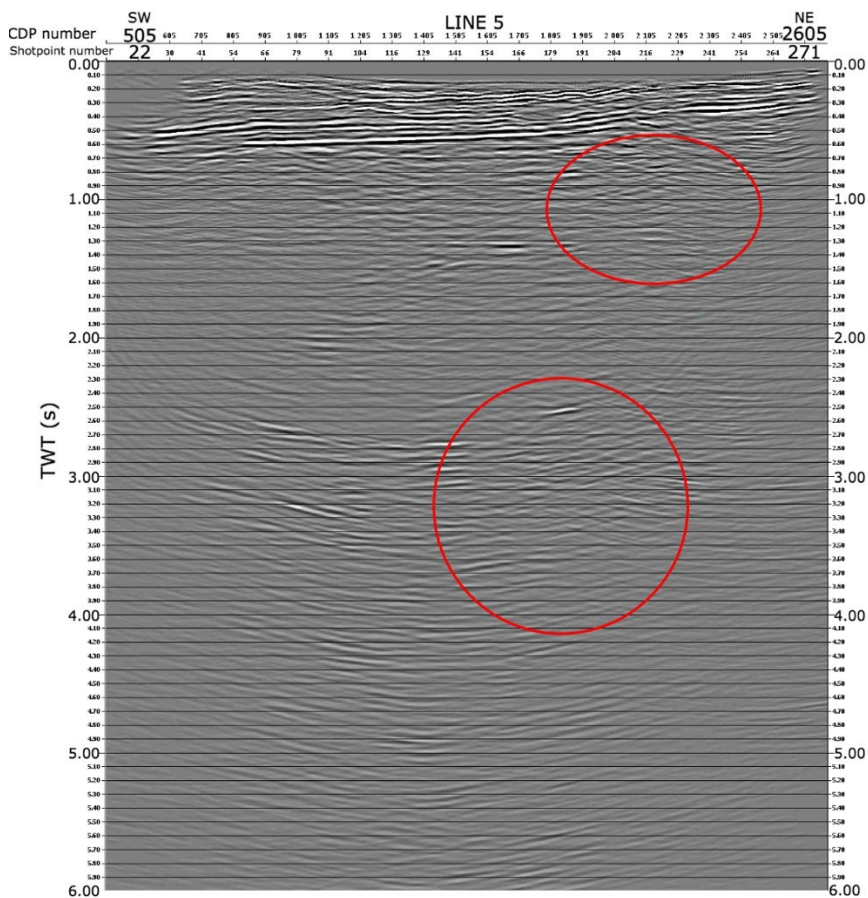
Figure 7.4: Seismic events appearing at around 1 s and 3 s in the Blomesletta Fault of line 5 (encircled in red) that look like diffraction noise but are likely to represent complex geological structures.

7.1.4 Streamer noise

Another type of noise present, is the streamer noise. This type of noise occurs when the vessel turns and is visible at the ends of a profile. Good seismic quality is not produced before the full streamer is in line behind the vessel. The start and end of a line will therefore suffer from poorer seismic data quality. It was attempted to reduce the streamer noise by applying a gradual downscaling of traces along the edges of a profile. This is illustrated in Figure 7.5 by the red lines. Despite this attempt, there is still noise present in the final migrated sections. Streamer noise and migration issues cause the deeper reflections to appear with a diffraction pattern that are "dragged out" along the edges. These do not represent real geological structures. An alternative to further reduce streamer noise would be to remove the noisy traces at the start and end of a line. However, this would also have shortened the lines (Ruud, pers. comm).
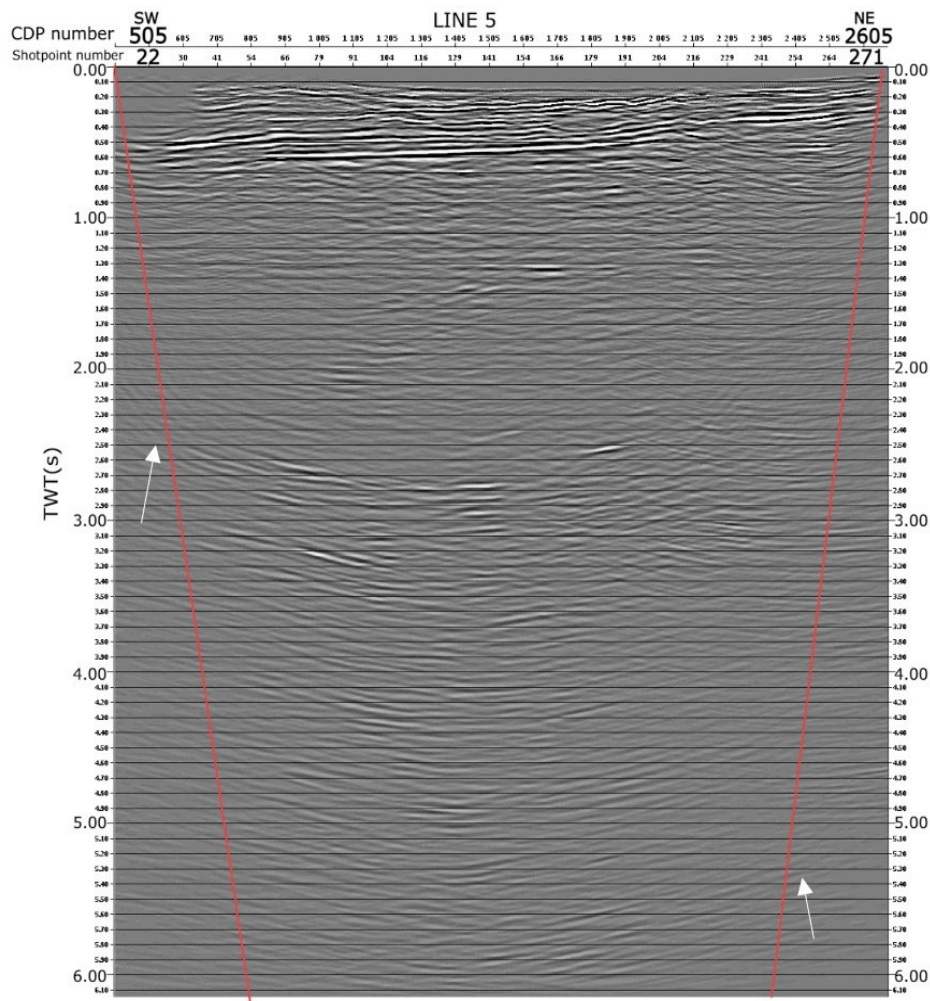
Figure 7.5: Down-scaling of streamer noise was applied for the zones indicated by the red lines. Noise is still present at the edges of the line after migration, which causes false "dragged-out" diffraction patterns in the deeper section. Examples of these are pointed out by the white arrows. The figure is derived from line 5.

During the attempts of removing noise, some primary reflections and "real events" may have been removed or attenuated as well. This could be a result of f-k filtering or muting processes that have been set "too strict". Moreover, removal of primary seismic events could occur during the velocity picking process, which is the most challenging part of processing. The larger the deviations between the real reflection velocities of a seismic event and the picked velocities, the weaker the reflections will appear in the stacked profile. An essential tool during velocity picking was up- and down- scaling of the velocity model (see Figure 5.10). If seismic events were better imaged in the stacked section with higher or lower velocities, then the velocity model was altered accordingly and stacked again. This procedure was executed until the final velocity model gave the best possible stacked seismic image, and was a crucial tool for picking correct velocities.

This study uses Kirchhoff 2D DMO-correction and post-stack migration for the final seismic images. Pre-stack migration was also attempted and compared to the results from post-stack migration combined with DMO-correction. The outcomes were very similar, but there were some larger problems with the shallow reflectors using pre-stack migration. Shallow reflectors were weaker and more muted, and generally noisier. This could probably have been improved by altering the f-k filter and the external mute module. However, as post-stack migration in combination with Kirchhoff 2D DMO-correction gave similar and satisfactory results, this method was chosen.

The seismic data quality is significantly improved. By comparing the near-trace plot from the editing sequence with the final migrated section, the noise is drastically reduced and real reflections are strong and continuous (Figure 5.16). The strong and short-interval multiples that initially dominated the seismic profiles are attenuated, and the results show significantly improved seismic sections that are possible to interpret. The results are satisfactory and the processing sequences have therefore been successful.

7.2 Interpretation

This subchapter will first present the discussion related to the sedimentary units and then present the structural interpretation. The latter includes several interpretation models, particularly for the BFZ. Both the sedimentary and structural interpretation will be discussed in relation to previous findings in the area.

7.2.1 Sedimentary units

7.2.1.1 Jurassic unit

The base of the Jurassic horizon is only interpreted in the SW part of line 3, which reaches the central part of Isfjorden (Figure 7.6). This interpretation correlates with the study conducted by Blinova et al. (2012), who identified Jurassic-Cretaceous strata in the central part of Isfjorden based on multichannel seismic data and multibeam echo sounding. Likewise, the geological map by Hjelle (1993) in Figure 2.2 indicates that this unit should be present across central Isfjorden. Based on the weak and chaotic seismic character and the first appearance of this unit, it is likely to include the low-velocity shales of the Janusfjellet formation of the lower Adventdalen Group. The unit shallows towards the NE before it is truncated by the seabed (Figure 7.7). For this reason, it is not present in any of the other lines. Décollements have been identified in the Middle Jurassic strata by previous studies (e.g., Blinova et al., 2013), but are not captured in this study due to its minimal appearance.
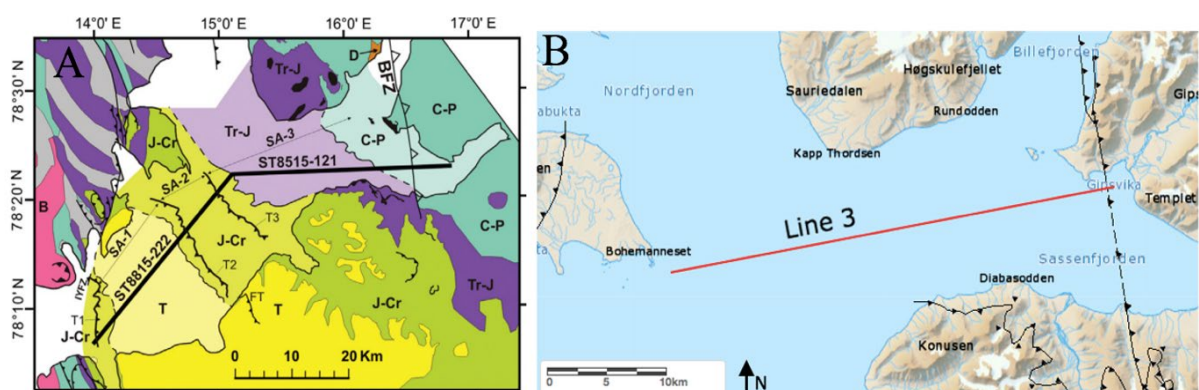
Figure 7.6: Blinova et al. (2012) identified geological boundaries beneath Isfjorden (figure A) based on several multichannel lines and multibeam echo sounding. Jurassic-Cretaceous strata was observed in an area

of Central Isfjorden, that is also covered by line 3 in this study (figure B, modified from Norsk Polarinstitutt, 2022). Note the different scales.
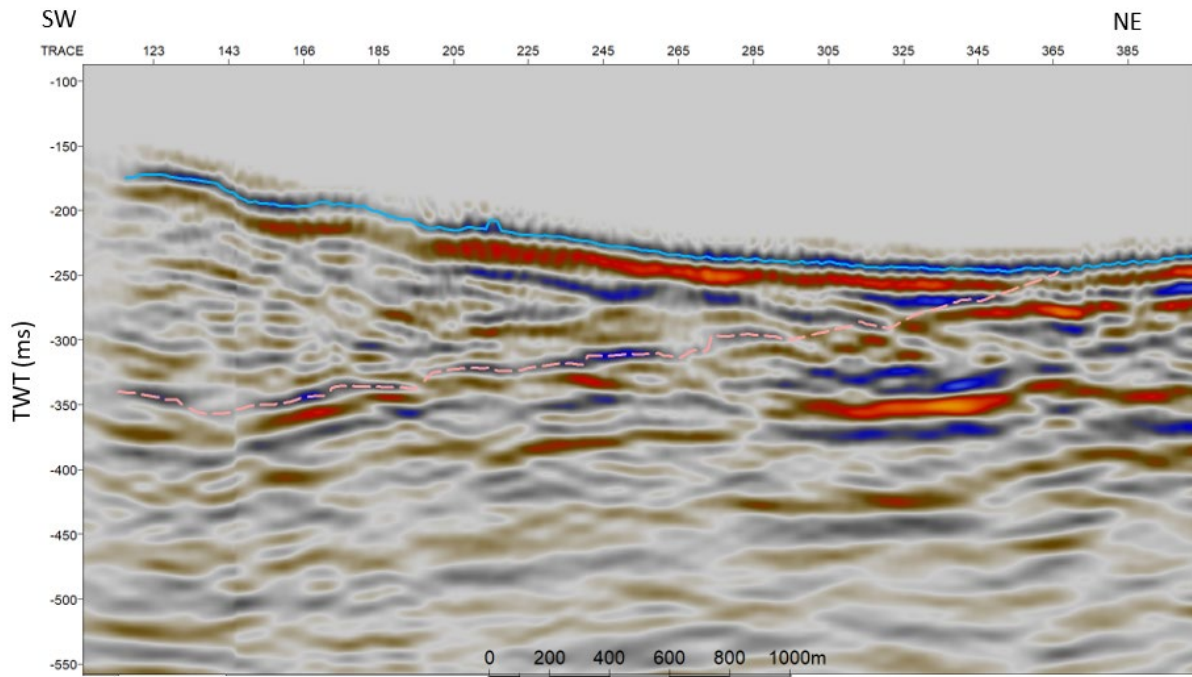
Figure 7.7: The Jurassic unit in line 3. The base Jurassic horizon is displayed as a dashed light pink line.

7.2.1.2 Triassic unit

The Triassic unit includes the sedimentary strata of the lower Kapp Toscana Group and Sassendalen Group. A lower unconformity, associated with the regional uplift during the Permian-Triassic transition (Blinova et al., 2013), distinctively separates the Triassic strata from the underlying strong and parallel Permian reflectors. Due to this uplift and erosion, the Triassic unit is not present across all lines, only in the SW part of the study area. The reflectivity pattern of the Triassic unit is classified based on the generally weak and discontinuous reflectors, but with occurrences of stronger amplitudes. This is likely to represent impedance contrasts that occur in the presence of altering sandstone and shale successions. Mesozoic sediments were deposited during stable platform conditions, varying from open marine to shelf settings (Bergh et al., 1997; Blinova et al., 2013).

A dipping reflector has been identified in the Triassic unit in line 4, indicated by the pink dotted line in Figure 7.8. The appearance of the reflector is distinct compared to the surrounding reflectivity pattern and recognised by onlaps. The reflectors within the observed structure seem to have a shallow eastward dip, while the surrounding strata has near-horizontal reflectors.

Onlaps do suggest the presence of a different stratigraphic package, deposited prior to the strata to the east. According to Dallmann (2015), Svalbard was a part of a large depositional basin during the Triassic that accumulated thick sedimentary successions. The structure could possibly occur from a submarine slide, but should be further addressed in seismic studies of Isfjorden to state with confidence.
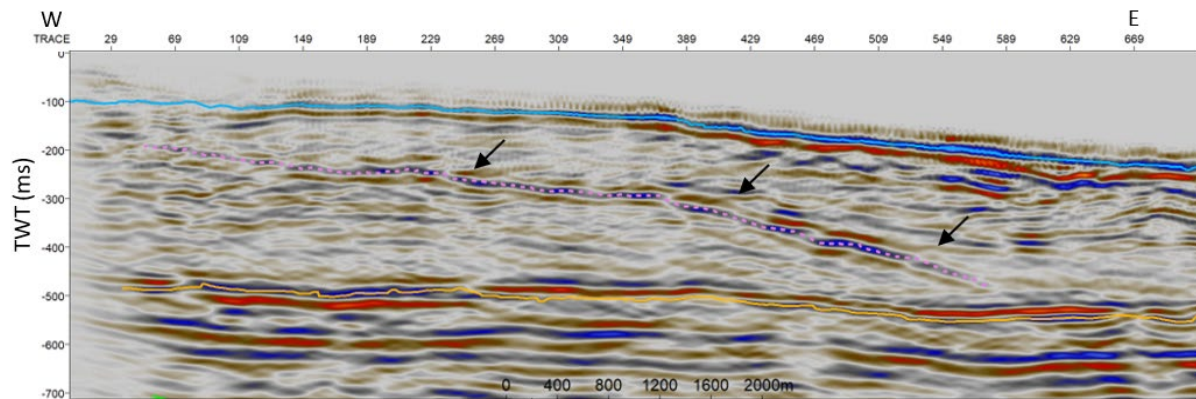
Figure 7.8: A bending structure is identified in unit 2 of line 4. The pink dotted line is plotted along this structure, which appears dominant in the profile. Onlaps are pointed out by black arrows. The orange line represents the Top Permian reflector, while the blue line represents the seabed reflector.

7.2.1.3 Permian and top mid-Carboniferous unit

This unit, comprising parts of the Tempelfjorden Group and Gipsdalen Group, is identified based on strong, continuous and parallel reflectors that are bounded by an overlying and underlying unconformity. Particularly the top mid-Carboniferous unconformity is easy to identify in the presence of an underlying angular unconformity, displayed in Figure 7.9. The strong reflectors occur due to the presence of carbonites and evaporites (Blinova et al., 2013). This results in a large impedance contrast to the overlying and underlying sedimentary units. The parallel reflectors indicate that deposition occurred during stable conditions (Bergh et al., 1997; Dallmann, 1999).
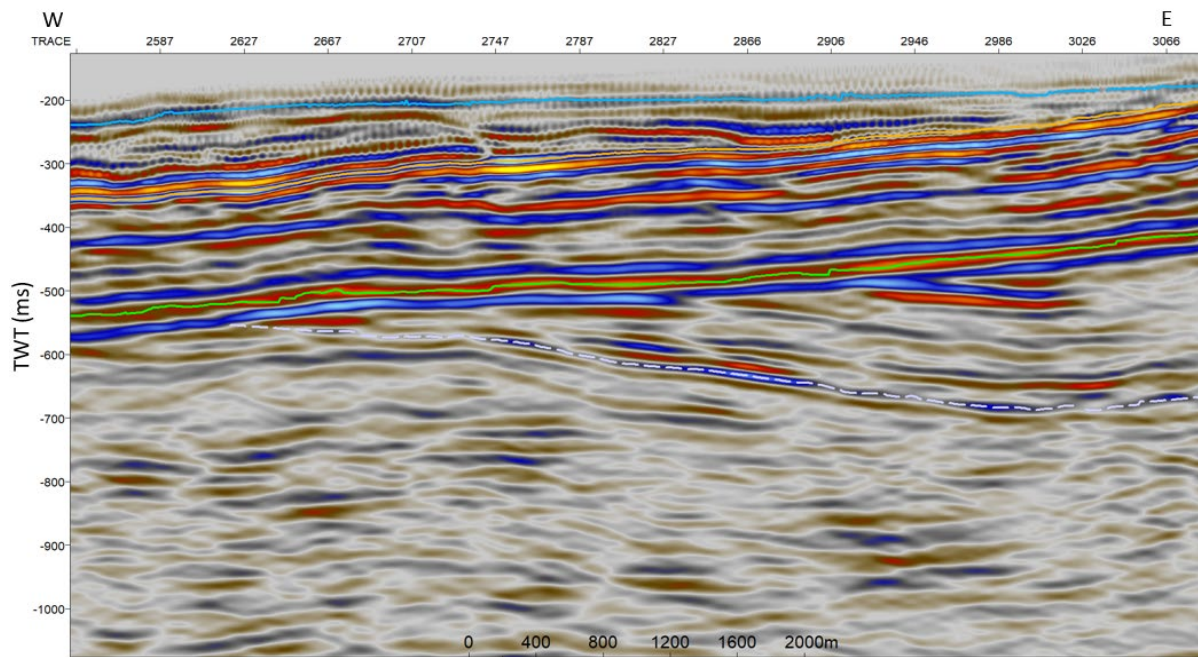
Figure 7.9: The underlying BFZ horizon (purple) is truncated by the top mid-Carboniferous horizon (green), which forms an angular unconformity that is distinct in the seismic. Displaying the western side of the BFZ in line 4.

The Permian and top mid Carboniferous unit is present in all lines. It is deepest in the SW and becomes gradually shallower towards the NW over the BFZ, where the top Permian reflector is truncated by the seabed. Svalbard experienced a great extent of uplift and erosion during the Cretaceous (Worsley, 1986), recognised from the dipping reflectivity pattern. All strata identified above the top mid-Carboniferous reflector have a similar trend. They become gradually shallower towards the NE and over the BFZ. The structure in the seismic resemble an anticline where the uppermost strata is eroded above the hinge, displayed in the figure below.
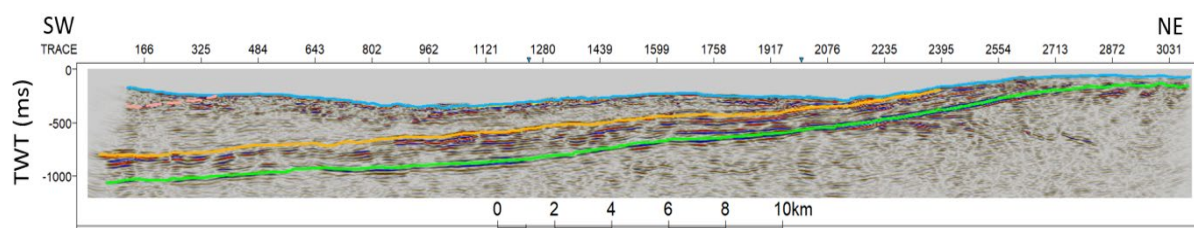
Figure 7.10: All strata above the top mid-Carboniferous horizon (green), which include the top Permian (orange) and base Jurassic (blush) horizon, are shallowing towards the NE and over the BFZ. Only the base of the Permian and top mid-Carboniferous unit is present above the fault zone, while the younger strata are truncated by the seabed. The structure resembles an anticline in the seismic. The figure is derived from line 3.

113

7.2.1.4 Devonian unit

This unit incorporates the Devonian sedimentary unit, which overlays the crystalline basement rock of Hecla Hoek. The unit is thickest along the BFZ in the E-NE, as the top Hecla Hoek horizon is interpreted to appear at greater depth due to normal faulting, and is thinning towards the W-SW (Figure 7.11). This west-ward thinning is found in several previous studies, including Skaara (2020) and Ågesen (2021). Similar to the findings in this study, Bergh et al. (1997) and Bælum & Braaten (2012) found a gradual subsidence in the eastern part of Isfjorden, reaching around 4 s at the deepest within the Nordfjorden block east of BFZ. The thick Devonian "Old-Red Sandstone" was deposited during the extensional collapse of the Caledonian Orogeny (Bælum & Braathen, 2012; Dallmann, 2015). Eroded sediments from the newly formed mountain chain accumulated in a major graben structure within the basement in the NW Spitsbergen, and was later exposed to contraction during the "Svalbardian phase" of the Late Devonian (Blinova et al., 2013).
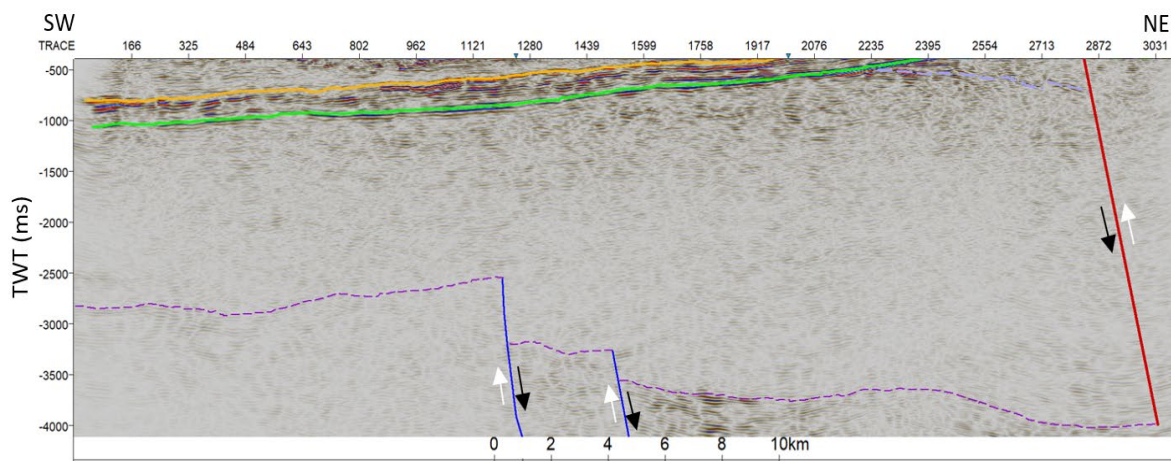
Figure 7.11: The figure shows the interpretation of the Devonian unit for line 3. A gradual subsidence of the Devonian unit to the E-NE is caused by normal faults (blue) in the underlying basement rock (dark purple). The top-mid Carboniferous reflector (light green) and the BFZ horizon (light purple) lie above the unit. The major reverse fault (red) in the NE is a part of the BFZ.

The package of the Devonian sandstones varies between chaotic to nearly transparent. The sequence of fine-grained sandstone does not have significant velocity contrast, which results in lack of strong reflectors (Bælum & Braathen, 2012). However, this study has identified appearances of stronger amplitude reflections in the upper Devonian unit (Figure 7.12). This corresponds to the finding by Ågesen (2021), who identified the presence of these at approximately the same depth and location. Bælum & Braaten (2012) identified an additional

sedimentary package of Late Carboniferous to Early Permian age to overlie the Devonian sandstone west of BFZ, as the first post-rift deposit. In such, this may suggest the presence of different sedimentary strata in the upper section of the Devonian unit. However, stronger upper reflectors relatively to deeper reflectors could also simply occur due to amplitude decay with increasing depth.
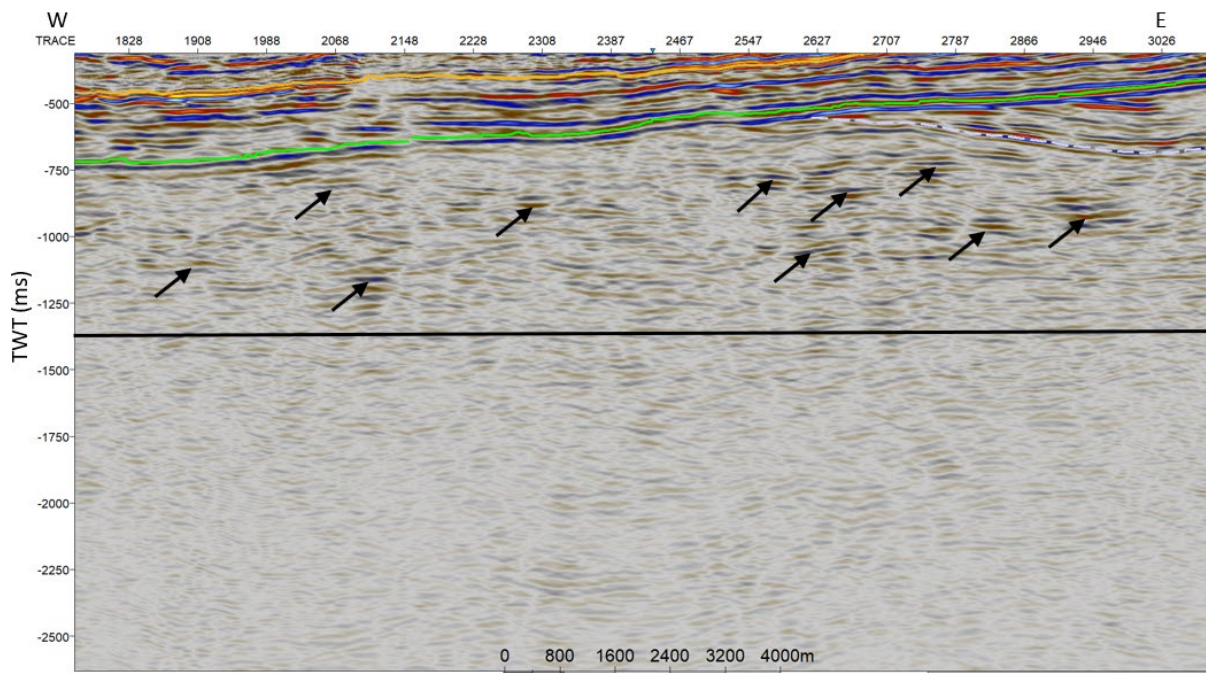
Figure 7.12: The upper part of the interpreted Devonian sandstone package (above the black line) appears with stronger reflectors than the lower section, which consists of chaotic and almost transparent reflectors. Some of the strong reflectors in the upper part are pointed out by the black arrows. This may signalise the presence of another sedimentary package of Late Carboniferous to Early Permian. The figure is derived from line 4.

7.2.2 Structural interpretation

7.2.2.1 Stratigraphy and structures in the BFZ Trough

This unit is recognised as The Billefjorden Trough, as it is only identified along the BFZ in line 3 and 4, above the BFZ horizon. The horizon is recognised by some strong downward-bending reflectors towards the fault centre, where they abruptly vanishes. The thickest section of the group is interpreted over the central BFZ. Due to very weak reflectors in the central fault zone, there is a large uncertainty attached to the interpretation in this location. The western horizon shows a distinct toplap onto the top mid-Carboniferous unconformity (see Figure 7.9),

also identified by Ågesen (2021). The sedimentary filling is however less pronounced on this side of the fault, with overall chaotic and discontinuous reflectors. The study by Bælum & Braathen (2012) does not acknowledge the presence of an angular unconformity to the west of the BFZ. An angular unconformity above the Devonian unit and below the Carboniferous-Permian evaporites was however identified by Bergh et al. (2011) in the SW of Svalbard. This was linked to Middle to Late Carboniferous rifting that produced rift-fill basins, found to occur at the same time as the eastern Billefjorden Trough was deposited. This may thus suggest that the western Billefjorden Trough also was deposited during Mid- to Late Carboniferous rifting.

The eastern sedimentary package forms a half-graben structure and is divided into reflective packages, shown in Figure 7.13. A distinctive wedge-shaped fill geometry is identified in the second package above the BFZ horizon, similar to the findings by Bælum & Braathen (2012). These geometries correspond to syn-rift extensional movement and the development of accommodation space. The wedge shape geometry suggests significant fault slip rates (Bælum & Braathen, 2012). Previous studies suggest that these west-dipping half-grabens were deposited during a phase of major crustal extension in the Early Carboniferous (Bergh et al., 1997; Bælum & Braathen, 2012). Additionally, a minor normal fault is interpreted within the lower part of the half-graben, which supports the presence of extensional forces. Braathen et al. (2011) argues that normal-sense movement along the eastern fault-stand has controlled the sedimentation. The wedge-shape in the half-graben could also suggest that the rift-basin has experienced some inversion, due to minor lifting. This is illustrated in the figure below.
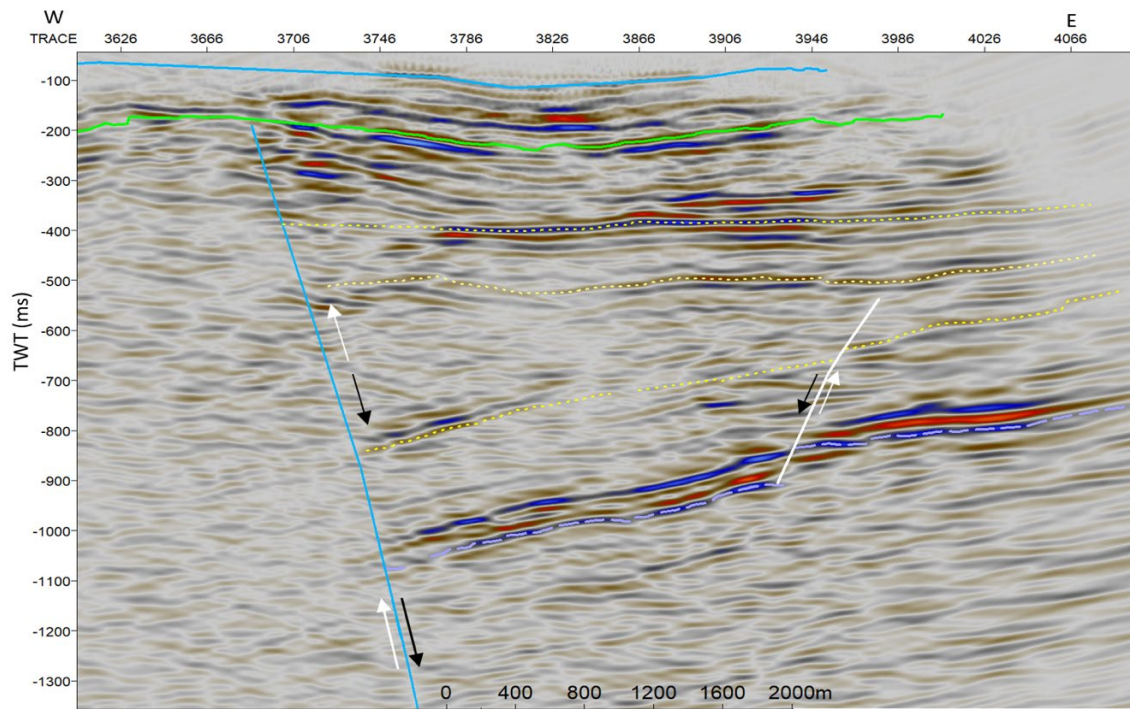
Figure 7.13: A distinctive half-graben is identified along the eastern Billefjorden Fault stand, and is divided into reflective packages (yellow) that were deposited syn-rifting. The wedge shape in the second stratal package above the BFZ horizon (purple), suggest significant fault slip rates and minor inversion. A normal fault within the half-graben support indicates the presence of extensional forces. The green line represents the top mid-Carboniferous horizon.

7.2.2.2 Structural models of the BFZ

Research connects the initial formation of the BFZ to transpression and sinistral strike-slip movement during the Caledonian Orogeny (e.g., Bælum & Braathen, 2012), which is widely accepted based on field data (e.g., Gee & Page, 1994). During the late-post-Caledonian times, the North Atlantic and Arctic region is believed to have undergone transtension deformation and extension (Krabbendam & Dewey, 1998). Scientists generally agree on the establishment of an extensive Devonian basin in the NW Spitsbergen during the collapse of the orogeny. During the formation of the WSFTB in the Tertiary, compressional forces reactivated the BFZ, along with uplift and erosion along the western part of Svalbard (Bælum & Braathen, 2012). In the present-day, the Devonian sandstone juxtaposes the Hecla Hoek to the east of the BFZ, identified from outcrop studies (e.g., Braathen et al., 2011, Maher & Braathen, 2011). The structural reasoning for this is however controversial. This section will therefore propose interpretation options of the BFZ in accordance with previous research and discuss the potential of these.

117

The BFZ runs almost straight N-S and is present in the eastern corner of line 3 and 4. The BFZ is a geological complex area. The reflectivity pattern is weak, discontinuous and chaotic, and almost transparent in some parts of the fault zone. There is little to no clear displacements in the seismic, which makes it particularly difficult to establish a structural interpretation model with confidence. Several interpretation options may therefore apply. This study will include three possible models of the BFZ. First, a positive flower structure model will be discussed (Figure 7.15), which forms in a restraining bend of a transform system (Figure 7.14). The possibility of a supra-detachment basin will be discussed in relations to the Hornelen Basin of SW Norway (Figure 7.16 and Figure 7.17), in which normal faults root in a detachment within the fault zone (Figure 7.18 and Figure 7.19). The final interpretation model suggests the presence of an extensive reverse fault and a normal fault (Figure 7.20 and Figure 7.21), and also discusses the possibility of a deep-level décollement to the west of the BFZ (Figure 7.22 and Figure 7.23).

7.2.2.2.1 Strike-slip model

The strike-slip regime that formed the BFZ is related to the large-scale structural trend in the North Atlantic during the Caledonian Orogeny (Figure 2.3). This system is also believed to have formed the Hornelen basin of western Norway (Fossen, 2010). A strike-slip model of the Hornelen basin was supported by Steel (1976) and Steel & Gloppen (1980). As the BFZ do not form a straight N-S line, this may suggest that transpression or transtension have occurred along the fault zone. Strike-slip faults form characteristic flower structures in cross-section view, in which faults zones split and widen upwards (Fossen, 2010). Depending on the fault geometry, a positive or negative flower structure will form. Strike-slip zones are associated with high-angled faults, which are commonly poorly imaged in seismic and consequently also difficult to interpret. Positive flower structures are associated with reverse faults, but also normal faults or folds, while negative flower structures commonly form a depression of normal faults (Fossen, 2010).

Interpretation option 1 (Figure 7.15) includes a positive flower structure of the BFZ, formed in a transpressional regime. A schematic illustration of the characteristics of this structure is given in Figure 7.14, which shows that the sediments are compressed and build upwards. The interpreted model consists of steep reverse and normal faults, bounded by two main faults that

gather towards the centre. The reverse faults can be connected to the contractional regime during the Caledonian Orogeny, while the normal faults can possibly be connected to the extensional post-orogenic collapse. The model forms an apparent anticline above the BFZ, which is characteristic of a positive flower structure.
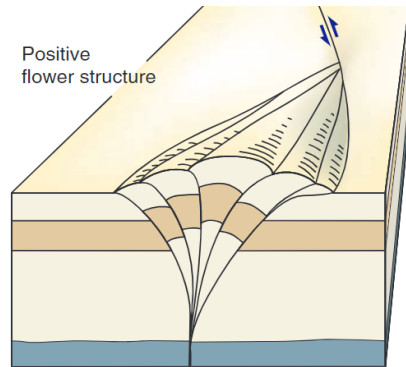
Figure 7.14: A schematic illustration of a positive flower structure that forms in a restraining bend of a strike-slip fault (Fossen, 2010).
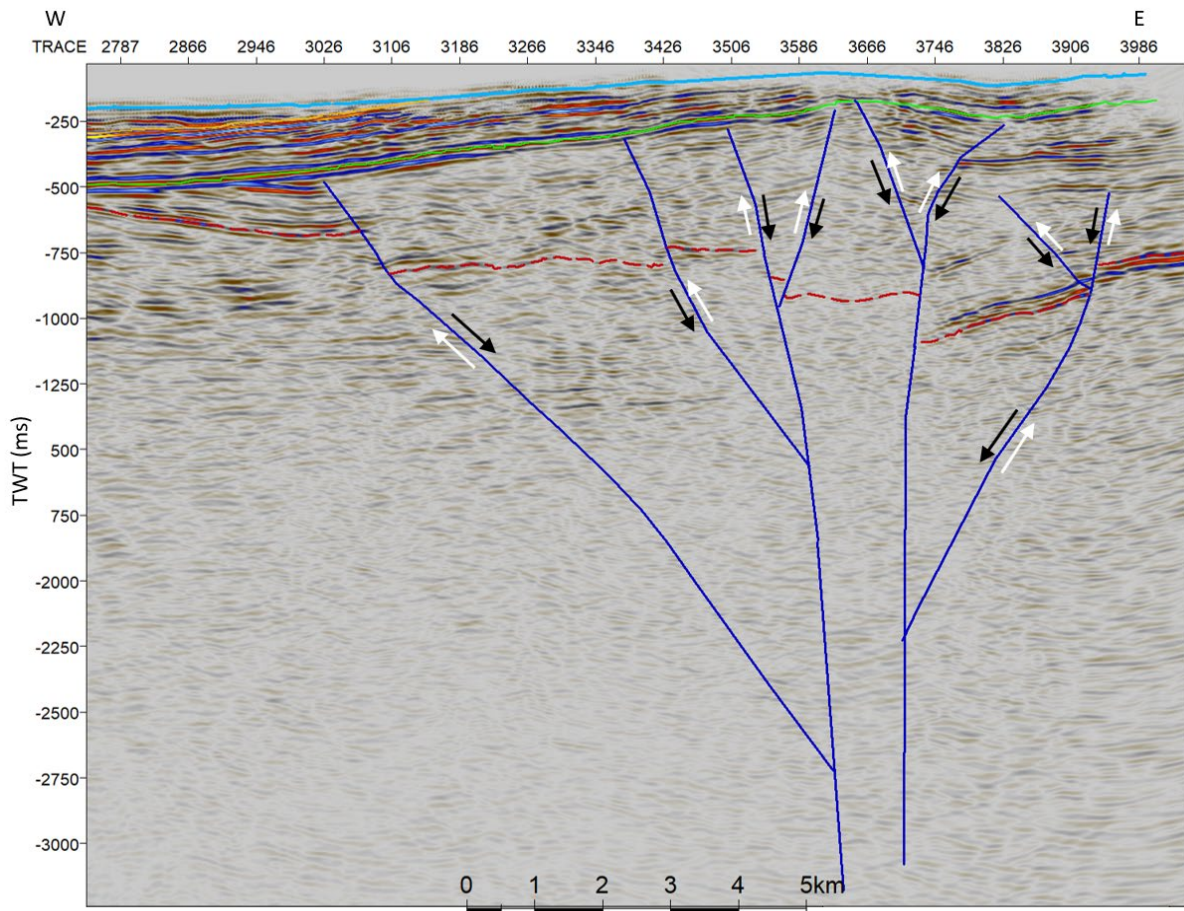
Figure 7.15: A positive flower structure interpretation option of the BFZ for line 4. Faults spring out from two main fault stands. The structure forms an apparent anticline above the fault zone, which is characteristic of a positive flower structure. The red dotted line represents the BFZ horizon.

The steep fault planes of a positive flower structure are poorly imaged in seismic, which represents a weakness of this model. Consequently, this model will be difficult to establish with confidence. In addition, a coexisting model is difficult to derive in line 3. It would therefore be necessary to perform a seismic survey that can capture the steep fault zones in order to further investigate this interpretation option. For these reasons, this model is not considered likely to represent the BFZ.

7.2.2.2.2 Supra-detachment (scoop) model

A more recent study by Braathen et al. (2017) conducted in the NW of the BFZ suggests the formation of a supra-detachment basin during the Late Silurian to Mid-Late Devonian extensional collapse of the Caledonian Orogeny, which separated the Devonian unit from the underlying metamorphic basement. Vetti & Fossen (2012) describe supra-detachment basins as "hanging-wall basins that has formed along the listric breakaway zone of a major detachment system in response to extensional tectonics". The Keisarhjelmen detachment in Svalbard is thought to have formed an extensional detachment of minimum 50 km horizonal separation. The basin consists of southern rotated beds with N-S displaced normal faults that terminate against a brittle tectonic contact in the core complex (Braathen et al., 2017).

Braathen et al. (2017) draw strong connections between the Keisarhjelmen detachment and the extensional collapse detachments of the Scandinavian Caledonides. Crustal scale extension dominated in the North Atlantic during the Silurian-Devonian times, and it has been suggested that the Keisarhjelmen formed in a similar manner to the supra-detachment basins along the coast of Norway (Figure 7.16) (Braathen et al., 2017). The scoop-shaped Hornelen Basin of SW Norway is argued to represent a supra-detachment basin that formed in the hanging wall of a major Devonian extensional shear zone (Vetti & Fossen, 2012). Braathen et al. (2017) suggest that this could represent an analogue for the Keisarhjelmen detachment. A schematic illustration of the Hornelen basin formation is given in Figure 7.17.
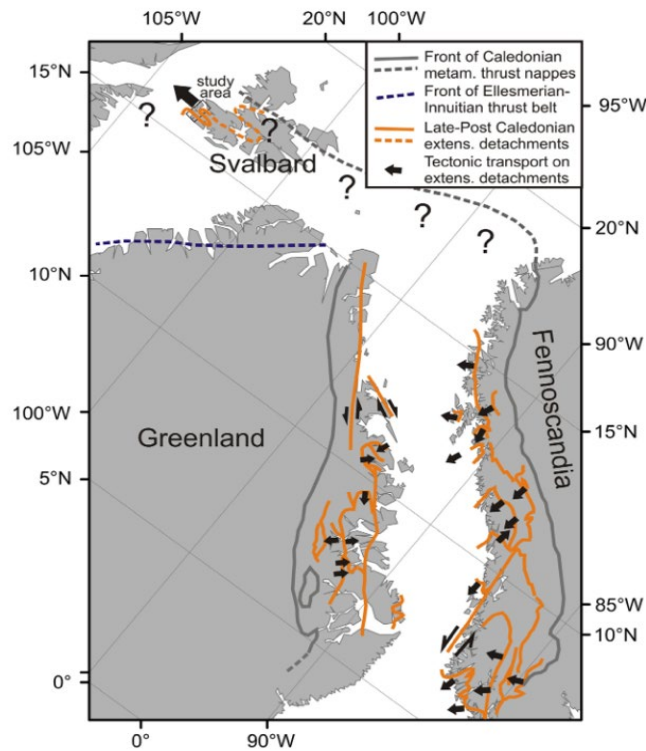
Figure 7.16: Reconstruction of the North Atlantic at 400 Ma. Late-post-Caledonian times involved the formation of extensional detachments and tectonic transport of their hanging wall nappes (Fossen, 2010).
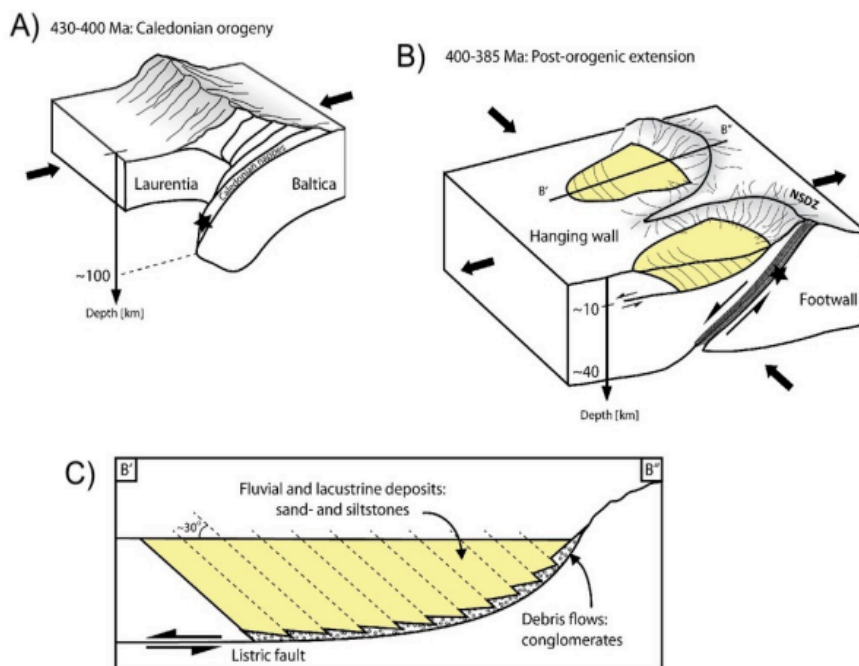
Figure 7.17: An illustration of the formation of the Hornelen basin of SW Norway. After the Caledonian Orogeny (A), the area experienced post-orogenic collapse and extension (B) that formed a scooped-shaped basin along a detachment surface (C). The figure is derived from Skaara (2020).

The structural trend of extensional detachments in the North Atlantic during the late-post-Caledonian times parallels to the BFZ (Figure 7.16). Ultimately, a supra-detachment model may be derived to explain the fault zone. Figure 7.18 displays the interpreted scoop-shaped model of the BFZ in line 4, which consists of at least three steep normal faults that root in a shallow-dipping décollement. The model stretches across the BFZ and shallows out of the study area to the east. The interpreted faults can be correlated with the supra-detachment geometry, which commonly includes steep normal faults. Furthermore, it coexists with the findings by Skaara (2020) and Ågesen (2021), who also suggested the presence of a supra-detachment basin along the BFZ, reaching about 1500 ms (TWT).

The model was then interpreted for line 3, which includes two steep faults above a detachment zone (Figure 7.19). The rest of the fault zone is not present in the line. Opposed to the faults interpreted in line 4, line 3 includes a western reverse fault and an eastern normal fault. Skaara (2020) also interpreted a few reverse faults within the supra-detachment modes that attached to a shallower décollement. Due to particularly weak reflectors within the BFZ in this study, this could be a possibility in this model as well.
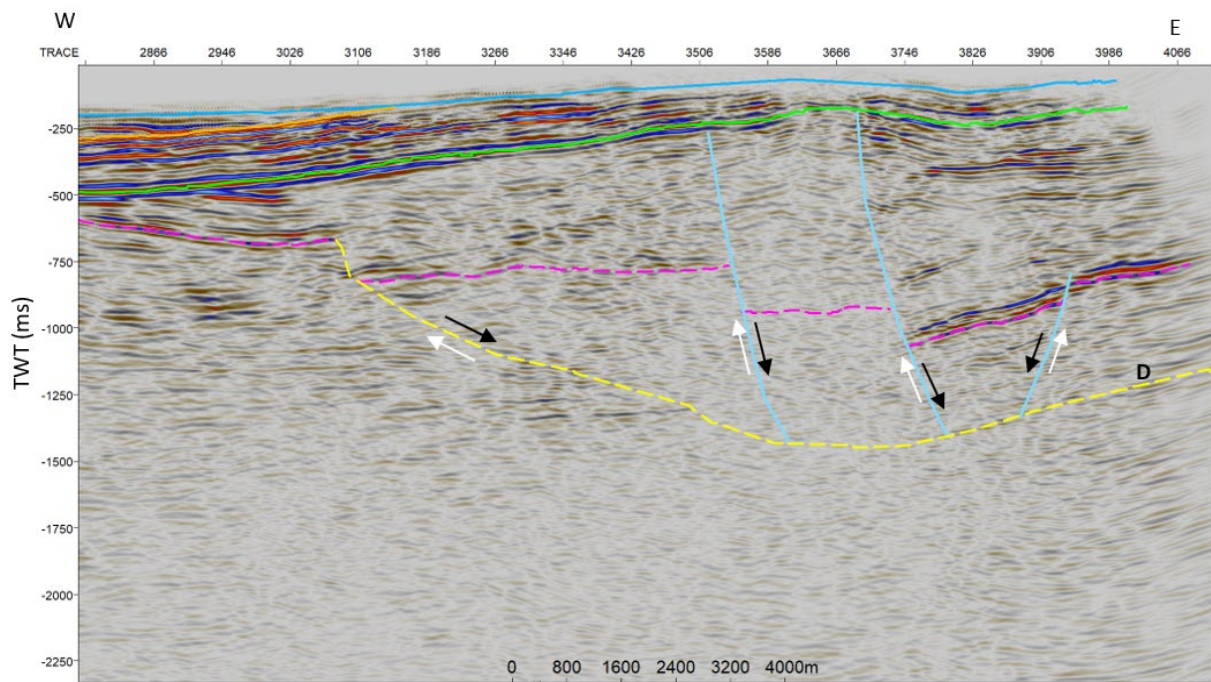
Figure 7.18: The second interpretation option of the BFZ is a supra-detachment model. Three normal faults (light blue) are interpreted to root in a detachment zone in line 4 (yellow dotted line).
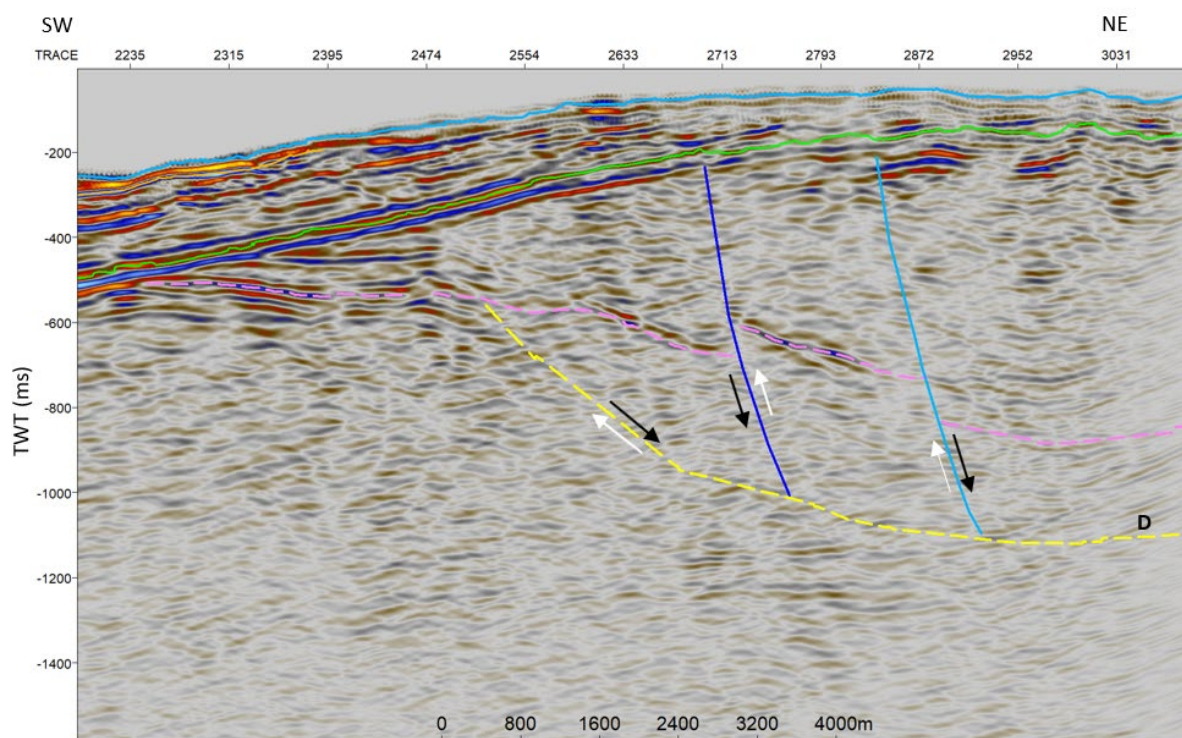
Figure 7.19: The supra-detachment model for the BFZ in line 3. The western fault (blue) appears as a reverse fault, while the eastern fault (light blue) is interpreted as a normal fault.

There are however several weaknesses of this model. First, it is difficult to correlate with the distinct N-S trending and west-dipping half-graben on the eastern side of the BFZ (see chapter 7.2.2.1 and Figure 7.13). The scoop-model by Braathen et al. (2017) rather assumes southern rotated normal faults along the detachment zone. Second, the chaotic and discontinuous reflectors around the BFZ make it particularly challenging to derive a detachment zone with confidence. Another counteracting point is that the study by Braathen et al. (2017) suggests a supra-detachment that includes the whole Devonian unit, and is therefore probably much larger than the derived scoop-model around the BFZ. It is challenging to derive a coexisting model due to almost transparent reflectors in the deeper section of the Devonian unit. For these reasons, the supra-detachment model is not included in the final results to represent the BFZ. Further research and higher seismic quality data is necessary.

7.2.2.2.3 Major reverse faulting of the basement and a possible deep-level décollement

Several previous studies have discussed the presence of a major east-dipping reverse fault in the BFZ that displaced the metamorphic basement in the east against the major half-graben Devonian basin in the west (Lamar et al., 1986; Braathen et al., 2011; Bælum & Braathen,

2012). The study by Lamar et al. (1986) suggests that the BFZ was not exposed to further large-scale strike-slip faulting after the deposition of the "Old Red" sandstone, but rather underwent a pre-Carboniferous reverse-slip. They link the E-W crustal shortening to the gentle dip of the individual faults stands and identified patterns of folds and thrusts in the pre-Carboniferous strata. Bælum and Braathen (2012) identified three major east-dipping fault stands in the BFZ, the Odelfjellet Fault, the Drønbreen Fault and Balliolbreen Fault. In the Isfjorden area, they recognised the presence of a major western reverse fault (Drønbreen Fault) and an eastern normal fault (Balliolbreen Fault) and connected these to outcrop findings in the Billefjorden and Pyramiden area (see Braathen et al., 2011). Outcrop studies show complex patterns of smaller faults and rotated fault blocks between the major fault stands. Previous studies (e.g., Braathen et al. 2011; Bælum & Braathen, 2012) state that there is no evidence for Devonian rocks on the eastern side of the BFZ and correlate this with the lack of Devonian rocks from outcrop studies in the north (e.g., Maher and Braathen, 2011).

The findings by Bælum & Braathen (2012) can be closely linked to this study. The interpretation model, displayed in Figure 7.20 (line 4) and Figure 7.21Figure 7.23 (line 3), includes a major reverse western fault and an eastern normal fault, both dipping steeply to the east. The reverse fault is consistent with the shallow basement in the east, identified in previous studies (e.g., Braathen et al. 2011). Braathen et al. (2011) suggest that the fault occurred in the Late Devonian, as the basement rocks are juxtaposed by the Devonian unit. The interpretation of an eastern normal fault is consistent with the identified half-graben structure and its wedge-shaped fill geometry, discussed in chapter 7.2.2.1. This fault is argued to first have been reactivated as a normal fault during the late-post-Caledonian collapse, then in subsequent tectonic events, such as during the Carboniferous extension (Braathen et al., 2011). The normal fault within the half-graben supports the presence of extensional forces. Faults are also interpreted along the BFZ horizon in the western basin. These are identified on the basis of reflector displacements, which are challenging to pinpoint with confidence in this area. Due to weak and chaotic surrounding reflectors, both dipping directions may be realistic. If the faults formed in correlation with the half-graben to the east, during Early Carboniferous extension, they could dip towards the east and form predominantly normal faults. One reverse fault is also interpreted in line 3. The BFZ area has repeatedly been exposed to both compressional and extensional forces over millions of years (Dallmann, 2015), meaning that it is likely that both normal and reverse faults are present.

No structures are interpreted within the BFZ due to the weak reflectors. A structurally complex area combined with the low resolution of a 2D seismic image makes it particularly difficult to locate structures or stratigraphic units between the two fault stands. This model rather assumes a complex area of smaller faults and rotated fault blocks, identified from outcrop studies (Braathen et al., 2011), that is not captured by the seismic.
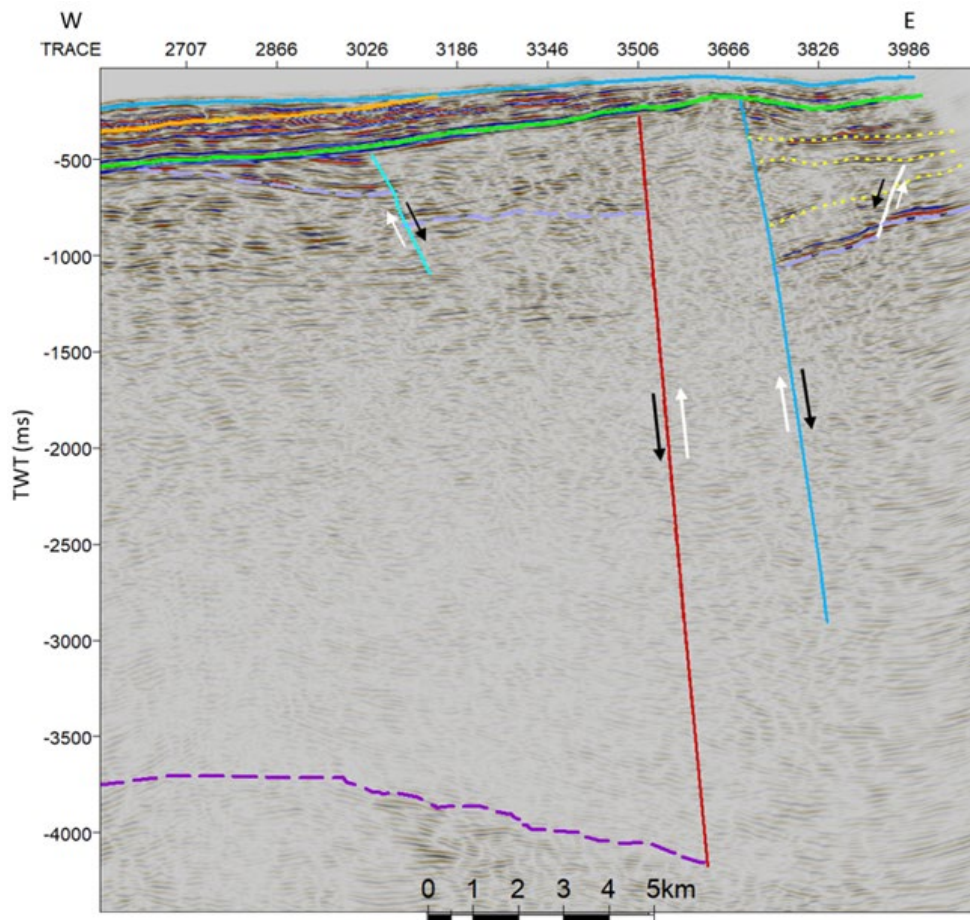
Figure 7.20: The third interpretation model of the BFZ is considered the most likely. The model includes a major reverse western fault (red) that displaces the basement rock, and a normal eastern fault (blue), both dipping to steeply to the east. A distinct half-graben structure of different stratal packages (yellow) is present along the eastern fault, and is displaced by a normal fault (white). An east-dipping normal fault (turquoise) is interpreted in the western basin, along the BFZ horizon (light purple). The figure displays line 4.
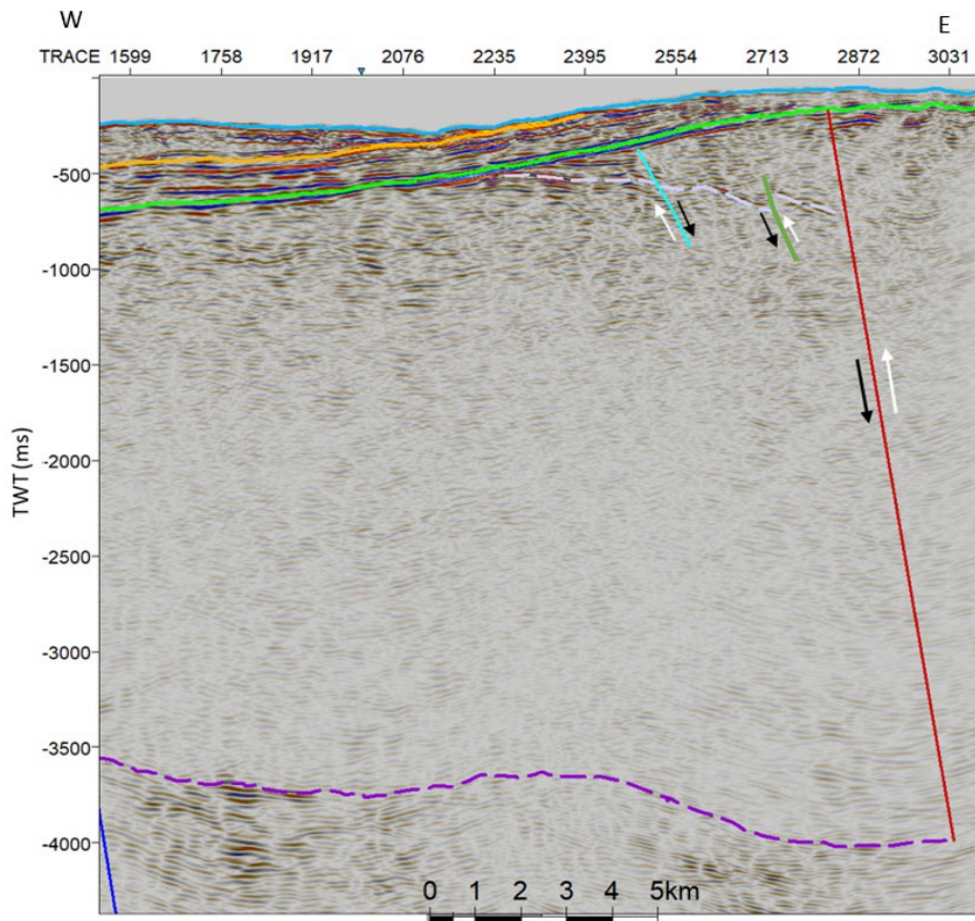
Figure 7.21: The third interpretation model, showing line 3, includes a major reverse fault (red) and two minor faults in the western basin. These are interpreted as a normal (turquoise) and a reverse fault (green). The light purple dotted line represents the BFZ horizon.

Another interpretation option of this model is the presence of a deep-level detachment zone, displayed in Figure 7.22 (line 4) and Figure 7.23 (line 3). As previously discussed, the upper part of the Devonian package appears with stronger and more continuous reflectors compared to the lower section, which consists of the characteristic weak and almost transparent "Old-Red" reflectors (see 7.2.1.4). Bælum & Braathen (2012) did suggest the presence of additional stratigraphic units between the top-mid Carboniferous unit and the Devonian Sandstone in a close-by line. Given these observations, the upper section of the interpreted Devonian unit could represent another younger sedimentary package, possibly of Carboniferous age. The detachment zone is interpreted along this strata. A study conducted by Bergh & Andersen (1990) did suggest the existence of deep-level décollement zones in areas of substantial Carboniferous basin fill material, in correlation with observations of lithological variations in the Carboniferous strata in the west and north of Svalbard. However, they stated that this would need further research. Altogether, there could be a detachment zone present in a unit that is

126

younger than previously assumed, formed in response to Tertiary compression. In such, the minor faults could dip towards the west, in correlation with the formation of the décollement. However, this detachment zone is interpreted with great uncertainty due to the weak and discontinuous reflectors in the area. It is particularly challenging to state its extent and exact location. For these reasons, a deep-level décollement is not included in the final results, as it would need further research to be stated with confidence.
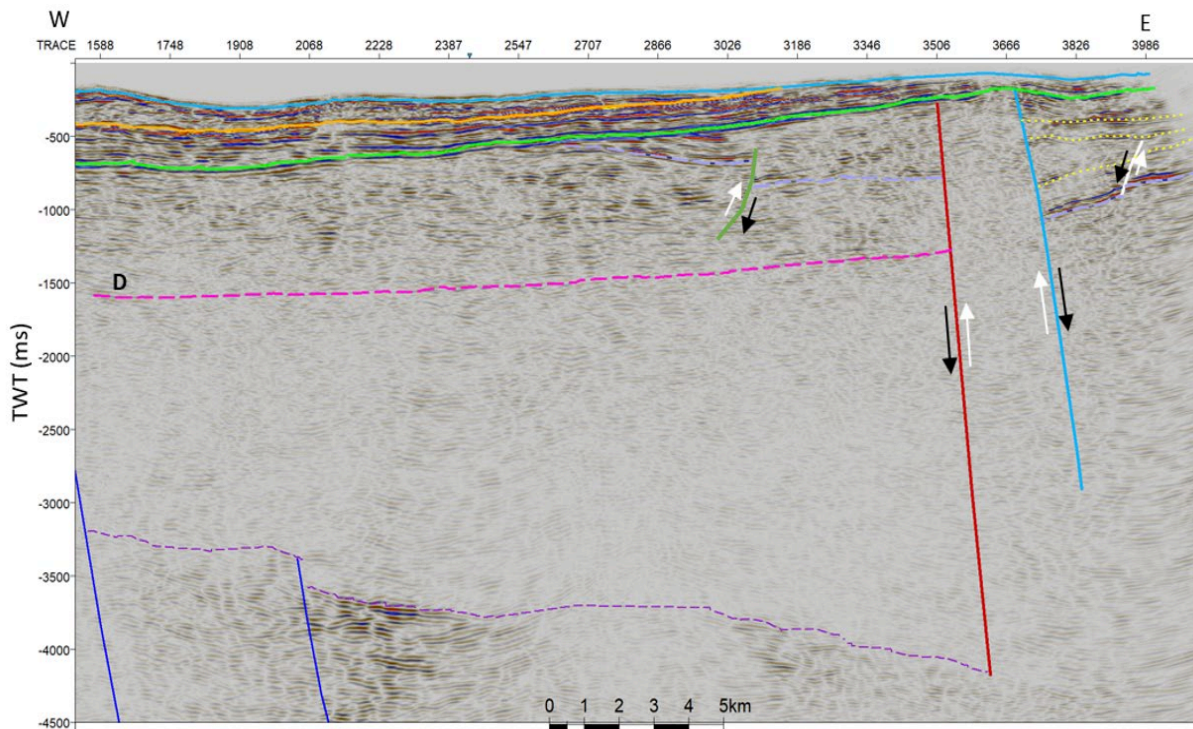
Figure 7.22: Interpretation of a possible detachment zone (dotted pink) in the upper part of the Devonian unit, which could possibly be of younger strata. The formation of the décollement may be linked to the WSFTB. A minor west-dipping reverse fault (green) is interpreted above the décollement in line 4.
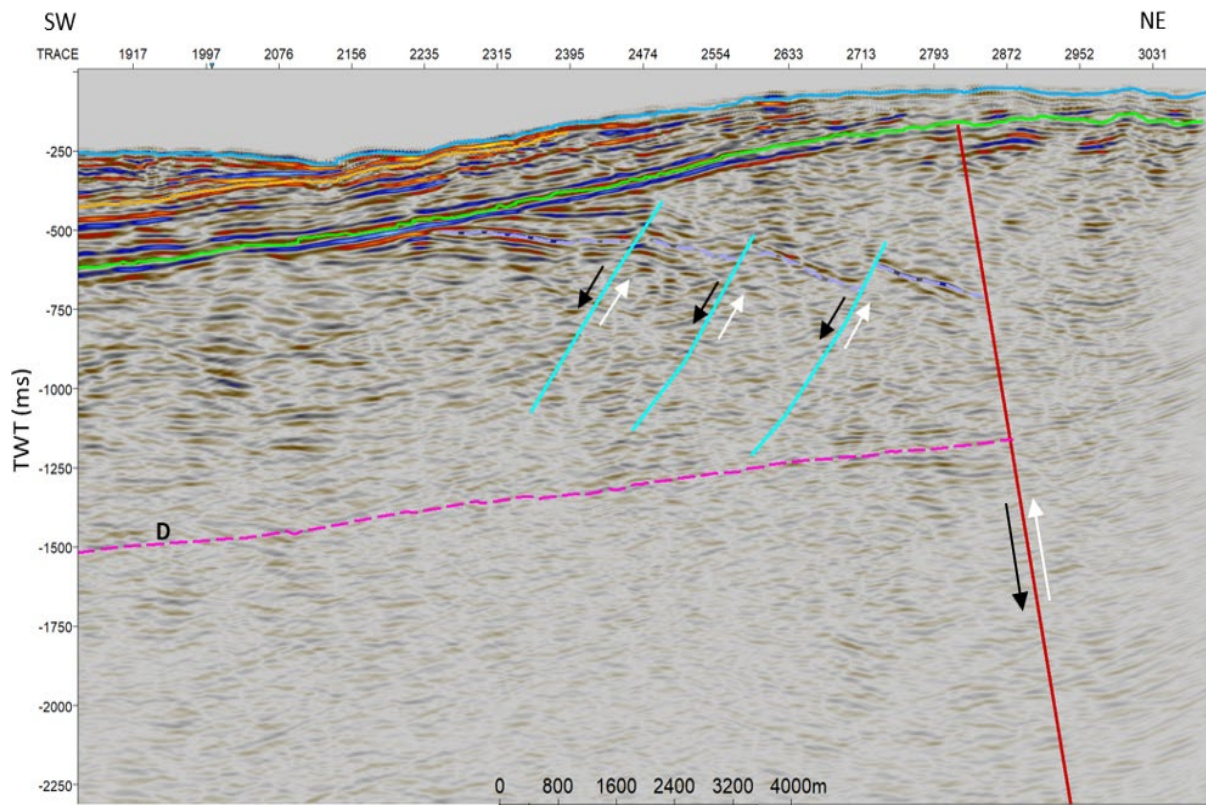
Figure 7.23: Interpretation of a possible detachment zone (dotted pink) in the upper Devonian unit in line 3. The décollement is overlain by a minor west-dipping normal faults (turquoise).

In summary, this study suggests that two steep east-dipping fault, a western reverse fault and an eastern normal fault, may describe the BFZ. However, this study has been limited by particularly weak and discontinuous reflectors within the complex BFZ, which has made it challenging to establish a structural model with confidence. Other interpretation options may therefore also apply. Hence, this study proposes the need for future research of denser and higher resolution seismic data in the BFZ to further elaborate these findings.

7.2.2.3   The Blomesletta Fault

The Blomesletta Fault is present in line 5 that covers an area in Nordfjorden, stretching in an WSW-ENE direction (Figure 1.1). Figure 7.24 displays the interpretation of a high-angled reverse fault that displaces the Devonian unit above the base of the Carboniferous strata. It dips steeply towards the east. The fault is interpreted to spring out to two minor reverse faults, based on the reflector displacements along the top mid-Carboniferous horizon. These faults seem to terminate in the Permian-Carboniferous strata. At least three west-dipping thrust faults can be interpreted above the reverse Blomesletta Fault, which are interpreted to attach to a common

sole thrust in the lower Permian evaporites. According to the findings by Bergh et al. (1997) and Blinova et al. (2013), this represents the lowermost décollement D1. A close-up of the décollement and overlying thrust faults is displayed in Figure 7.25.
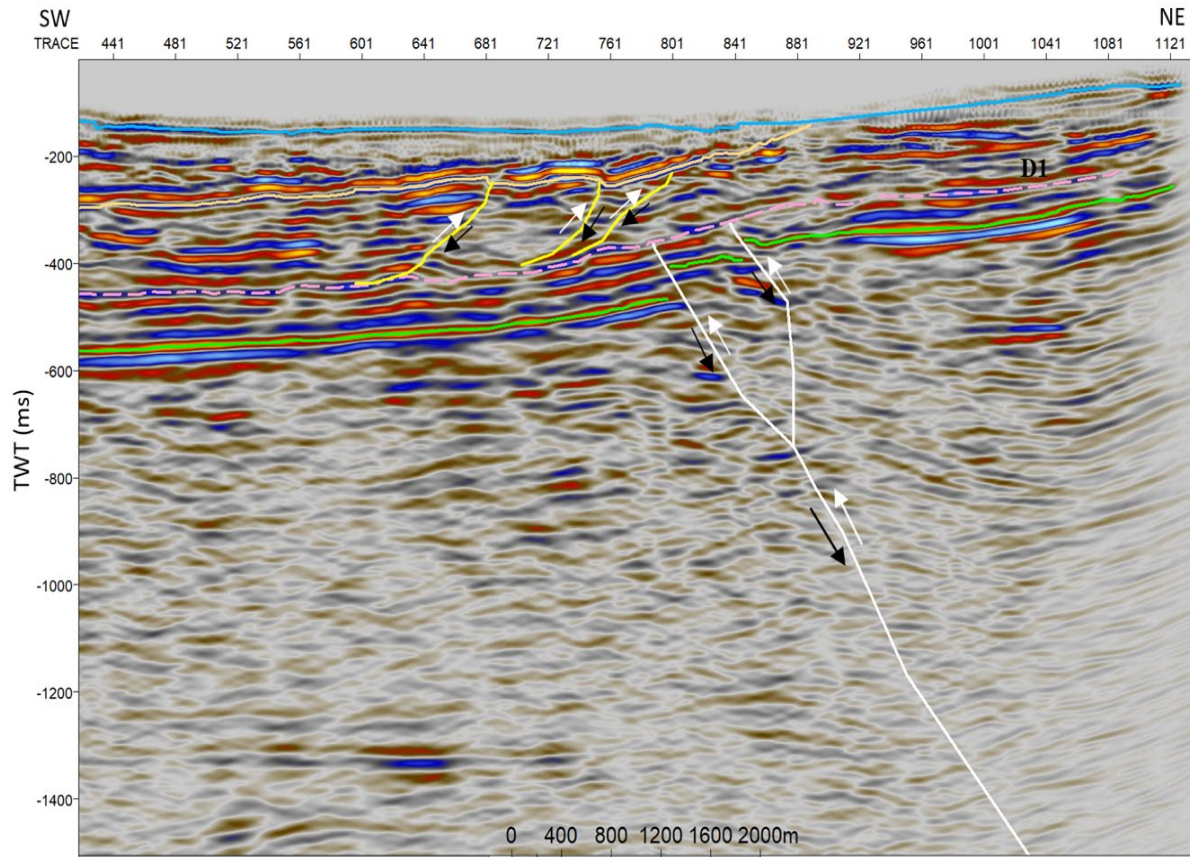
Figure 7.24: The Blomesletta Fault is interpreted as an east-dipping reverse fault (white), which displaces the top mid-Carboniferous horizon (green). West-dipping thrust faults (yellow) above the major reverse fault attach to the lower décollement D1 (pink dashed line) along the Permian-Carboniferous strata (orange).
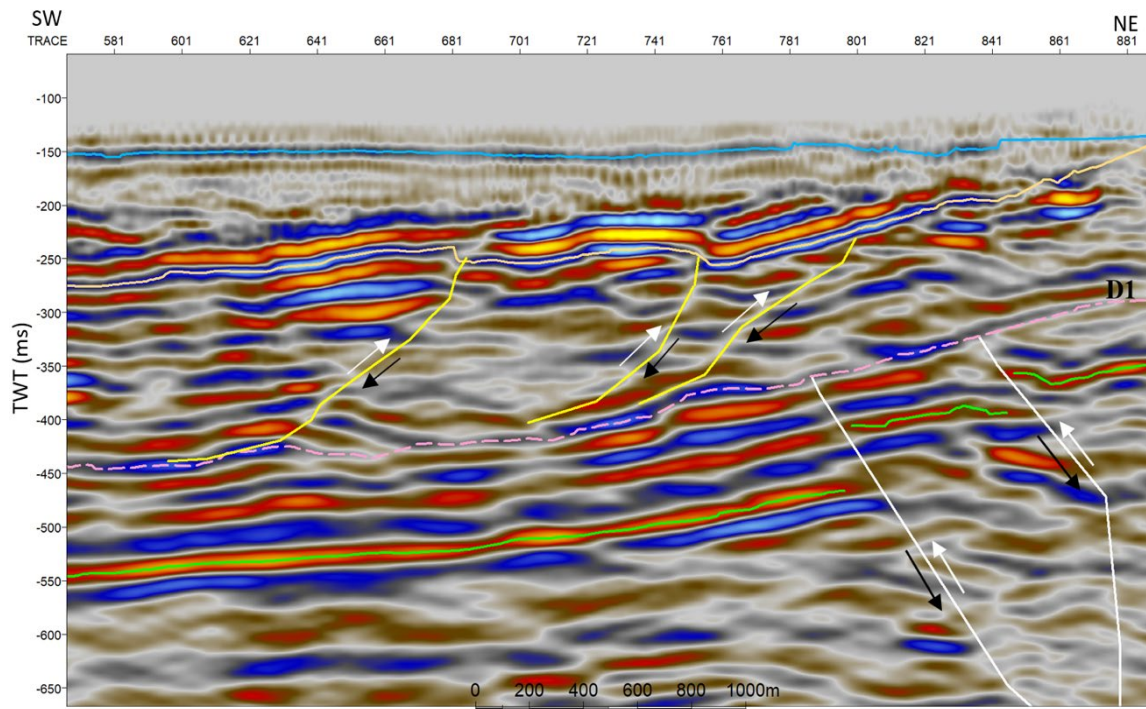
Figure 7.25: A close-up of the interpreted west-dipping thrust faults (yellow) above the Blomesletta fault, which are connected to a décollement (D1) along the Permian-Carboniferous strata (pink dashed line).

The observations in the Blomesletta Fault are in agreement with the findings by Bergh et al. (1997) and Blinova et al. (2013). The latter identified a vertical throw of ca. 50 ms, while Bergh et al. (1997), who studied the fault onshore, found a throw of ca. 200 ms. The vertical throw in this study approximates 100 ms. The reverse-slip of the Blomesletta Fault is suggested to have formed in response to compressional forces during the formation of the WSFTB in the Tertiary, but may also originate from waning tectonic movement in the Late Carboniferous (Blinova et al., 2013).

7.2.2.4 Stratigraphy and structures in Hecla Hoek

The basement is generally interpreted deep (2200 - 4000 ms) in the seismic lines. The top basement reflectors appear scattered in the seismic, which makes it challenging to pinpoint the horizon in some places. In other areas, the basement appears with a clear contrast to the overlying almost-transparent Devonian sandstone. The basement is shallowest in the SW and deepest in the NE. It reaches 2200 ms in the eastern most location of the study area, in line 3, while reaching a depth of around 4000 ms along the BFZ (see Figure 6.10). Likewise, Bælum & Braathen (2012), Skaara (2020) and Ågesen (2021) identified gradual subsidence to the NE, reaching around 4000 ms.

The overall weak and chaotic reflectors of the Hecla Hoek make it possible to derive several interpretation models for the structures in the unit. Two interpretation options are included in this study, one with two east-dipping normal faults (Figure 7.26) and the other with two west-dipping reverse faults (Figure 7.27). The correlation across the lines gives large displacement in the weak amplitude areas, which is likely caused by the presence of high angle faults. The weak reflectors in the Hecla Hoek make it difficult to determine the dipping direction, so both options may be realistic. Earlier research states that the basement rock of Svalbard has likely undergone several orogenic episodes and is therefore strongly folded and faulted (Hjelle, 1993). In such, the undulating appearance of the Hecla Hoek is interpreted to be related to folding. A prominent N-S trending graben-topography has been identified in the basement rock of Svalbard (Bergh et al., 1997; Blinova et al., 2012; Blinova et al., 2013; Skaara, 2020; Ågesen, 2021). The study by Bergh et al. (1997) was conducted on land, while the latter studies used seismic marine data from Isfjorden, Nordfjorden and Sassenfjorden. Blinova et al. (2013) observed a normal fault-bounded topography. Likewise, Skaara (2020) and Ågesen (2021) argued for the presence of east-dipping normal faults. These are likely to originate from the extension and orogenic collapse that occurred post-Caledonian, which formed the large fault-bounded Devonian rift basin (Dallmann, 2015). For these reasons, the interpretation of two east-dipping normal faults is chosen as most likely for the Hecla Hoek. These structures are interpreted in line 3 and 4. Figure 7.26 displays the interpretation derived in figure 4.
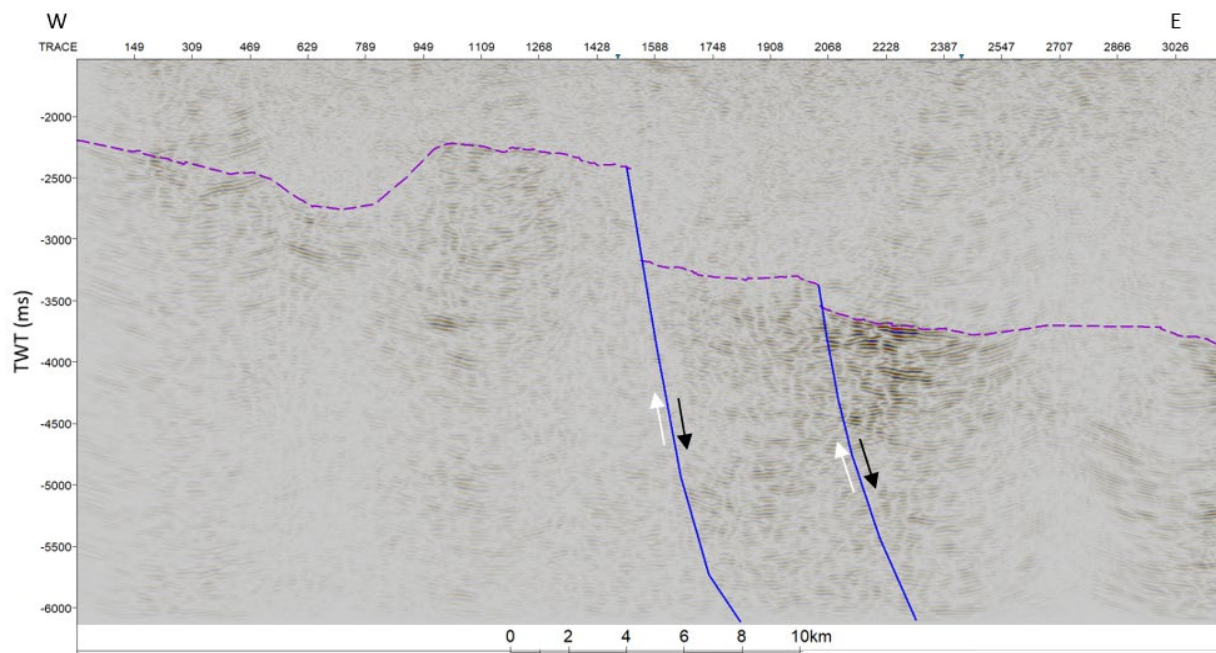
Figure 7.26: The first and most likely interpretation option of the Hecla Hoek, line 4. The top Hecla Hoek horizon (purple) is interpreted with an undulating appearance and two east-dipping normal faults (blue).
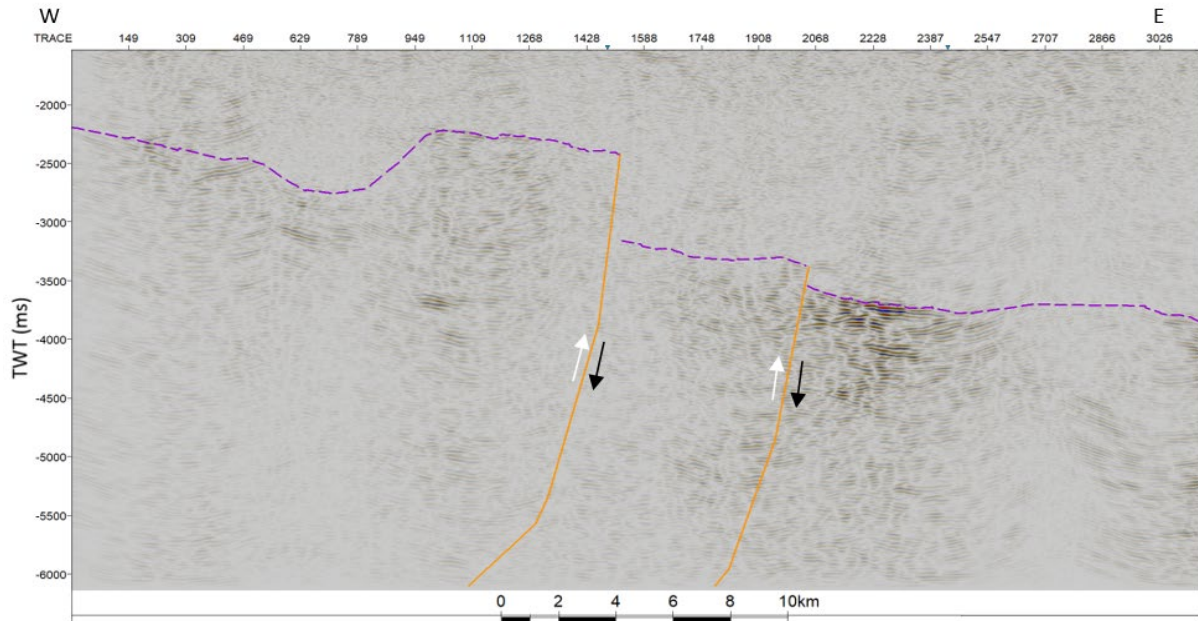
Figure 7.27: The second interpretation option of the Hecla Hoek, line 4. The top Hecla Hoek horizon (purple) is interpreted with an undulating appearance and two west-dipping reverse faults (orange).

A NE-dipping reverse fault has been interpreted in the Hecla Hoek for line 5, shown in Figure 7.28. The displacement of the fault is minor compared to the other lines and underlies the reverse Blomesletta Fault. Thus, the displacement of the Hecla Hoek may be linked to Tertiary deformation, or it may originate from waning tectonic movement in the Late Carboniferous (Blinova et al., 2013).
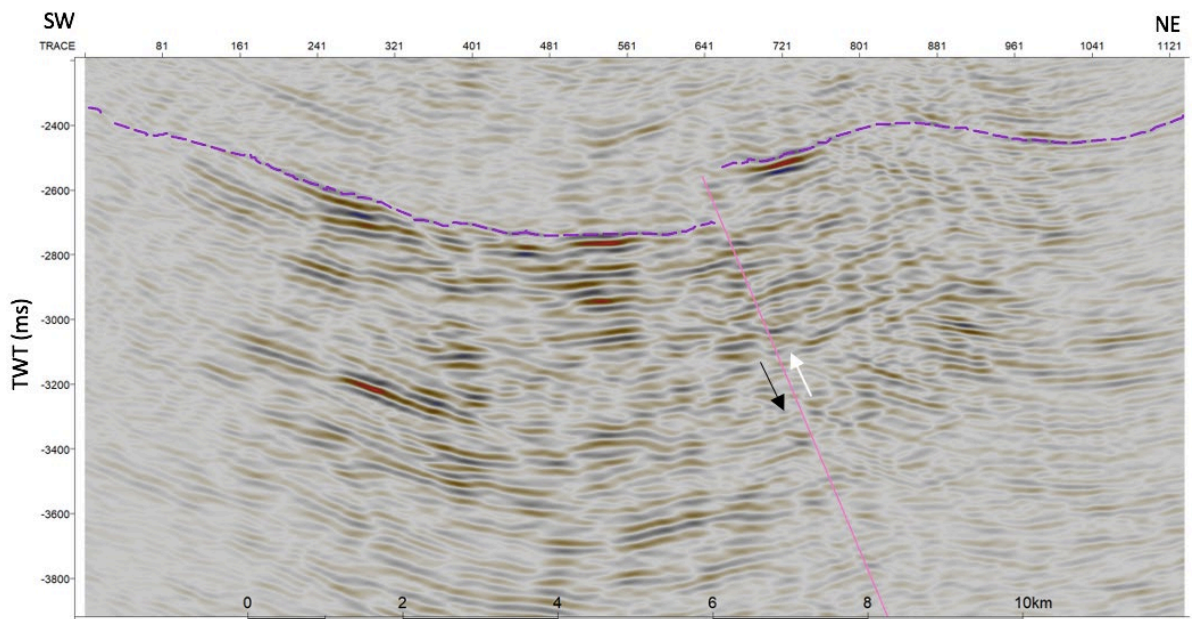
Figure 7.28: A NE-dipping reverse fault is interpreted in the Hecla Hoek for line 5.

7.2.2.5 Intrusions

Digranes & Kristoffersen (1995) and Senger et al. (2013) found well-exposed igneous intrusions in Central Spitsbergen. They identified extensive, layer-parallel high amplitude reflections in Sassenfjorden and in the SE of Nordfjorden that was partially coincident with the Top Permian reflector, and connected this to outcrop findings along the shore (Figure 7.29). Likewise, Skaara (2020) and Ågesen (2021) argued for the presence of igneous intrusions along the top Permian reflector in close-by seismic lines. Dolerite intrusions have also been identified in several wells in the surrounding area. The DH4 2009 well of Adventdalen found a 2 m thick dolerite intrusion, penetrating the Early Cretaceous and Triassic successions (Senger et al. 2014).

Based on previous research and findings in the area, both in marine seismic and onshore outcrops, sill intrusions are likely to be present in the study area. Planke et al. (2005) state that sills have a high amplitude, saucer-shape and/or abrupt reflector termination. Based on these criteria, possible sill intrusions are interpreted in line 6 and line 4, close to the Top Permian reflector (Figure 7.30 and Figure 7.31). However, it should be noted that geological structures visible in the seismic are constrained by the seismic resolution, given in Table 6.1. Thus, intrusions smaller than the vertical and horizontal resolution will not be observed in the seismic, but may be present in the area.
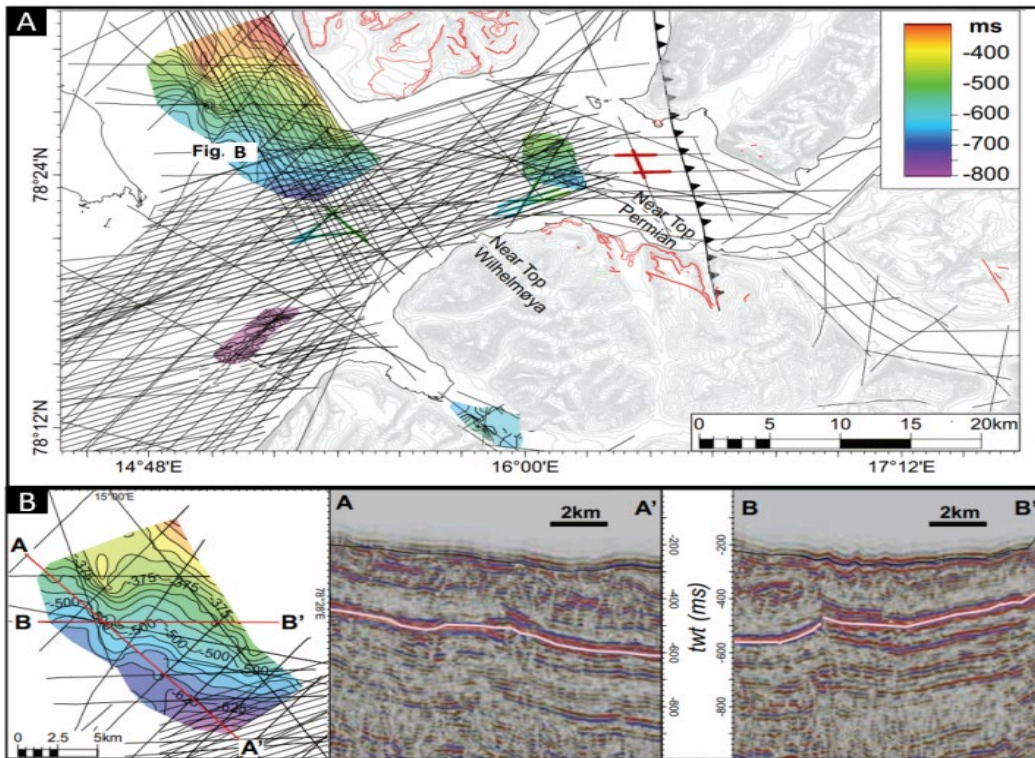
Figure 7.29: Senger et al. (2013) identified sill intrusions offshore in Isfjorden, in correlation with outcrop finding along the shore, highlighted in red (fig. A). The figures in B show that they identified sill intrusions along the Permian reflector. Modified from Senger et al. (2013).
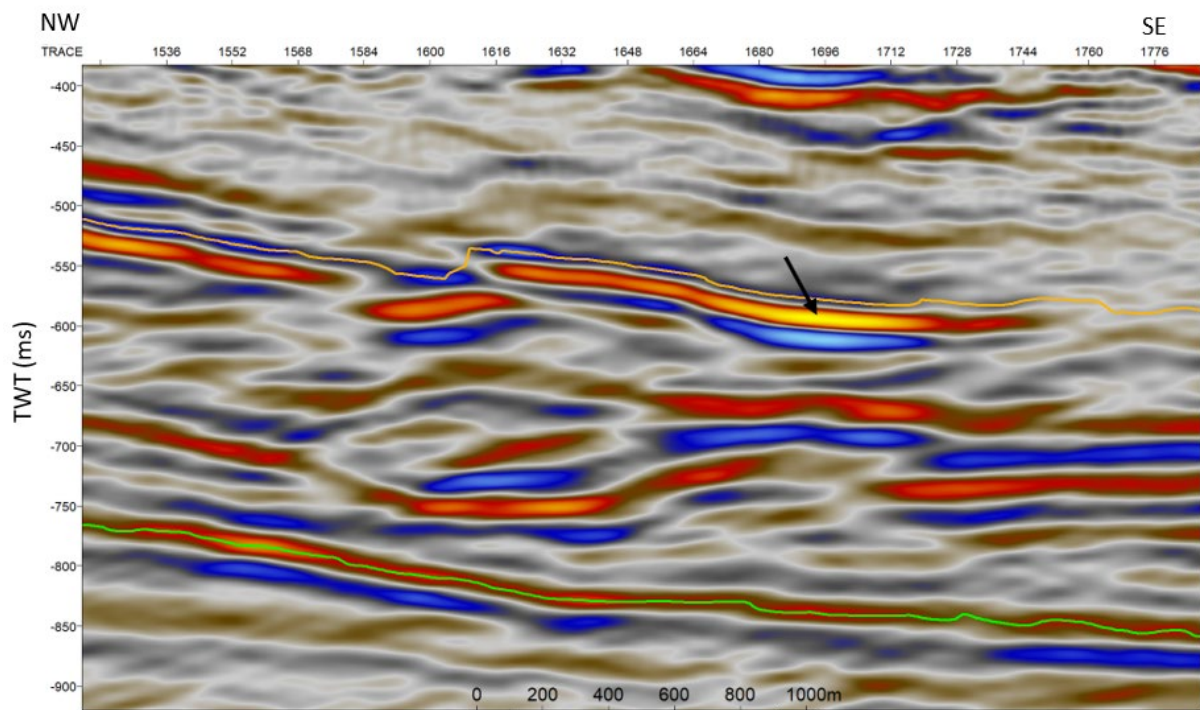
Figure 7.30: A possible sill intrusions in line 6, pointed out by the black arrow. The orange line represents the top Permian reflector, while the green line is the top mid-Carboniferous horizon.
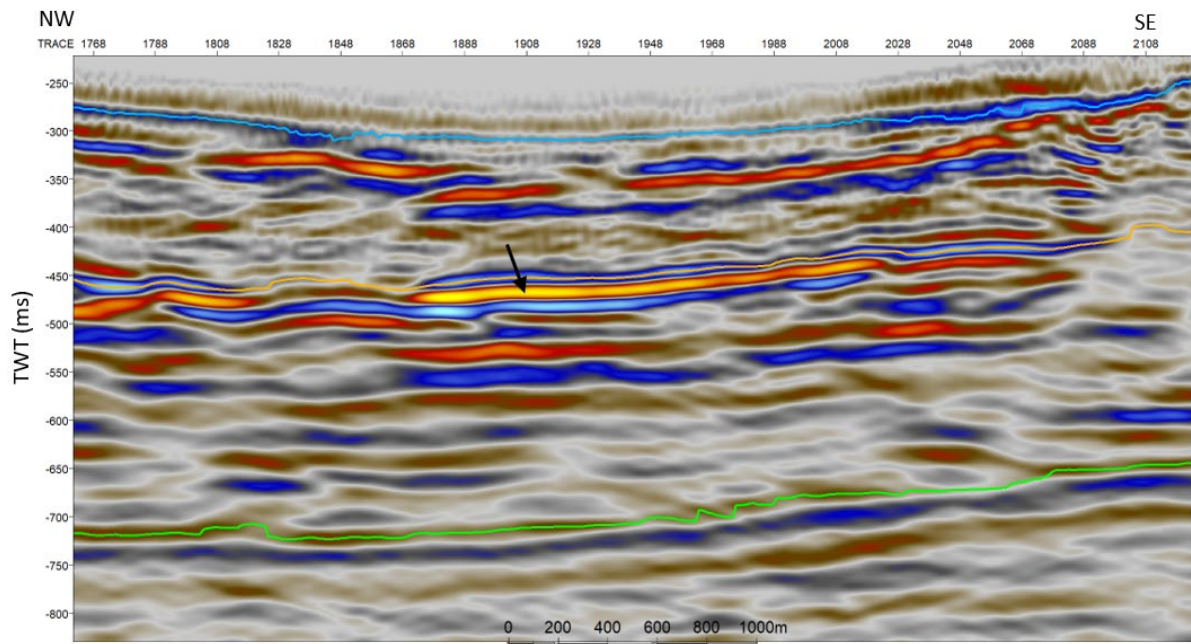
Figure 7.31: A possible sill intrusion in line 4, pointed out by the black arrow. The orange line represents the Top Permian reflector, while the green line is the top mid-Carboniferous horizon.

7.2.2.6 Décollements and fault structures

Bergh et al. (1997) and Blinova et al. (2013) identified three levels of detachments, which formed in response to the Tertiary deformation and WSFTB formation. The lowermost décollement (D1) is found in the Gipshuken Formation of Lower Permian evaporites, the middle (D2) in the Triassic shale of Braviasberget and the upper (D3) in the Jurassic-Cretaceous shales of Janusfjellet formation. The two uppermost décollements are not present in any of the seismic lines of this study, as Middle Triassic successions and younger units are eroded in the NE part of Isfjorden. However, the lowermost detachment layer is present in the study area. The décollement D1 was discussed in the chapter for the Blomesletta Fault (chapter 7.2.2.3). The major east-verging reverse fault seems to terminate in a detachment layer in the lower Permian unit (Figure 7.32). West-verging reverse thrust faults are interpreted in the upper Permian unit, splaying from the sole thrust of D1.
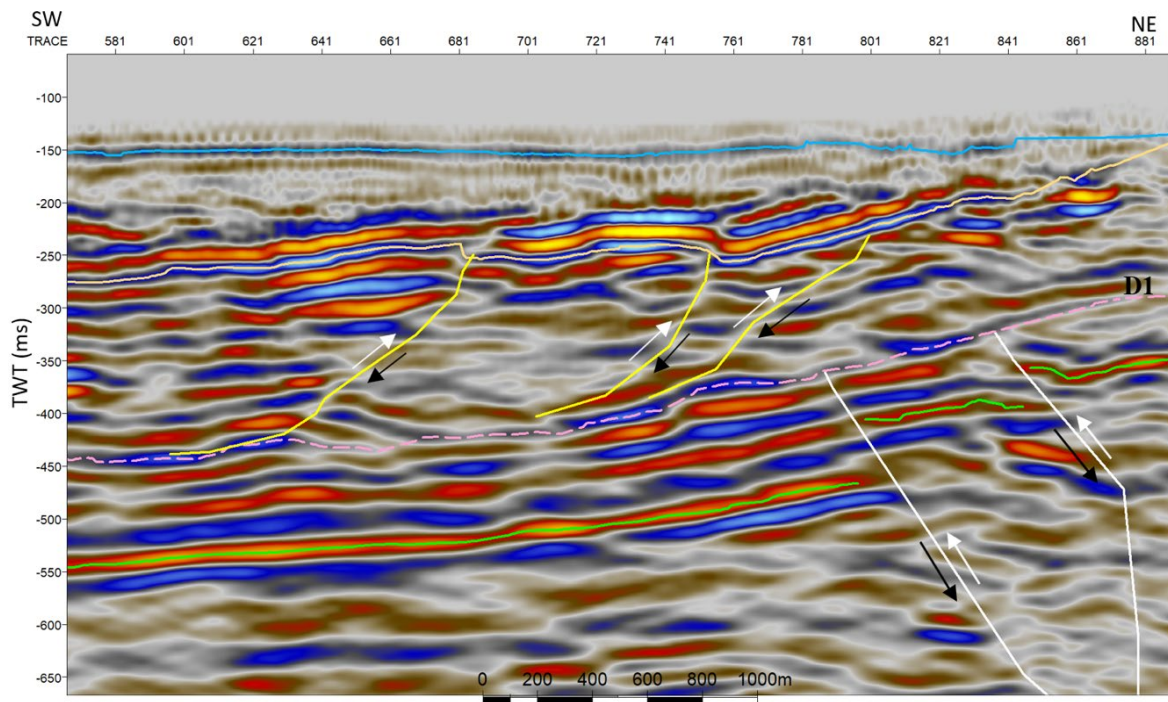
Figure 7.32: Reverse thrust faults (yellow) splay from the detachment layer D1 (pink dashed line), above the major reverse Blomesletta Fault (white) in line 5.

A normal fault and reverse fault have been identified in line 4, displayed in Figure 7.33. The displacement of the parallel Carboniferous and Permian reflectors are easily detected in the seismic. The steep west-dipping normal fault has a greater displacement than the reverse fault, with a vertical throw of about 50 ms, and is interpreted to extend into the Triassic unit. An east-dipping reverse fault of minor vertical displacement is interpreted to interact with the normal fault. Due to weak reflectors in the surrounding strata, it is difficult to pinpoint which were in-place prior to the other. The reverse fault may have developed during the formation of the WSFTB, which induced WSW–ENE shortening to western Spitsbergen (Bergh et al., 1997; Blinova et al., 2012), while the normal fault may have formed in response to the extensional regime after the collision.
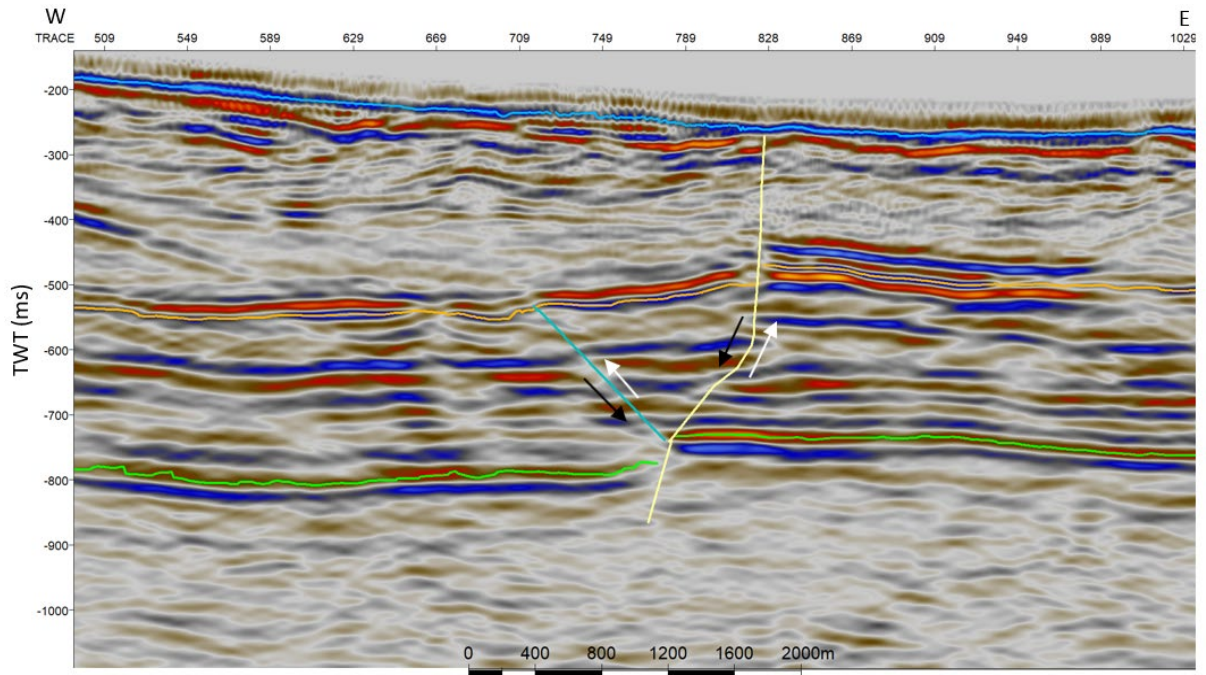
Figure 7.33: Two faults in the Carboniferous-Permian unit, a normal and reverse fault, are interpreted in line 4. These are possibly linked to the formation of the WSFTB in the Tertiary.

8 Conclusions

8.1 Processing

Four 2D multichannel seismic lines from inner Isfjorden, Sassenfjorden and Nordfjorden have been processed. The raw data suffered from strong short-interval water-bottom multiples due to the abnormal high seabed velocity in the area. The main focus during processing was to attenuate these in the best possible way to obtain a multiple-free seismic image, without significantly reducing the overall data quality. This was accomplished by the following approaches:

- The processing sequences include editing, deconvolution, frequency and velocity filtering, static correction, Kirchhoff 2D DMO-correction, velocity analysis, stack, muting and post-stack migration.

- Several velocity filters were applied throughout the processing sequences, which gave good results in the attenuation of multiples and diffraction noise. The filter limits were set to +/- 6 km/s, but were scaled up in the application just before migration to exclude more noise.

- The application of surface-consistent predictive deconvolution resulted in a distinct reduction of multiples in the seismic.

- The last remaining multiples were attenuated through stacking and muting. Velocity scaling was an essential tool in picking the correct stacking velocities, to exclude multiples and enhance the reflection from primary seismic events.

- Amplitude recovery balanced the seismic energy in the stacked sections, which also had a positive effect in attenuating diffraction noise. The module was set to amplify seismic energy in the shallow part, while scaling down the strong reflections in the deeper section.

- The seabed reflectors suffered from lack of seismic energy during processing. Some energy was regained by adding an energy regaining module and by scaling up the velocity of the seabed in the external mute module. However, due to the absence of near-offset traces in conventional acquisition, the seabed reflectors in the shallowest areas are completely removed.

- The quality of the seismic sections is significantly enhanced. The processing has been successful, and the multiples are strongly attenuated. The resulting seismic sections are concluded to contain real seismic events from subsurface geological structures.

8.2 Interpretation

The processed seismic lines were interpreted with the intention of deriving a better understanding of the geology in the study area. The process involved mapping and interpretation of stratigraphic horizons and units, followed by structural interpretation of the fault geometries in the Billefjorden Fault Zone (BFZ), Blomesletta Fault and basement. This has made it possible to derive an understanding of the geological evolution and tectonic processes that has affected the study area. The findings coincide to a large extent with previous research.

- Stratigraphic horizons and unit are interpreted from the Hecla Hoek to the seabed, which include the Devonian, top mid-Carboniferous, Permian, Triassic and a minor part of the lower Jurassic.

- The stratigraphic units above the mid-Carboniferous surface are shallowing to the north-east, which resemble an anticline where the hinge is located over the Billefjorden Fault Zone. In contrast, the basement and Devonian unit are shallowing to the south-west.

- Two distinct unconformities are identified along the top Permian and top mid-Carboniferous horizon. The latter was identified by a distinct underlying angular unconformity.

- A discrete half-graben structure is identified to the east of the BFZ and is interpreted as Early Carboniferous syn-rift filling that was deposited during the extensional, post-Caledonian regime. The half-graben is linked to the basin on the western side of the BFZ.

- Several structural interpretation models have been discussed to represent the BFZ due to the great uncertainty attached to the weak reflectors in the fault zone. The final and most likely model suggests two major east-dipping fault stands: a western reverse fault that displaced the basement rock and an eastern normal fault that formed the distinctive half-graben. Minor faults have been identified along the BFZ horizon, possibly formed during Early Carboniferous extension. No faults are interpreted within the main fault zone due to the almost transparent reflectors, which likely represent a complex area of an abundance of fault and folds.

- The Blomesletta Fault is interpreted as an east-verging high-angle reverse fault that terminates in an overlying Permian décollement (D1). At least three minor thrust faults splay from this sole thrust, likely occurring in response to the formation of the WSFTB in Early Tertiary.

- The Hecla Hoek has an undulating appearance, interpreted as folding, and is displaced by two steep east-dipping normal faults. A reverse fault is interpreted in the basement under the Blomesletta Fault with minor displacement.

- Possible sill intrusions are interpreted along the top Permian reflector, which coincide with the presence of magmatic activity in Svalbard during Late Jurassic and Early Cretaceous.

- The distinct displacement of a normal and reverse fault is identified in the Permian-Carboniferous unit, which possibly formed in response to the WSFTB.

References

Austegard, A. (2013). *Processing of mulichannel seismic data: An introduction, including exercises and Matlab programs.* Bergen: Dep. Earth Science, UiB.∫

Bacon, M., Simm, R., & Redshaw, T. (2003). *3-D seismic interpretation.* Cambrigde: Cambridge University Press.

Bergh, S. G., & Andersen, A. (1990). Structural development of the Tertiary fold-and-thrust belt in east Oscar II Land, Spitsbergen. *Polar Research, 8*(2), 217-236.

Bergh, S. G., Braathen, A., & Andersen, A. (1997). Interaction of Basement-Involved and Thin-Skinned Tectonism in the Tertiary Fold-Thrust Belt of Central Spitsbergen, Svalbard. *AAPG Bulletin, 81*(4), 637-661.

Bergh, S. G., Maher, H. D., & Braathen, A. (2011). Late Devonian transpressional tectonics in Spitsbergen, Svalbard, and implications for basement uplift of the Sørkapp–Hornsund High. *Journal of the Geological Society, London, 168*, 441-456.

Blinova, M., Faleide, J. I., Gabrielsen, R. H., & Mjelde, R. (2012). Seafloor expression and shallow structure of a fold-and-thrust system, Isfjorden, west Spitsbergen. *Polar Research, 31*(1), 11209-11213.

Blinova, M., Faleide, J. I., Gabrielsen, R. H., & Mjelde, R. (2013). Analysis of structural trends of sub-sea-floor strata in the Isfjorden area of the West Spitsbergen Fold-and-Thrust Belt based on multichannel seismic data. *Journal of the Geological Society, 170*(4), 657-668.

Braathen, A., Bælum, K., Maher, H., & Buckley, S. J. (2011). Growth of extensional faults and folds during deposition of an evaporite-dominated half-graben basin; the Carboniferous Billefjorden Trough, Svalbard. *Norsk Geologisk Tidsskrift, 91*(3), 137-160.

Braathen, A., Bergh, S. G., & Maher, H. D. (1999). Application of a critical wedge taper model to the Tertiary transpressional fold-thrust belt on Spitsbergen, Svalbard. *Geological Society of American Bulletin, 111*(10), 1468-1485.

Braathen, A., Osmundsen, P. T., Maher, H. D., & Granerød, M. (2017). The Keisarhjelmen detachment records Silurian–Devonian extensional collapse in Northern Svalbard. *Terra Nova, 30*(1), 34-39.

Bælum, K., & Braathen, A. (2012). Along-strike changes in fault array and rift basin geometry of the Carboniferous Billefjorden Trough, Svalbard, Norway. *Tectonophysics, 546-547*, 38-55.

Cartwright, J., & Huuse, M. (2005). 3D seismic technology: the geological 'Hubble'. *Basin Research, 17*, 1-20.

CGG & Lundin Norway. (2017). *TopSeis - The Tailor Made Solution for Subsurface Exploration and Development in the Barents Sea.* Retrieved April 26 2022, from http://www.ipt.ntnu.no/rose/lib/exe/fetch.php?media=2017:vinje_edit.pdf

CGGVertias. (2008). Geocluster 5.0 Release Notes.

Dallmann, W. K. (1999). *Lithostratigraphic lexicon of Svalbard: review and reccomendations for nomenclature use : Upper Palaeozoic to Quaternary bedrock.* Tromsø: Norwegian Polar Institute, Polar Environmental Centre.

Dallmann, W. K. (2015). *Geoscience Atlas of Svalbard.* Tromsø: Norwegian Polar Institute.

Digranes, P. & Kristoffersen, Y. (1995). Use of Mode-converted Waves in Marine Seismic Data to Investigate the Lithology of the Sub-bottom Sediments in Isfjorden, Svalbard. *Pure and applied geophysics, 145*(2), 313-325.

Faleide, J. I., Tsikalas, F., Breivik, A. J., Mjelde, R., Ritzmann, O., Engen, O., . . . Eldholm, O. (2008). Structure and evolution of the continental margin of Norway and the Barents Sea. *Episodes, 31*(1), 82-91.

Fookes, P. G. (2008). Some aspects of the Geology of Svalbard. *Geology today, 24*(4), 146-152.

Fossen, H. (2010). *Structural Geology.* Cambridge: Cambridge University Press.

Gadallah, M., & Fisher, R. (2009). *Exploration geophysics, An introduction.* Heidelberg: Springer-Verlag.

Gee, D., & Page, L. M. (1994). Caledonian terrane assembly on Svalbard: New evidence from (40)Ar/(39)Ar dating in Ny Friesland. *American Journal of Science (1880), 294*(9), 1166.

Gelius, L. J., & Johansen, T. A. (2010). *Petroleum geophysics.* Bergen: UniGEO.

Hart, B. S. (2000). *3-D seismic interpretation: A primer for geologists.* Tusla, Okla: Society for Sedimentary Geology.

Herron, D. A. (2011). *First steps in seismic interpretation.* Tusla, Okla: Society of Exploration Geophysics.

Hjelle, A. (1993). Geology of Svalbard. Oslo: Norsk Polarinstitutt.

Kandilarov, A., R, M., Okino, K., & Murai, Y. (2008). Crustal structure of the ultraslow spreading Knipovich Ridge, North Atlantic, along a presumed amagmatic portion of oceanic crustal formation. *An International Journal for the Study of the Earth Beneath the Sea, 29*(2), 109-134.

Kearey, P., Brooks, M., & Hill, I. (2002). *An introduction to geophysical exploration.* Oxford: Blackwell Science.

Krabbendam, M., & Dewey, J. F. (1998). Exhumation of UHP rocks by transtension in the Western Gneiss Region, Scandinavian Caledonides. *Geological Society, London, Special Publications, 135*(1), 159-181.

Lamar, D. L., Reed, W. E., & Douglass, D. N. (1986). Billefjorden fault zone, Spitsbergen: Is it part of a major Late Devonian transform? *GSA Bulletin, 97*(9), 1083-1088.

Maher, J., & Braathen, A. (2011). Lovehoven Fault and Billefjorden rift basin segmentation and development, Spitsbergen, Norway. *Geological Magazine, 148*(1), 154-170.

Mitchum, R. M., Vail, P. R., & Thompson, S. (1977). The depositional sequence as a basic unit for stratigraphic analysis. *AAPG Memoir, 26*, 53-62.

Mjelde, R. (2003). *Cruise report: SVALEX 2002: MCS survey Isfjorden and shelf by use of Håkon Mosby.*

Mjelde, R. (2010). *Seismic Equipment.* Retrieved March 1 2022, from http://buster.geo.uib.no/emodules/modules/Seismic%20equipment/index.html

Mjelde, R. (2011). *Seismic Acquisition: Geophysical Principles*. Retrieved March 1 2022, from http://buster.geo.uib.no/emodules/modules/Seismic%20acquisition%20principles/index.html

Obeid, H., Khettab, H., Marais, L., Hallab, M., Laurent, S., & Boutouyrie, P. (2017). Evaluation of arterial stiffness by finger–toe pulse wave velocity: optimization of signal processing and clinical validation. *Journal of Hypertension, 35*(8), 1618-1625.

Planke, S., Rasmussen, T., Rey, S. S., & Myklebust, R. (2005). Seismic characteristics and distribution of volcanic intrusions and hydrothermal vent complexes in the Vøring and Møre basins. *6*(1), 833-844.

Norsk Polarinstitutt. (2022). *Svalbardkartet*. Retrieved March 2 2022, from https://www.npolar.no/kart/

Poley, J, PH. (1964). Critical-angle effects in seismic exploration. *Geophysical Prospecting, 12*(4), 397-421.

Recept, G., Hakan, K. & Derman, D. (2019). Optimum parameter selection in offset-dependent predictive deconvolution: testing on multichannel marine seismic data. *Marine geophysical researches, 40*(4), 601-617.

Samson, C., & West, G. F. (1992). Correction for water depth variations of marine crustal reflection seismic data using refraction statics. *Marine Geophysical Research, 14*(1), 65-76.

Schlumberger. (2022). *Petrel E&P Software Platform*. Retrieved May 3 2022, from https://www.software.slb.com/products/petrel

Senger, K., Roy, S., Braathen, A., Buckley, S., Bælum, K., Gernigon, L., . . . Tveranger, J. (2013). Geometries of doleritic intrusions in central Spitsbergen, Svalbard: an integrated study of an onshore-offshore magmatic province with implications for CO2 sequestration. *Norwegian Journal of Geology, 93*, 143-166.

Senger, K., Tveranger, J., Ogata, K., Braathen, A., & Planke, S. (2014). Late Mesozoic magmatism in Svalbard: A review. *Earth-science reviews, 139*, 123-144.

Sheriff, R. E. (2002). *Encyclopedic Dictionary of Applied Geophysics* . Society of Expolration Geophysics, Geophysical Reference Series No. 12.

Sheriff, R. E., & Geldart, L. P. (1995). *Exploration seismology.* Cambridge: Cambridge University Press.

Skaara, S. (2022). Prosessering og tolkning av refleksjonsseismiske data fra Isfjorden, Svalbard. *Mastergrad i Geovitenskap, Institutt for Geovitenskap: Universitetet i Bergen.*

Steel, R. J. (1976). Devonian Basins of Western Norway – Sedimentary response to tectonism and to varying tectonic context. *Tectonophysics, 36*(1), 207-224.

Steel, R. J., & Gloppen, T. G. (1980). *Late Caledonian (Devonian) Basin Formation, Western Norway: Signs of Strike-Slip Tectonics during Infilling.* Oxford, UK: Blackwell Publishing Ltd.

Stewart, S. A. (2012). Interpretation validation on vertically exaggerated reflection seismic sections. *Journal of structural geology, 41*, 38-46.

Van der Pluijm, B., & Marshak, S. (2004). *Earth structure: an introduction to structural geology and tectonics.* New York: W.W. Norton Co.

Vetti, V. V., & Fossen, H. (2012). Origin of contrasting Devonian supradetachment basin types in the Scandinavian Caledonides. *Geology, 40*(6), 571-574.

Worsley, D. (1986). *The geological history of Svalbard: evolution of an Arctic archipelago.* Stavanger: Den norske stats oljeselskap as.

Yilmaz, Ö. (2001). *Seismic data analysis: Processing, inversion, and interpretation of seisimc data.* Tusla, Okla: Society of Exploration Geophysics.

Ågesen, L. (2021). Processing and interpretation of reflection seismic data from Isfjorden, Svalbard. *Master of Science thesis, Department of Earth Science: University of Bergen*.

Appendix

Appendix A: Estimations

Reflection coefficient of water-bottom multiples (for vertical incident angle)

Assuming a water velocity of 1480 m/s (found from the direct line), a seabed velocity of 4500 m/s (measured from the refractions) and a density of 2g/cm³, then the reflection coefficient of the water-bottom is given by:

$$R = \frac{V_2\rho_2 - V_1\rho_1}{V_2\rho_2 + V_1\rho_1} = \frac{4.5 * 2 - 1.48 * 1}{4.5 * 2 + 1.48 * 1} = 0.72$$

As the sea-surface reflection coefficient equals -1, this means that the amplitude of the seabed reflection and the following multiples is given by: R, $-R^2$, R^3, $-R^4$ etc. This is valid after correction for spherical spreading (Ruud, pers. comm).

Static correction

The static correction assumes a water velocity of 1480 m/s and seabed velocity of 4500 m/s. Travel-time differences are estimated and applied to the receiver and shot water depth separately, before the total correction for all traces is found. The average is then removed for each CDP-gather, before the static correction is applied to all traces in the dataset. In this way, the average water depth is kept, while local variations are corrected. First, the water-bottom estimation of the depth (*d*) is given by:

$$d = \frac{1480 * TWT}{2}$$

Followed by a travel-time difference (dT) estimation:

$$dT = \frac{TWT}{2} \frac{1 - 1480}{4500}$$

Total internal reflection for the seabed

The calculation of the total internal reflection is derived using Snell's law, where p is the raypath parameter:

$$p = \frac{sin\theta_1}{v_1} = \frac{sin\theta_2}{v_2}$$

The critical angle is given by:

$$\frac{sin\theta_c}{v_1} = \frac{1}{v_2}$$

By assuming a seabed velocity of 4500 m/s and a water velocity of 1480 m/s, the angle of the total internal reflections is calculated by:

$$Asin \frac{1.48}{4.5} = 19.2$$

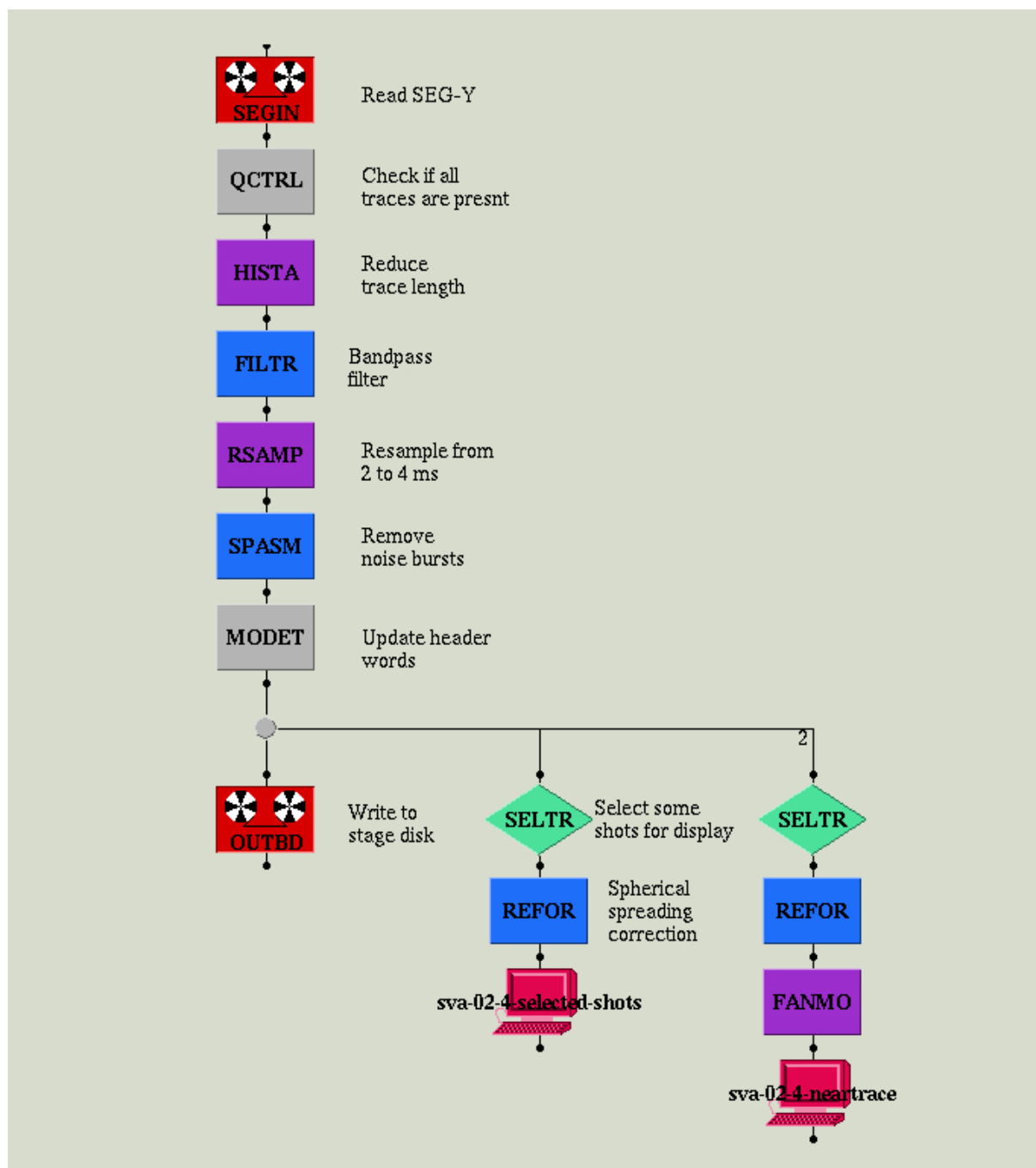The offset at which total internal reflections occur is estimated for a water depth of 50 m (TWT 66 ms):

$$2\tan(19.2) * 50 = 34.8$$

In such, all seabed reflections with an offset greater than 34.8 m will represent total internal reflections. These have a velocity somewhat lower than 4500 m/s.
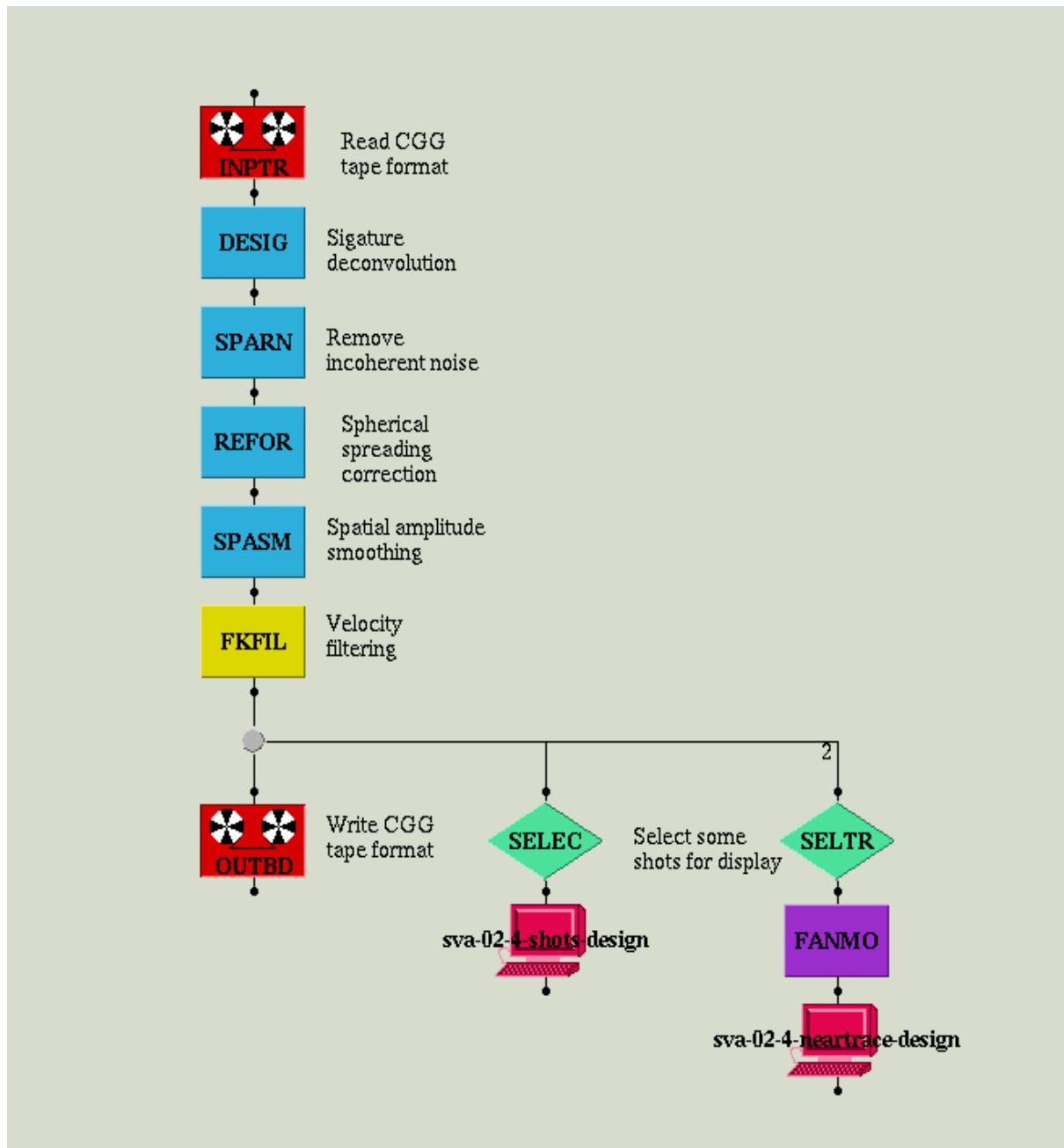
Appendix B: Processing sequences

This section includes the processing sequences from Xjob that was used during processing.
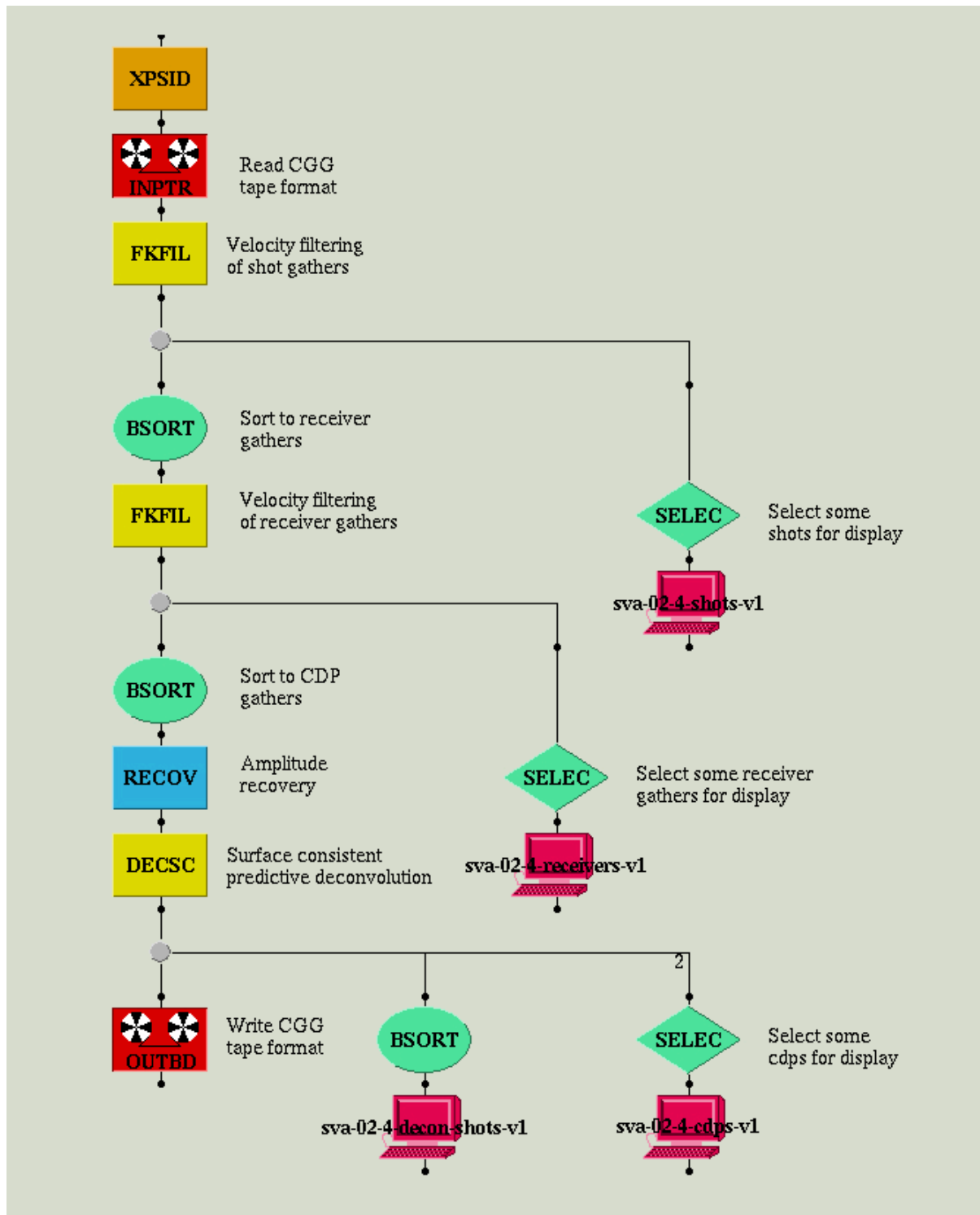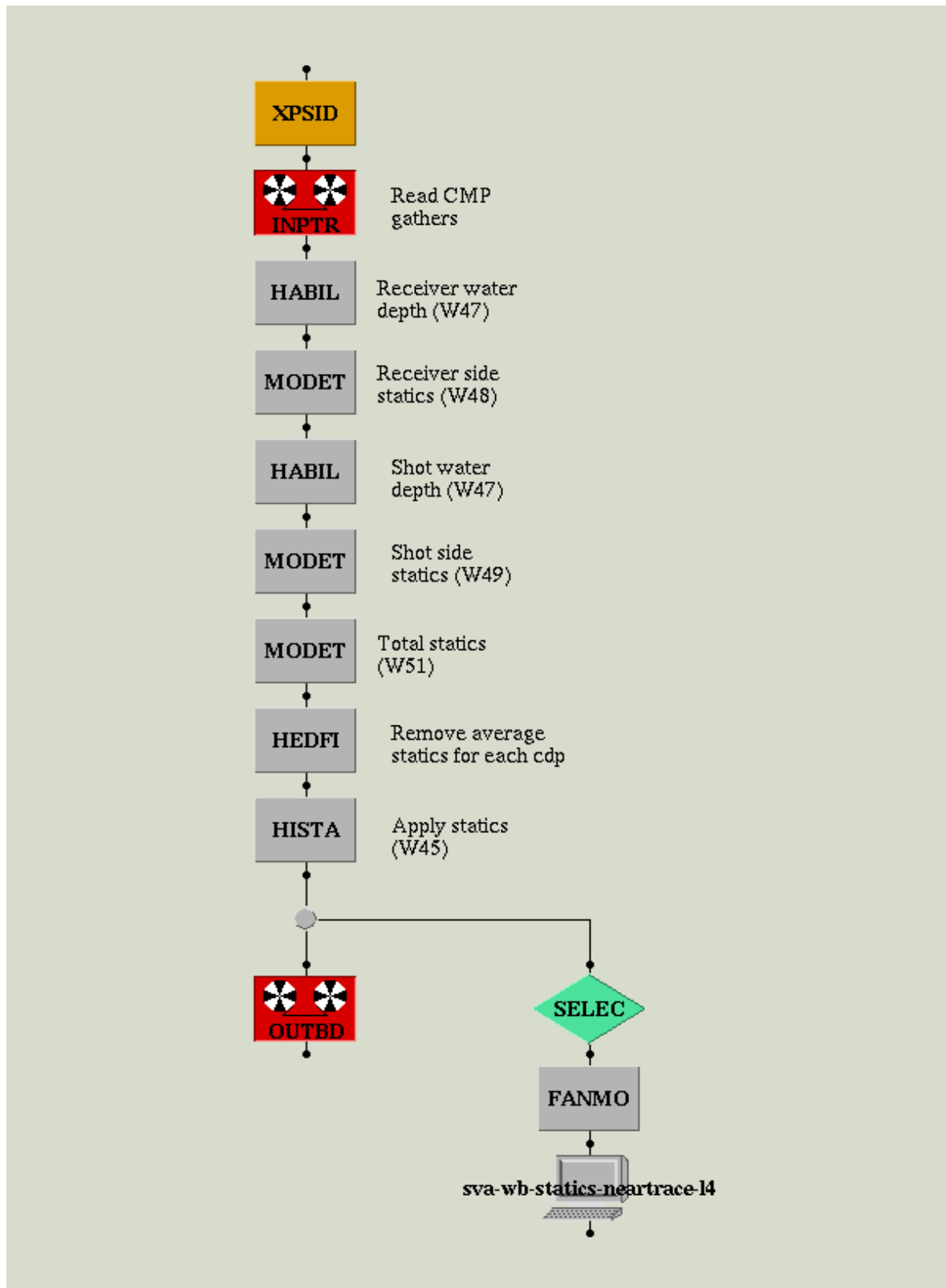
Editing
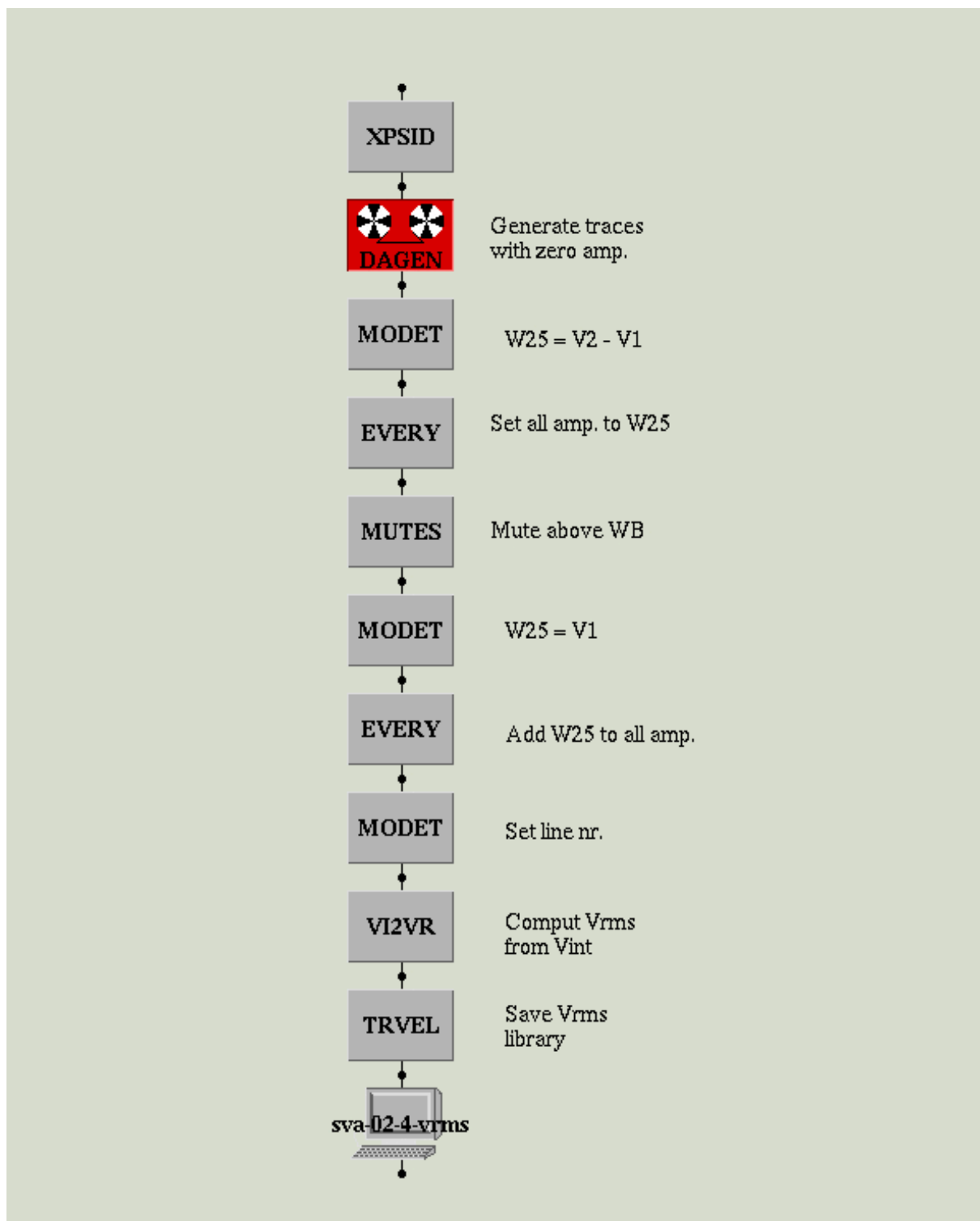
Filtering and deconvolution (1)
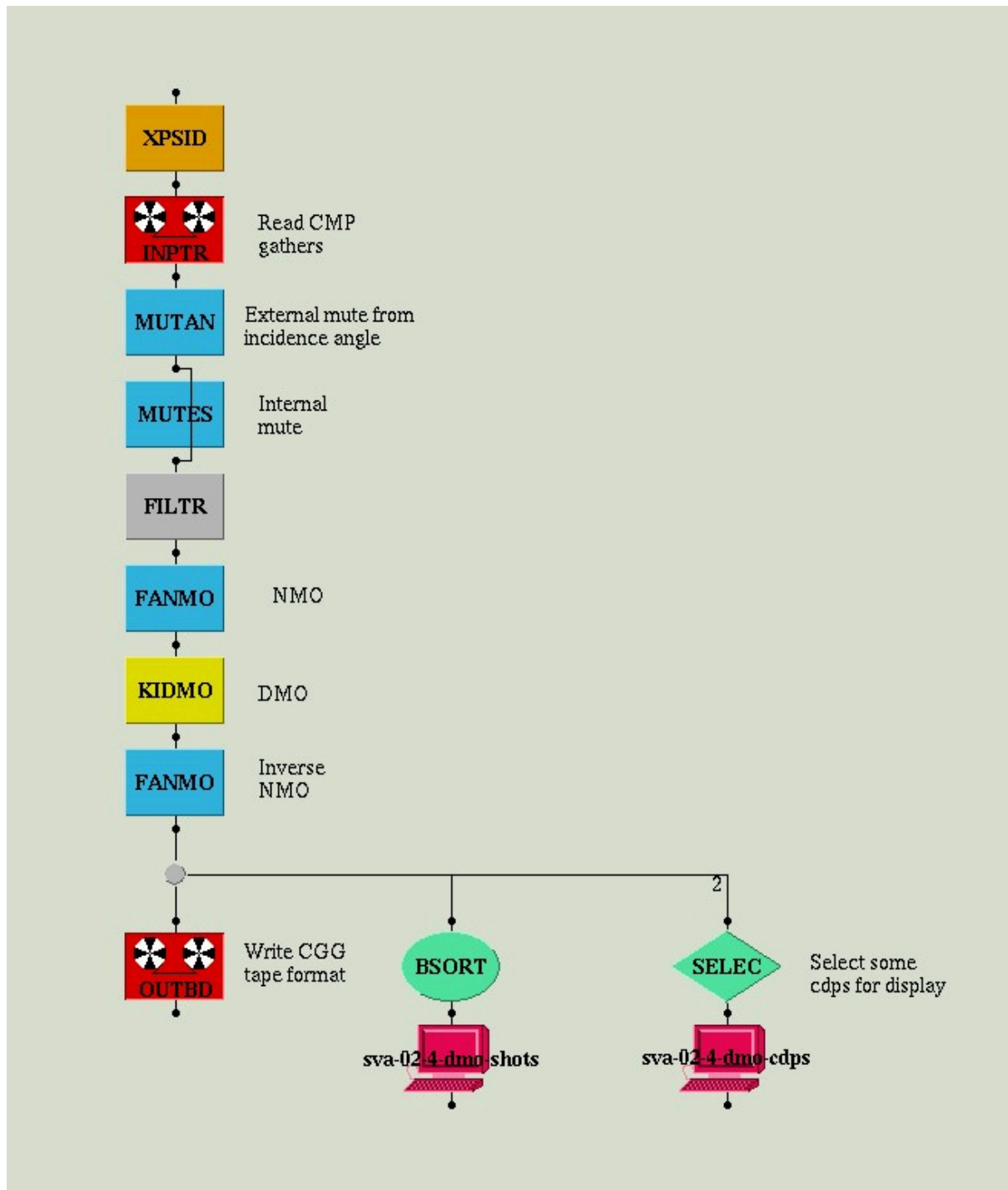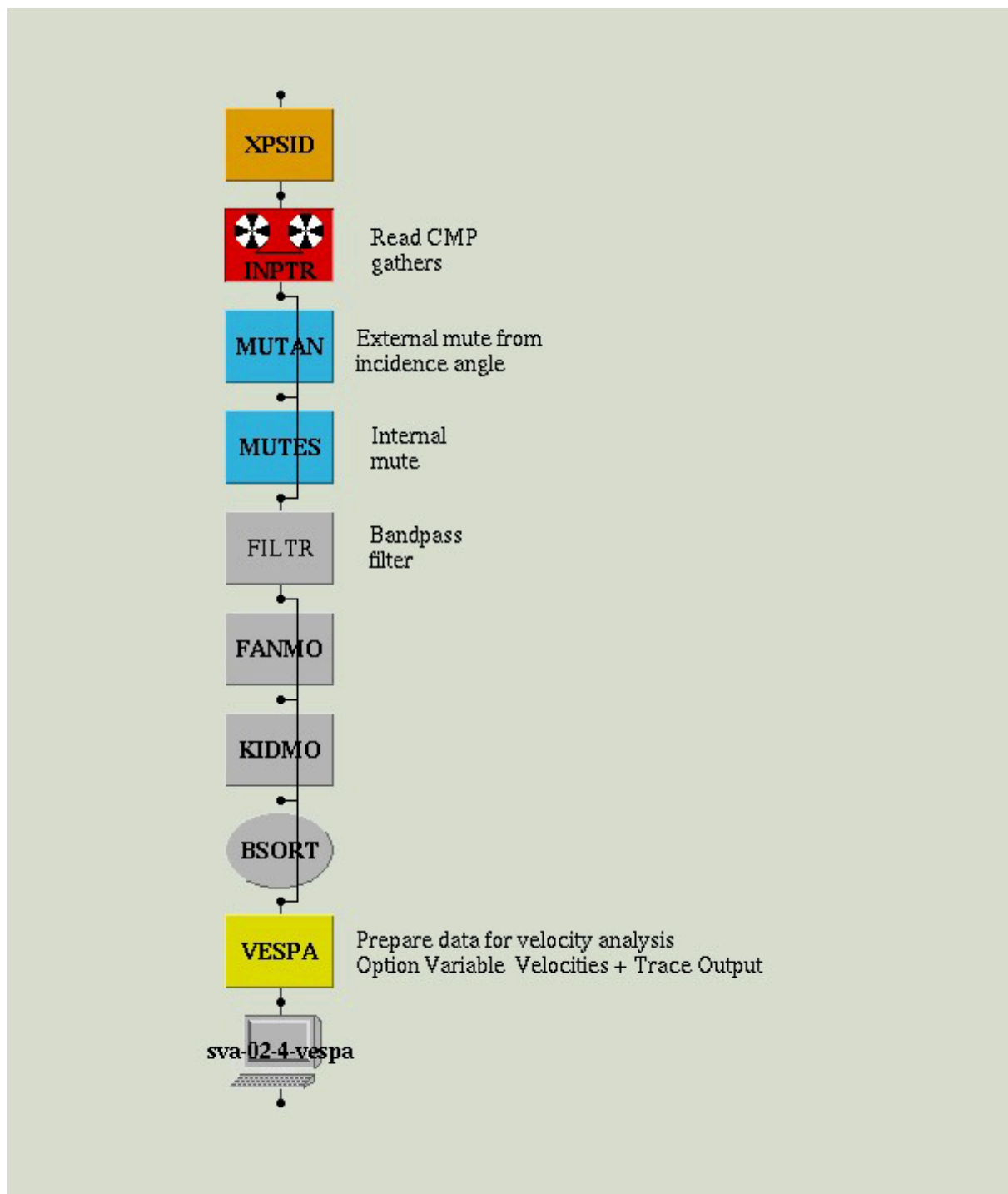
Filtering and deconvolution (2)

XPSID

INPTR — Read CGG tape format

FKFIL — Velocity filtering of shot gathers

BSORT — Sort to receiver gathers

FKFIL — Velocity filtering of receiver gathers

SELEC — Select some shots for display

sva-02-4-shots-v1

BSORT — Sort to CDP gathers

RECOV — Amplitude recovery

DECSC — Surface consistent predictive deconvolution

SELEC — Select some receiver gathers for display

sva-02-4-receivers-v1

OUTBD — Write CGG tape format

BSORT

sva-02-4-decon-shots-v1

SELEC — Select some cdps for display

sva-02-4-cdps-v1
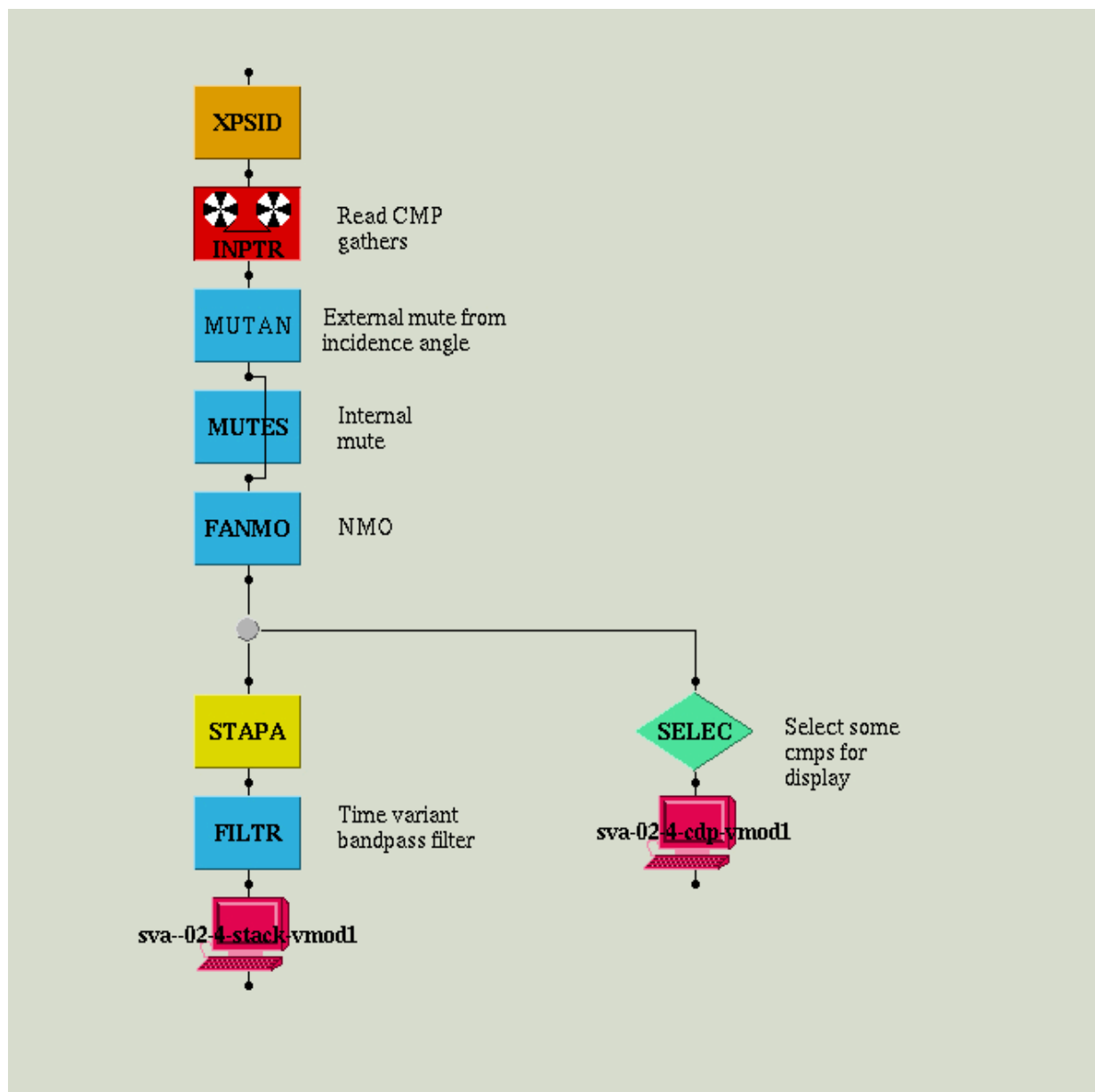
Static correction

Velocity model

DMO-correction

Preparation for velocity analysis

Stacking

Post-stack migration

XPSID

sva--02-4-stack-vmod2.15237.cst

MNGTY

MODET

MUTES

FILTR

TSFIL

FKFIL — Velocity filtering

RECOV

REFOR — Spherical spreading correction

SCALE

FXMIG

PFILT — Phase filter

MUTES

SELTR

sva-02-4-mig
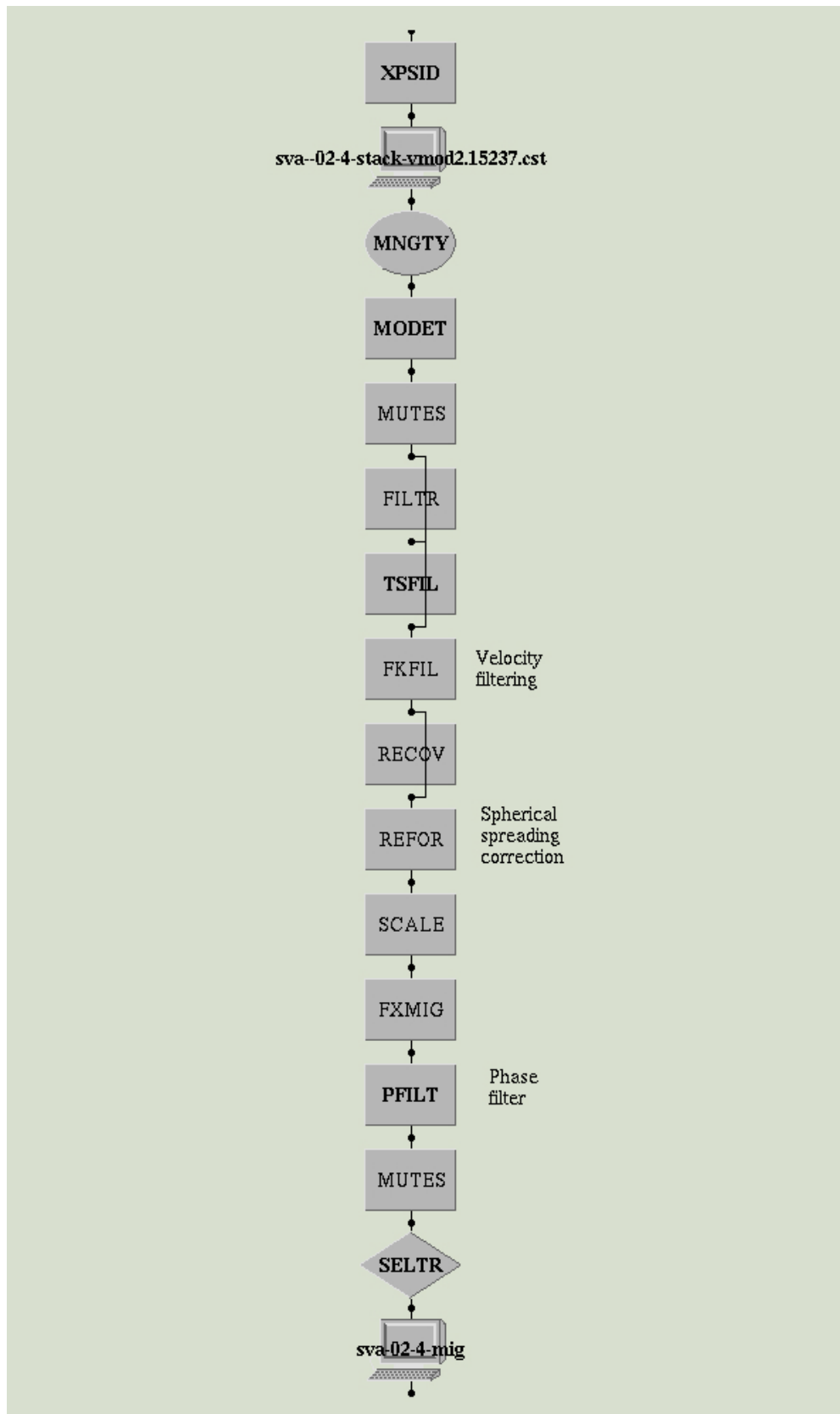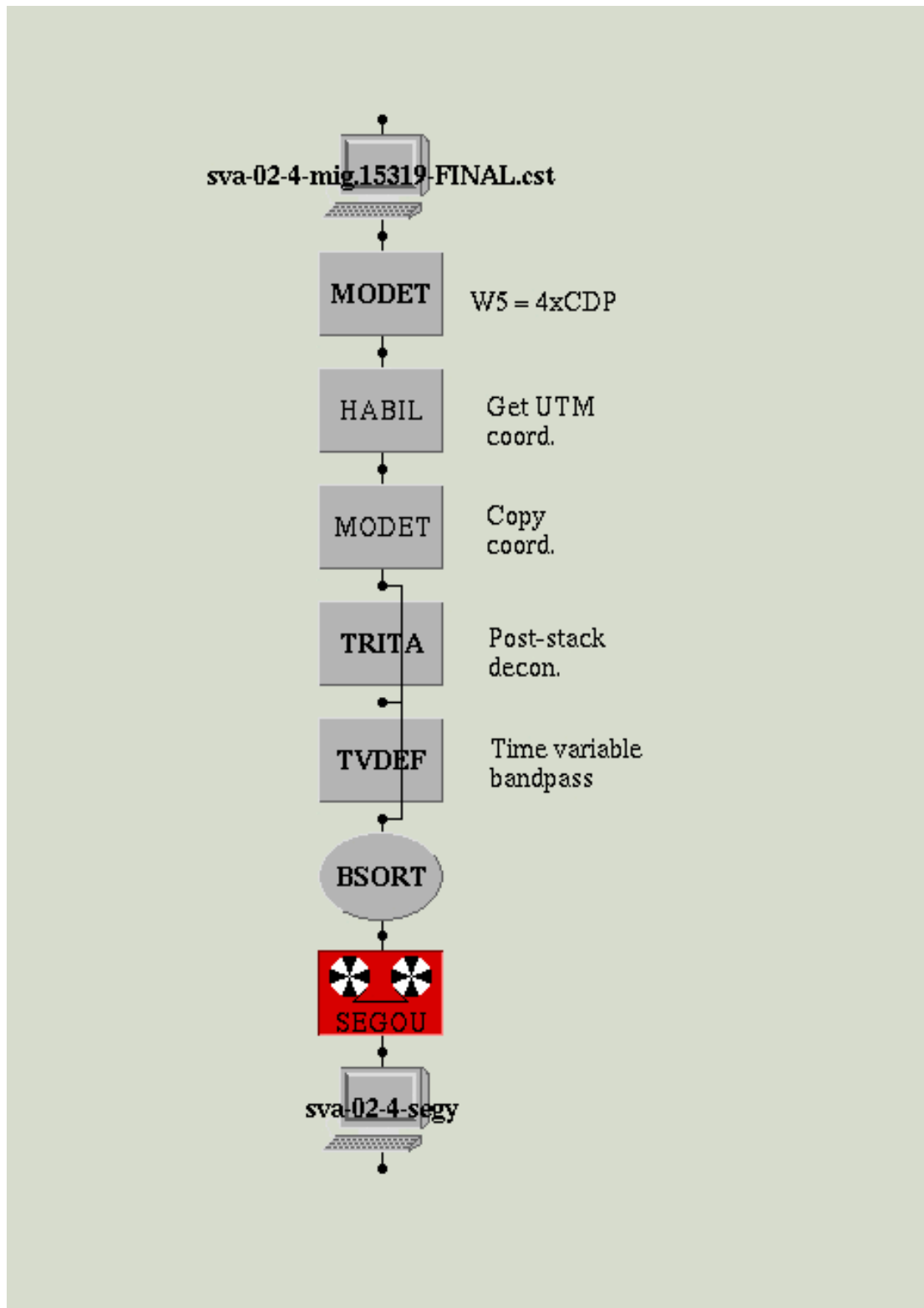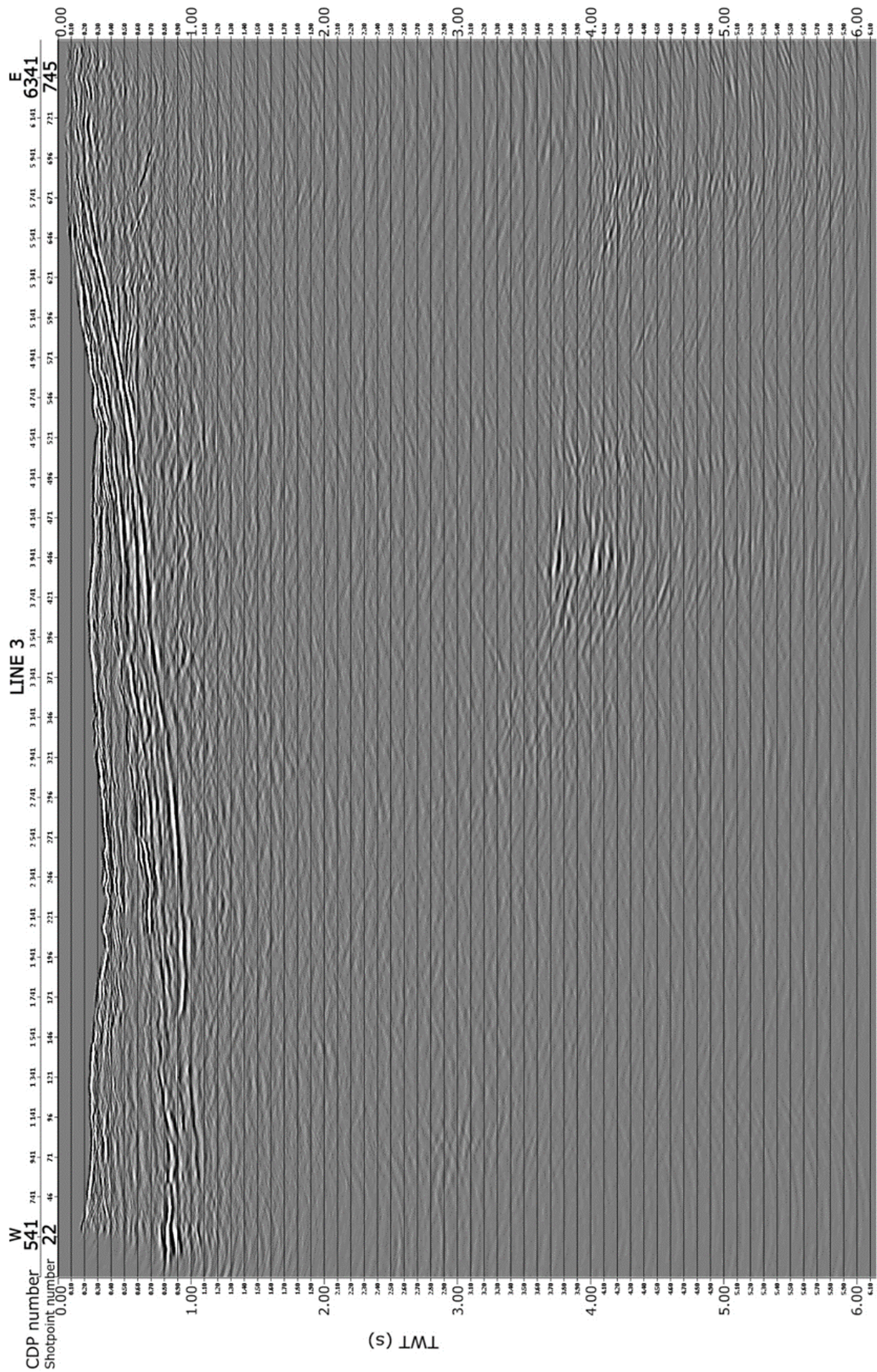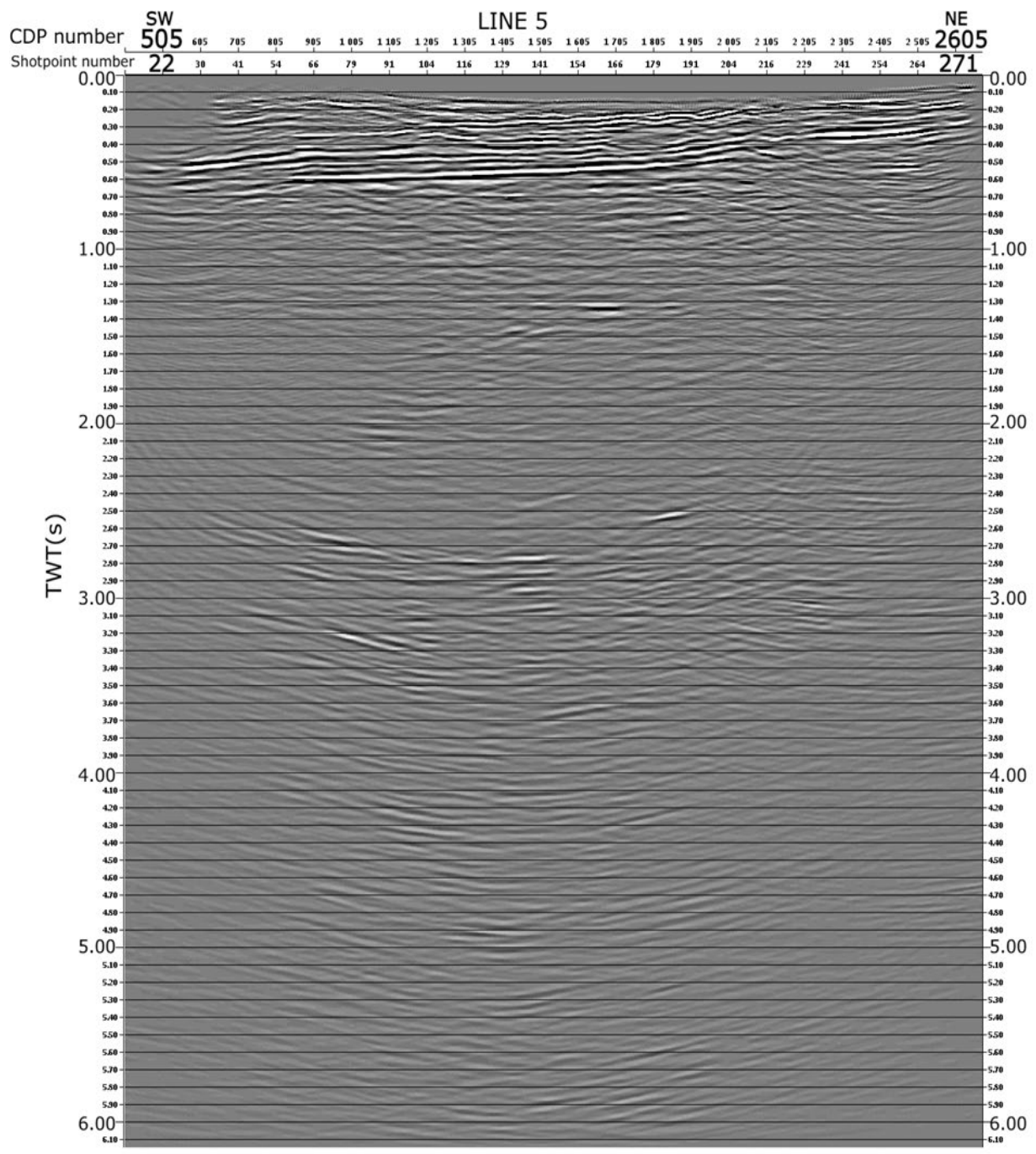
Converting to SEG-Y format

Appendix C: Processed lines

The final processed lines are presented with a variable density plot, reaching 6.10 s (TWT). Amplitude scaling (ratio): 0.2.

LINE 4

SW — LINE 5 — NE

| CDP number | 505 | 605 | 705 | 805 | 905 | 1 005 | 1 105 | 1 205 | 1 305 | 1 405 | 1 505 | 1 605 | 1 705 | 1 805 | 1 905 | 2 005 | 2 105 | 2 205 | 2 305 | 2 405 | 2 505 | 2605 |
| Shotpoint number | 22 | 30 | 41 | 54 | 66 | 79 | 91 | 104 | 116 | 129 | 141 | 154 | 166 | 179 | 191 | 204 | 216 | 229 | 241 | 254 | 264 | 271 |

TWT(s)

161

162

Appendix D: Interpreted lines

The final interpreted profiles are displayed in full section, i.e., reaching 6100 ms. All lines are displayed without and with the interpretation, respectively.

Line 3

165

Line 4

166

167

Line 5

168